

**Fatigue Behavior of Notched Carbon Epoxy Laminates
During Reversed Cyclic Loads**

by

Charles Emanuel Bakis

Dissertation submitted to the Faculty of the
Virginia Polytechnic Institute and State University
in partial fulfillment of the requirements for the degree of
Doctor of Philosophy
in
Engineering Mechanics

APPROVED:

K. L. Reifsnider, Co-chairman

W. W. Stinchcomb, Co-chairman

E. G. Henneke

D. T. Mook

R. H. Plaut

August 5, 1988

Blacksburg, Virginia

**Fatigue Behavior of Notched Carbon Epoxy Laminates
During Reversed Cyclic Loads**

by

Charles Emanuel Bakis

K. L. Reifsnider, Co-chairman

W. W. Stinchcomb, Co-chairman

Engineering Mechanics

(ABSTRACT)

The relationships between fatigue damage, stress redistribution, and residual stiffness and strength were investigated for notched graphite epoxy laminates during fully-reversed cyclic loads. Two material systems, AS4/3501-6 and AS4/1808, two lamination arrangements, $(0,45,90,-45)_{s4}$ and $(0,45,0,-45)_{s4}$, and two notch configurations, central hole and opposing semi-circular edge notches, were used to obtain a fundamental understanding of the fatigue effect in specimens under low and high cycle lifetimes. Damage was evaluated with penetrant-enhanced X-ray radiography and laminate deply. Tensile and compressive residual strengths were measured at three stages of damage development. A recently developed nondestructive testing technique, Stress Pattern Analysis by Thermal Emission, was implemented to obtain full-field measurements of surface stresses during damage initiation and growth. A new micromechanical theory of the adiabatic thermoelastic effect in laminated fiber composites was conceived to assist the interpretation of SPATE measurements.

Acknowledgements

It is a pleasure to acknowledge the following agencies and persons for contributing, directly or indirectly, to this dissertation:

- The Air Force Office of Scientific Research, for funding this work through contract 85.0087.
- Professors Reifsnider and Stinchcomb, for providing the opportunity to perform this work, for highly competent service as co-advisors, for intellectual stimuli, and for "going to bat" for the author innumerable times.
- Professor Stinchcomb, for six years of infinite patience and sound advice on all matters.
- Professors Henneke, Mook, and Plaut, for serving on the author's committee.
- The irrepressible, irreplaceable, Laid Back Research Group, for comradery, annual conferences, and informal seminars.
- The laid back guys in the ESM shop — — for somehow machining the 400+ specimens for this project.
- and , for helping to get things done.
- and , for efficient and proficient secretarial work.
- (Dr. Vocab), for new vocabulary words, grammatical advice, and philosophical discussions.
- (Dr. Deploy), for deploying all the specimens for this investigation.
- , and , for helping with the enormous test matrix.
- , for assistance with the figures and, more important, for continued patience and understanding during the preparation of this dissertation.
- The author's parents, , for years of encouragement.

Table of Contents

Introduction	1
1.1 Problem Statement	1
1.2 Objectives	3
1.3 Approach	3
1.4 Literature Review	4
Investigative Approach	13
2.1 Experiments	13
2.1.1 Mechanical Testing	13
2.1.2 Test Specimens	16
2.1.3 Stiffness Measurement	20
2.1.4 Ultrasonic C-Scan	21
2.1.5 X-Ray Radiography	21
2.1.6 Laminate Deploy	22
2.1.7 Adiabatic Thermography	23
2.1.7.1 Thermographic Apparatus	24
2.1.7.2 Mechanical Excitation	26
2.1.7.3 Specimen Preparation	27
2.1.7.4 SPATE Setup	29
2.1.7.5 Interpretation of Results	30
2.2 Analysis	35
2.2.1 Adiabatic Thermoelastic Effect	35

- Basic Material Characterization** **63**
- 3.1 Monotonic Strength 63
- 3.2 Fatigue Life 66
- 3.3 Stiffness Measurements 69

- Fatigue Damage Mechanisms** **75**
- 4.1 AS4/3501-6, Orthotropic Laminate 76
 - 4.1.1 Center-Notched Specimens 76
 - 4.1.1.1 High Load Level 76
- 4.2 AS4/1808, Quasi-Isotropic Laminate 81
 - 4.2.1 Center-Notched Specimens 81
 - 4.2.1.1 High Load Level 81
 - 4.2.1.2 Low Load Level 89
 - 4.2.2 Double-Edge-Notched Specimens 97
 - 4.2.2.1 High Load Level 97
- 4.3 AS4/1808, Orthotropic Laminate 100
 - 4.3.1 Center-Notched Specimens 100
 - 4.3.1.1 High Load Level 100
 - 4.3.1.2 Low Load Level 110
- 4.4 Summary of Damage Mechanisms 117
 - 4.4.1 Effect of Lamination Arrangement 120
 - 4.4.2 Effect of Load Level 121
 - 4.4.3 Effect of Material System 123
 - 4.4.4 Effect of Notch Configuration 124

- Stress Redistribution Mechanisms** **125**

- Residual Strength** **152**

6.1 AS4/1808, Quasi-Isotropic Laminate	153
6.2 AS4/1808, Orthotropic Laminate	158
6.3 AS4/3501-6, Orthotropic Laminate	166
6.4 Summary of Residual Strength Data	169
Considerations for a Strength Model	171
7.1 Background	171
7.2 Elliptical Hole Model	174
Conclusions	182
8.1 Investigative Methods	182
8.2 Fatigue Response	183
8.2.1 Damage Development	183
8.2.2 Stress Redistribution	184
8.2.3 Residual Strength	185
Recommendations	186
References	189
Vita	200

List of Illustrations

Figure 1. Test specimen gripping arrangement	15
Figure 2. Test specimen configurations	17
Figure 3. Specimen axis and quadrant notations	19
Figure 4. Theoretical stress sensitivity of SPATE with various materials	25
Figure 5. SPATE signal in AS4/3502 laminates as a function of loading frequency	28
Figure 6. SPATE thermographs of 8-ply carbon epoxy laminates	31
Figure 7. Radiographs of 8-ply carbon epoxy laminates with fatigue damage	33
Figure 8. SPATE thermographs of 8-ply carbon epoxy laminates with fatigue damage	34
Figure 9. Dependence of adiabatic thermoelastic temperature change on in-plane stress components	39
Figure 10. Representative area of a fiber composite material	41
Figure 11. Effect of ply orientation on the temperature change in a unidirectional ply under constant axial stress or strain	48
Figure 12. Effect of ply orientation on the temperature change in an angle-ply laminate under constant axial stress or strain	49
Figure 13. Effect of ply orientation on the temperature change in a quasi-isotropic laminate under a constant global strain field	50
Figure 14. Effect of laminate Poisson's ratio on the temperature change in a 0-deg. ply under a constant longitudinal strain	51
Figure 15. Effect of fiber volume fraction on the adiabatic temperature change in a 0-deg. carbon epoxy lamina under constant longitudinal stress or strain	53
Figure 16. Predicted SPATE patterns in two center-notched carbon epoxy laminates	55
Figure 17. SPATE thermograph of a (0,90,45,-45) _s carbon epoxy laminate with the resin-rich surface layer removed	58
Figure 18. Predicted SPATE patterns in a center-notched (0,90,45,-45) _s carbon epoxy laminate with varied contributions of the constituents in the surface ply	60
Figure 19. Predicted SPATE patterns in a center-notched (0,90,45,-45) _s carbon epoxy laminate with varied ply influences	61
Figure 20. Stress vs. life data for test specimens	67
Figure 21. Stiffness change in AS4/3501-6 specimens	71

Figure 22. Stiffness change in AS4/1808 specimens	72
Figure 23. Schematic of incremental, step-wise surface ply fractures influenced by matrix cracks in adjacent plies	77
Figure 24. Radiographs of center-notched, AS4/3501-6, (0,45,0,-45) _{s4} specimens during high-load fatigue	79
Figure 25. Edge radiographs of center-notched, AS4/3501-6, (0,45,0,-45) _{s4} specimens during high-load fatigue	80
Figure 26. Radiographs of center-notched, AS4/1808, (0,45,90,-45) _{s4} specimens during high-load fatigue	83
Figure 27. Edge radiographs of center-notched, AS4/1808, (0,45,90,-45) _{s4} specimens during high-load fatigue	84
Figure 28. A deplieed, center-notched, AS4/1808, (0,45,90,-45) _{s4} specimen at an early stage of damage development under the high load level	85
Figure 29. A deplieed, center-notched, AS4/1808, (0,45,90,-45) _{s4} specimen at a late stage of damage development under the high load level	87
Figure 30. Radiographs of center-notched, AS4/1808, (0,45,90,-45) _{s4} specimens during low-load fatigue	90
Figure 31. Edge radiographs of center-notched, AS4/1808, (0,45,90,-45) _{s4} specimens during low-load fatigue	91
Figure 32. A deplieed, center-notched, AS4/1808, (0,45,90,-45) _{s4} specimen at an early stage of damage development under the low load level	92
Figure 33. A deplieed, center-notched, AS4/1808, (0,45,90,-45) _{s4} specimen at a late stage of damage development under the low load level	95
Figure 34. Radiographs of double-edge-notched, AS4/1808, (0,45,90,-45) _{s4} specimens during high-load fatigue	98
Figure 35. Edge radiographs of double-edge-notched, AS4/1808, (0,45,90,-45) _{s4} specimens during high-load fatigue	99
Figure 36. Radiographs of double-edge-notched, AS4/1808, (0,45,90,-45) _{s4} specimens after fatigue failure	101
Figure 37. Radiographs of center-notched, AS4/1808, (0,45,0,-45) _{s4} specimens during high-load fatigue	103
Figure 38. Edge radiographs of center-notched, AS4/1808, (0,45,0,-45) _{s4} specimens during high-load fatigue	104
Figure 39. A deplieed, center-notched, AS4/1808, (0,45,0,-45) _{s4} specimen at an early stage of damage development under the high load level	105
Figure 40. A deplieed, center-notched, AS4/1808, (0,45,0,-45) _{s4} specimen at a middle stage of damage development under the high load level	107

Figure 41. A depled, center-notched, AS4/1808, (0,45,0,-45) _{s4} specimen at a late stage of damage development under the high load level	108
Figure 42. Radiographs of center-notched, AS4/1808, (0,45,0,-45) _{s4} specimens during low-load fatigue	111
Figure 43. Edge radiographs of center-notched, AS4/1808, (0,45,0,-45) _{s4} specimens during low-load fatigue	112
Figure 44. A depled, center-notched, AS4/1808, (0,45,0,-45) _{s4} specimen at an early stage of damage development under the low load level	113
Figure 45. A depled, center-notched, AS4/1808, (0,45,0,-45) _{s4} specimen at a middle stage of damage development under the low load level	115
Figure 46. A depled, center-notched, AS4/1808, (0,45,0,-45) _{s4} specimen at a late stage of damage development under the low load level	118
Figure 47. SPATE thermographs of matrix crack development	126
Figure 48. SPATE thermograph of a 0-deg. surface ply fracture	129
Figure 49. SPATE thermographs of four center-notched, AS4/1808, (0,45,90,-45) _{s4} specimens during high-load fatigue	131
Figure 50. SPATE signal along Section B-B' in three center-notched, AS4/1808, (0,45,90,-45) _{s4} specimens during high-load fatigue	133
Figure 51. SPATE thermographs of four center-notched, AS4/1808, (0,45,0,-45) _{s4} specimens during high-load fatigue	136
Figure 52. SPATE signal along Section C-C' in three center-notched, AS4/1808, (0,45,0,-45) _{s4} specimens during high-load fatigue	138
Figure 53. SPATE thermographs of four center-notched, AS4/3501-6, (0,45,0,-45) _{s4} specimens during high-load fatigue	141
Figure 54. SPATE thermographs of three center-notched, AS4/1808, (0,45,90,-45) _{s4} specimens during low-load fatigue	144
Figure 55. SPATE thermographs of AS4/3501-6, (0,45,0,-45) _{s4} , DEN specimens during high-load fatigue	147
Figure 56. SPATE thermographs of four double-edge-notched, AS4/1808, (0,45,90,-45) _{s4} specimens during high-load fatigue	150
Figure 57. Normalized residual strength of center-notched, AS4/1808, (0,45,90,-45) _{s4} specimens during high-load fatigue	155
Figure 58. Normalized residual strength of center-notched, AS4/1808, (0,45,90,-45) _{s4} specimens during low-load fatigue	156
Figure 59. Normalized residual strength of double-edge-notched, AS4/1808, (0,45,90,-45) _{s4} specimens during high-load fatigue	160

Figure 60. Normalized residual strength of center-notched, AS4/1808, (0,45,0,-45) _{s4} specimens during high-load fatigue	162
Figure 61. Normalized residual strength of center-notched, AS4/1808, (0,45,0,-45) _{s4} specimens during low-load fatigue	163
Figure 62. Schematic illustration of 0-deg. ply fracture and delamination in AS4/1808, (0,45,0,-45) _{s4} specimens after residual strength tests	165
Figure 63. Normalized residual strength of center-notched, AS4/3501-6, (0,45,0,-45) _{s4} specimens during high-load fatigue	168
Figure 64. Infinite plate with an elliptical hole under uniform uniaxial stress	175
Figure 65. Strain concentration factors in the quasi-isotropic and orthotropic laminates with an elliptical hole	176
Figure 66. Normalized tensile strength of a plate with an elliptical hole	177
Figure 67. Normalized, effective stiffness in a plate with an elliptical hole	180

List of Tables

Table 1. Thermoelastic properties for carbon epoxy	54
Table 2. Force equilibrium assessment in the micromechanical model	57
Table 3. Monotonic strength of virgin specimens	64
Table 4. Cyclic load levels ($R=-1$) for fatigue tests	68
Table 5. Tensile and compressive stiffnesses of virgin specimens	70
Table 6. Actual and expected normalized tensile strengths of center-notched, AS4/1808 specimens during high-load fatigue	135
Table 7. Normalized residual stiffness and strength of center-notched, AS4/1808, (0,45,90,-45) _{s4} specimens	154
Table 8. Averaged, normalized, residual strength data	157
Table 9. Normalized residual stiffness and strength of double-edge-notched, AS4/1808, (0,45,90,-45) _{s4} specimens	159
Table 10. Normalized residual stiffness and strength of center-notched, AS4/1808, (0,45,0,-45) _{s4} specimens	161
Table 11. Normalized residual stiffness and strength of center-notched, AS4/3501-6, (0,45,0,-45) _{s4} specimens	167
Table 12. Ellipse aspect ratios for middle-life tensile specimens	178

Chapter I

Introduction

1.1 Problem Statement

Composite materials consisting of high-strength, high-stiffness fibers in a supporting matrix of a relatively compliant material are becoming the "material of choice" in performance-driven design applications. Pound for pound, the strength, stiffness and fatigue properties of fiber composites are generally superior to those of conventional, homogeneous materials, with the added benefits of designed-in strength and stiffness anisotropy and excellent vibration damping characteristics. Although fiber composites are frequently more expensive than conventional materials in bulk quantity, it is often true that cost savings are realized over the life-cycle of the product when the economies of fabrication and weight savings are considered.

Carbon fiber reinforced plastic (CFRP) composites have been the subject of much investigation because of their widespread use in the aerospace industry, and will be the focus of the present study. Such composite materials are being increasingly used in primary load-bearing

structures which can have nonuniform shapes (including access and conduit openings, and bolt holes) and can be subjected to varying tensile and compressive service loads over extended periods of time. Hence, there is a need for a sound understanding of the fatigue response of CFRP composites containing stress concentrations and the ability to predict that response with confidence. In particular, the characteristics of strength, stiffness and life are of paramount importance.

The phenomenon of failure in most practical CFRP laminates is more complex than in homogeneous materials because of the lack of a single, dominant flaw to which failure can be attributed. For example, a laminate may undergo matrix cracking, delamination, fiber fracture, and phase debonding prior to a catastrophic failure event [1]. The stress redistribution associated with the subcritical damage sites, along with the highly three-dimensional microscopic stress state caused by the mismatch of elastic properties of the constituent phases, lead to an intractable mechanics problem that cannot be solved with methods, such as linear elastic fracture mechanics, that may have been entirely adequate for conventional materials. Novel approaches to predict the strength of fiber composites must therefore be based on a complete understanding of heterogeneous damage mechanisms and complex failure modes through carefully controlled experiments.

Published experimental results suggest that the strength of notched CFRP laminates is altered by the presence of damage. Fatigue failure can occur if this "residual" strength degrades to the level of the applied load. Residual tensile and compressive notched strengths may undergo an increase, decrease, or both, during cyclic load histories, depending on the material system, fiber architecture, stacking sequence, and peak load excursions [2-10]. This effect has often been attributed to a change in notch sensitivity due to damage localization and stress redistribution, and seems to be most pervasive in laminates fabricated with layers of unidirectional material.

The effects of parameters such as notch type, material, stacking sequence, and cyclic load level on fatigue damage and residual strength are not well understood. An in-depth study involving variations of these parameters would provide a unique opportunity to make general

observations and conclusions based on a broad data base. Resolution of the dependence of residual compressive and tensile strengths on the above parameters or more generic observables, such as damage, residual stiffness, and stress distribution near the notch would be a significant step in the understanding of the long-term behavior of structural components.

1.2 Objectives

The overall goal of the investigation is to develop knowledge required for the mechanistic modeling of residual strength in notched CFRP laminates. This goal is accomplished through two specific objectives: (1) to study, in a systematic and disciplined manner, the effect of different material systems, lamination arrangements, load levels, and notch configurations on the damage development and attendant stiffness change and residual strength of notched CFRP laminates under fully-reversed cyclic loads; and (2) to identify generic observables, such as global and local stress redistributions, that may explain (or at least correlate with) the material response. An emphasis will be placed on the identification of factors that control residual strength.

1.3 Approach

The objectives are addressed through experiments involving two graphite epoxy material systems, two lamination arrangements, two fully-reversed cyclic load levels, and two notch configurations. One of the two carbon fiber composite material systems has a so-called "first generation" epoxy resin, and is thought by many to be insufficiently damage tolerant for future

high-strain applications. The second material system has a "toughened" epoxy resin that was developed specifically for improved damage tolerance (particularly in compression). Both laminate configurations represent those typically found in structures. The $(0,45,90,-45)_{s4}$, quasi-isotropic laminate is relatively matrix-dominated, and the $(0,45,0,-45)_{s4}$, orthotropic laminate is relatively fiber-dominated. The two load levels chosen for each specimen type result in fatigue lifetimes as short as approximately 10^3 cycles and as long as approximately 10^6 cycles. The two notch configurations — central, circular hole and opposing, semi-circular edge-notches — provide slightly different stress gradients and significantly different boundary conditions for damage initiation and growth.

Damage development is documented with penetrant-enhanced X-ray radiography and laminate deply. The effect of damage on stress patterns in the surface plies is evaluated with full-field, infrared measurements of the cyclic temperature change during cyclic loading. These temperature changes are related to stresses by the adiabatic, thermoelastic effect. A new micromechanical theory developed during this investigation is used to assist the interpretation of thermal patterns. Tensile and compressive strengths measured at four times in the fatigue lifetime (virgin, early life, middle life, and late life) are related to the damage and stress redistribution information obtained beforehand by nondestructive means.

1.4 Literature Review

Some of the earliest work on the strength of fiber composite materials concerned the load concentration caused by broken fibers in a unidirectional lamina. Hedgepeth [11] used a simple shear-lag analysis to estimate the amount of load transferred from a broken fiber into adjacent, intact fibers assuming that the uniformly-spaced fibers carry all the axial load and the matrix carries only shear load. In later work, Hedgepeth and Van Dyke [12,13] analyzed the effects of matrix plasticity and fiber-matrix debonding. Two general conclusions from the

three papers were that fiber debonding or matrix splitting results in a greater reduction in the maximum load concentration factor than matrix yielding, and that a well-bonded matrix reduces tensile strength in notched materials.

In 1964, Rosen carried out a statistical analysis of unidirectional composite strength using an approximate shear-lag-type analysis in the vicinity of a broken fiber end and a statistical representation of fiber strength [14]. The fibers were represented as a chain of links, each layer a bundle of links, and the composite was a series of such bundles. With this "chain of bundles" model, the composite strength was dependent on the fiber and matrix characteristics.

Zweben [15] modified the shear-lag model to analyze the fracture of multidirectional laminates. This "materials modeling" approach incorporates material heterogeneity as well as the interactions between layers in the vicinity of broken fibers. Comparison of this theory and available experimental data resulted in no definitive conclusions regarding the validity of the materials modeling approach. In the same article, Zweben examined macromechanical and micromechanical classical fracture mechanics predictions of notched strength and saw reasonably good indications that macromechanical fracture mechanics may apply to unidirectional materials having a notch parallel to the fibers.

In 1980, Goree and Gross [16] analyzed the unidirectional fiber fracture problem for the case of an arbitrary number of broken fibers. Using a modification of Zweben's "materials modeling" approach, they found significantly different stresses in the matrix compared to earlier shear lag models. The analysis yielded no new information concerning fiber stresses. unaltered. It was also shown that closer fiber spacing increased some components of matrix stress without bound. In an extension of this work, Goree and Gross later analyzed the stresses near broken fibers with longitudinal yielding and splitting of the matrix [17]. It was found that the number of broken fibers (arranged in a line to form a "notch") influenced the material's fracture strength if there was matrix yielding without splitting. For large splitting, however, the strength was independent of notch length.

Batdorf [18] introduced an approach to the unidirectional tensile fracture problem that was different from the previous "chain of bundles" model. His approach focused on the creation and growth of multiple fiber fractures and the eventual failure due to a Griffith-type instability. Weakest link theory was used to determine the number of isolated fiber fracture (singlets), double fractures (doublets) and multiplsets of arbitrary order as a function of stress. In a follow-up paper, Batdorf and Ghaffarian compared this approach with one set of experimental data and found mostly satisfactory agreement [19]. An area of weakness, it was pointed out, is the dearth of knowledge regarding the stress distribution in fibers adjacent to cracks.

Realizing that in practical composites the fibers do not form a perfect geometric array, Batdorf and Ghaffarian modified the shear-lag model to account for irregular fiber spacing [20]. Taking this variability into account improved the agreement of theory and observations on the strength-size relation of composites in one experiment, but impaired the agreement in another experiment.

The above models for fiber fracture concern microscopic events that are only part of the damage accumulation process in complex-shaped, multidirectional laminates, and are therefore of little use in practical (engineering) models of structures. On a more macroscopic scale, several two-parameter models for the monotonic fracture of notched composite laminates have been proposed [21-24]. A key feature of these models is the incorporation of a zone of intense stress or damage near the notch, defined by a characteristic dimension, in which non-linear deformations occur. Ultimate failure of the laminate is based on point stress, average stress, or critical stress intensity factor calculations in the linear elastic region of material adjacent to the notch. The advantage of these models is their simplicity and ability to predict the notch size effect with engineering accuracy. That is, as the size of the notch is increased, the structural strength decreases. Some of the models work better than others as the notch size becomes quite large compared to the width of the structure being analyzed. The two parameters that need to be determined experimentally are the unnotched laminate strength and the notched strength for any one notch size. Since the effect of stacking sequence on the strength of notch laminates is unclear at this time [4,25,26], it is necessary to

evaluate both parameters for each laminate considered (i.e. the parameters are not characteristic of a given material system).

Pipes, Wetherhold and Gillespie [27] developed a three parameter macroscopic model of tensile fracture of notched laminates that followed the dependence of tensile strength on the notch size better than most of the two parameter models mentioned earlier. In order to evaluate the third parameter, though, a third test is required in which the strength for a second notch size must be measured. As with the two parameter models, the predictions are based on empirical data and, therefore, correlate well with the data. None of the two- or three-parameter models, as proposed, account for damage that may occur prior to structural failure; and none predict the change in residual strength that can accompany fatigue damage development.

Garbo and Ogonowski [28] and Tan [29] used the essential features of the two- and three-parameter strength models to compute the tensile strength of laminates with circular and elliptical holes and sharp slits. The method presented in these papers uses the full-field elasticity solution for stresses in an infinite, homogeneous, anisotropic plate by Lekhnitskii [30] to estimate the ply-level stresses in the laminate near the notch. At a certain distance away from the notch opening (determined from experiments), a failure criterion such as the point-stress or tensor polynomial failure criterion is evaluated at the ply-level along a path surrounding the notch. In this manner, different fracture initiation sites due to arbitrary biaxial loadings can be predicted. Good correlation with experiments was observed in both of these papers when the failure mode remained constant. Given that failure modes are sensitive to the type, amount, and distribution of subcritical damage near a notch (which, in turn, depend on the load history), it is apparent that this technique is not sufficient for predicting residual (remaining) strength.

Poe and Sova [31] developed a macroscopic tensile failure model for boron/aluminum laminates based on a general fracture toughness parameter that was shown to depend on the ultimate tensile strength of the unnotched laminate. Fibers in the principal load-bearing plies were assumed to fail if longitudinal fiber strains ahead of the notch end reached a critical

level. However, the predictions were not accurate when appreciable matrix yielding and other subcritical damage preceded failure. If an improved stress analysis accounting for the nonlinearities was available, this model could potentially provide reasonable strength predictions for fiber-dominated materials. In a situation with a contrasting damage mode, Morley [32] analyzed the growth of a single crack bridging 0-deg. fibers in a notched laminate. No longitudinal matrix cracks in the 0-deg. plies were considered. This model is obviously valid only when the matrix material fails at a lower strain than the reinforcing fibers, as in some ceramic matrix composites.

The models outlined above point to the need for general approaches that can accommodate the variety of subcritical damage modes appearing in notched laminates of different material systems. In response to this need, several efforts to predict damage growth in and the strength of notched fiber composite laminates under monotonic loading have utilized two- or three-dimensional finite element models [33-38]. In finite element models of damage development, load is typically applied incrementally until a specified failure criterion indicates that a certain failure mode has occurred in one or more elements. The constitutive properties of those elements are then modified to reflect the failure mode. With the same applied load, the stresses are recomputed with the new stiffness matrix. If no additional elements fail, the load is increased to the next specified level. If unstable propagation of damage occurs and the laminate can no longer bear the applied load, failure is assumed to have occurred. In most of these cases, it is beneficial to know beforehand the mode of damage propagation in order to properly refine the element mesh. The two dimensional models are generally incapable of accounting for third-dimension damage modes, such as delamination. Computer storage limitations and expense limit the utility of a three-dimensional analysis as a design tool, although at this time it seems to be the only way to accurately represent the fully three-dimensional nature of damage development in laminates.

Models used for tensile failure of notched laminates have been adopted for predicting compressive failure as well. Among these are the point-stress [39] and average-stress [40] criteria of Whitney and Nuismer. The difficulty in formulating a sound compressive strength

model for notched laminates is partly due to the complexities involved in the experimental verification of compressive strength and the difficulty in utilizing laboratory strengths in practical design situations. Considering that a value of "compressive strength" measured in the laboratory is highly dependent on the geometry of the specimen (eg. length, width, thickness), engineering judgment is required in the extrapolation of laboratory data to the field. Models of pure compressive strength (a true material quantity, as opposed to a structural quantity) are available for unnotched composite materials [41-43] and have been applied to notched configurations using a global-local type of analysis by Gurdal [44]. Using approximate engineering methods, Nemeth [45] analyzed the global buckling of rectangular isotropic and orthotropic laminated composite plates with centrally located cutouts. An additional complication in the prediction of compressive strength in laminated structures is the tendency of the material to delaminate. Shivakumar and Whitcomb [46] studied the buckling of sublaminates in unnotched material resulting from delamination but did not attempt to predict failure.

None of the above notched strength models were applied to the residual strength problem. However, it is possible that, with modifications, one of the models might be used for this purpose. Only a few articles in the literature address the strength issue from a standpoint that considers the cumulative damage process that typically precedes failure in fiber composite laminates. For example, the analyses of Halpin, et al. [47], Broutman and Sahu [48], and Reifsnider, et al. [49] focus on unnotched material, but could be extended to accommodate the nonuniform global stress field present near a notch, possibly through the use of one of the above notched failure criterion [5,50]. An essential aspect of a mechanistic model of residual notched strength is that the extensive damage growth prior to failure and the resulting stress redistribution in the individual plies must be considered. The major aspects of damage initiation and growth in carbon fiber composites and the limited amount of stress redistribution data available in the literature will be reviewed next.

The review of damage mechanisms in carbon fiber composites begins with the three most pervasive damage modes: matrix cracks, delamination, and fiber fracture. Matrix cracks oriented parallel to the fibers typically occur first in those plies subjected to the largest shear

or tensile transverse strain (perpendicular to the fibers). Plies oriented parallel to the load axis and having a negative transverse strain can also undergo this longitudinal mode of matrix cracking because of the biaxial stress state in the individual plies of a multidirectionally-laminated structure. Since the failure strain of carbon fibers is much less than that of most polymeric matrix materials, matrix cracking perpendicular to the fiber direction is not an issue of practical importance. Matrix cracks in any ply reduce the stiffness of a laminate by effectively removing the load carrying capacity of the material immediately adjacent to the crack and causing a transfer of load to the unbroken material in adjacent plies. The resulting three-dimensional perturbation of the stress field causes local stress concentrations in the adjacent plies and, consequently, further damage events, such as delamination or fiber fracture [51-53]. Reifsnider et al. [54] have shown that prior to tensile laminate failure there exists a characteristic array of matrix cracks that is independent of loading history and dependent solely on laminate properties. The existence of such a regular array of cracks prior to failure provides a groundwork upon which models of ultimate strength may be built.

The second major damage mode, delamination, is a planar matrix crack that most often occurs between plies of different orientation, but can also occur within a single ply. A principal driving force of delamination is the interlaminar stresses that occur between plies due to the mismatch of Poisson's ratios of the two sublaminates formed after the delamination. In a uniform laminate of infinite extent, there are no such stresses. Near a discontinuity, such as a free edge or an internal damage site, though, interlaminar stresses can be sufficiently high to cause delamination initiation and growth. Much like matrix cracks, delaminations reduce the stiffness of the laminate [55] and cause stress concentrations in the adjacent material [56]. In the presence of compressive load excursions, delaminations pose a more severe problem to structural integrity because of their tendency to promote local buckling of the sublaminates. The local buckling of sublaminates, in turn, reduces support and causes higher damage growth rates and instability-related failures [46].

Fiber fracture, the third major damage mode, is perhaps the most important damage mode in fiber composites because it is the fibers that typically carry most of the applied load. As

mentioned in the earlier discussion of unidirectional strength theories, fibers fractures occur alone or in small groups prior to ultimate failure [52,53,57]. Because of the small volume of material influenced by the stress concentration near a broken fiber, there is little, if any, measurable stiffness change associated with individual fracture events. Macroscopic clusters of broken fibers extending through the thickness of a ply, however, do cause a significant laminate stiffness change and stress concentration in adjacent plies, and lead to matrix cracks and delamination [58].

Simonds et al. [3,59] have shown that material system and loading history significantly influence the relative abundance of the three damage modes in CFRP materials. Two contrasting matrix materials, Narmco 5208 (a highly cross-linked epoxy resin) and ICI PEEK (poly etheretherketone, a high-toughness thermoplastic), were used to demonstrate the different damage modes and failure mechanisms in $(0,45,90,-45)_{s4}$ carbon fiber reinforced laminates with central circular holes. The general conclusions of the investigations were that the thermoplastic matrix composite had less matrix damage than the more brittle epoxy matrix composites, particularly under monotonic loads to failure or low cycle fatigue tests. Under fully-reversed, high amplitude cyclic loads resulting in fatigue lifetimes of less than approximately 10^4 cycles, tensile, fiber-dominated failures occurred in the PEEK composite, and compressive, matrix-dominated failures occurred in the 5208 composite. However, under fully-reversed, low amplitude cyclic loads resulting in fatigue lifetimes of more than 10^4 cycles, both material systems suffered extensive matrix damage and compressive failure modes. In Simonds's work, the stress-life (S-N) curve of the epoxy composite was steeper than that of the thermoplastic composite, which contrasts with the results of other investigators using unnotched, unidirectional and multidirectional laminates under fully-tensile cyclic loads [60-62]. Curtis [60] and Baron [61,62] noted that the tougher matrix composites had steeper S-N curves than the more brittle matrix composites. One aspect in which Curtis and Baron agreed with Simonds was that there was, overall, less matrix damage in the tougher matrix composites, even though this quality did not necessarily translate to improved fatigue performance in all cases.

Within the framework of a mechanistic model of strength of composites, the change in load path associated with subcritical damage in the material must be measured and understood. This requires knowledge of the in-plane laminate strain distribution, or in cases where delaminations exist, the ply-by-ply strain distribution in the vicinity of the failure location. Hence, the need for experimental measurement of such quantities arises. Previous investigations of stress redistribution in the presence of damage have been carried out by Daniel [63] and Wood [64] for static loading, and by Kress and Stinchcomb [4] and Highsmith [56] for tensile cyclic loading. Daniel used the photoelastic coating method to obtain full-field principal shear strain data near a notch. Wood and Kress used moiré interferometry to obtain full-field displacement data in unnotched and notched composites, respectively. Highsmith measured the strain concentration at the border of a surface-ply delamination in an unnotched laminate with moiré interferometry. All four investigations revealed that significant strain redistributions occur during subcritical damage initiation and growth. In notched laminates, a reduction of the global strain concentration was observed with increasing damage. This stress relaxation effect caused by damage near the notch has been cited as the cause of increasing tensile and compressive strengths [4,8]. Of course, unlimited damage growth in notched laminates eventually leads to failure as the effect of material degradation exceeds that of stress relaxation (commonly referred to as the wear-in/wear-out process [8,65]). A limitation of both the photoelastic coating and moiré interferometry methods is that the data obtained are valid only on the surface of observation and, as such, do not necessarily measure deformations in the interior of the laminate. Aside from imbedded strain gages (which introduce strain disturbances in the surrounding material), no suitable technique for measuring deformations inside a laminate is known to the author.

Chapter II

Investigative Approach

2.1 Experiments

2.1.1 Mechanical Testing

Mechanical tests were carried out on servo controlled, hydraulically actuated, MTS load frames equipped with hydraulically actuated wedge grips. Hydraulic wedge grips are essential for the through-zero loading of the flat coupon-type specimens chosen for the present study for reasons of practicality and economy. Monotonic strength tests were carried out in the stroke control mode of operation with a displacement rate of 0.06 in./min. Stroke control was selected to avoid crushing the specimen after a compressive strength measurement. Monotonic tension and compression tests were carried out on virgin and fatigue-damaged specimens to characterize the strength components of the laminates throughout the lifetime. Residual strengths were measured at the "early," "middle," and "late" stages of fatigue.

damage development (to be defined in the characterization of basic material properties). Most strength tests were carried out in triplicate to evaluate the amount of scatter in the data and to establish some statistical significance to the results.

Fatigue tests were carried out with a constant amplitude, fully-reversed ($R=-1$), sinusoidal loading regime in load control. Reversed cyclic loads are considered by many to be the most detrimental to fiber composites because of the activation of both tensile and compressive damage modes. Depending on the relative competition of these damage modes, either tensile or compressive failure modes ensue. Hence, the fully-reversed loading regime provides a good opportunity to observe different damage mechanisms in composite laminates. To obtain static stiffness data or document damage development during the first 100 cycles of a fatigue test, reduced load cycle frequencies were used (1 Hz until 10 cycles, 5 Hz until 100 cycles, and 10 Hz thereafter). No significant differences in material response were observed when the present technique was compared to truly constant 10 Hz tests.

External support along a specimen's gage length prevents global buckling and, to a lesser extent, surface delamination growth, resulting in longer fatigue lifetimes and, in some cases, altered failure modes [66]. The present test methodology, detailed in Ref. [67], is founded on the tenets that damage should be allowed to develop in an unconstrained manner in the gage length, much the same as damage grows in engineering structures, and that competing failure modes may not be manifested under the influence of external constraint devices. The gripping arrangement is shown schematically in Figure 1. During testing, the specimens were exposed to the ambient, air-conditioned, laboratory environment.

Two fully-reversed cyclic load levels were chosen such that the load-dependent fatigue response could be observed. The "high" load, corresponding to a fatigue life of 1K to 30K cycles, and the "low" load, corresponding to a fatigue life of 300K to 3M cycles, bracketed the range of fatigue lives over which it was practical to obtain data in the laboratory. Higher loads often resulted in fatigue failures before the load span on the test frame was accurately set, and lower loads resulted in no different fatigue mechanisms and, in many cases, infinite fatigue lives.

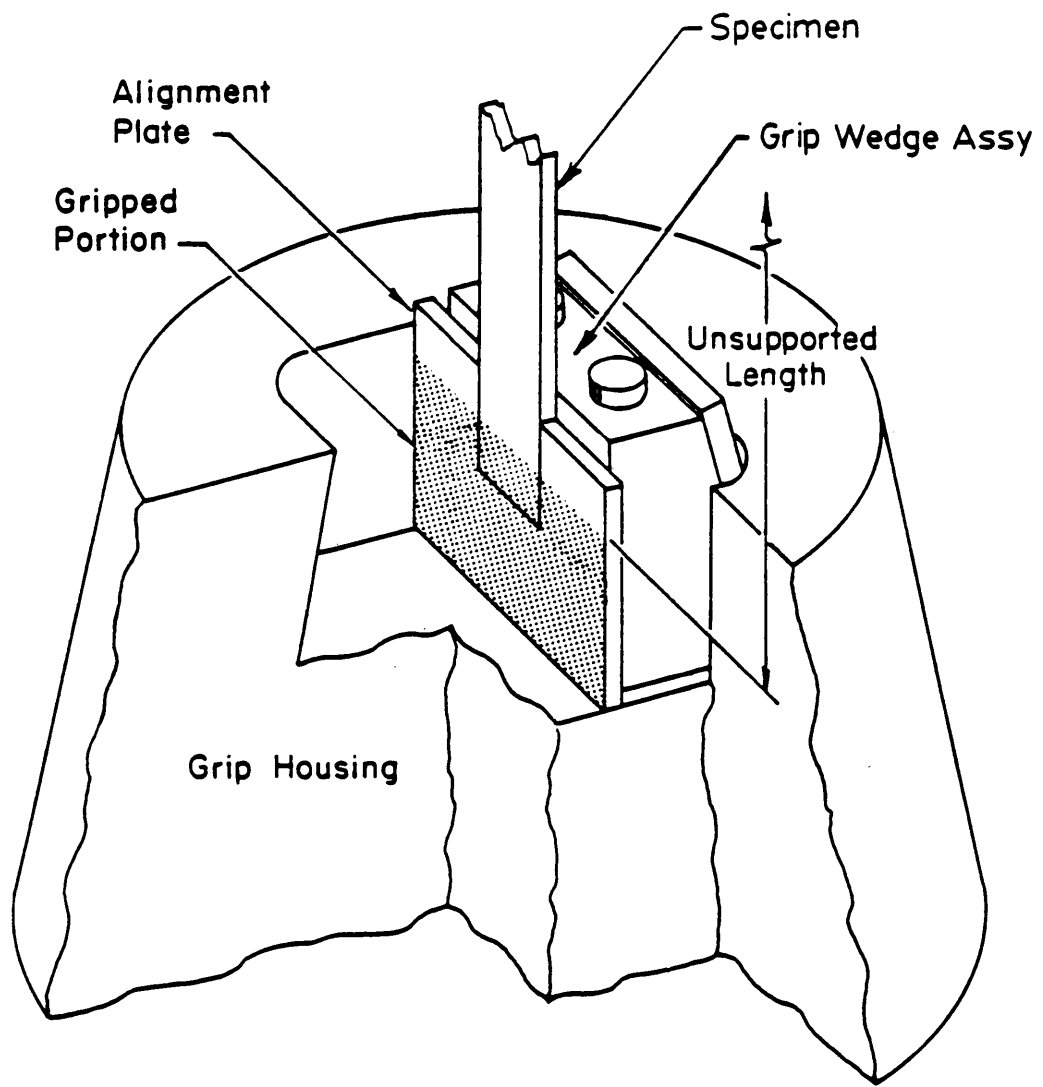


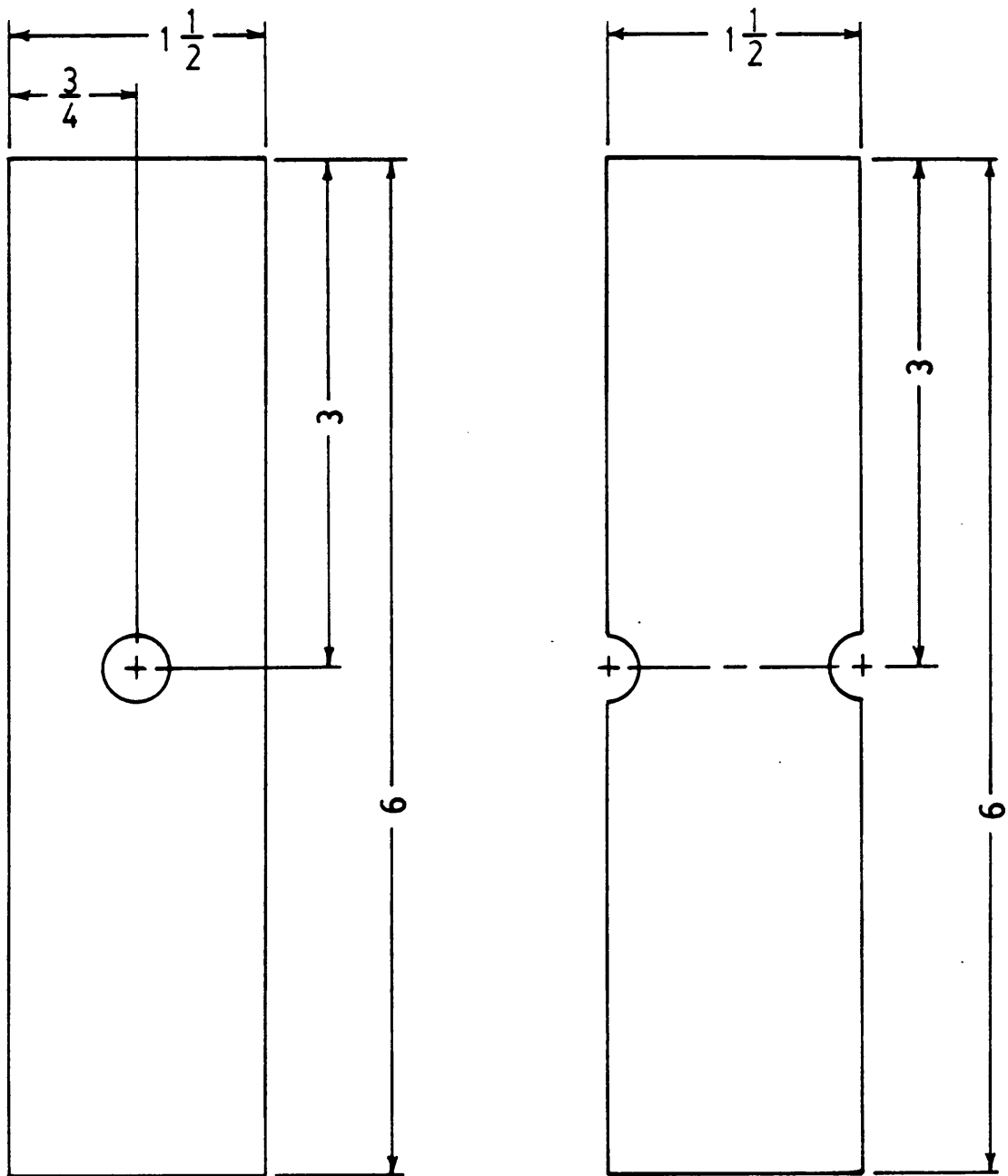
Figure 1. Test specimen gripping arrangement

2.1.2 Test Specimens

Two carbon epoxy material systems were chosen to provide contrasting material responses under cyclic loading. The Hercules AS4/3501-6 material is representative of “first generation” CFRP materials because of the relatively brittle nature of the 3501 epoxy resin. A newer CFRP formulation, American Cyanamid’s AS4/1808, has a relatively ductile epoxy matrix, and is therefore considered a “second generation” or “toughened epoxy” composite [68]. The relatively ductile Cycom 1808 epoxy resin is supposed to exhibit less cracking and delamination prior to laminate failure than the relatively brittle 3501-6 resin [69]. Much of the data in the present investigation was produced with the AS4/1808 center-notched specimens. However, since the objective of the present work is to identify different fatigue responses and their causes, the other material system and notch geometry was included for generality and to provide contrasts.

Ply orientation and stacking sequence have been shown to be important in the damage development, residual strength, and failure mode of notched laminates [4,10,70]. The two layups chosen for the present investigation — $(0/45/90/-45)_{s4}$ and $(0/45/0/-45)_{s4}$ — are representative of practical structural material configurations. (The 0-deg. direction is defined to be parallel to the loading axis. Positive ply orientations are measured clockwise looking at the “front” side of the specimen.) The first layup has quasi-isotropic planar elastic properties, and the second has orthotropic properties. The differing amounts of 90- and 0-deg. plies in the two configurations provided contrasting material responses to fatigue damage development. For brevity, the $(0,45,90,-45)_{s4}$ laminate was denoted the “A” laminate, and the $(0,45,0,-45)_{s4}$ laminate was denoted the “B” laminate.

After nondestructively inspecting the laminated plates with an ultrasonic C-scan unit (as described later), the specimens were machined with diamond-coated abrasive circular wheels and core-drills. The test specimen configurations are illustrated in Figure 2. The width and notch radius were selected such that the radius to half-width diameter was equal to 0.25, fa-



NOTCH RADIUS: $\frac{3}{16}$

Figure 2. Test specimen configurations

cilitating the use of closed-form solutions for strains in an infinite plate with an elliptical opening to approximate the strains in the coupons. The length of the coupons was selected according to the test procedure detailed in [67]. Briefly, the procedure specifies that an unsupported length that provides the maximum compressive strength of undamaged material is the length to be used in the fatigue tests. Typically, there is an upper limit on such a length above which compressive strength is reduced due to global buckling effects. Below the buckling length, compressive strength is nearly independent of unsupported length. The results of the compression tests with various unsupported lengths indicated that 2.5-in. would be an appropriate unsupported length for the fatigue tests [71].

The primary notch configuration is a center hole, chosen because of the availability of closed form solutions for the approximate stresses and strains in the test specimens and because it is fairly representative of typical cutouts in structural applications. For comparison, some tests were performed with double semi-circular edge notches, but no closed-form stress solution exists for this configuration (to the author's knowledge). An advantage of the edge-notched configuration over the center-notched configuration is that all damage growth emanates from the notches. In the center-notched specimens, damage growing inward from the straight edges of the specimen late in the fatigue life frequently complicates the analysis of damage growth near the notch. However, the interaction of damage zones emanating from the opposing notches is a problem with the edge notched configuration. For brevity, the center-notched specimens were denoted "CN", and the double-edge-notched specimens were denoted "DEN".

Specimens were labelled according to their matrix type, stacking sequence, panel identification number, specimen identification number within the panel, and notch type. For example, "3501-A-1-2-CN" designates the AS4/3501-6 material system, the quasi-isotropic stacking sequence, panel 1, specimen 2, center notch. Another possibility is "1808-B-1-2-DEN", signifying the AS4/1808 material system, the orthotropic stacking sequence, panel 1, specimen 2, double edge notch. Axis and quadrant notations used in the description of damage are illustrated for the two specimen geometries in Figure 3. The seemingly back-

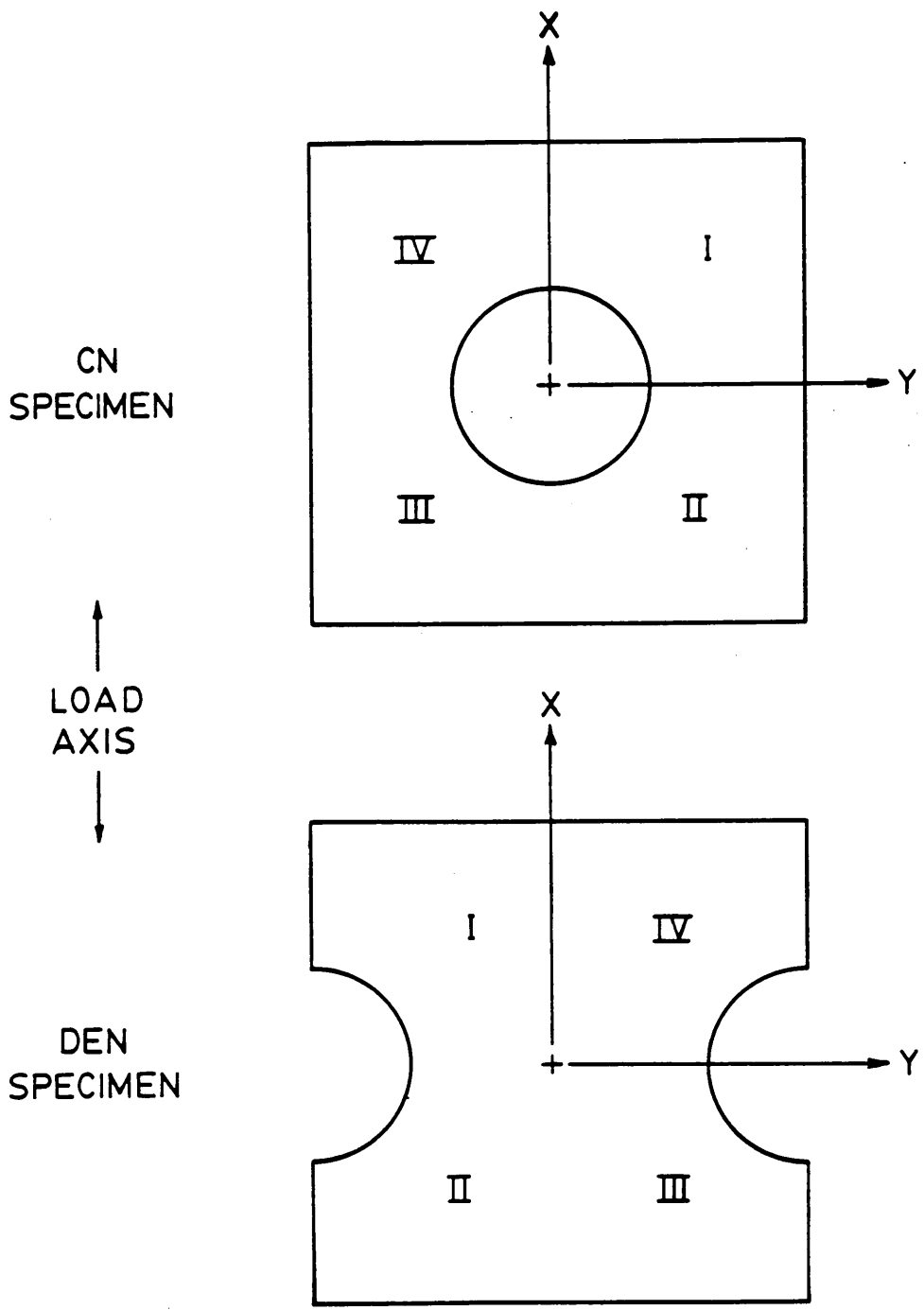


Figure 3. Specimen axis and quadrant notations

ward quadrant notation for the DEN specimen is intended to facilitate comparisons with CN specimens. (For example, note that quadrant I in the CN case is located at the same position relative to the notch as quadrant I in the DEN case.) Quadrant numbers become reversed left-to-right if the back side of the specimen is being viewed. The sequential numbering of plies and their interfaces progresses from the front to the back of the specimens.

2.1.3 Stiffness Measurement

Stiffness change has been shown to be an effective nondestructive means of monitoring damage growth in carbon epoxy laminates [72-74]. As damage initiates and grows in the material, the stiffness decreases due to internal load redistributions.

In the present investigation, effective tensile and compressive stiffnesses were measured with a 1-in. gage-length extensometer located on the geometric center of the specimens. The knife-edges of the extensometer were positioned firmly on V-notched aluminum tabs bonded to the specimen with silicone adhesive, as detailed in [75]. The dimensions of these tabs were 5/16-in. long (along the V-notch), 5/32-in. wide, and 1/16-in. thick. Different sized tabs will result in different effective stiffness measurements due to the strain gradient near the notch. Dynamic stiffness was continuously monitored during fatigue tests, and static stiffness was periodically measured when a change in dynamic stiffness indicated the need to do so.

Previous investigations revealed that a characteristic stiffness response exists for a given material, stacking sequence, notch configuration and load level [75,76]. That is, the fraction of life consumed in a particular experiment can be roughly estimated by monitoring the specimen's stiffness. Given the typically large amount of scatter in fatigue lifetimes of composite laminates (as much as one order of magnitude), the ability to make such estimates helps establish the actual "age" of the specimen prior to a destructive test, such as deply (described later) or residual strength measurement. To reduce the effect of bending on

stiffness measurements in DEN specimens, effective stiffnesses in some tests were computed by averaging strains recorded with extensometers attached to the front and back surfaces.

2.1.4 Ultrasonic C-Scan

Prior to machining, the laminated panels were nondestructively inspected for irregularities using a Sperry/Automation laboratory C-scanning device. The Panametrics transducer, operated in the pulse-echo mode, had a nominal frequency of 15 MHz, a tip diameter of 0.25 in., and a focal length of 1.0 in. During C-scanning, ultrasonic sound waves are passed through the material by a sweeping transducer such that a full-field map of transmitted signal amplitude is obtained. Nonuniformities in the material, such as voids, cracks, or delaminations, attenuate the transmitted sound waves in proportion to the severity of those nonuniformities. Three separate scans of each plate were carried out with progressively higher gate thresholds to obtain three contours of different attenuation. The three thresholds used most often were 80, 50 and 10 percent of the maximum signal on the plate. A plate with substantial regions of less than 80 percent signal strength was rejected for the test program.

2.1.5 X-Ray Radiography

The primary nondestructive technique for evaluating damage mechanisms throughout the fatigue life was liquid-penetrant-enhanced X-ray radiography. The penetrant — zinc iodide in a carrier of water, ethyl alcohol, and Kodak Photo-Flo (wetting agent) — highlighted damaged regions of the laminate by blocking the transmission of X-rays [76-78]. Only those areas of damage with connectivity to the surface of the specimen were highlighted. Once the penetrant was applied to the surface of the specimen, it was allowed to soak in for approximately 15 minutes while the specimen was cycled at 1 Hz ($R=-1$) with a maximum load of about 25

percent of the maximum fatigue load. If the specimen had no prior application of penetrant, the penetrant was allowed to soak in for an additional 12-hour period with no applied load. If penetrant was previously introduced to the specimen, the specimen could be radiographed without the additional 12-hour soak-in period. The specimens were placed directly on top of the Kodak Industrex SR5 (single emulsion, fine grain) film inside a Hewlett Packard 43805N Faxitron Series X-ray cabinet. With the aid of a 3-in.-high adjustable tilt platform, the specimens were radiographed three times with the X-ray beam impinging at angles of 0, 15, and 90 degrees to the specimens's plane. In this manner, some three-dimensional information on the damage distribution could be obtained. The distance between the X-ray tube and the specimen was the maximum possible — approximately 45 in. without the platform. Shorter distances resulted in blurred images of the specimen's edges, particularly in the 90-deg. view. Exposure settings were 3 minutes at 43 kVp (approximately 2.5 mA) for the 0- and 15-deg. radiographs, and 4 minutes at 85 kVp (approximately 2.5 mA) for the 90-deg. radiographs.

Areas permeated with zinc iodide appear as relatively dark areas in positive prints of radiograph negatives. In the 0-deg. view, matrix cracks parallel to the fibers are fine lines, while delaminations are broad, dark areas, (the darkness depends on the thickness of the layer of zinc iodide). Large, dark, rectangular areas above and below the notch in some radiographs are the aluminum tabs used to attach the extensometer to the specimen. In the 90-deg. view, delaminations are lines extending along the length of the specimen. Matrix cracks are visible only in the 90-deg. plies in the 90-deg. view since the other ply orientations are oblique to the X-ray beam.

2.1.6 Laminate Deply

Laminate deply is a destructive damage evaluation technique developed by Freeman [79] that enables the "destacking" of a laminate by pyrolyzing the resin-rich zone between plies of different orientation. The pyrolyzation was carried out at 785° F for two hours in an argon

atmosphere (in order to prevent oxidation). A liquid penetrating marking agent (eg., a gold chloride solution) applied before pyrolyzation enabled the detection of regions of the laminate that contained matrix damage. It was found during the course of the present investigation that zinc iodide residue from previous X-ray radiographs provided sufficient contrast to observe delaminated areas. Fiber damage on the surface of each ply was detected by optical and electron microscopy. Tracings of optically visible damage patterns at each interface were used to map damage patterns at various times in the fatigue lifetime. Compared to X-ray radiography, the deply technique facilitated a higher resolution of fiber damage modes and a more accurate spatial resolution of damage (especially through the thickness). On the other hand, it was generally difficult to identify any evidence of matrix cracks on the deplied laminae.

Specimens were deplied at the same early, middle, and late stages of fatigue lifetime chosen for residual strength measurements. Only AS4/1808 specimens were successfully deplied. Several attempts to deply AS4/3501-6 specimens were unsuccessful due to the excessive amount of matrix residue that prevented separation of the plies without causing additional fiber damage.

2.1.7 Adiabatic Thermography

The adiabatic thermoelastic effect in elastic solids is the small, reversible temperature change resulting from the dilatational deformation of matter. If cyclic extensional strains are applied at a rate that is high enough to preclude heat transfer between elements of the material and their surroundings (i.e., ensuring adiabatic conditions), the temperature of the material will vary with the same wave form and frequency as the applied load. Pointwise temperature changes can then be related to stress and strain on the surface with the theory of thermoelasticity. This technique is not to be confused with dissipative thermography, where the quasi-steady-state temperature measurements reflect the heat generated in the material

due to hysteretic effects such as viscous damping or friction near defects. Stress patterns measured via adiabatic thermography during the fatigue process provide an essential "bridge" between damage data and residual strength data by allowing the investigator to observe the global stress redistributions resulting from damage growth in notched laminates. A new, micromechanical model of the adiabatic thermoelasticity of laminated fiber composites developed as part of this investigation will be presented in the analysis section of this chapter. Since adiabatic thermography is a new experimental technique and little information on the application of the technique to composite materials is available in the literature, the experimental apparatus and procedure used in the present investigation will be presented next. Aspects of the procedure not detailed in the SPATE operator's manual will be emphasized. The manual should be consulted for routine procedures.

2.1.7.1 Thermographic Apparatus

Modern infrared radiometers have the sensitivity and response time required to measure temperature changes on the surface of a dynamically-stressed material. The radiometer used in the present investigation is marketed by Ometron Inc. under the trade name SPATE (Stress Pattern Analysis by Thermal Emission), specifically for full-field stress measurements. The SPATE apparatus has been used previously with homogenous materials and, more recently, nonhomogeneous materials, to quickly evaluate stress and strain fields in a non-contact manner [80]. The SPATE 8000 consists of a scanning infrared photon detector coupled to a correlator (lock-in amplifier) and computer. The temperature sensitivity of the system is 0.002 °F. The uniaxial stresses corresponding to a temperature change of 0.002 °F in several materials are illustrated in Figure 4. The functions of the computer and correlator are to control the camera's scan activities and to condition the measured photon emittance such that the sinusoidal temperature variation occurring at the same frequency as the sinusoidal load can be determined. The correlator rejects a temperature variation having no sinusoidal content

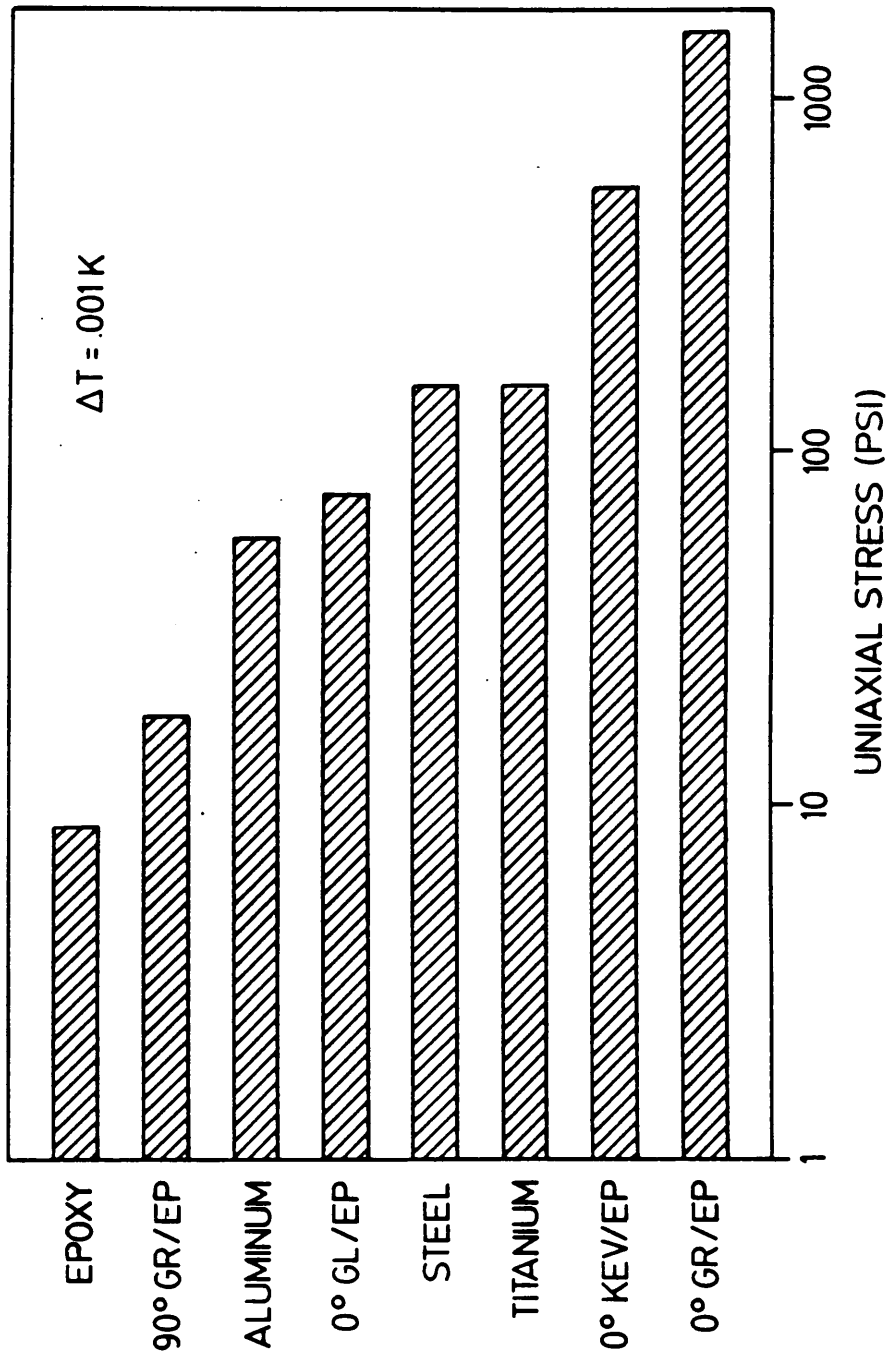


Figure 4. Theoretical stress sensitivity of SPATE with various materials

at the test frequency, such as that caused by dissipative heating. The camera scans the test specimen pointwise in a raster-like manner, enabling the computer to store the recorded signal at each point as a digital quantity. The smallest area that can be sampled at each point in the scan area is a 0.02-in.-diameter circle. If the raster scan takes a long time to complete (up to two hours is common), it is necessary to apply a cyclic load amplitude that is low enough to inhibit damage development during the scan. Two factors influencing the scan time are the scan resolution (the number of data points to be recorded over a given area) and the sample time (the amount of time spent acquiring data at a single position on the specimen). In situations where the measured signal is small, electronic averaging must be applied over a selectable time period associated with a filter "time constant" to reduce high frequency noise. Averaging is necessary since only a single value of temperature change is recorded at each point. As the time constant increases, the amount of time spent sampling data at a particular point on the specimen must also increase. Once a scan has been completed, the digital information may be stored on a magnetic disk for future examination. A video monitor enables the operator to observe the results of the scan as each point in the scan is sequentially displayed on a color-coded contour map of temperature change.

A variety of material systems, including carbon epoxy, carbon PEEK, aramid epoxy, boron aluminum, and glass epoxy, to name a few, have been studied with the SPATE apparatus. Of these, fiber-dominated carbon epoxy and aramid epoxy are the most difficult to examine because of their relatively low temperature change during cyclic loading (Figure 4). A detailed review of the procedure for obtaining high quality, repeatable data with fiber reinforced composites follows.

2.1.7.2 Mechanical Excitation

Any source of periodic mechanical excitation can be used with the SPATE 8000 apparatus, although the high cyclic load amplitudes required to obtain a good temperature signal-to-noise

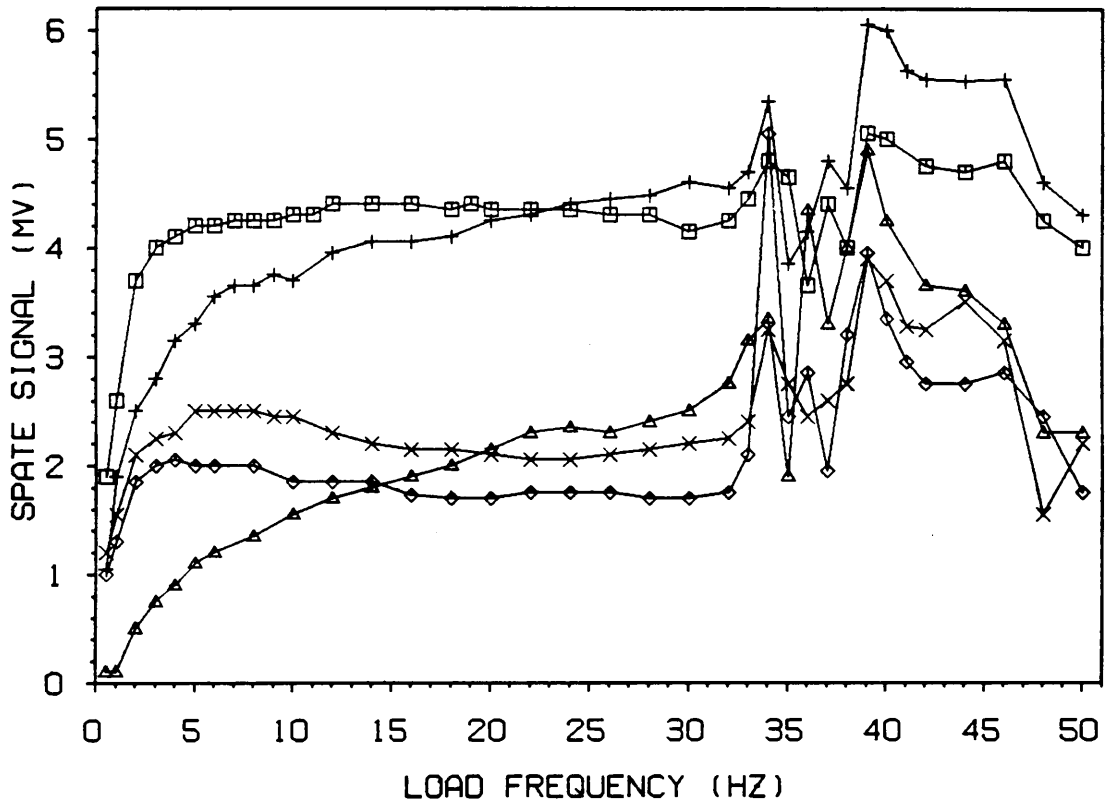
ratio with fiber-dominated carbon epoxy laminates are most readily obtained via a servo-hydraulic load frame equipped with a function generator. Because the SPATE lock-in amplifier output is proportional to the sinewave content of the temperature change, it is essential to maintain a constant load form for quantitative experiments. Unless specifics of the test dictate otherwise, one should maintain a load that does not cause damage growth during the scan. It is also important to maintain loads within the linear-elastic range of the material if stresses or strains are to be computed with the linear theory reviewed in the analysis section of this chapter; otherwise, modifications to the theory must be made to account for the inelastic deformation. In most instances, a sinusoidal load with a maximum of 30-40% of the specimen's tensile strength is appropriate.

To ensure adiabatic deformations and the validity of the theory, it is necessary to increase the load frequency until no further increase in the SPATE signal is realized. Frequency-dependent thermal emission was observed with several unnotched AS4/3502 carbon epoxy laminates (Figure 5), but this phenomenon may be peculiar to the specific laminates interrogated. For example, Potter [81] reported a constant thermal emission for frequencies above 5 Hz with XAS/914 carbon epoxy. It is therefore desirable to maintain a constant loading frequency in quantitative comparisons of data.

In the present investigation, cyclic loadings for the SPATE scans were all carried out with a frequency of 5 Hz. For $(0,45,90,-45)_{s4}$ laminates, the maximum and minimum loads were 4100 and 100 lb., respectively. For $(0,45,0,-45)_{s4}$ laminates, the maximum and minimum loads were 5100 and 100 lb., respectively. These load amplitudes provided correlator signals between +10 and -10 mV.

2.1.7.3 Specimen Preparation

A flat-finish paint was applied to the specimen in order to obtain a high and uniform surface emissivity in the infrared spectrum and to reduce the possibility of reflected heat sources be-



LEGEND: □ ALUMINUM, 4235 PSI
 △ (0)8T GR/EP, 45090 PSI
 ◇ (+45/-45)2S GR/EP, 9950 PSI
 + (90/0)2S GR/EP, 19510 PSI
 × (0/90)2S GR/EP, 20510 PSI

Figure 5. SPATE signal in AS4/3502 laminates as a function of loading frequency

ing modulated at the test frequency. Krylon ultra-flat black spray paint applied in two thin coats, for example, serves this purpose well [80], and is easily removed with acetone. Where possible, it is wise to avoid the use of paint since investigators have observed an attenuation of the photon emittance due to the paint's thickness. This effect is especially evident at increased frequencies (>20 Hz) and paint thicknesses (>12 spray passes) [82,83]. Black-colored composites (eg. carbon epoxy) that have a rough, non-reflecting surface finish do not require any surface preparation.

2.1.7.4 SPATE Setup

It is advantageous to maximize the spatial resolution (i.e., minimize the distance between the detector and specimen) in order to observe the effect of localized damage that typically occurs in composites prior to catastrophic failure. A constant distance of 12 in. from the detector to the specimen was maintained in order to minimize variations in the attenuation of the infrared radiation over the distance between the detector and the specimen. With a proper surface preparation, the angle of obliquity between the detector and the specimen can be as high as 55 deg. before measurement inaccuracies become significant [82], though, for the present investigation, such angles were kept less than approximately 10 deg.

When analyzing carbon epoxy or aramid epoxy composites, typical output voltage amplitudes from the lock-in amplifier range from 0 to ± 10 mV. The low-pass filter time constant for this range of signal should be at least 0.1 to 0.3 sec. to produce an adequate signal-to-noise ratio and stable output. The sample time should be 3 to 10 times greater than the time constant for an accurate spatial resolution of temperature change on the color monitor. If the sample time is too short, the output cannot stabilize before the camera advances to the next sample point. Hence, sample times of 0.3 to 3 sec. are typical — leading to very long scan times with these "worst-case" material systems.

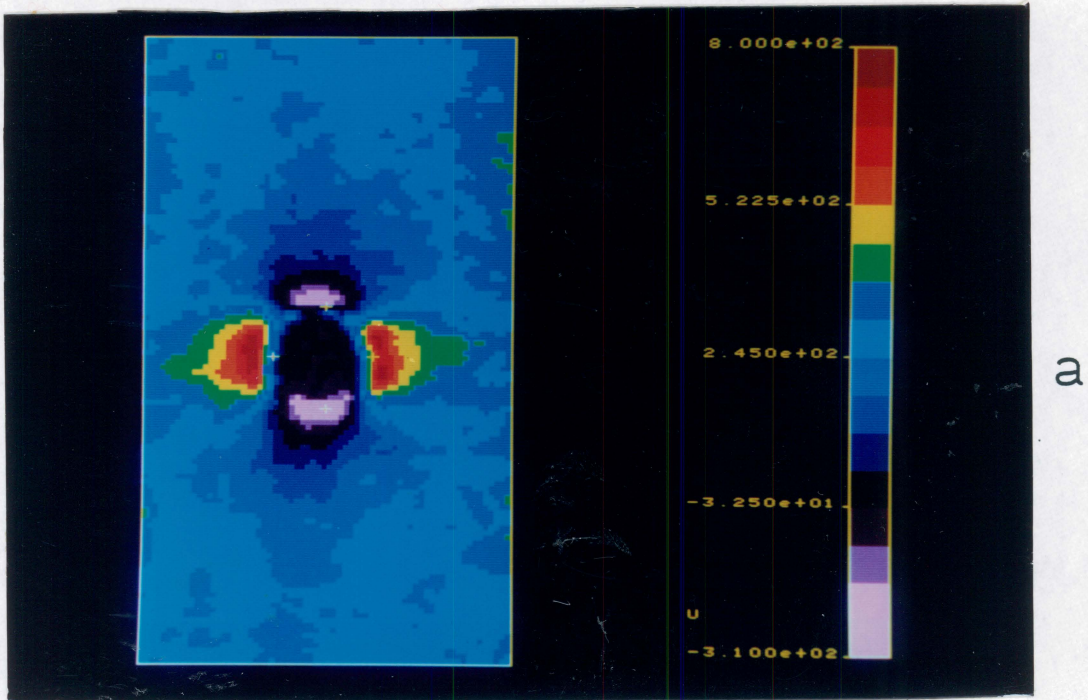
Adjustment of the electronic "zero" on the lock-in amplifier is essential for accurate stress analysis. This can be done quickly by performing line scans across several sections of the area of interest with no load applied to the specimen (a reference signal must still be supplied to the lock-in amplifier, though, to scan the specimen). If there is a signal variation along any section of the specimen, the optimum adjustment is such that the *average* signal is zero.

During a scan, one can expect to obtain spurious data when the focal area lies partly on and partly off of an edge of the specimen (particularly along the top and bottom portions of the notch). These data points are inaccurate because the stressed material cyclically enters and leaves the focal area, resulting in a false apparent temperature change.

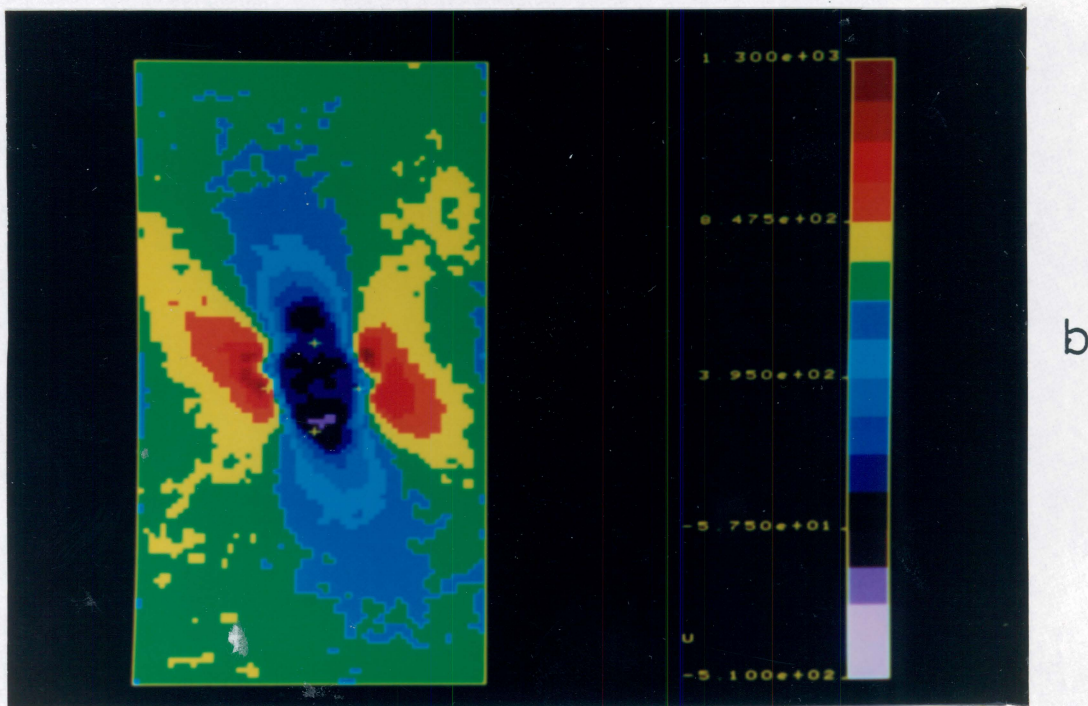
Calibration of the SPATE's thermal emission scale can be accomplished with the use of high sensitivity, low response time thermocouples placed at several locations on the specimen (though, this was not done for the present investigation). Care must be exercised, however, to ensure that all test variables previously mentioned are held constant for a particular calibration.

2.1.7.5 Interpretation of Results

Due to the adiabatic nature of the SPATE technique, the surface ply dominates infrared temperature measurements. Figure 6 illustrates this phenomenon in two undamaged, center-notched quasi-isotropic, carbon epoxy laminates with different stacking sequences: $(0,90,45,-45)_S$ and $(45,90,-45,0)_S$. The black color on the thermal emission scale corresponds to no temperature change during the load cycle. Colors above black quantify the amount of (uncalibrated) cooling during positive load increments (commonly associated with tensile stresses), while colors below black quantify heating (commonly associated with compressive stresses) during positive load increments. In the first laminate, the disturbance in the temperature field caused by the stress concentration was symmetric about the hole, while in the second laminate the pattern was unsymmetric. Despite the identical, symmetric global strains



a



b

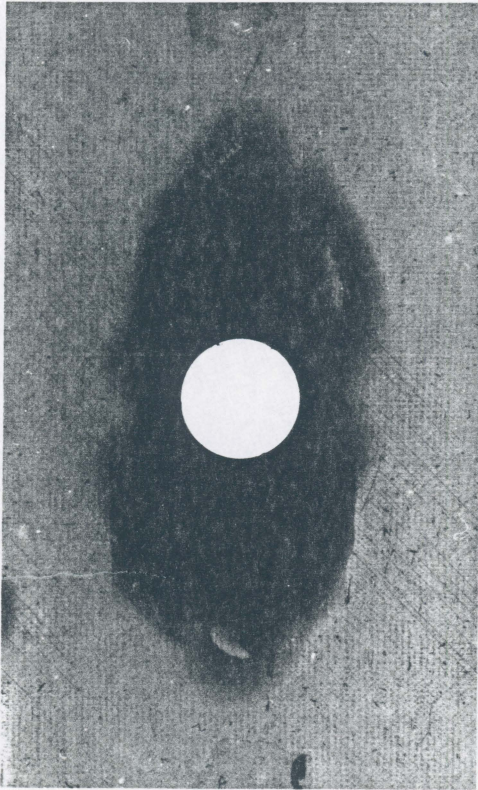
Figure 6. SPATE thermographs of 8-ply carbon epoxy laminates: (a) $(0,90,45,-45)_s$; (b) $(45,90,-45,0)_s$

in these laminates, the unsymmetric thermal emission pattern in Figure 6b can be predicted by considering the unsymmetric stress pattern about the hole in the 45-deg. surface ply (as will be shown later in the analysis).

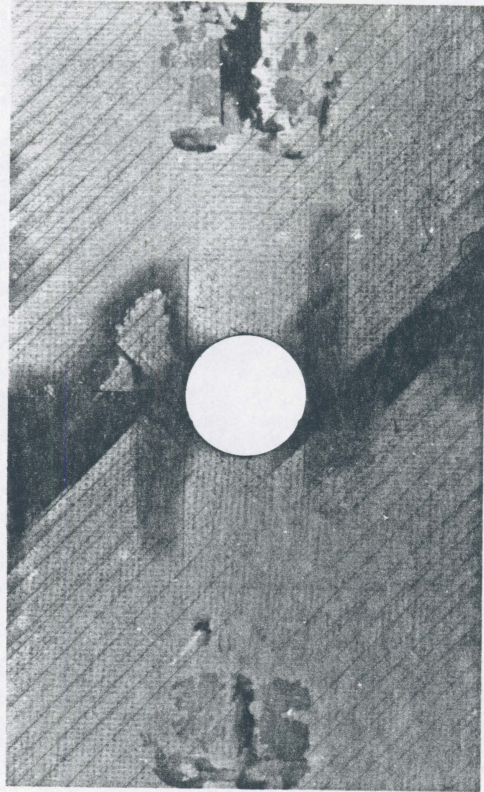
The utility of the SPATE technique for monitoring damage development in fiber composite laminates is exemplified by the penetrant-enhanced X-ray radiographs and SPATE thermographs of fatigue damaged carbon epoxy laminates in Figure 7 and Figure 8. The first example involves the same (0,90,45,-45)_s carbon epoxy laminate as in Figure 6a. The advanced damage condition around the notch resulted in a very low temperature change during the load cycle. Based on the information obtained in the radiograph, it is known that the 0-deg. surface ply was delaminated near the notch and had several associated cracks parallel to the fibers. It is therefore obvious that delaminated regions of this ply were under a nearly-pure uniaxial stress state because of the lack of transverse constraint from the adjoining sublaminates. The very low temperature change measured near the notch was caused not by the total absence of stress in the surface ply, but by the absence of transverse stress in that ply. The surface ply continued to bear load in the 0-deg. fiber direction, but since the coefficient of thermal expansion in this material system is extremely low in the fiber direction, there was little resultant thermal emission.

Consider next the radiograph and SPATE thermograph of the fatigue-damaged (45,90,-45,0)_s carbon epoxy laminate in Figure 7b and Figure 8b. This is the same laminate shown in the undamaged state in Figure 6b. Damage in the surface ply consisted of matrix cracks and delaminations. Due to the relaxation of stresses transverse to the cracks in the surface ply, each matrix crack on the surface of observation appeared as a line of low thermal emission in the thermograph. Delaminated portions of the surface ply that were bounded on three sides by the hole boundary and two parallel matrix cracks in the surface ply carried no load and, therefore, had no thermal emission.

In summary, reduced thermal emissions in carbon epoxy laminates can be due to a relaxation of some or all components of stress in the surface ply. Another cause for pointwise variations of the thermal emission in composites is the existence of manufacturing irregularities.

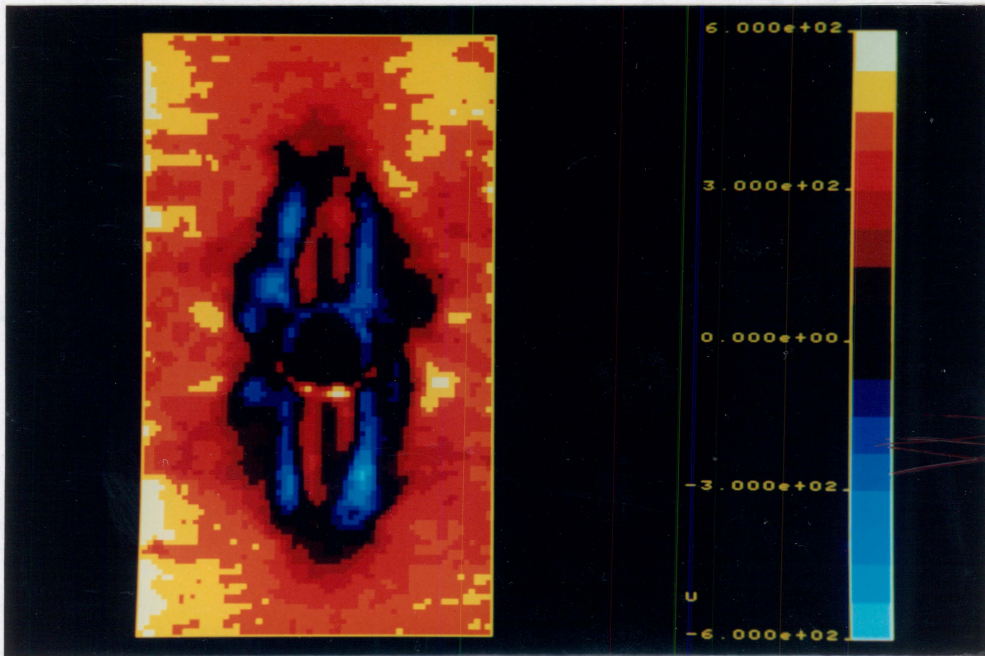


a

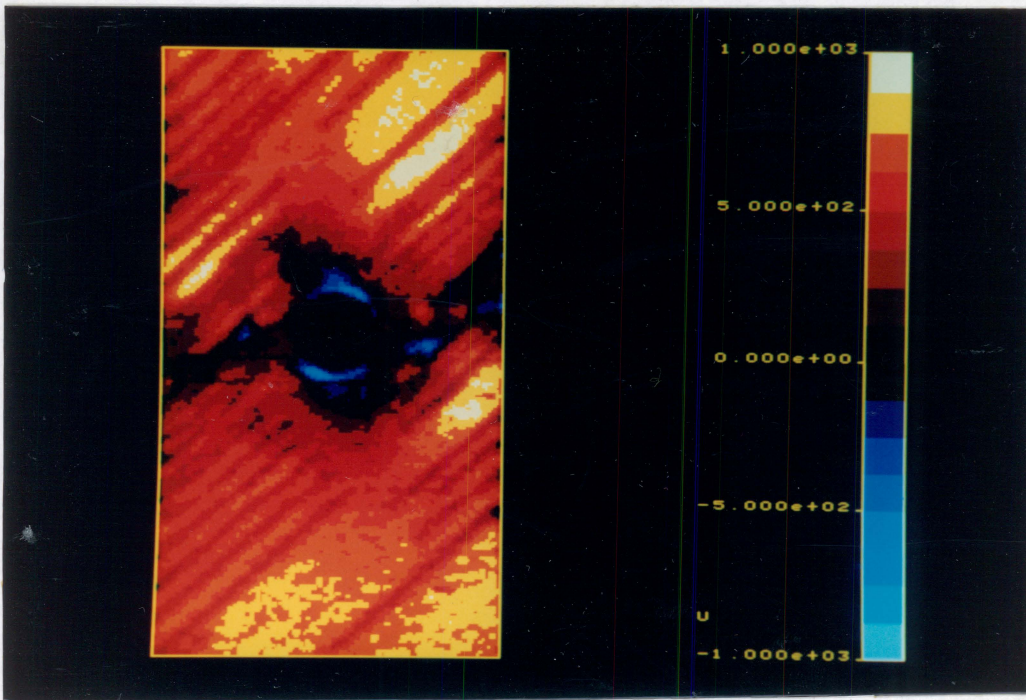


b

Figure 7. Radiographs of 8-ply carbon epoxy laminates with fatigue damage: (a) $(0,90,45,-45)_s$ and (b) $(45,90,-45,0)_s$ laminates



a



b

Figure 8. SPATE thermographs of 8-ply carbon epoxy laminates with fatigue damage: (a) $(0,90,45,-45)_s$ and (b) $(45,90,-45,0)_s$ laminates from Figure 7

ties — in particular, nonuniform phase and void distribution. For example, matrix-rich regions of a composite can be resolved from matrix-poor regions because of their different thermoelastic responses [84]. Additional papers demonstrating the applicability of adiabatic thermoelastic emission as an effective nondestructive testing technique for CFRP materials can be found in Refs. [85-88].

2.2 Analysis

2.2.1 Adiabatic Thermoelastic Effect

Nomenclature: Superscripts f , m , and ℓ refer to fiber, matrix, and lamina, respectively. Subscripts L and T refer to longitudinal and transverse directions of the lamina relative to the fibers. Subscripts 1, 2, 3 and x , y , z refer to lamina- and laminate-aligned coordinates, respectively.

The adiabatic thermoelastic effect was first explained by Thomson (later to become Lord Kelvin) in 1853 [89,90]. Using fundamental laws of thermodynamics, he derived Eq. (1), which relates the pointwise change in infinitesimal extensional strain components, ε_i ($i = 1,2,3$), in homogeneous, isotropic, linear-elastic matter and the small, reversible, adiabatic temperature change, Θ ,

$$\Theta = -\frac{3 T_0 \alpha K}{c_\sigma} (\varepsilon_1 + \varepsilon_2 + \varepsilon_3) \quad (1)$$

where T_0 is the initial temperature of the material, α is the linear thermal expansion coefficient, K is the bulk modulus, and c_σ is the *volumetric* specific heat at constant stress. Equation (1) can be written in terms of the change in extensional stress components, σ_j , as in Eq. (2):

$$\Theta = -\frac{T_0 \alpha}{c_\sigma} (\sigma_1 + \sigma_2 + \sigma_3) \quad (2)$$

Two well-known implications of Eqs. (1) and (2) are: (a) the temperature of isotropic matter with a positive thermal expansion coefficient increases with a negative dilatation, and decreases with a positive dilatation; and (b) a state of pure shear strain or stress produces no adiabatic thermoelastic temperature change in isotropic matter. The accuracy of Thomson's thermoelastic relationship has been verified with metals by numerous investigators, including Joule [91], Compton and Webster [92], Dillon and Tauchert [93], Belgen [83], and Stanley and Chan [94]. Gilmour, et al. [95] showed that several glassy polymers, including epoxy resin, obeyed Eq. (1) if elastic deformations were maintained. Haward and Trainor [96] demonstrated the validity of (1) for poly(methyl methacrylate) (PMMA) for tensile and compressive loads below the creep threshold. Deviations in the measured temperature change from (1) have been attributed to plasticity in metals by Jordan and Sandor [97], Enke and Sandor [98], and Stanley and Chan [82], and to viscoelasticity in polymers by Higuchi and Imai [99]. In situations where adiabatic conditions are not maintained, the temperature variation is not reversible, and additional terms must be included in Eqs. (1) and (2) to account for heat transfer.

Biot gives the counterpart of Eq. (1) for anisotropic solids as:

$$\Theta = -\frac{T_0}{c_\epsilon} \alpha_{kl} C_{ijkl} \epsilon_{ij} \quad (3)$$

where α_{kl} is the linear thermal expansion tensor, c_ϵ is the volumetric specific heat at constant strain, C_{ijkl} is the stiffness tensor, and ϵ_{ij} is the linear strain tensor [100]. The volumetric specific heat at constant stress or strain is related to the corresponding mass specific heat,

c' , by the expression $c = \rho c'$, where ρ is the mass density. Rewriting Eq. (3) in terms of the stress tensor, we have:

$$\Theta = -\frac{T_0}{c_\varepsilon} \alpha_{kl} \sigma_{kl} \quad (4)$$

The difference between c_σ and c_ε for anisotropic solids, though quite small, is given by Eq. (5) [101]:

$$c_\sigma - c_\varepsilon = T_0 \alpha_{ij} \alpha_{kl} C_{ijkl} \quad (5)$$

Equations (3) and (4) imply that a state of pure shear strain or stress in anisotropic matter can result in a non-zero adiabatic thermoelastic temperature change only if there exists a non-zero shear-extension coupling term in the thermal expansion tensor or the stiffness tensor. Unidirectionally-reinforced fiber composite materials have no such shear-extension coupling, and, furthermore, are considered to be transversely isotropic. Equation (3) for such materials then becomes

$$\Theta = -\frac{T_0}{c_\varepsilon} \{ \alpha_L [C_{11}\varepsilon_1 + C_{12}(\varepsilon_2 + \varepsilon_3)] + \alpha_T [2C_{12}\varepsilon_1 + (C_{22} + C_{23})(\varepsilon_2 + \varepsilon_3)] \} \quad (6)$$

where the contracted notation has been employed on the indices of the elastic constants and strain components, and the thermal expansion coefficients have been expressed in terms of the longitudinal and transverse components. An additional simplification for isotropic materials is given by Eq. (7):

$$\Theta = -\frac{T_0}{c_\varepsilon} \alpha (C_{11} + 2C_{12})(\varepsilon_1 + \varepsilon_2 + \varepsilon_3) \quad (7)$$

where only one thermal expansion coefficient and two elastic constants are required.

Equations (1-4) can be recast in the form given by Eq. (8) in order to express the adiabatic thermoelastic temperature change in terms of the two planar components of extensional stress acting on the surface of a unidirectional fiber-reinforced material:

$$\Theta = K_1\sigma_1 + K_2\sigma_2 \quad (8)$$

Here, K_1 and K_2 represent the influence of the thermoelastic constants in the orthogonal 1 and 2 directions, respectively. The 1 and 2 directions correspond to the principal material directions in orthotropic matter (such as unidirectionally-reinforced composite materials). If the material is isotropic, $K_1 = K_2$, and Θ is proportional to the sum of the normal stresses; otherwise $K_1 \neq K_2$, and Θ is proportional to a nonuniformly-weighted sum of the normal stresses. An apparent limitation of the adiabatic thermoelastic measurement technique is that the two stress components in Eq. (8) cannot be individually calculated from a given temperature change except in special cases where one component is known by some boundary condition [102]. For a series of measured temperature changes, Θ_j , the locus of possible combinations of σ_1 and σ_2 can be graphically represented by one of a series of parallel lines in the σ_1 - σ_2 plane (Figure 9). The line passing through the origin suggests that, in addition to the null stress state, there are an infinite number of stress states resulting in no adiabatic thermoelastic temperature change.

Equation (8) can be used to describe the "smeared" thermoelastic response of a composite material if the effective (average) thermoelastic constants of the material are known. In those situations where the constitution or relative amount of each phase of the composite is variable, a more general approach is to evaluate the temperature change in each constituent separately using Eq. (3) or (4), and to combine these changes in some manner to derive the net temperature change of the composite. Expression (9) represents one method of computing a weighted average of the several temperature changes in a non-layered composite,

$$\Theta^{\text{net}} = \Theta^j X^j \quad (9)$$

where Θ^j is the temperature change of the j -th constituent and X^j is an "influence factor" for the j -th constituent (such as the volume fraction). A difficulty associated with using Eq. (9) is that an accurate micromechanical model for constituent extensional strains or stresses is required to compute each Θ^j .

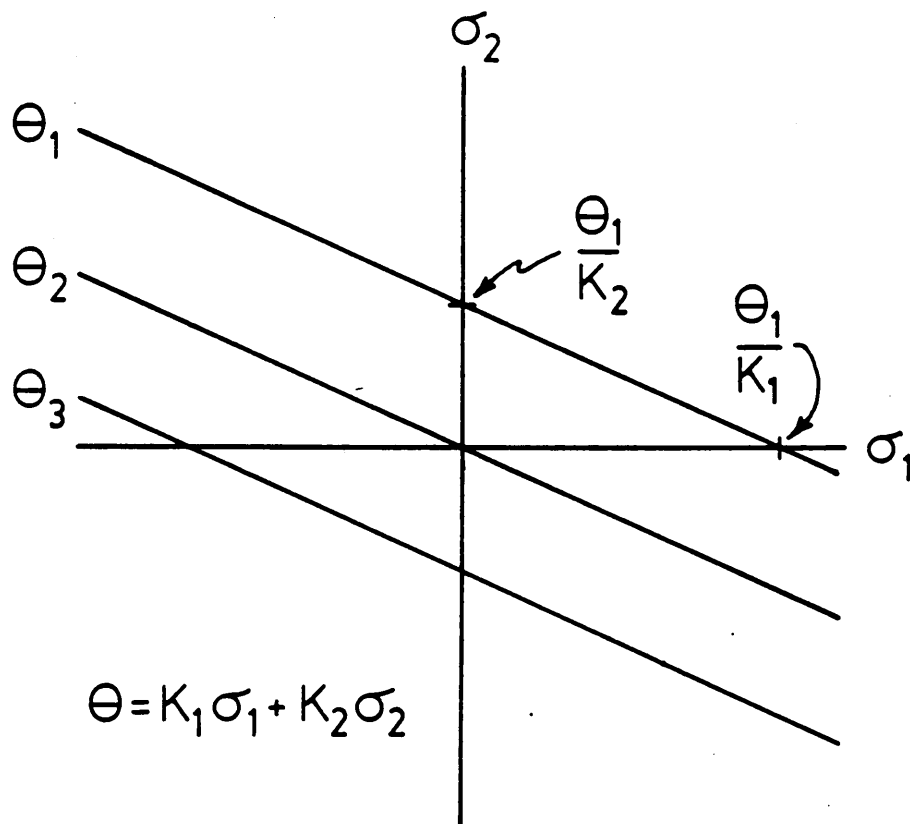


Figure 9. Dependence of adiabatic thermoelastic temperature change on in-plane stress components

Considering that photons from a depth of only a few microns reach the infrared detector [103] and that there is no heat transfer between layers of a laminate during an adiabatic deformation, it is obvious that SPATE measurements are sensitive to the deformation of just the top ply on the surface of observation. (A typical ply thickness is approximately 0.005 in.). Since the deformations and resulting temperature changes of the constituent phases of the composite will differ in layers of dissimilar orientation, laminate stacking sequence must be known to interpret the measurements. That is, Eq. (9) needs to be evaluated only for the surface ply. Of course, the deformation of the surface ply reflects the deformation of the entire laminate if the plies remain bonded together during the measurement. If heat generation, heat conductance, and heat capacitance are taken into account during a mechanical excitation, stresses a small distance below the surface of observation can be computed as well [104].

The approach taken to develop a micromechanical model of the adiabatic thermoelastic effect in undamaged fiber composites is to begin with Lekhnitskii's elasticity solution for global strains in an infinite, homogeneous, anisotropic plate with an elliptical opening [30], realizing that those strains are valid only in regions away from the free edges in a laminated plate. After transforming those strains to the surface ply's local coordinates, a simple micromechanical model of fiber and matrix deformation is used to compute the temperature change in those constituents. Finally, a rule of mixtures relation, such as Eq. (9), is used to compute the net temperature change of the surface ply.

In the micromechanical analysis of strains in the constituents, "mechanics of materials" assumptions [105] will be invoked to maintain simplicity. The problem is formulated by first identifying the unknown quantities to be computed, which, for Eq. (3), would be the three extensional stresses and strains in the fibers and matrix: σ_i^f , σ_i^m , ϵ_i^f , and ϵ_i^m ($i=1,2,3$). In the most general three-dimensional case, the assumed force equilibrium equations in the longitudinal and transverse directions of a representative volume (or area) of material in a plane state of stress (Figure 10) are given by Eqs. (10-12),

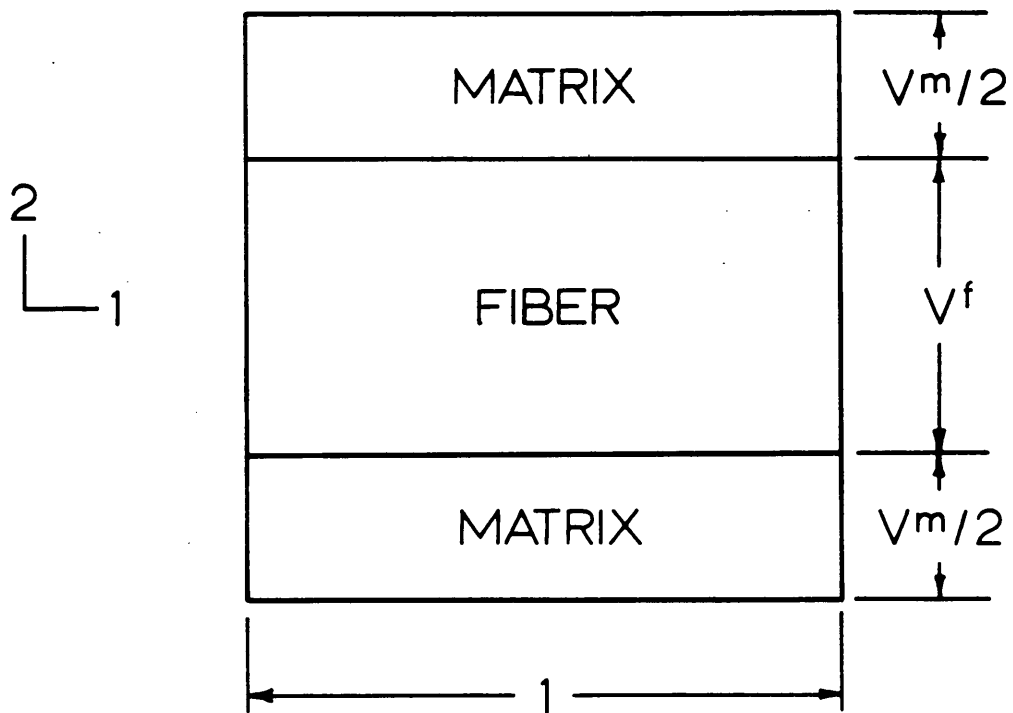


Figure 10. Representative area of a fiber composite material

$$V^f \sigma_1^f + V^m \sigma_1^m = \sigma_1^{\ell} \quad (10)$$

$$\sigma_2^f = \sigma_2^{\ell} \quad \text{and} \quad \sigma_2^m = \sigma_2^{\ell} \quad (11a,b)$$

$$\sigma_3^f = 0 \quad \text{and} \quad \sigma_3^m = 0 \quad (12a,b)$$

where V^f and V^m are volume fractions of the fibers and matrix, respectively. The assumed kinematic relations in the longitudinal and transverse directions are given by Eqs. (13-15):

$$\varepsilon_1^f = \varepsilon_1^{\ell} \quad \text{and} \quad \varepsilon_1^m = \varepsilon_1^{\ell} \quad (13a,b)$$

$$\varepsilon_2^f V^f + \varepsilon_2^m V^m = \varepsilon_2^{\ell} \quad (14)$$

$$\varepsilon_3^f V^f + \varepsilon_3^m V^m = \varepsilon_3^{\ell} \quad (15)$$

The constitutive relations between normal stresses and strains in transversely isotropic media are given by Eq. (16):

$$[\sigma_1 \ \sigma_2 \ \sigma_3]^T = [C] [\varepsilon_1 \ \varepsilon_2 \ \varepsilon_3]^T \quad (16)$$

where C_{ij} are elements of the stiffness matrix given by Eq. (17):

$$[C] = \begin{bmatrix} \frac{1}{E_L} & -\frac{\nu_{LT}}{E_L} & -\frac{\nu_{LT}}{E_L} \\ -\frac{\nu_{LT}}{E_L} & \frac{1}{E_T} & -\frac{\nu_{TT}}{E_T} \\ -\frac{\nu_{LT}}{E_L} & -\frac{\nu_{TT}}{E_T} & \frac{1}{E_T} \end{bmatrix}^{-1} \quad (17)$$

Implicit in Eq. (16) is the assumption of no shear coupling in any plane of the material. This assumption is based on the fact that the 1, 2, and 3 axes coincide with the principal directions of orthotropy. Of course, in the isotropic matrix material the transverse and longitudinal directions are immaterial. It will also be assumed that hygrothermal self-stresses have no dynamic variation during cyclic loading and that intralaminar stress gradients due to the

mismatch of fiber and matrix thermoelastic properties are negligible. Edge-induced interlaminar stresses will not be considered in the micromechanical analysis since the global solution for strain near an edge is invalid there.

Including the six constitutive relations for the fibers and matrix implied by (16), there are now fifteen equations for twelve unknowns. Clearly, the formulation is overdetermined due to the redundant nature of several of the equations. The formulation must therefore be altered to obtain a tractable system of equations. To this end, only the six extensional strains are to be computed through the use of Eqs. (13a,b), (14), and three conditions given by Eqs. (18), (19), and (20):

$$C_{12}^f \varepsilon_1^f + C_{22}^f \varepsilon_2^f + C_{23}^f \varepsilon_3^f = C_{12}^m \varepsilon_1^m + C_{22}^m \varepsilon_2^m + C_{23}^m \varepsilon_3^m \quad (18)$$

$$C_{13}^f \varepsilon_1^f + C_{23}^f \varepsilon_2^f + C_{33}^f \varepsilon_3^f = 0 \quad \text{and} \quad C_{13}^m \varepsilon_1^m + C_{23}^m \varepsilon_2^m + C_{33}^m \varepsilon_3^m = 0 \quad (19,20)$$

Equation (18) results from equating the in-plane transverse stress components of the matrix and fibers ($\sigma_2^f = \sigma_2^m$), and does not require that the transverse constituent stresses equal the transverse lamina stress. This potential violation of equilibrium is inevitable with the present formulation. Equations (19) and (20) are the conditions of vanishing stress normal to the surface of the material ($\sigma_3^f = 0$ and $\sigma_3^m = 0$), and are chosen to represent the stress state of particles of material near the surface of the test specimen that most strongly influence the adiabatic thermoelastic emission of infrared radiation. Solving Eqs. (19) and (20) for the out-of-plane strains, we find:

$$\varepsilon_3^f = -\frac{1}{C_{33}^f} (C_{13}^f \varepsilon_1^f + C_{23}^f \varepsilon_2^f) \quad \text{and} \quad \varepsilon_3^m = -\frac{1}{C_{33}^m} (C_{13}^m \varepsilon_1^m + C_{23}^m \varepsilon_2^m) \quad (21,22)$$

The assumption of homogeneous strain in the longitudinal direction of all constituents, given by Eqs. (13a,b), can be used to replace ε_1^f and ε_1^m in the previous equations with the known lamina strain, ε_1^L . Expressing Eq. (18) in terms of ε_2^m , ε_1^L , and ε_2^L with the use of Eqs. (13), (14), (21), and (22), we have:

$$\begin{aligned}
C_{12}^f \varepsilon_1^\ell + \frac{C_{22}^f}{V^f} (\varepsilon_2^\ell - V^m \varepsilon_2^m) - \frac{C_{23}^f}{C_{33}^f} \left[C_{13}^f \varepsilon_1^\ell + \frac{C_{23}^f}{V^f} (\varepsilon_2^\ell - V^m \varepsilon_2^m) \right] \\
= C_{12}^m \varepsilon_1^\ell + C_{22}^m \varepsilon_2^m - \frac{C_{23}^m}{C_{33}^m} (C_{13}^m \varepsilon_1^\ell + C_{23}^m \varepsilon_2^m)
\end{aligned} \tag{23}$$

Solving Eq. (23) for ε_2^m in terms of ε_1^ℓ and ε_2^ℓ results in Eq. (24),

$$\varepsilon_2^m = D_1 \varepsilon_1^\ell + D_2 \varepsilon_2^\ell \tag{24}$$

where D_i are unitless material constants defined by:

$$\begin{aligned}
D_1 &= \frac{C_{12}^f - C_{12}^m - \frac{C_{23}^f C_{13}^f}{C_{33}^f} + \frac{C_{23}^m C_{13}^m}{C_{33}^m}}{C_{22}^m - \frac{(C_{23}^m)^2}{C_{33}^m} + \frac{V^m}{V^f} \left[C_{22}^f - \frac{(C_{23}^f)^2}{C_{33}^f} \right]} \\
D_2 &= \frac{C_{22}^f - \frac{(C_{23}^f)^2}{C_{33}^f}}{V^f \left[C_{22}^m - \frac{(C_{23}^m)^2}{C_{33}^m} \right] + V^m \left[C_{22}^f - \frac{(C_{23}^f)^2}{C_{33}^f} \right]}
\end{aligned}$$

Substituting Eqs. (13b) and (24) into Eq. (22) provides the remaining unknown matrix strain component in terms of the in-plane lamina strains,

$$\varepsilon_3^m = D_3 \varepsilon_1^\ell + D_4 \varepsilon_2^\ell \tag{25}$$

where

$$D_3 = -\frac{1}{C_{33}^m} (C_{13}^m + C_{23}^m D_1) \quad \text{and} \quad D_4 = -\frac{C_{23}^m}{C_{33}^m} D_2$$

The volume change of the matrix material per unit original volume is given by the sum of the infinitesimal, extensional strains in Eqs. (13b), (24), and (25),

$$\varepsilon_1^m + \varepsilon_2^m + \varepsilon_3^m = D_5 \varepsilon_1^\ell + D_6 \varepsilon_2^\ell \quad (26)$$

where $D_5 = (1 + D_1 + D_3)$ and $D_6 = (D_2 + D_4)$.

It is assumed that the fibers are transversely isotropic in elastic as well as thermal expansion properties, with the plane of isotropy being perpendicular to the fiber longitudinal axis. For the present, we ignore the contradiction of this assumption with the "mechanics of materials" assumptions stated earlier. The in-plane, transverse component of fiber strain is expressed in terms of the known lamina and matrix strains by rearranging Eq. (14):

$$\varepsilon_2^f = \frac{1}{V^f} (\varepsilon_2^\ell - V^m \varepsilon_2^m) \quad (27)$$

Equations (13a) and (27) are used to express the out-of-plane, transverse component of fiber strain in Eq. (21) as

$$\varepsilon_3^f = -\frac{1}{C_{33}^f} \left[C_{13}^f \varepsilon_1^\ell + \frac{C_{23}^f}{V^f} (\varepsilon_2^\ell - V^m \varepsilon_2^m) \right] \quad (28)$$

The strain ε_2^m in Eqs. (27) and (28) can be eliminated using Eq. (24) to finally arrive at the expressions for the extensional fiber strains in terms of the in-plane lamina strains,

$$\begin{aligned} \varepsilon_1^f &= \varepsilon_1^\ell \\ \varepsilon_2^f &= D_7 \varepsilon_1^\ell + D_8 \varepsilon_2^\ell \\ \varepsilon_3^f &= D_9 \varepsilon_1^\ell + D_{10} \varepsilon_2^\ell \end{aligned} \quad (29)$$

where the unitless material constants D_i are given by

$$\begin{aligned} D_7 &= -\frac{V^m}{V^f} D_1 & D_8 &= \frac{(1 - V^m D_2)}{V^f} \\ D_9 &= \frac{1}{C_{33}^f} (D_1 C_{23}^f \frac{V^m}{V^f} - C_{13}^f) & D_{10} &= \frac{C_{23}^f}{C_{33}^f V^f} (D_2 V^m - 1) \end{aligned}$$

In the application of Eq. (6), relating temperature change to strain in a transversely isotropic material, it is convenient to group the transverse fiber strains as in Eq. (30)

$$\varepsilon_2^f + \varepsilon_3^f = D_{11} \varepsilon_1^f + D_{12} \varepsilon_2^f \quad (30)$$

where

$$D_{11} = \frac{1}{C_{33}^f} \left[D_1 \frac{V^m}{V^f} (C_{23}^f - C_{33}^f) - C_{13}^f \right] \quad \text{and} \quad D_{12} = \frac{1}{V^f} (1 - V^m D_2) \left[1 - \frac{C_{23}^f}{C_{33}^f} \right]$$

Up to this point, the equations expressing the three extensional components of micro-constituent strains in terms of the in-plane lamina strains have been developed. The temperature change of the fibers and matrix can now be obtained simply by substituting the proper material properties and lamina strains into Eqs. (6) and (7), respectively.

The last remaining step in calculating the effective lamina temperature change is to combine the constituent temperature changes. Within the context of adiabatic, reversible temperature change, it is natural to combine the constituent temperature changes based on the area fraction of each micro-constituent material influencing the temperature sensor. For the present discussion, the effective lamina temperature change is approximated with the rule of mixtures expression, Eq. (31):

$$\Theta^f = \Theta^f V^f + \Theta^m V^m \quad (31)$$

Substitution of Eqs. (6) and (7) into Eq. (31) provides the final expression for the effective temperature change of the lamina in terms of the in-plane strains from classical laminated plate theory:

$$\Theta^f = D_{13} \varepsilon_1^f + D_{14} \varepsilon_2^f \quad (32)$$

where D_{13} and D_{14} are material constants given by:

$$D_{13} = -T_0 \left[\frac{V^f}{C_\epsilon^f} \{ \alpha_L^f [C_{11}^f + C_{12}^f D_{11}] + \alpha_T^f [2 C_{12}^f + (C_{22}^f + C_{23}^f) D_{11}] \} + \frac{V^m}{C_\epsilon^m} \alpha^m D_5 (C_{11}^m + 2 C_{12}^m) \right]$$

$$D_{14} = -T_0 \left\{ \frac{V^f}{C_\epsilon^f} D_{12} [\alpha_L^f C_{12}^f + \alpha_T^f (C_{22}^f + C_{23}^f)] + \frac{V^m}{C_\epsilon^m} \alpha^m D_6 [C_{11}^m + 2 C_{12}^m] \right\}$$

To illustrate the effect of surface ply orientation on the thermoelastic temperature change measured via infrared thermography, several theoretical calculations for continuous fiber carbon epoxy laminates are considered next. (Experimental data were not available, and could differ somewhat from the present predictions which were calculated using Eq. 32). The highly anisotropic thermoelastic constants of unidirectional laminae of carbon epoxy were taken from Ref. [106]. Figure 11 is a prediction of the effect of ply orientation on the adiabatic temperature change for a unidirectional ply under constant axial stress or strain change. There is a monotonic increase in temperature change as the ply orientation, θ , is changed from 0-deg. to 90-deg. Analogous behavior is predicted for $\pm\theta$ angle-ply laminates (Figure 12). Note that there are two values of θ resulting in no thermal emission for angle-ply laminates, according to the calculations. The global transverse strains of a laminate vary with θ because of the dependence of the global Poisson's ratio on θ . In order to separate the effects of surface ply orientation and global Poisson's ratio, the surface ply angle in a quasi-isotropic laminate was varied while a constant global strain field was maintained (Figure 13). Again, the temperature change is greatest when the surface ply orientation is perpendicular to the load direction. As a final example, the effect of laminate Poisson's ratio on the temperature change in a 0-deg. surface ply under a constant longitudinal strain change is considered (Figure 14). The temperature change of the surface ply can be either greater than zero, less than zero, or equal to zero, depending on the magnitude of the transverse strain. This effect is caused by the opposite signs of a carbon epoxy ply's thermal expansion coefficients in the longitudinal and transverse directions (typically, $-0.43 \mu/^\circ\text{F}$ and $13.5 \mu/^\circ\text{F}$, respectively).

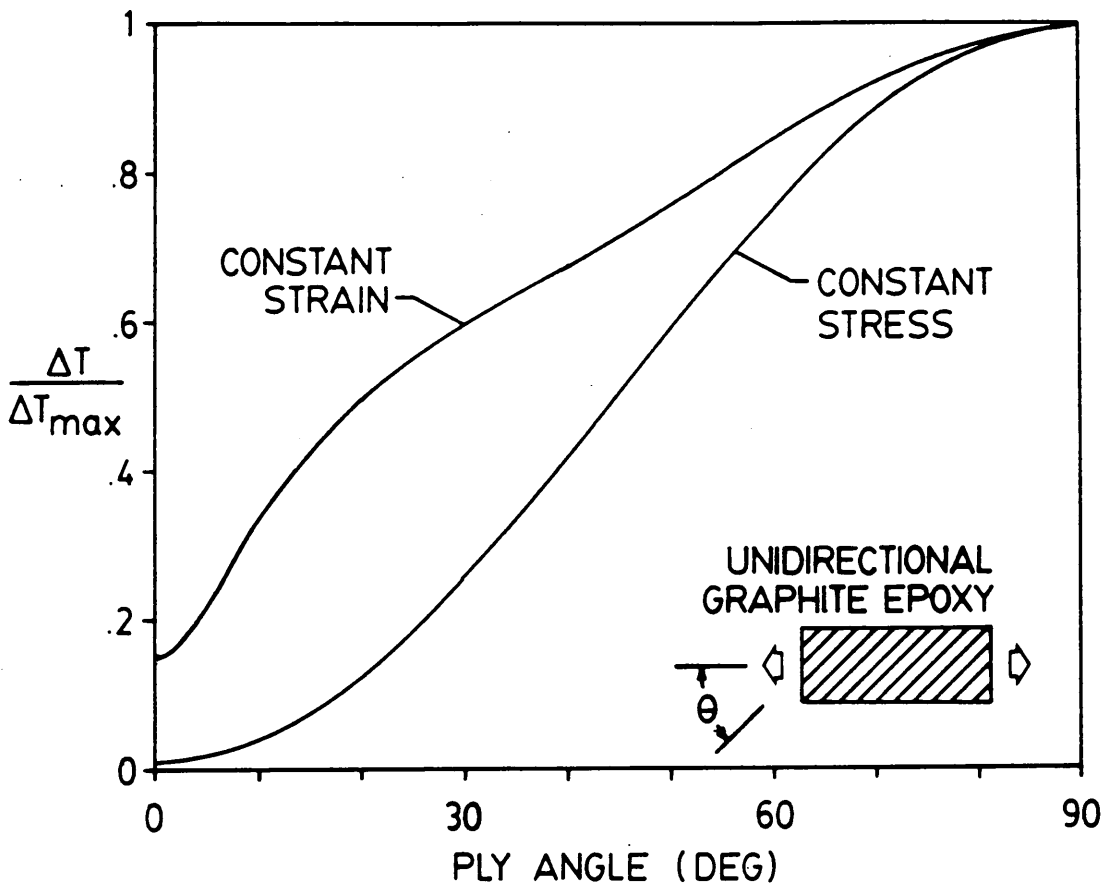


Figure 11. Effect of ply orientation on the temperature change in a unidirectional ply under constant axial stress or strain

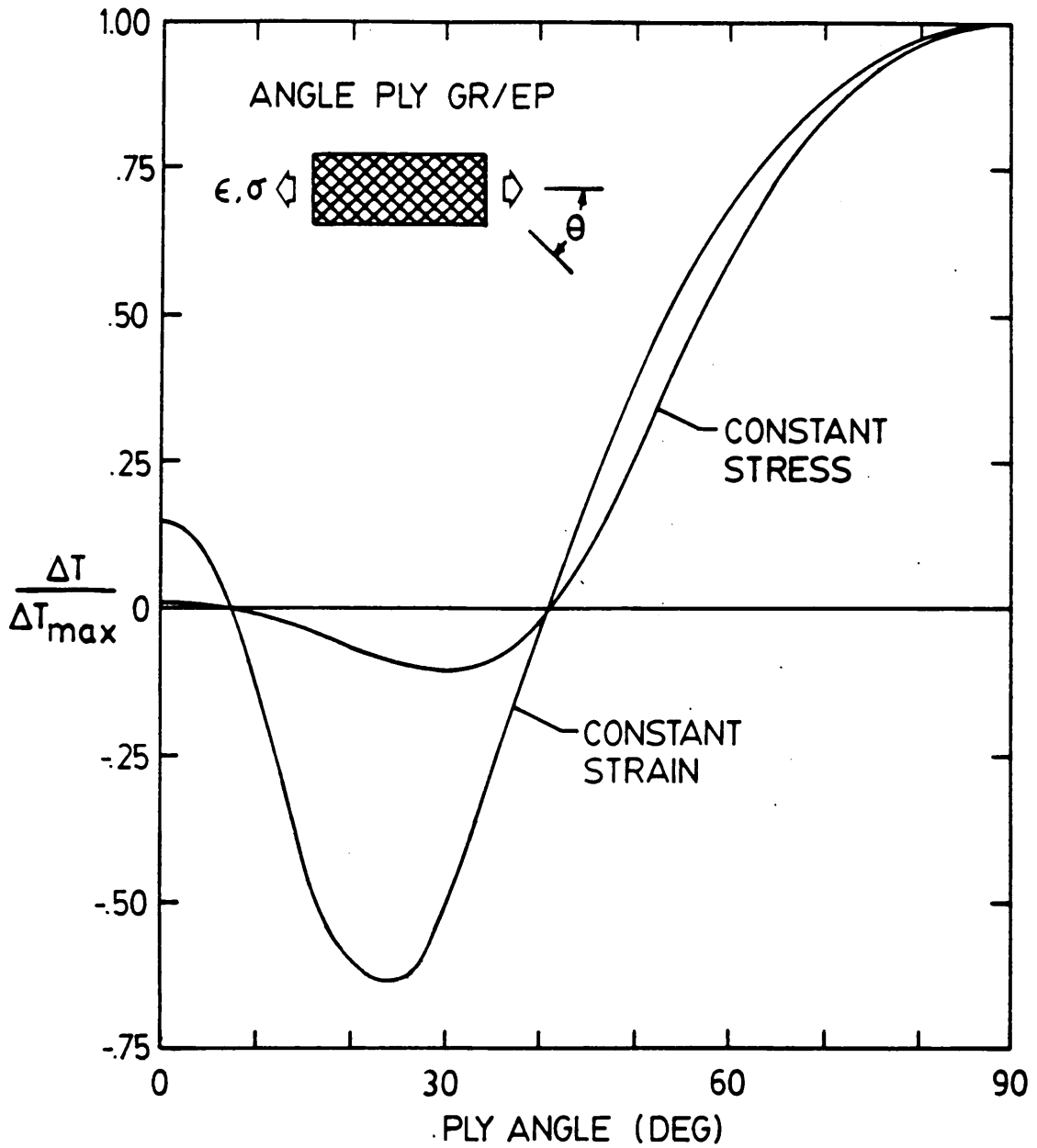


Figure 12. Effect of ply orientation on the temperature change in an angle-ply laminate under constant axial stress or strain

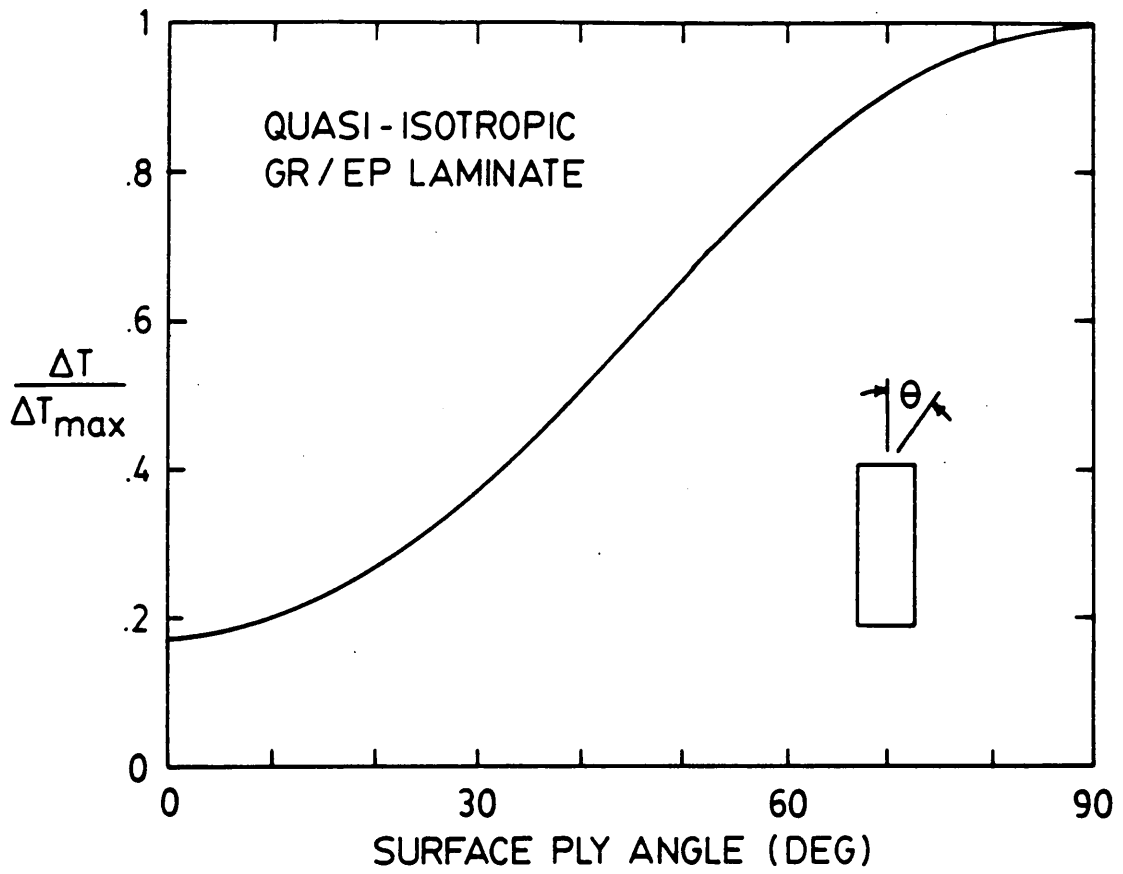


Figure 13. Effect of ply orientation on the temperature change in a quasi-isotropic laminate under a constant global strain field

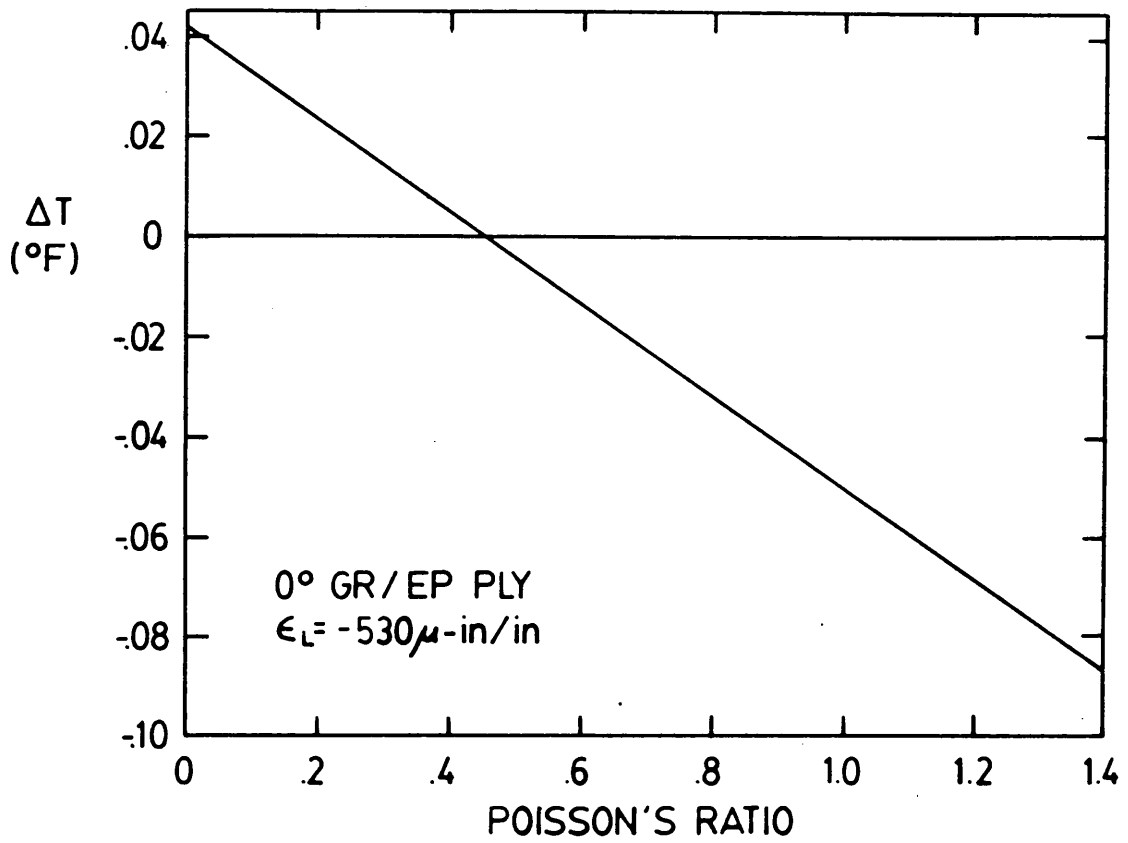


Figure 14. Effect of laminate Poisson's ratio on the temperature change in a 0-deg. ply under a constant longitudinal strain

The generality of the present analysis for thermoelastic temperature changes in laminated fiber composites with arbitrary properties and constitution facilitates our understanding of laboratory measurements by enabling the prediction of the effect of various material properties on the measurements. For instance, using the micromechanical expressions for effective elastic properties of a lamina given by Chamis [106] in conjunction with the present model for adiabatic thermoelastic response, the effect of the fiber volume fraction on the adiabatic temperature change during a constant longitudinal stress or strain a 0-deg. carbon epoxy lamina can be predicted (Figure 15). Under constant strain, the temperature change varied linearly with V^f . Under constant stress, however, the variation was nonlinear due to the increased longitudinal stiffness of the material at higher fiber volume fractions. In this particular calculation, a fiber volume fraction of 0.67 resulted in no temperature change. Lower fiber volumes resulted in cooling under tensile loads, and higher fiber volumes resulted in heating under tensile loads.

To verify the accuracy of the analysis, the predicted and measured thermoelastic emissions in two center-notched, quasi-isotropic, T300/5208 laminates with either a 0 or 45-deg. surface ply were compared. Global stresses from Lekhnitskii's elasticity solution [30] were used in conjunction with the present micromechanical model to compute constituent strains and the average adiabatic temperature change in the surface ply. The thermoelastic properties in Table 1 were used in the analysis, along with $V^f = 0.55$ and $T_0 = 297$ K. Predictions were normalized by their respective far-field values to facilitate comparisons of the patterns. The thermoelastic emission pattern for the (0,90,45,-45)_s laminate (Figure 16a) was not in very good agreement with the measurement in Figure 6a. On the other hand, the prediction for the (45,90,-45,0)_s laminate (Figure 16b) was in excellent agreement with the measurement in Figure 6b. Laminates with 0-deg. surface plies were the most challenging to model since there was great variation from one material system to another, and from one stacking sequence to another. Seemingly, the order of the interior plies influenced measurements more than would be expected in a purely adiabatic process. Given that the analytical results of Figure 16 represented the temperature change of only the surface ply, and that there was fair-to-very good

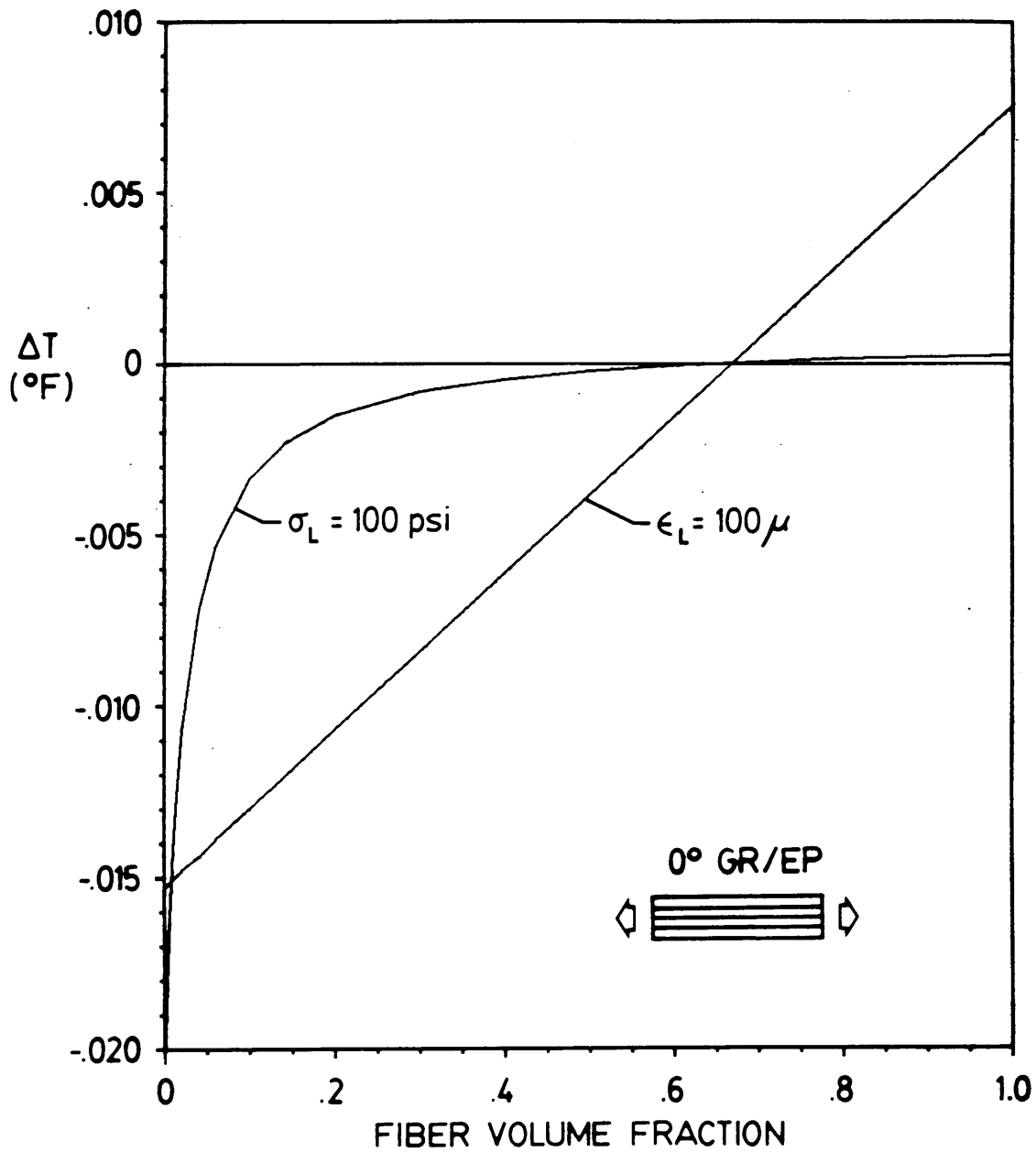


Figure 15. Effect of fiber volume fraction on the adiabatic temperature change in a 0-deg. carbon epoxy lamina under constant longitudinal stress or strain

Table 1. Thermoelastic properties for carbon epoxy

Fiber	Matrix	Lamina
$E_L^f = 33.6 \text{ Msi}$	$E^m = .78 \text{ Msi}$	$E_L^l = 18.8 \text{ Msi}$
$E_T^f = 2.1 \text{ Msi}$	$\nu^m = 0.35$	$E_T^l = 1.41 \text{ Msi}$
$\nu_{LT}^f = 0.29$	$\alpha^m = 40 \mu/\text{°F}$	$G_{LT}^l = 0.782 \text{ Msi}$
$\nu_{TT}^f = 0.49$	$c_\epsilon^m = 105 \text{ lb./in.}^2/\text{°F}$	$\nu_{LT}^l = 0.308$
$\alpha_{LL}^f = -0.55 \mu/\text{°F}$		
$\alpha_{TT}^f = 5.6 \mu/\text{°F}$		
$c_\epsilon^f = 125 \text{ lb./in.}^2/\text{°F}$		

Taken from Refs. [106,107].

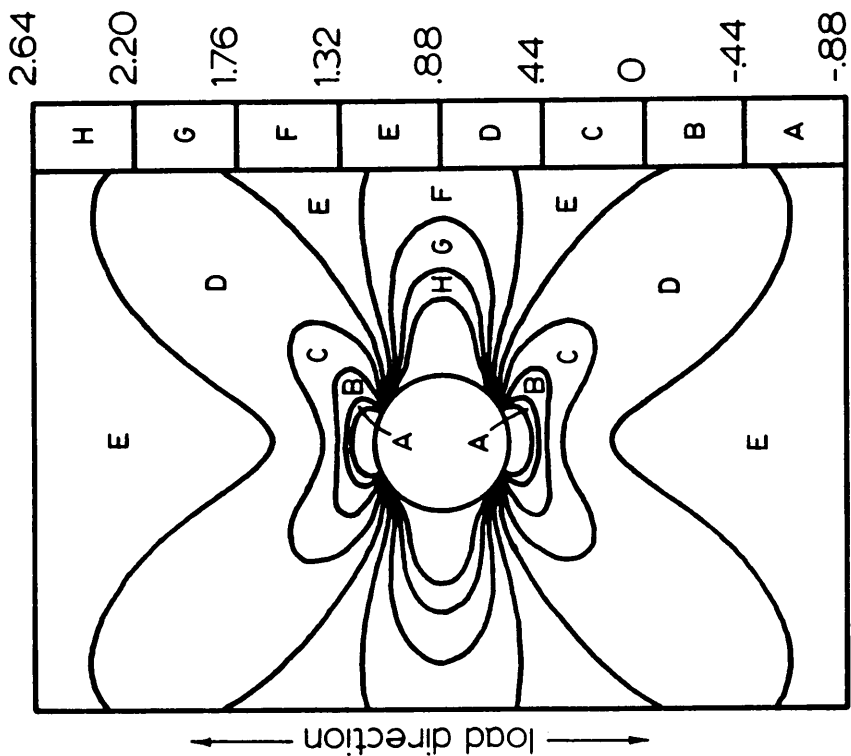
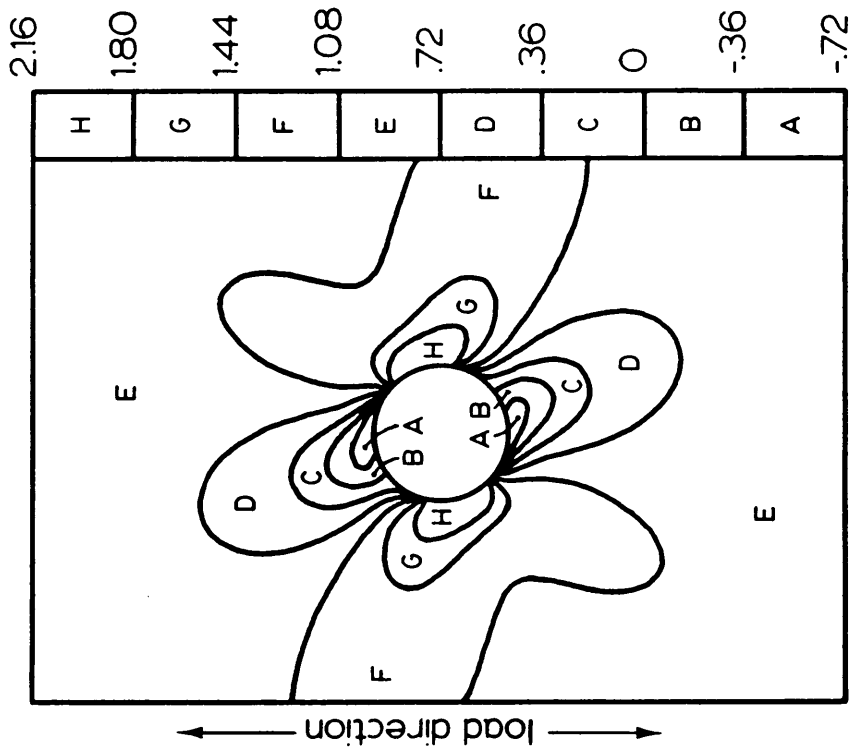


Figure 16. Predicted SPATE patterns in two center-notched carbon epoxy laminates: (a) $(0,90,45,-45)_s$; (b) $(45,90,-45,0)_s$

correlation of the analysis and experiments, it can be concluded that the assumptions of the analysis are reasonable, but could be improved by addressing several uncertainties. The notched (0,90,45,-45)_s laminate was chosen for these additional exploratory-type analyses because the theory and experiments disagreed most severely for laminates with 0-deg. surface plies.

There are several plausible causes for the discrepancy between the measured and predicted thermoelastic emissions. By computing stresses in the fibers and matrix with strains evaluated in the micromechanical analysis, and checking force equilibrium in the longitudinal and transverse directions (Eqs. 10 and 11), it is found that the analysis produced constituent stresses that were quite consistent with the lamina stress state on an absolute scale, but, in some instances, significantly in error on a percentage basis for several simple laminates (Table 2). (The carbon epoxy material properties used in the calculations for Table 2 were slightly different than those given in Table 1. However, for the present discussion this does not matter.) Furthermore, the accuracy of the constituents' thermoelastic properties are questionable for the dynamic problem at hand. An inaccuracy in any one of the thermoelastic properties or micro-stress components could cause the discrepancies. It may also be necessary to alter expression (31) to account for the actual contributions of the individual constituent phases (perhaps in adjacent plies) on the infrared radiation under conditions that may not be purely adiabatic.

A second modeling uncertainty was addressed by modifying a test specimen. Specifically, the resin-rich layer of epoxy on the surface of the notched (0,90,45,-45)_s T300/5208 laminate in Figure 6a was removed by sanding until bare fibers were visible with an optical microscope. In this manner, it could be determined whether or not the resin-rich layer was masking the temperature variation of the fibers. The SPATE scan of the sanded specimen is shown in Figure 17. Despite the increased surface fiber area visible to the infrared detector, the overall magnitude of thermoelastic emission increased. There was also a slight change in the contour pattern, although disagreement with the prediction (Figure 16a) persisted. The analysis was then modified to allow the specification of different contributions of the fibers and matrix

Table 2. Force equilibrium assessment in the micromechanical model

Laminate†	σ_1^f ‡	σ_2^f ‡	$(V^f \sigma_1^f + V^m \sigma_1^m)$ ‡	σ_2^f and σ_2^m ‡
(0) _{8t}	20.00	0	20.39	-0.09
(90) _{8t}	0	1.31	-0.09	1.36
(0/90) _{2s}	20.12	.36	20.49	.29
(90/0) _{2s}	-.45	1.29	-.54	1.35
(±45) _{2s}	2.97	.25	3.02	.25

† Applied longitudinal strain (ϵ_x) = 1000 μ .

‡ Units of stress are ksi.

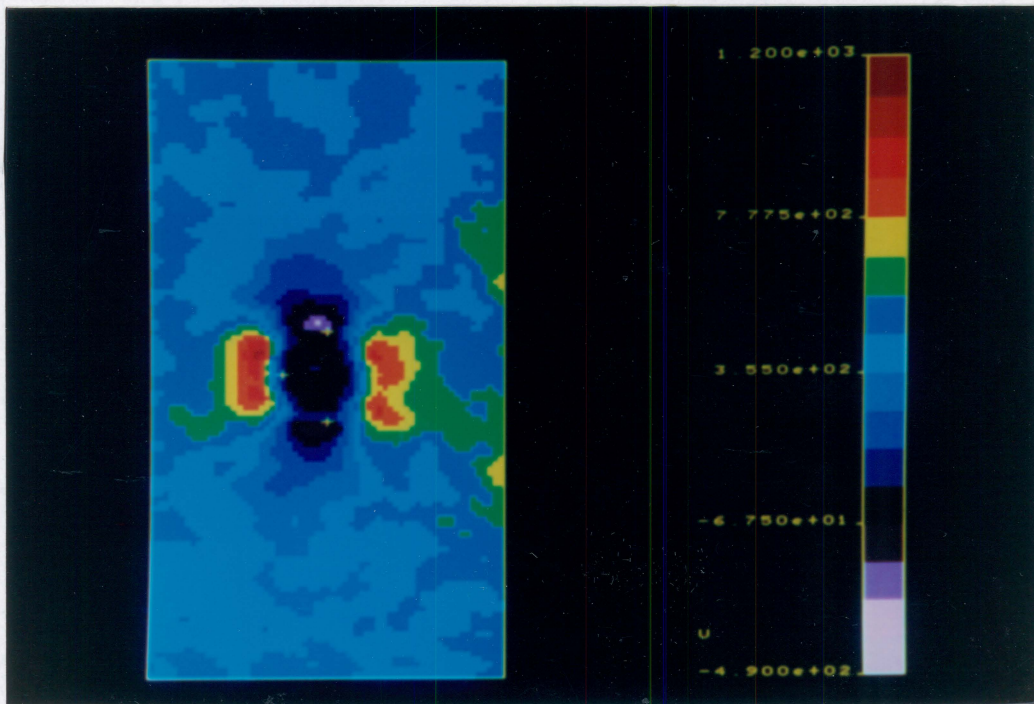


Figure 17. SPATE thermograph of a (0,90,45,-45)_s carbon epoxy laminate with the resin-rich surface layer removed: (c.f. Figure 6a)

to the rule of mixtures expression for net temperature change (Eq. 31). The results of this modification are shown in Figure 18, where the contribution of the fibers varied from zero to 100 percent. At 67.5 percent fiber contribution, the predicted far-field thermoelastic emission was zero. Above 67.5 percent fiber contribution, the far-field thermoelastic emission was greater than zero under tensile loads, and below 67.5 percent it was less than zero. Since the measurements indicated that the far-field thermoelastic emission was less than zero under tensile loads, the theory predicted that the fibers must contribute less than 67.5 percent to the measurements. In any case, none of the patterns shown in Figure 18 agree remarkably with the measurements before or after sanding.

The third modeling uncertainty addressed was the influence of interply heat conduction. A fully-three-dimensional analysis of in-plane and out-of-plane conduction with the sole source of heat generation being the adiabatic thermoelastic effect in various layers was beyond the scope of the present investigation. Hence, the temperature changes of the outermost one to four plies were averaged with unequal weights. The justification for neglecting intraply conduction was that the thickness of the plies (0.005 in.) was very small, providing a short conduction path relative to those distances involved in intraply conduction that were likely to affect the contour patterns. The results, shown in Figure 19 for the (0,90,45,-45)_s laminate, were calculated using $V^f = 0.55$ in the rule of mixtures expression (31) as well as in the computed material constants. The prediction using a 70 percent first ply contribution, and 30 percent second ply contribution agreed best with the measurements, although there is still room for improvement. It is interesting to note that, on a point-to-point basis, the average of the adiabatic temperature changes in the 0- and 90-deg. plies equaled that for the +45- and -45-deg. plies, which also equaled the average for all eight plies in the laminate.

Despite the difficulties in predicting SPATE measurements discussed above, we still face the ill-posed problem of computing the state of deformation in the material from temperature change measurements. Recalling Figure 9 on page 39, there are infinitely-many combinations of stress components that produce the same temperature change. This fact is especially problematic when damage is introduced into the specimen and the evaluation of the stress

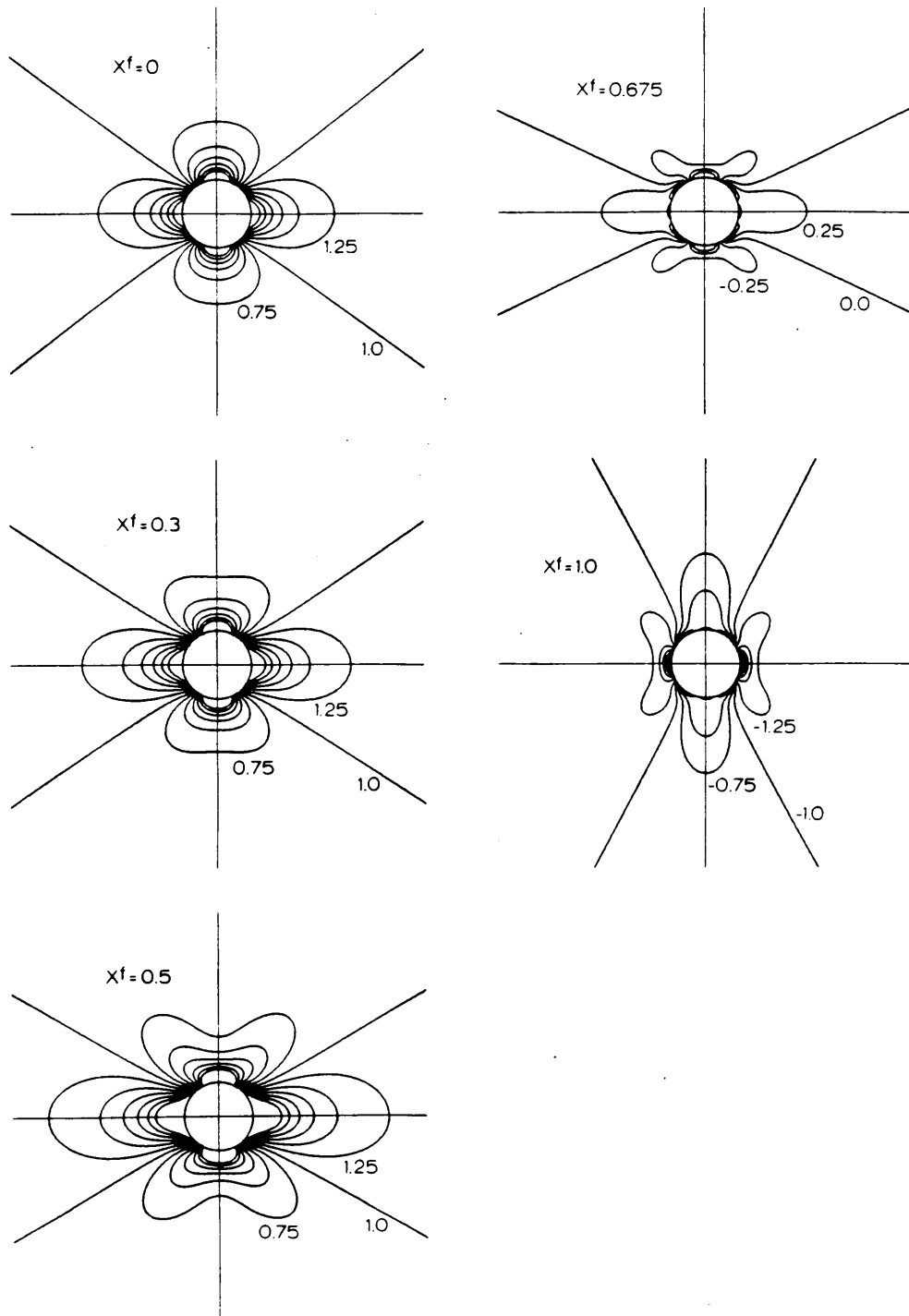


Figure 18. Predicted SPATE patterns in a center-notched (0,90,45,-45)_s carbon epoxy laminate with varied contributions of the constituents in the surface ply

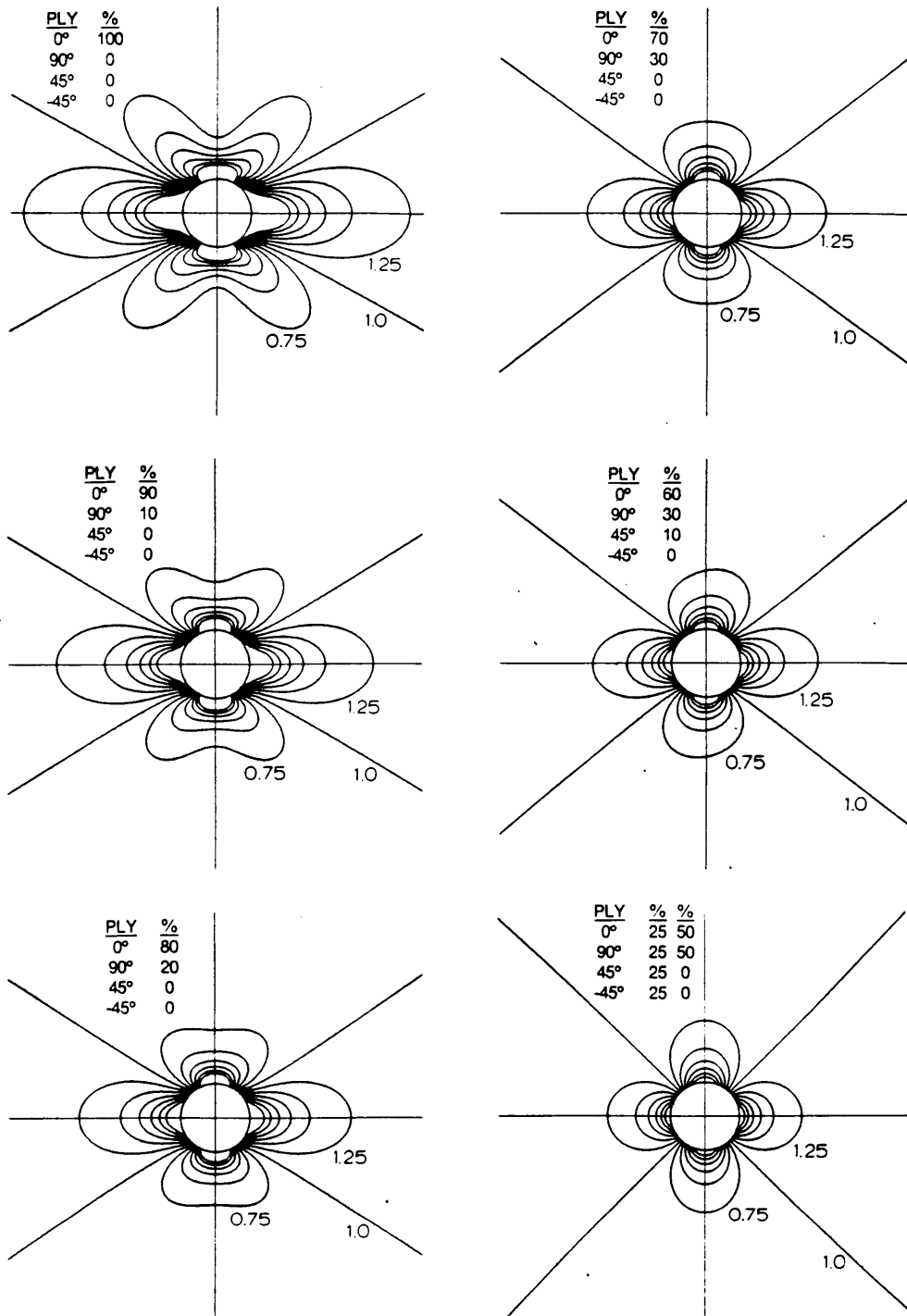


Figure 19. Predicted SPATE patterns in a center-notched (0,90,45,-45)_s carbon epoxy laminate with varied ply influences

or strain field associated with the damage is attempted. Therefore, the evaluation of stress or strain redistribution due to damage is to be approached with this limitation in mind.

Chapter III

Basic Material Characterization

3.1 *Monotonic Strength*

As was mentioned in the description of specimen design, a series of compression tests with different unsupported gage lengths revealed that a 2.5-in. gage length would be sufficiently small to avoid the weakening effects of column-type buckling in all specimens. A longer unsupported length could have been used with the orthotropic stacking sequence, but a uniform length was chosen for all specimens for simplicity of fabrication. The orthotropic stacking sequence occasionally exhibited an in-plane, shearing failure mode along a -45 deg. angle, which, in the case of DEN specimens, would extend into the grips if the specimen was shorter than 2.4 inches. The tensile and compressive strengths of virgin specimens loaded monotonically to failure are listed in Table 3. Specimens with an unsupported length (UNSL) of 2.4 or 2.5 in. were used to compute the mean, standard deviation and variance of the ultimate gross section stress for each specimen type [71]. A few noteworthy items from these data are highlighted below.

Table 3. Monotonic strength of virgin specimens

Specimen Type	Tensile Strength, S_t^o (ksi)*			Compr. Strength, S_c^o (ksi)*		
	\bar{x}	s	var, %	\bar{x}	s	var, %
3501-A-CN	42.3	3.8	9.1	-43.8	.95	2.2
3501-A-DEN	45.8	2.4	5.2	-44.2	3.2	7.3
3501-B-CN	59.2	1.9	3.2	-52.8	.32	.6
3501-B-DEN	64.9	2.2	3.4	-53.6	1.3	2.5
1808-A-CN	39.4	.81	2.0	-45.2	1.0	2.3
1808-A-DEN	42.5	2.7	6.2	-48.1	3.8	7.9
1808-B-CN	54.1	2.8	5.1	-55.2	1.7	3.0
1808-B-DEN	55.9	1.6	2.8	-56.6	2.9	5.1

* Stresses computed over the gross, unnotched cross-sectional area. Data include mean (\bar{x}), standard deviation (s), and variance (var); sample size is three.

- The quasi-isotropic 3501-6 material was stronger in compression than in tension, while the opposite situation prevailed with the orthotropic layup. One may surmise that the in-plane shear failure mode of the orthotropic laminate in compression may contribute to the relative lack of compressive strength, but no such relationship between tensile and compressive strengths was observed in the orthotropic 1808 material. Indeed, 1808 specimens of either stacking sequence were always stronger in compression than in tension.
- In tension, 3501-6 specimens were about 10% stronger than analogous 1808 specimens. In compression, 1808 specimens were slightly stronger than 3501-6 specimens.
- A lower local strain (measured by a small strain gage near the notch) was measured near failure in the orthotropic layup of both material systems [71]. The orthotropic layup was also approximately 50% stronger in tension and 25% stronger in compression than the quasi-isotropic layup for both materials.
- Near failure, there was less local strain near the notch tip in the DEN configuration than in the analogous CN configuration [71].

Briefly, failure modes in tension consisted of clean laminate fractures (little delamination) initiating at the point of highest stress concentration near the notch or adjacent to but not directly in contact with the notch. In the latter mode, the surface 0-deg. ply fractured along an underlying +45 deg. ply direction, beginning at the point where the large matrix cracks tangent to the notch in these two plies intersect. In the DEN configurations, failure almost always initiated at one of the notches first (with audible acoustic emissions and visible fiber breaks in the surface ply). In some cases, failure was instantaneous after the first notch failure, and in other cases the specimen continued to bear additional load after the first acoustic event.

Under compression loading, delaminations were widespread in all specimen types. There were also signs of local crushing and ply buckling near the notches. As described earlier, the orthotropic laminates occasionally exhibited an in-plane shear mode of failure which either extended entirely or partially across the specimen width. The fracture surface of the outer-

most 0-deg. ply in the shear failures was either a staircase-type or extremely smooth. In all specimen types except 1808-B, there was at least one compression failure where a portion of the surface 0-deg. ply was intact, but delaminated.

3.2 *Fatigue Life*

Plots of applied stress amplitude versus fatigue lifetime for the eight specimen types are shown in Figure 20. Each figure illustrates the S-N data for a particular material system and lamination arrangement (both notch configurations) on a semi-log scale. If it is hypothesized that the data must pass through one of the components of strength (either tensile or compressive, depending on the failure mode) for failure during the first cycle, it is obvious that a more complete data set would have either a knee or a gradual bend to achieve the necessarily concave-down appearance of a continuous curve. The data would appear more linear without the semi-log scale. Comparing the data, it can be seen that the S-N curve of the (0,45,0,-45)_{s4} laminate is steeper than that of the (0,45,90,-45)_{s4} laminate for both materials and notch types. The DEN data points fall either on or above the CN points, which is consistent with the superior monotonic strength of virgin DEN specimens.

In Table 4, the two load levels chosen for the primary tests of each specimen type are listed in two forms: absolute units, and normalized by the corresponding monotonic tensile and compressive strength of virgin specimens. Except for the high-load, quasi-isotropic, CN specimens, there were no large differences in the normalized load levels for the AS4/3501-6 and AS4/1808 materials. The higher high load level in the AS4/3501-6 (0,45,90,-45)_{s4} CN specimens compared to similar AS4/1808 specimens resulted in shorter fatigue lifetimes in the AS4/3501-6 specimens (about 1K cycles vs. 10K cycles). To obtain the targeted high- and low-load fatigue lifetimes, normalized loads had to be higher in the (0,45,0,-45)_{s4} laminates

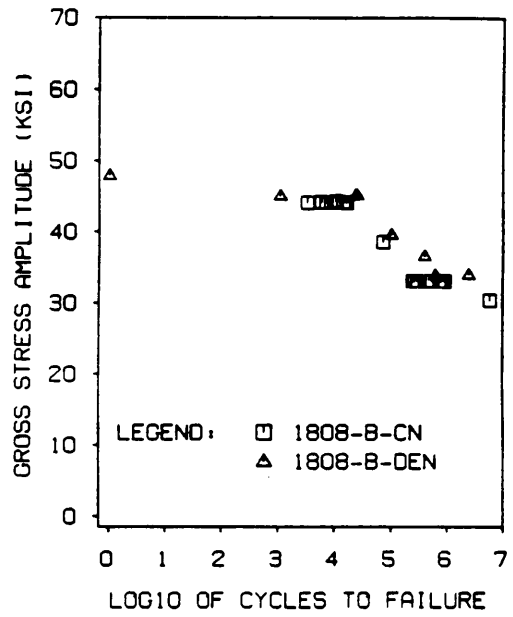
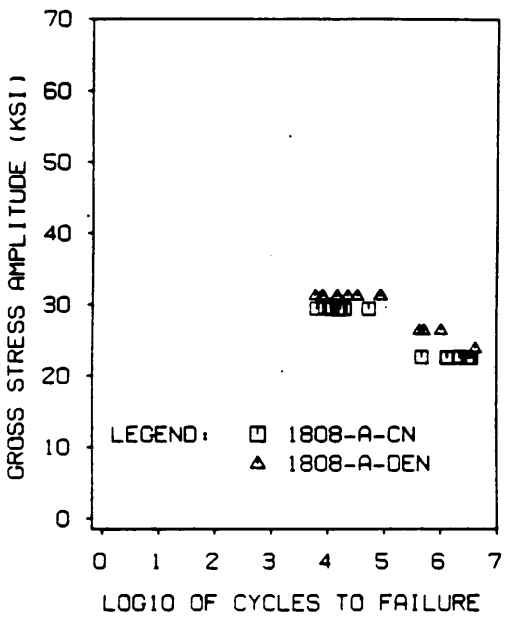
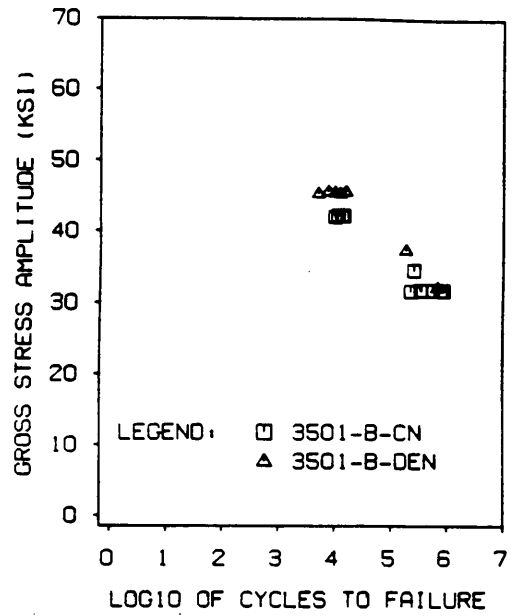
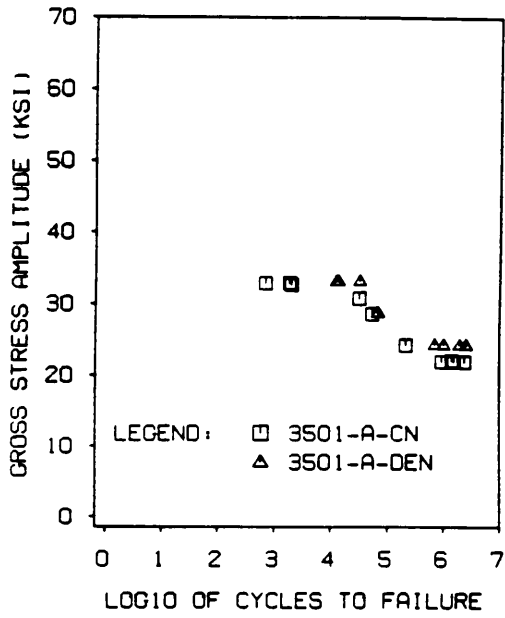


Figure 20. Stress vs. life data for test specimens

Table 4. Cyclic load levels (R=-1) for fatigue tests

Material	Stack	Notch	High Load, S_a			Low Load, S_a		
			ksi	S_a/S_t^0	S_a/S_C^0	ksi	S_a/S_t^0	S_a/S_C^0
AS4/3501-6	(0/45/90/-45) _{s4}	CN	32.8	.78	.75	21.9	.52	.50
		DEN	33.2	.72	.75	24.3	.53	.55
	(0/45/0/-45) _{s4}	CN	42.2	.71	.80	31.7	.54	.60
		DEN	45.6	.70	.85	32.2	.50	.60
AS4/1808	(0/45/90/-45) _{s4}	CN	29.4	.75	.65	22.6	.57	.50
		DEN	31.3	.74	.65	26.5	.62	.55
	(0/45/0/-45) _{s4}	CN	44.2	.82	.80	33.1	.61	.60
		DEN	45.3	.81	.80	34.0	.61	.60

than in the $(0,45,90,-45)_{s4}$ laminates, especially for the high load level. This requirement is consistent with the steeper S-N curve of the $(0,45,0,-45)_{s4}$ specimens.

3.3 Stiffness Measurements

Initial stiffness measurements of virgin specimens during the first load cycle of fatigue tests are given in Table 5. Due to the slight non-linearity of the stress-strain behavior of the notched specimens, stiffness measurements at the low and high load amplitudes are listed separately. The AS4/3501-6 material was slightly stiffer than the AS4/1808 material in all cases. The tensile stiffness of the AS4/3501-6 material increased slightly with increased load, while that of the AS4/1808 material remained approximately the same. In both material systems, the compressive stiffness decreased with higher loads. Scatter in the measurements was higher in the DEN specimens than in the CN specimens. A possible explanation of this observation is that the in-plane deformations directly over the notch dominate the slight, though inevitable, out-of-plane deformations, reducing the scatter when the extensometer is positioned across the notch.

Throughout each fatigue test, tensile and compressive stiffness measurements were normalized by their respective values recorded during the first load cycle of the subject specimen. Typical stiffness records during the lifetime of each of the eight specimen types during high-load and low-load fatigue are illustrated in Figure 21 and Figure 22, in which high-load tests are indicated by (H), and low-load tests are indicated by (L). The horizontal axes in the stiffness plots are normalized life axes obtained by dividing the actual number of cycles by the number of cycles to failure for that particular specimen. Stiffness curves recorded with CN specimens and low-load levels were more repeatable than those recorded with DEN specimens and high load levels. In fact, variations caused by the unsymmetric development of damage in DEN specimens were so great that strains measured by front- and back-mounted

Table 5. Tensile and compressive stiffnesses of virgin specimens

Specimen Type	High Load						Low Load					
	E_t^o (Msi)*			E_c^o (Msi)*			E_t^o (Msi)*			E_c^o (Msi)*		
	\bar{x}	s	n									
3501-A-CN	4.59	.06	12	4.20	.13	12	4.51	.14	7	4.21	.17	7
3501-A-DEN	6.33	.29	6	5.84	.49	6	6.28	.21	4	5.90	.34	4
3501-B-CN	6.28	.22	14	5.45	.26	14	6.20	.12	6	5.73	.14	6
3501-B-DEN	9.69	.36	13	8.50	.50	13	9.42	—	1	8.56	—	1
1808-A-CN	4.57	.11	22	4.18	.13	22	4.59	.07	23	4.28	.09	23
1808-A-DEN	6.26	.10	21	5.67	.19	21	6.19	.16	3	5.74	.15	3
1808-B-CN	6.25	.15	23	5.56	.19	23	6.26	.15	22	5.70	.12	22
1808-B-DEN	9.46	.18	3	8.34	.23	3	9.31	.37	3	8.61	.41	3

* Measured with a front-mounted, 1-in. extensometer. Data include mean (\bar{x}), standard deviation (s), and sample size (n).

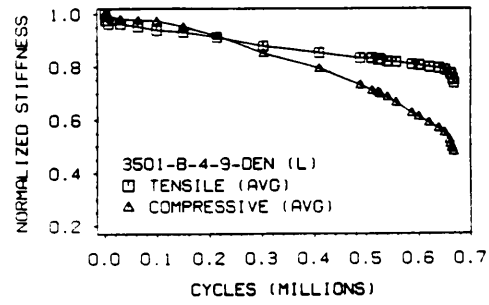
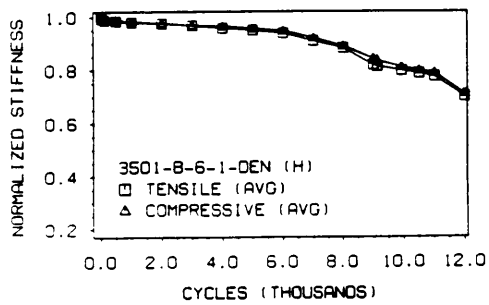
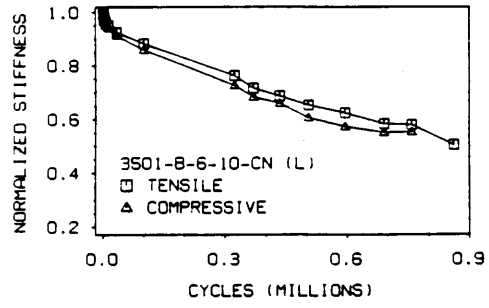
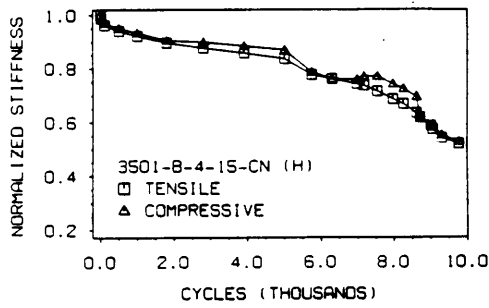
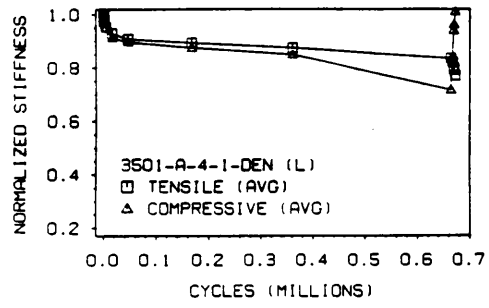
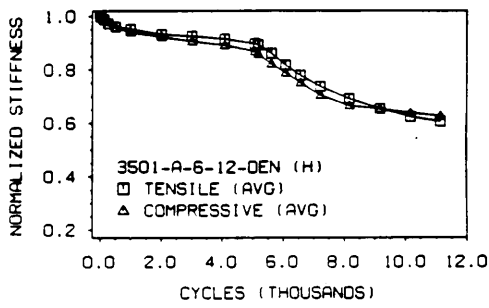
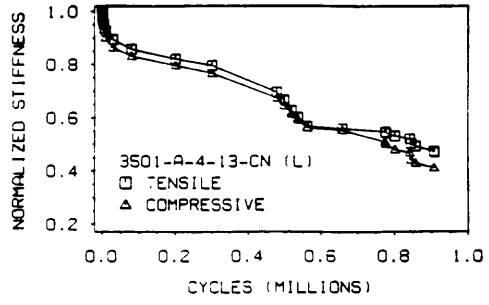
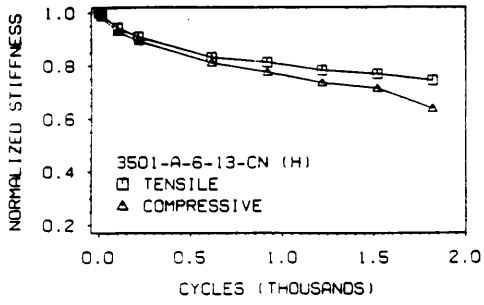


Figure 21. Stiffness change in AS4/3501-6 specimens

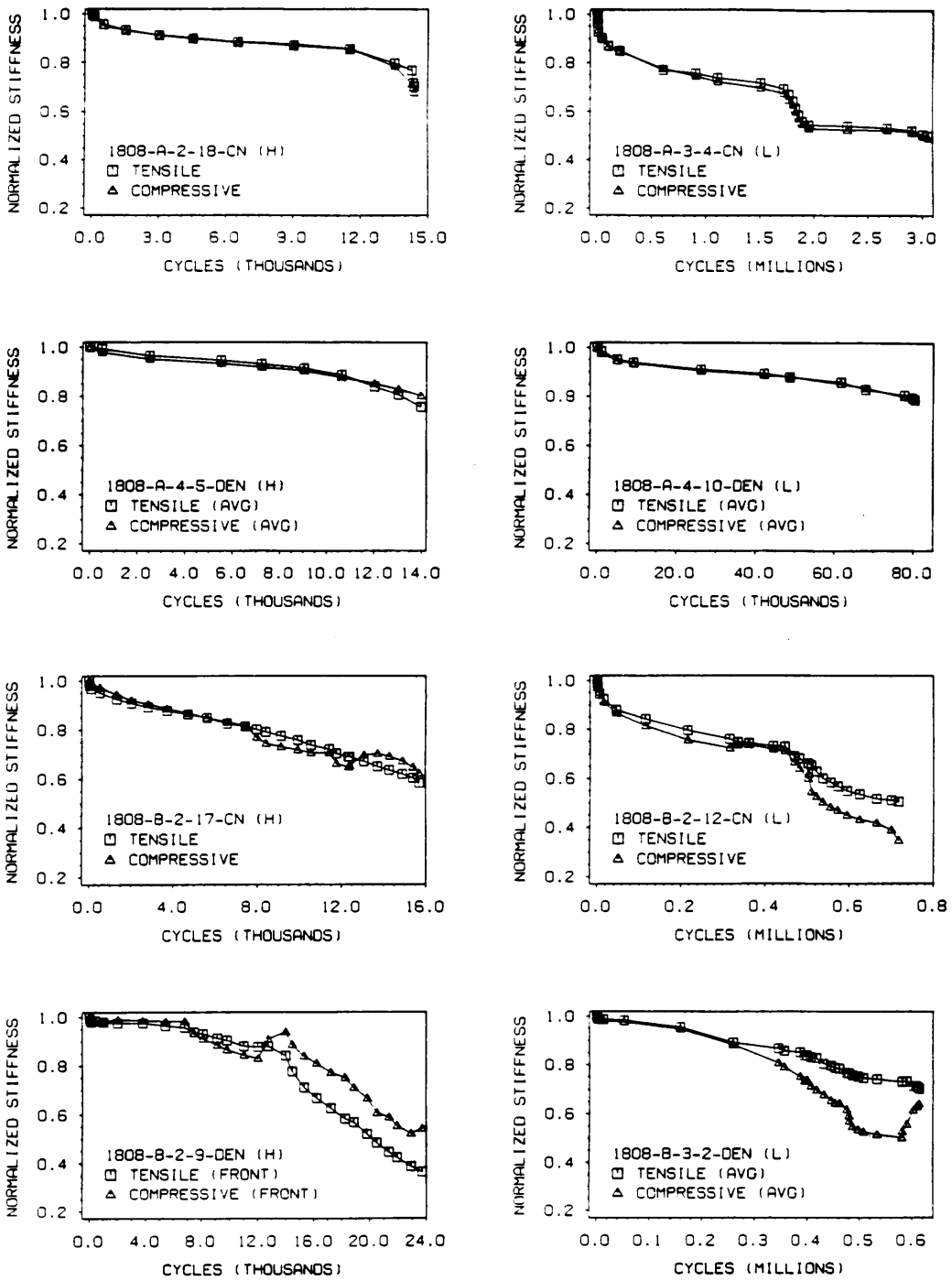


Figure 22. Stiffness change in AS4/1808 specimens

extensometers had to be averaged to eliminate the bending strain component. The large in-plane deformations across the notch prevented the relatively small out-of-plane deformations from becoming a problem in CN specimens. Most of the stiffness data for DEN specimens in Figure 21 and Figure 22 were computed by averaging front and back surface strains (indicated by "AVE"), though, in some cases, only front surface stiffnesses were available (indicated by "FRONT"). Stiffness changes in high-load specimens reflected the highly concentrated nature of damage growth in those specimens. For example, damage that initiated first in one area of the specimen (eg. front side) grew most rapidly in that same area and led to failure of the specimen before damage at analogous locations in the laminate (eg. back side) initiated and grew an equal amount. These variations in damage growth paths caused variations in the stiffness curves as well. Because of its more symmetric nature, low-load fatigue damage resulted in less stiffness variation among specimens.

In general, the rates of change of stiffness corresponded well with the associated rates of damage growth. Separate periods (or stages) of damage growth could be identified during a fatigue test by observing the slope of the stiffness versus cycles curves. The occurrence of rapid damage initiation and growth near the notch(es) was easily identified by the rapid, but slowing, stiffness drop at the beginning of each test. The DEN specimens had less stiffness drop during this first stage of damage development than the CN specimens, especially in the orthotropic laminates. Part of this behavior can be attributed to the more remote location of the extensometer relative to the damage initiation sites in the DEN specimens, and part to the lesser tendency of $(0,45,0,-45)_{s4}$ laminates to delaminate during "stage I" damage development.

After stage I was complete, stiffness measurements were greatly influenced by the particular patterns of damage growth that appeared in the different specimen types. For example, after a second period of relatively slow matrix cracking during low-load fatigue, the center-notched $(0,45,90,-45)_{s4}$ laminates usually underwent a third period of rapid delamination growth in the longitudinal direction, resulting in a short-lived period of rapid stiffness decline. A fourth period of slower matrix cracking ensued, followed by a fifth stage reflecting the rapid

delamination growth that typically preceded fatigue failure in this type of test. In contrast, during high-load tests of $(0,45,90,-45)_{s4}$ CN specimens, there were only three stages of damage growth and stiffness change during the lifetime. Among the specimen types investigated presently, the difference between high- and low-load fatigue response was most dramatic in $(0,45,90,-45)_{s4}$ CN specimens.

The $(0,45,0,-45)_{s4}$ laminates had about the same net stiffness drop at failure as the $(0,45,90,-45)_{s4}$ laminates; their rate of change, however, was more uniform. A prominent feature of all tests, especially those involving $(0,45,0,-45)_{s4}$ laminates, was that the second half of fatigue life was characterized by a "bumpy" stiffness curve due to the non-symmetric appearance of delaminations near the front and back surfaces of the specimens. This "bumpiness" occurred at a relatively larger fraction of life during high-load tests.

The three stopping points for destructive testing techniques — the early, middle, and late stages of fatigue life — were estimated using the characteristic stiffness curves and damage development patterns recorded with X-ray radiography. The early stopping point, about 5-10 percent of life, was at or slightly before the stabilization of the stiffness decline at the end of stage I. The middle stopping point was the most difficult to find due to the lack of repeatable stiffness values or changes in rate of the stiffness decline between 40 and 60 percent of life in many tests. Most often, the beginning of the undulations of the stiffness curves (especially compressive stiffness) and the attainment of a particular cumulative stiffness change were used to predict the middle-life stopping point. The late-life stopping point was also difficult to detect because the actual stiffness values near the end of life were typically scattered over 10-30 percentage points in CN specimens (more in DEN specimens, due to bending effects). To avoid this problem, late life was estimated based on the fairly-predictable sudden increase in damage growth, audible acoustic emissions, and stiffness change during the last 10 percent of life. In cases where the percentage of life based on stiffness was in doubt, X-ray radiographs usually provided definitive information.

Chapter IV

Fatigue Damage Mechanisms

In the following description of fatigue damage mechanisms in notched specimens, certain orientations and locations are referred to repeatedly. The longitudinal direction is along the load axis of the specimen, coinciding with the 0-deg. fiber direction. The transverse direction is oriented at 90 degrees to the longitudinal direction in the plane of the specimen.

Specific damage mechanisms are also referred to often in the text. Two of the more ubiquitous damage types are primary and secondary matrix cracks parallel to the fibers in a particular ply. Primary matrix cracks are those which emanate directly from any boundary of the specimen, including the notch(es) and straight edges. Secondary matrix cracks are identified by the cracks that do not directly intersect a boundary. Incremental, step-wise ply fractures denote the through-the-ply fracture of fibers that occur in short, sudden steps in certain specimens.

This documentation of fatigue damage mechanisms in notched composite laminates is based on the large experimental program discussed earlier. Of course, due to the nature of experimental investigations, there is some degree of variability in the results. The results included herein represent *typical* behaviors, and are not meant to be comprehensive. Due to

space limitations, not all of the specimen types will be discussed here. Similarities in damage mechanisms in specimens with different notch configurations are used to reduce the volume of material presented. Hence, the most complete descriptions are to be found in the sections on CN specimens. The effects of material system, lamination arrangement, load level, and notch configuration on fatigue damage mechanisms are discussed in the summary at the end of this chapter. For organizational purposes, the discussions on stress redistribution and residual strength during the fatigue process are presented in separate chapters.

4.1 AS4/3501-6, Orthotropic Laminate

4.1.1 Center-Notched Specimens

4.1.1.1 High Load Level

The high load level for AS4/3501-6, (0,45,0,-45)_{s4}, CN specimens, 42.2 ksi, resulted in fatigue lifetimes of 10K-14K cycles. After two load cycles, matrix cracks in all plies were evident around the hole. Zero-deg. ply matrix cracks appeared tangent to the hole and nearly perpendicular to the hole, as were matrix cracks in the +45- and -45-deg. plies. Also, secondary +45-deg. matrix cracks initiated along the 0-deg. tangent cracks. No delaminations were seen on the second load cycle, yet, surface 0-deg. ply fracture — a frequent cause of 0/45 interface delamination — was seen at that time (Figure 23a). Note that the 0-deg. ply fracture path did not initiate on the hole boundary. Instead, the localized fracture began at the intersection of the 0-deg. and 45-deg. matrix cracks tangent to the hole, suggesting the importance of the stress concentration associated with the crossing cracks. Based on audible acoustic emissions and visual observations during the manual load ramping required for stiffness

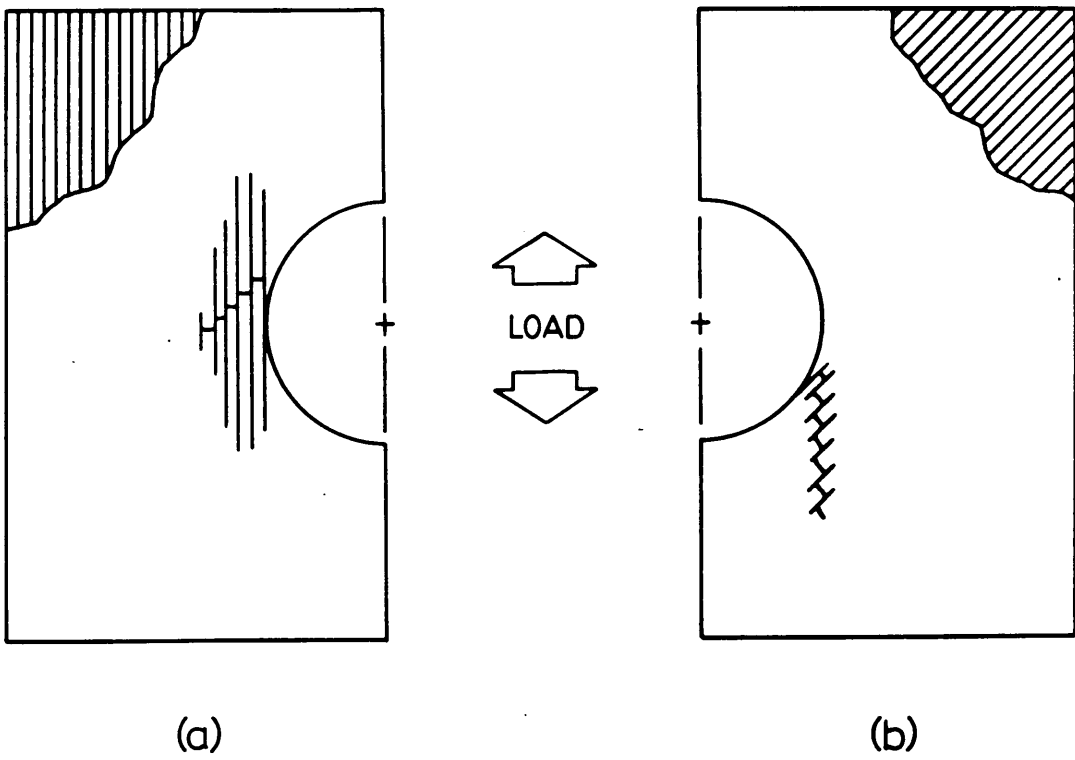
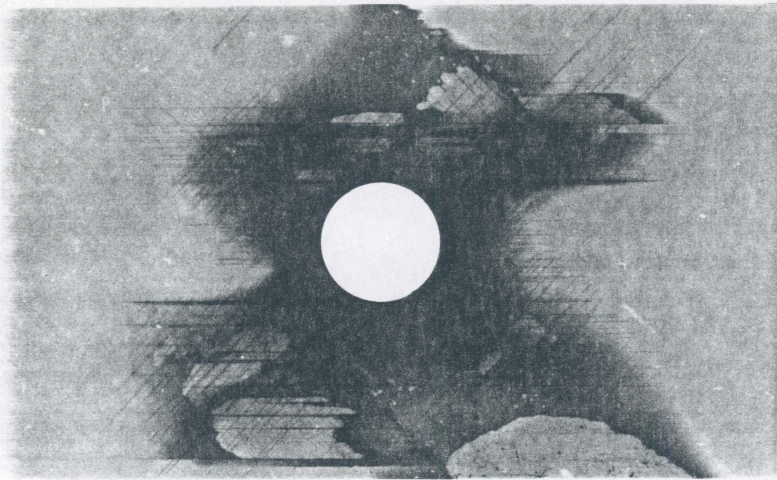


Figure 23. Schematic of incremental, step-wise surface ply fractures influenced by matrix cracks in adjacent plies: (a) 0-deg. ply in $(0,45,90,-45)_{s4}$ and $(0,45,0,-45)_{s4}$ laminates; (b) 45-deg. ply in $(0,45,0,-45)_{s4}$ laminates

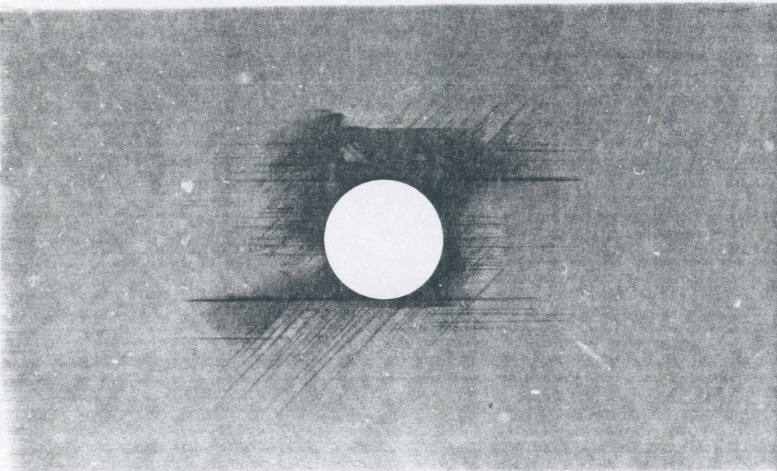
measurements, it is known that the 0-deg. ply fractures occurred during the compressive portion of the load cycle. Occasionally, a short, narrow strip of surface 0-deg. ply delaminated tangent to the hole before the occurrence of 0-deg. ply fracture. In such situations, 0-deg. ply fracture did not occur in that delaminated strip for the remainder of the fatigue lifetime. A second mode of through-the-ply fiber fracture appeared as soon as the first or second cycle in the +45-deg. plies in the second and fourth quadrants (Figure 23b). This mode of ply fracture was caused by the stress concentration imposed on the +45-deg. plies along the 0-deg. matrix cracks tangent to the hole. The -45₂ ply groups are less likely to fracture along the 0-deg. matrix cracks than the +45-deg. plies because of their greater thickness. Fractures in the +45-deg. plies occurred only in the even quadrants because of the high stresses borne by the fibers tangent to the hole in those quadrants (the +45-deg. fibers in the odd quadrants intersect the hole boundary and, thus carried little load).

With further load cycles, secondary 0-deg. cracks initiated and grew at the tip of the 0-deg. ply fracture paths, leading to strip-like 0/45 delaminations growing longitudinally from the fracture site. Delaminations at the next two or three interfaces frequently followed the appearance of surface 0-deg. ply fractures. In addition to the delaminations induced by 0-deg. ply fracture, other delaminations soon initiated at the hole boundary where the 45- and -45-deg. plies tend to "pull out" (where their fibers are nearly tangent to the hole). Interior delaminations were all of equal length in the longitudinal direction during this delamination initiation period, but later became longer at the interfaces closest to the surface. The 0-deg. matrix cracks in the second and fourth quadrants were longer than those in the first and third quadrants due to their interaction with the 45-deg. ply fracture paths in adjacent plies in the even quadrants. Radiographs of a typical early-life residual strength specimen are shown in Figure 24a and Figure 25a.

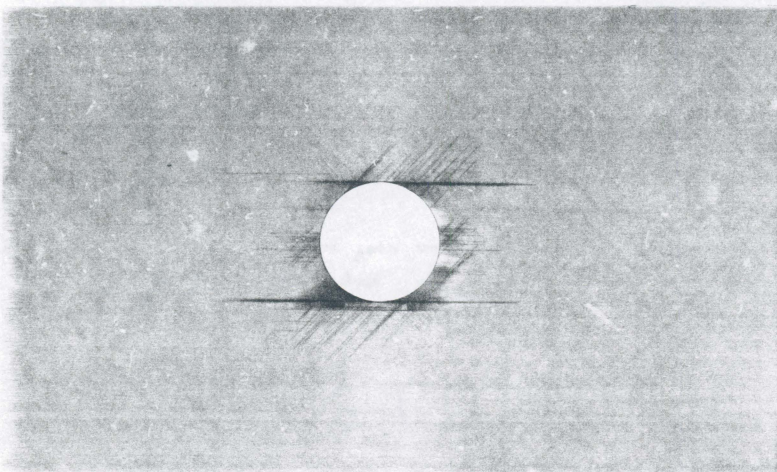
During the second stage of fatigue lifetime, delaminations adjacent to the -45₂ ply groups continued to grow longitudinally and, to a lesser extent, transversely from the notch. In specimens used for middle-life residual strength measurements, delaminations had grown in the transverse direction either with or without the assistance of 0-deg. ply fractures. New



a



b



c

Figure 24. Radiographs of center-notched, AS4/3501-6, (0,45,0,-,45)_{s4} specimens during high-load fatigue: (a) early; (b) middle; and (c) late life

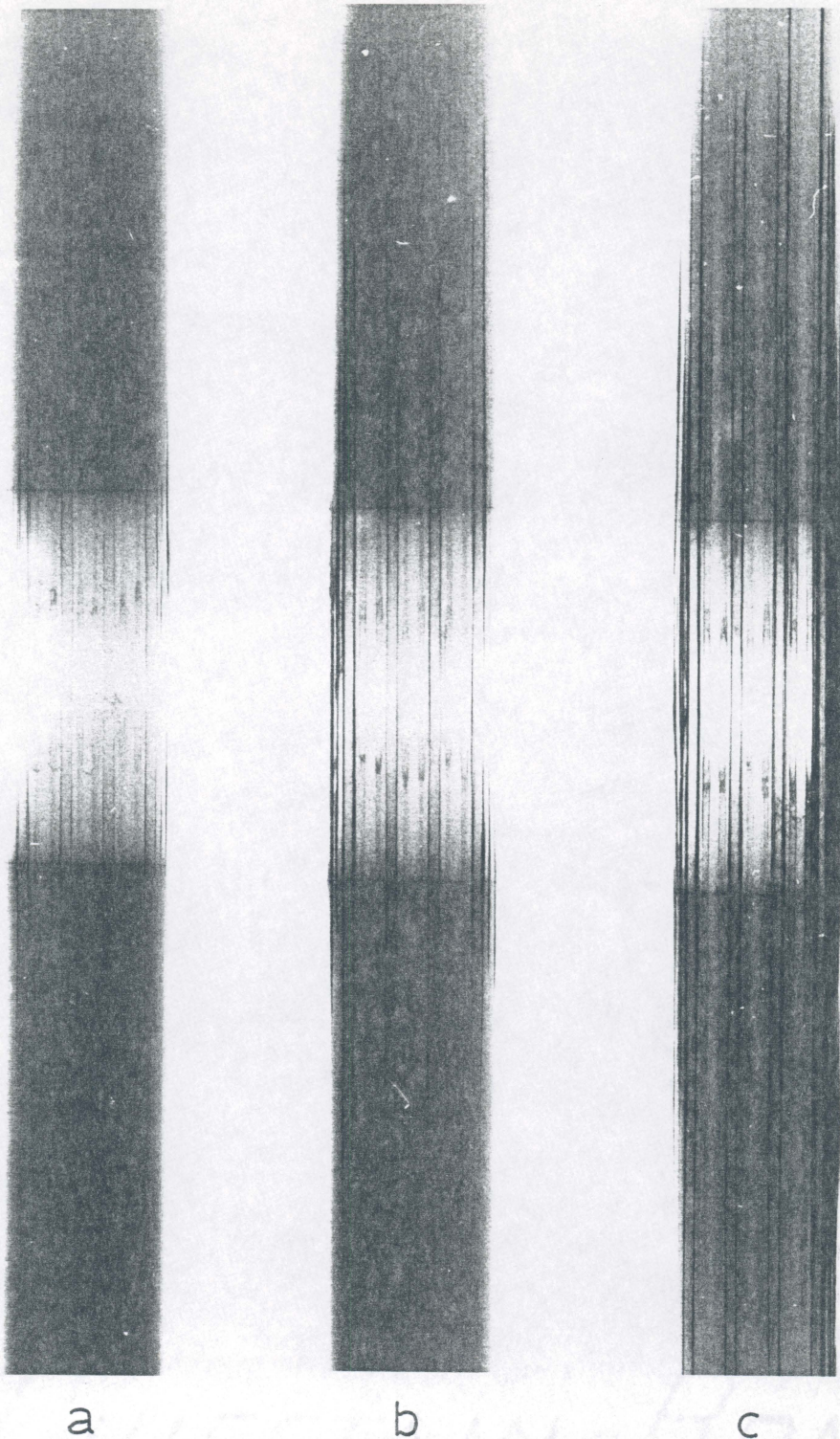


Figure 25. Edge radiographs of center-notched, AS4/3501-6, $(0,45,0,-45)_{s4}$ specimens during high-load fatigue: (a) early; (b) middle; and (c) late life

delamination growth along -45_2 ply groups occurred at this time at the tips of the 0-deg. tangent cracks in the even quadrants. (Figure 24b and Figure 25b). In several instances, 0-deg. ply fractures were observed in the third ply from the surface, at the intersection of matrix cracks tangent to the hole in the subject 0-deg. ply and the adjacent -45 -deg. ply. These 0-deg. ply fractures were followed by delaminations along the broken plies that grew in all directions and prevented additional step-wise fractures of the 0-deg. ply.

Late in the second half of the fatigue lifetime, 0-deg. surface ply fracture paths and their associated delaminations began to grow more rapidly toward the straight edges of the specimen, and delaminations closest to the surface of the specimens continued to grow faster than those in the interior. Near the end of the fatigue lifetime, large surface ply delaminations extended across the entire width of the specimen on one or both surfaces. Most interior 0-deg. plies were not yet broken, and the 0/45-interface delaminations were still much smaller than those on the -45 -deg. ply interfaces (Figure 24c and Figure 25c). Failure of this type of specimen in all observed cases was by the unstable growth of near-surface delaminations and crushing of the interior plies. Which of these two damage mechanisms occurred first could not be ascertained.

4.2 AS4/1808, Quasi-Isotropic Laminate

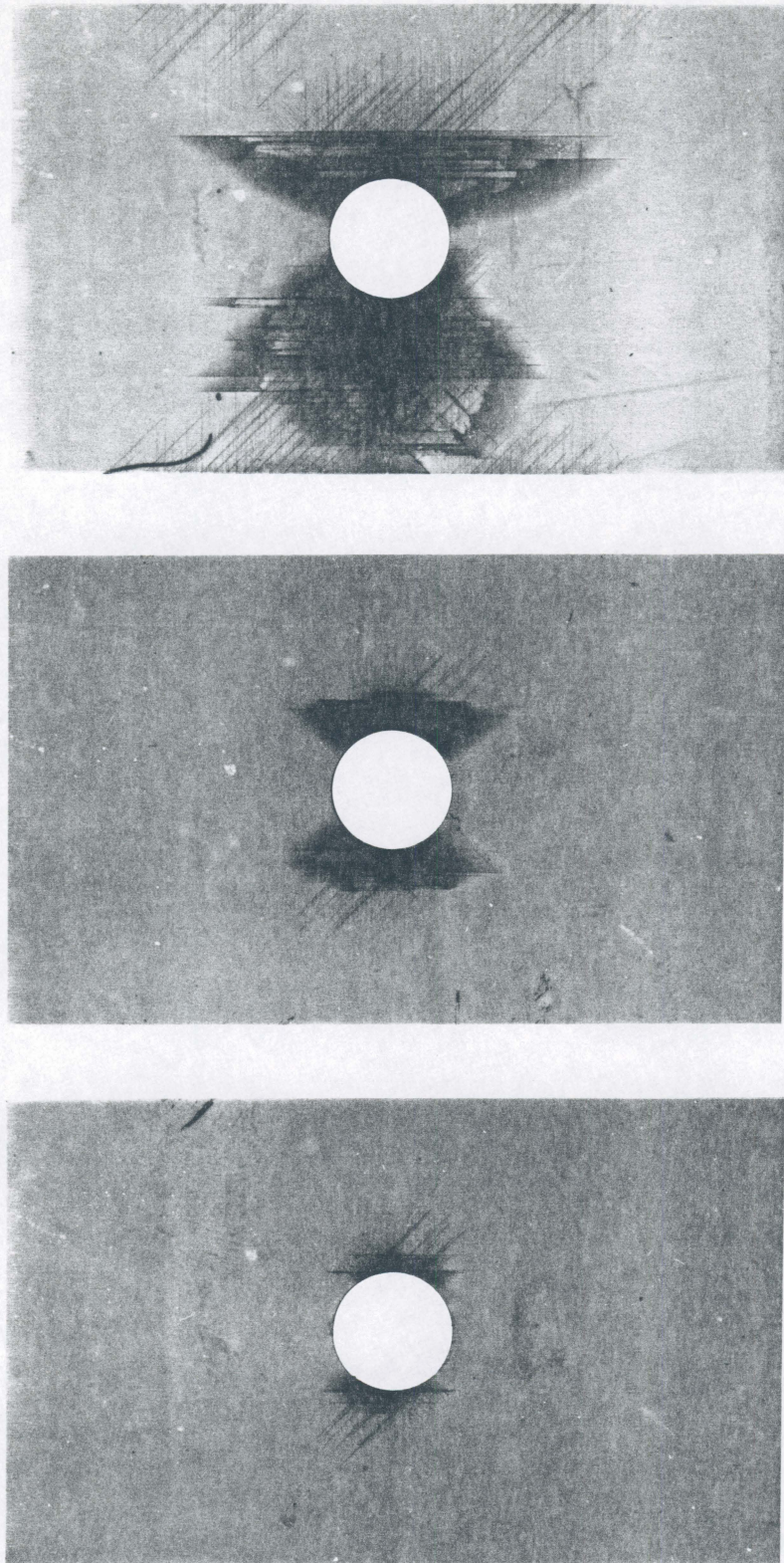
4.2.1 Center-Notched Specimens

4.2.1.1 High Load Level

The high load level for center-notched, AS4/1808, $(0,45,90,-45)_{34}$ laminates, 29.4 ksi, resulted in fatigue lifetimes between 6K and 50K cycles. During the first one or two cycles,

matrix cracks appeared almost perpendicular to the hole in all off-axis plies, and tangent to the hole in the 0-deg. plies. In the next 100 cycles, secondary matrix cracks initiated first in the 45-deg. plies along the 0-deg. tangent cracks, and next in the 90-deg. plies along the -45-deg. cracks. The first occurrence of delamination was at the outermost 0/45 interface at the corner formed by the 0- and 45-deg. matrix cracks and the hole boundary in the even quadrants. At the time of early-life residual strength measurement, step-wise 0-deg. surface ply fractures began to form during compression at the point where the primary 0- and 45-deg. matrix cracks tangent to the hole boundary intersect, a small distance away from the hole. These small, incremental fractures followed a 45-deg. path as they grew away from the notch (Figure 23a). Zero-deg. ply matrix cracks soon followed the incremental fractures, as did strip-like, longitudinal delaminations between those matrix cracks (Figure 26a and Figure 27a). Occasionally, strip-like 0-deg. surface delaminations initiated without the presence of 0-deg. ply fractures. Such delaminations initiated along a +45-deg. matrix crack emanating from the hole (like the step-wise 0-deg. ply fractures), and grew in the longitudinal direction. However, when a 0/45 interface delamination occurred before a 0-deg. ply fracture, decoupling between the 0- and 45-deg. plies isolated the 0-deg. ply from the stress concentration of the 45-deg. matrix crack and prevented fracture of the 0-deg. ply. Delaminations at this early time in the fatigue life appeared on all 0-deg. ply interfaces throughout the thickness, but those on the outermost 0/45 interfaces were larger than those in the interior, as shown in the damage sketches obtained from a deplied specimen (Figure 28). The deply data also revealed the existence of delaminations where the 45- and -45-deg. plies "pulled out" tangent to the hole, along the 90-deg. plies nearest to the surface.

After additional load cycles, delaminations adjacent to the 90-deg. plies stabilized in size, while those along the 0-deg. plies continued to grow, albeit slower than before. During this second stage of life, the rate of damage growth, as evidenced by the stiffness record in Figure 22 on page 72, was slower than at other times in the fatigue lifetime. Off-axis matrix cracks emanating from the hole reached off-axis matrix cracks growing inward from the edges, and some interior 0₂ ply groups fractured locally near the hole. Two general types of



a b c

Figure 26. Radiographs of center-notched, AS4/1808, (0,45,90,-45)_{s4} specimens during high-load fatigue: (a) early; (b) middle; and (c) late life

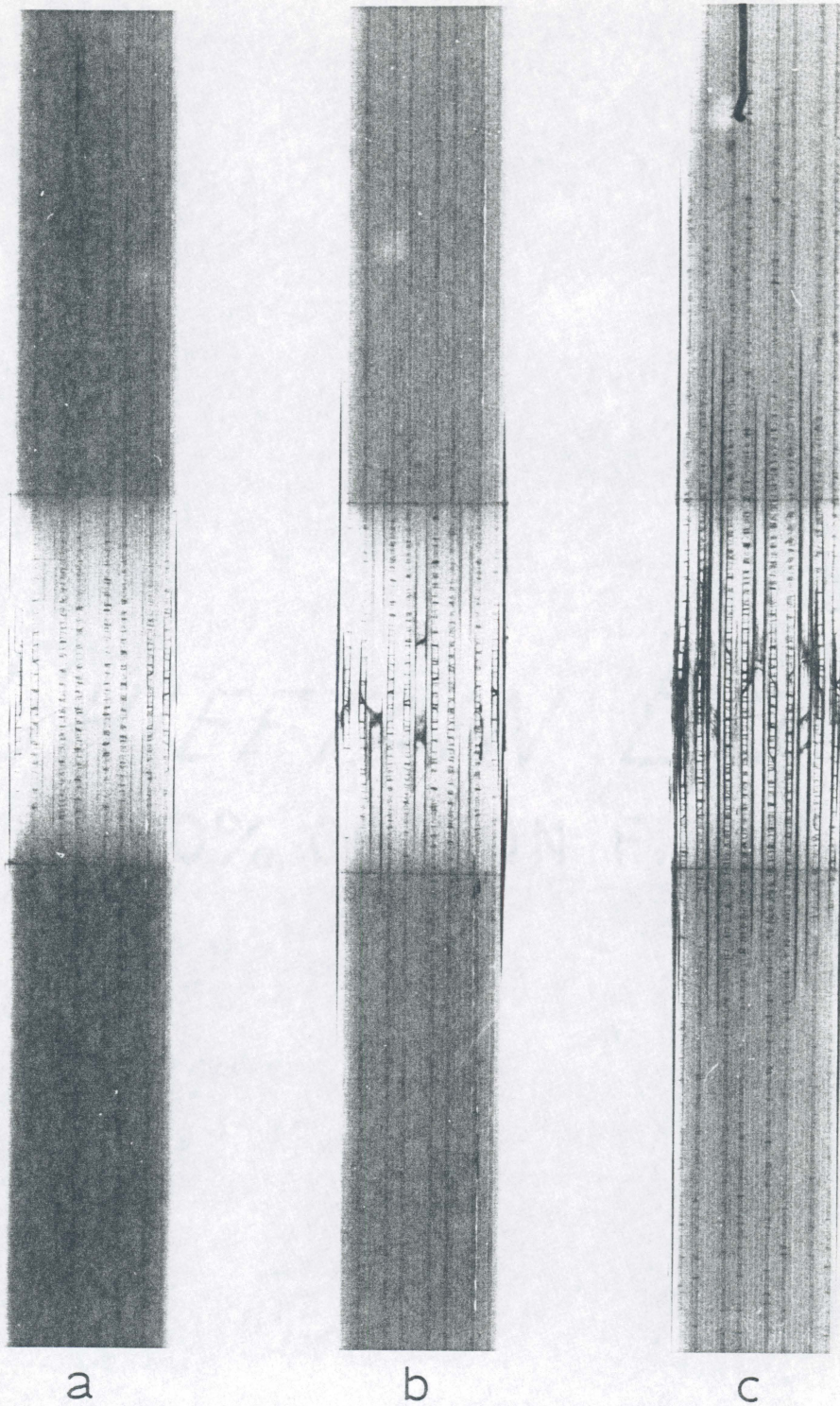


Figure 27. Edge radiographs of center-notched, AS4/1808, $(0,45,90,-45)_{s4}$ specimens during high-load fatigue: (a) early; (b) middle; and (c) late life

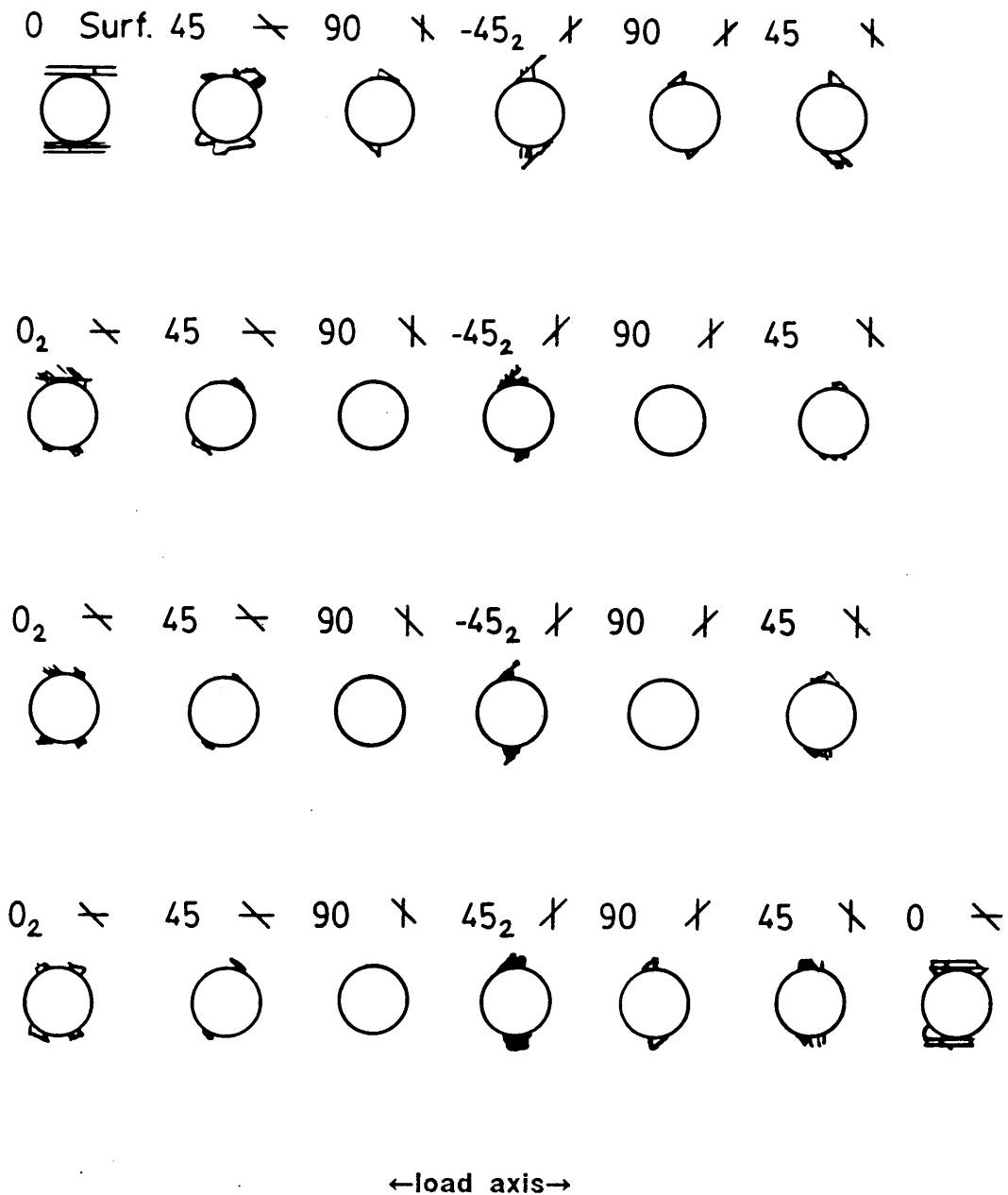


Figure 28. A depled, center-notched, AS4/1808, (0,45,90,-45)_{s4} specimen at an early stage of damage development under the high load level

damage patterns became evident at this time in the fatigue lifetime. The first was characterized by the longitudinal growth of 0/45 delaminations, particularly at the interfaces closest to the surface, and also by little or no 0-deg. ply fracture in the interior of the laminate. The second type of damage pattern was characterized by the fracture of all 0-deg. plies near the hole, and a more transversely-oriented direction of damage associated with those 0-deg. ply fractures. Apparently, the "high" load level chosen for the current test program was on the transition between load levels that caused dramatically different damage patterns. Cyclic load levels above 29.4 ksi favored 0-deg. ply fracture and the transverse mode of damage growth, while loads below 29.4 ksi favored the longitudinal mode of damage growth and little 0-deg. ply fracture until the second half of the fatigue lifetime (see the next section on low-load damage mechanisms). Radiographs of a typical middle-life residual strength specimen are shown in Figure 26b and Figure 27b. This particular example illustrates the fiber fracture dominated mode of damage growth, as evidenced by the broken 0-deg. ply groups in the interior of the laminate (see the edge view radiograph). The several interfaces adjoining a 0-deg. ply group fracture site delaminated faster than the remaining interfaces, resulting in an unstable-type of non-symmetric damage growth and compressive instability.

Near the end of the high-load fatigue lifetime, most of the 0-deg. ply groups fractured near the hole. Some of these internal 0-deg. ply fracture paths grew away from the hole in the same manner as the surface 0-deg. ply fractures described earlier. The ply fracture paths and associated matrix damage, however, covered a larger area in the surface plies. The rate of damage growth during the last 10 percent of life accelerated greatly, as evidenced by the stiffness data in Figure 22a. In a typical late-life residual strength specimen (Figure 26c and Figure 27c), delaminations extended across nearly the entire width. Sketches of damage on the interfaces of a deplied late-life specimen near fatigue failure are shown in Figure 29. Numerous ply fractures in the 0-, 45-, and -45-deg. plies formed a nearly continuous crack through the thickness of the specimen near the transverse centerline through the hole. The close association between internal ply fractures and delaminations was also indicated in the

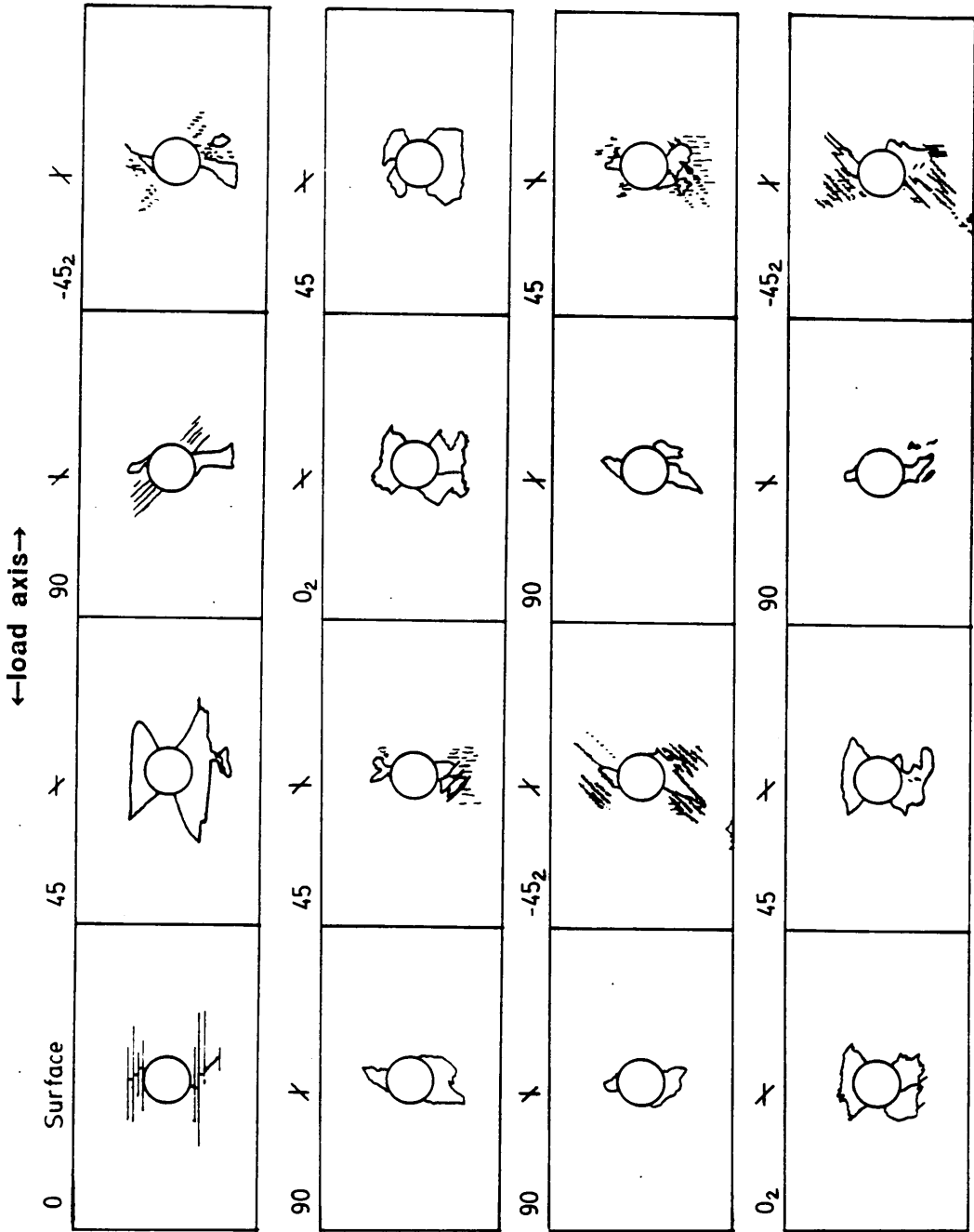


Figure 29. A depled, center-notched, AS4/1808, (0,45,90,-45)_{s4} specimen at a late stage of damage development under the high load level

←load axis→

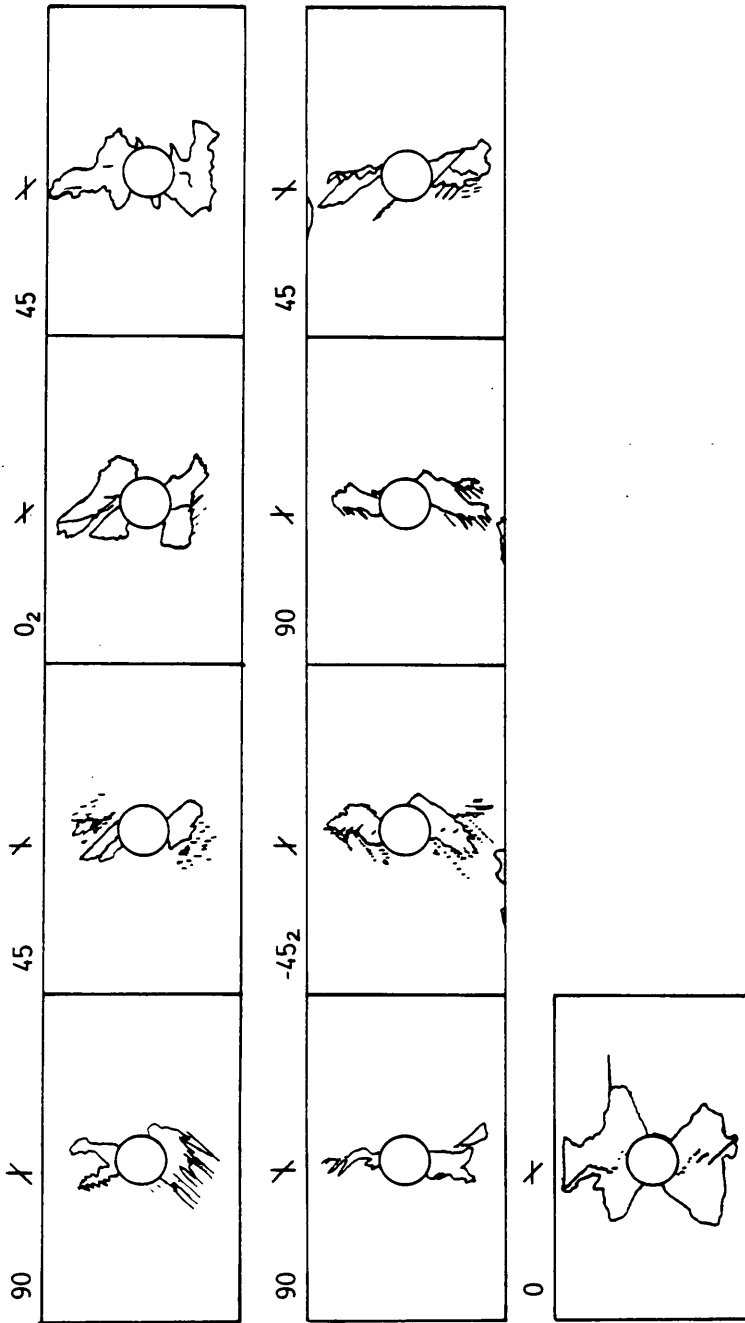


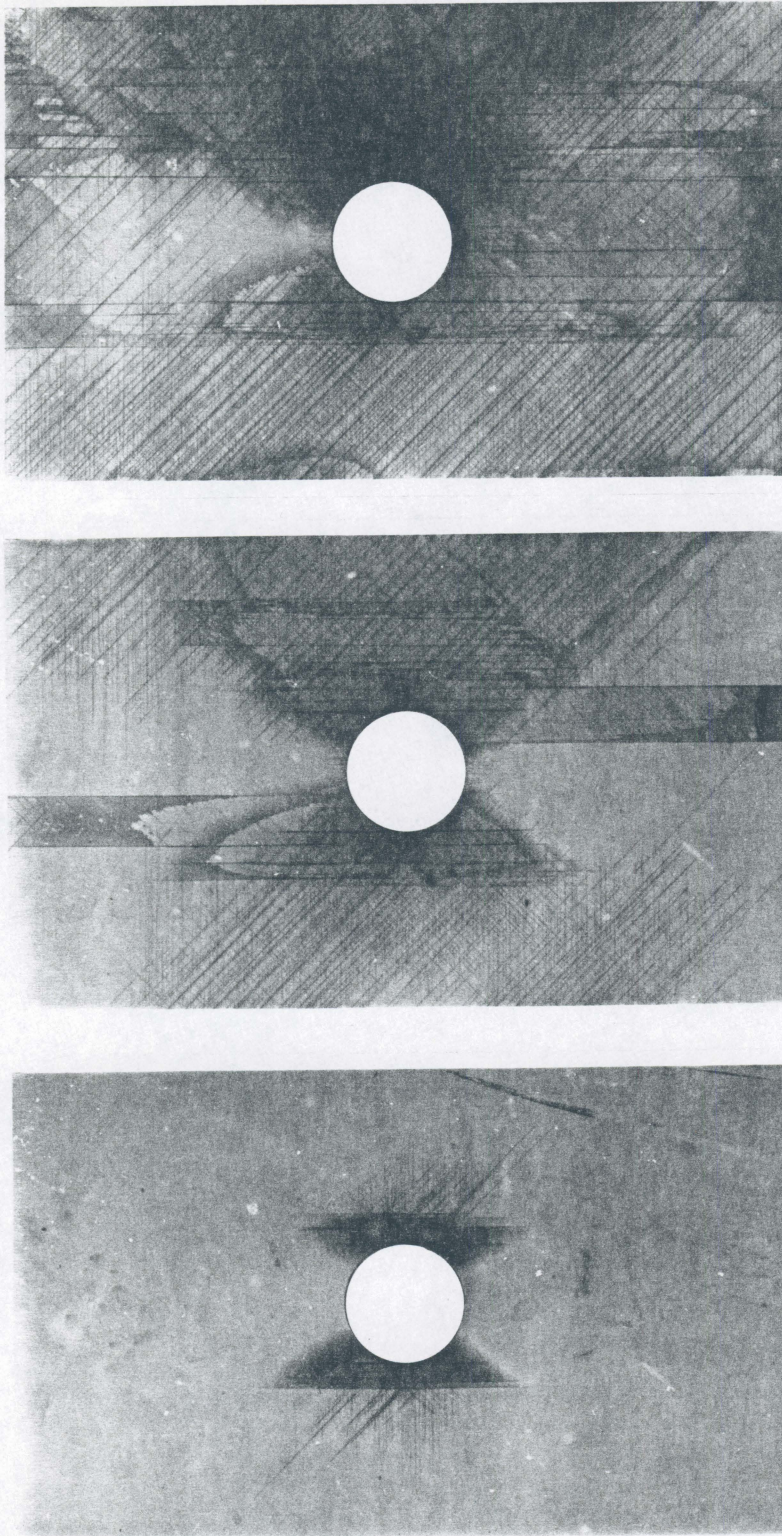
Figure 29 (Concluded)

deply data. In all observed cases, fatigue failure was by delamination of the outer plies and crushing of the less-delaminated interior plies.

4.2.1.2 Low Load Level

The low load level, 22.6 ksi, resulted in fatigue lifetimes of 500K to 3.5M cycles. As early as the first cycle, 0-deg. matrix cracks initiated and grew tangent to the hole and off-axis ply matrix cracks initiated and grew roughly perpendicularly to the hole. These were followed by -45- and +45-deg. matrix cracks tangent to the hole. In the first 1000 cycles, delaminations initiated on the outermost 0/45 interfaces in all four quadrants around the notch (usually beginning in the even quadrants) and on the outermost 90-deg. ply interfaces. Eventually, all 0/45 interfaces delaminated in a similar fashion through the thickness, as did the 90-deg. ply interfaces. The near-surface 0/45 delaminations remained larger, though, for the remainder of the lifetime. At the time of the early-life residual strength measurement, incremental step-type fractures in the surface 0-deg. plies had formed along the underlying 45-deg. matrix cracks, though they were less pervasive than in the high-load specimens (i.e., they were interspersed with 0-deg. strip delaminations which prevented their occurrence) (Figure 30a and Figure 31a). Sketches of damage in a deplied, early-life specimen (Figure 32) indicated that 0/45 interface delaminations were larger when closer to the surface, but 45/90 and 90/-45 interface delaminations were about the same size through the thickness.

Additional load cycles caused continued growth of the 0/45 interface delaminations, especially at locations closer to the surface. The 90-deg. ply delaminations remained confined to the area bounded by the 45- and -45-deg. matrix cracks tangent to the hole boundary for much of the second stage of the fatigue lifetime. In the third of five observed stages of the fatigue lifetime in these specimens, the sudden, rapid change in stiffness shown in Figure 22 on page 72 at approximately 40-60 percent of the lifetime was caused by the rapid growth (and subsequent arrest) of strip-like delaminations on the outermost 0/45 interface between the hole and



a b c

Figure 30. Radiographs of center-notched, AS4/1808, (0,45,90,-45)_{s4} specimens during low-load fatigue: (a) early; (b) middle; and (c) late life

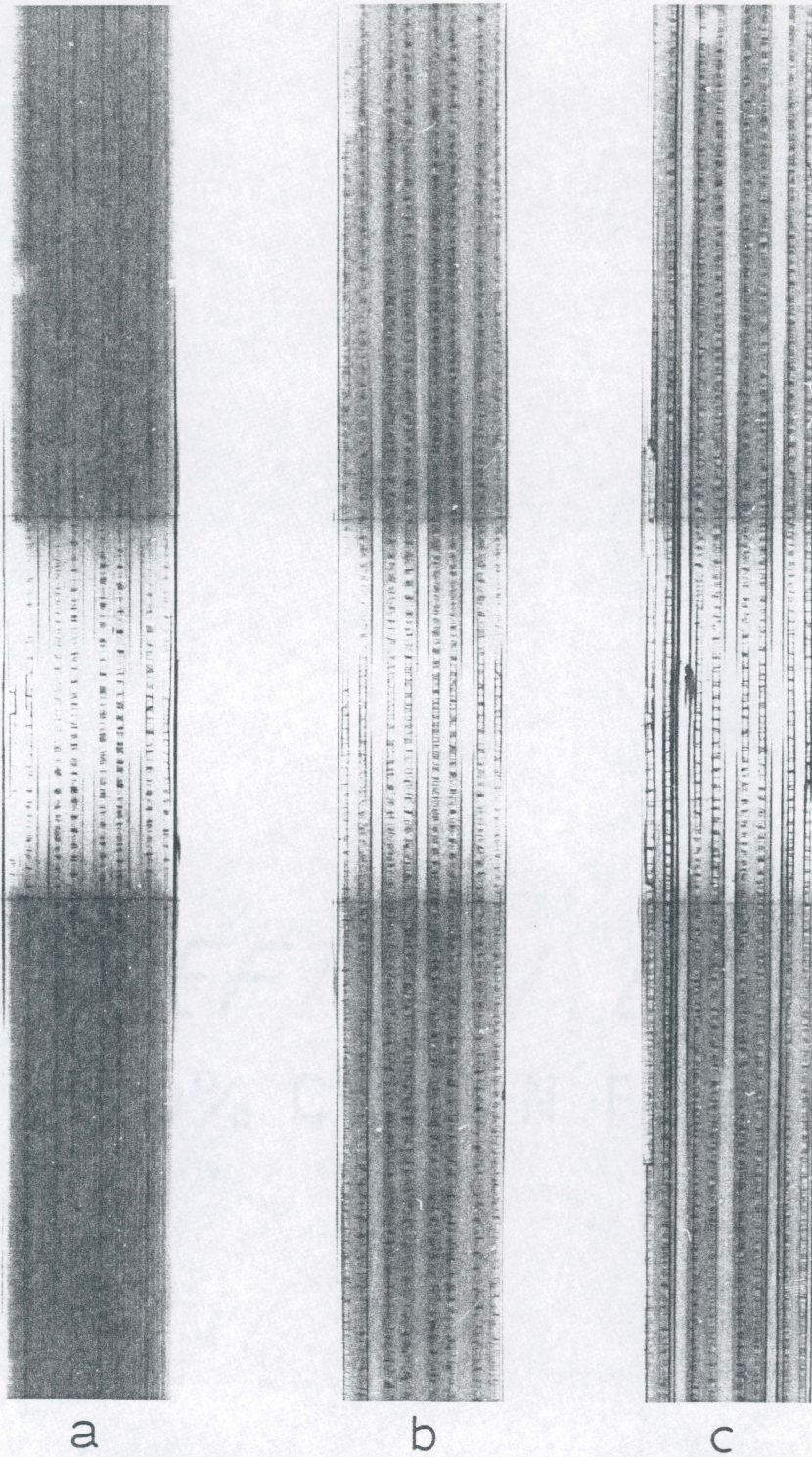


Figure 31. Edge radiographs of center-notched, AS4/1808, $(0,45,90,-45)_{s4}$ specimens during low-load fatigue: (a) early; (b) middle; and (c) late life

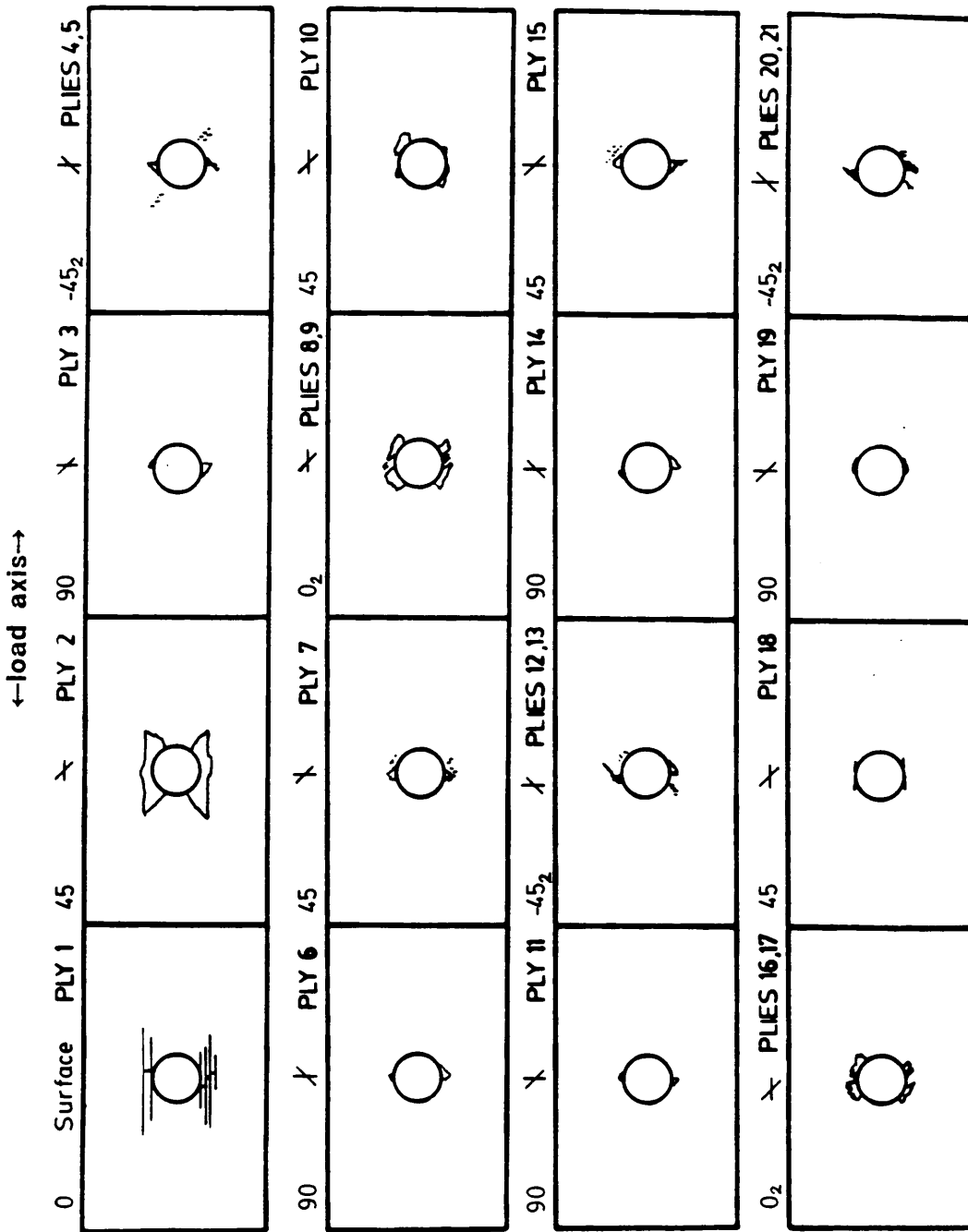


Figure 32. A depled, center-notched, AS4/1808, (0,45,90,-45)_{s4} specimen at an early of damage (development under the low load level)

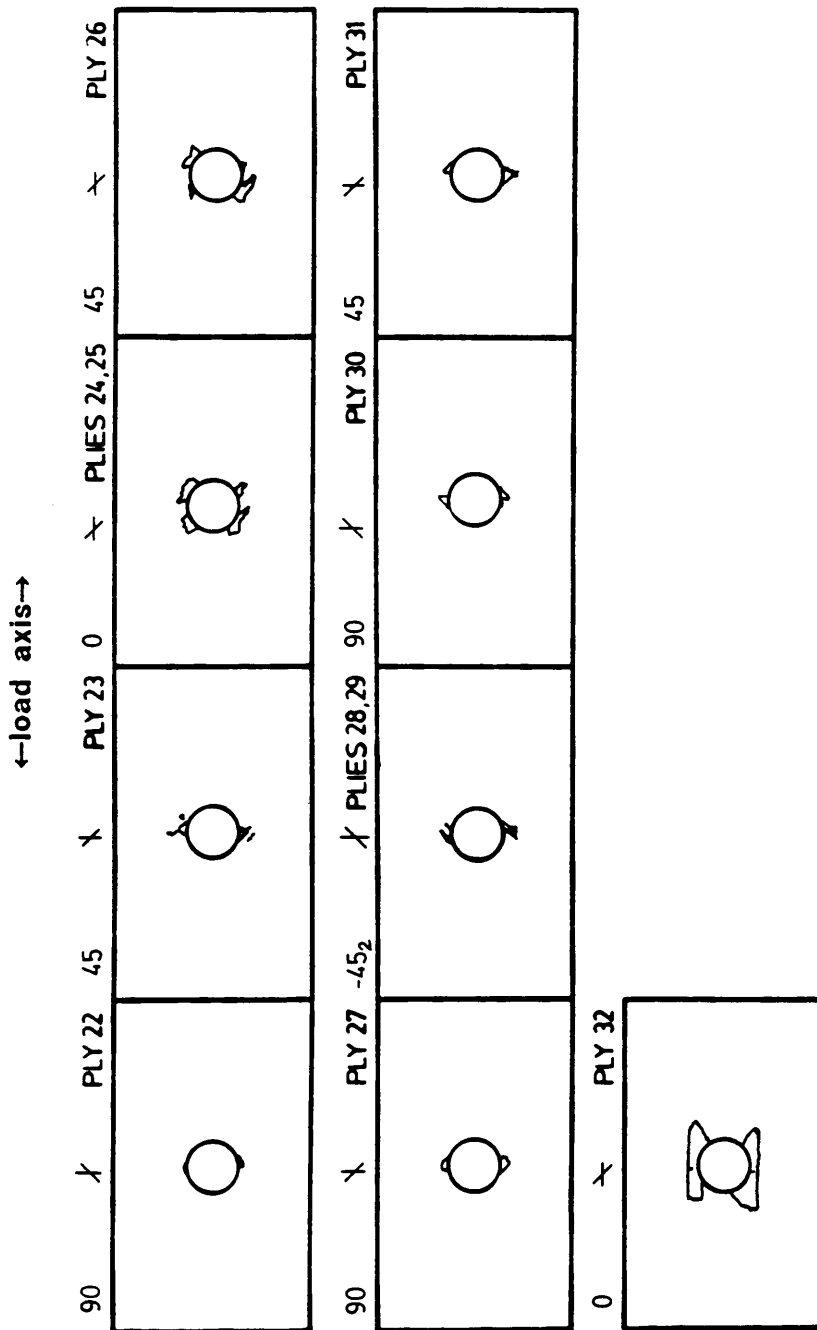


Figure 32 (Concluded)

the grips, particularly in the even quadrants. Typical radiographs of middle-life residual strength specimens resembled those shown in Figure 30b and Figure 31b. Usually, delaminations under one or both of the surface 0-deg. plies extended outward to at least one straight edge. However, only occasionally had 0/45 interface delaminations in the interior of the laminate grown transversely to the hole at half of the lifetime.

In the fourth stage of fatigue lifetime, matrix damage intensified in the ligaments of material adjacent to the notch (little stiffness change occurred during this time). During the last (fifth) stage of life, interior 0-deg. ply fractures occurred near the notch and surface ply delaminations grew rapidly toward the straight edges. As in other cases mentioned earlier, these delaminations initiated along an underlying +45-deg. matrix crack and rapidly formed strip-like delaminations along longitudinal 0-deg. matrix cracks. Frequently, 0-deg. ply fractures and straight edge delaminations associated with the surface plies grew such that, when combined with the delaminations growing outward from the hole, a continuous delamination extending from the notch to one or both of the straight edges, along the entire gage length was formed. Interior interface delaminations also grew longitudinally near the end of life, as shown in the radiographs of a typical late-life residual strength specimen in Figure 30c and Figure 31c.

Sketches of damage seen in a deploded late-life specimen reinforced the radiographic data by also indicating a larger extent of delamination on interfaces closer to the surface (Figure 33). Compared to the high-load specimens, there was a greater difference in the extent of near-surface versus interior delaminations in the low-load specimens. Near failure, delaminations beyond the third or fourth interfaces from each surface were similar in shape and size with both load levels. Ply fractures in most 0-deg. plies in the laminate initiated and grew close to the longitudinal centerline of the hole. As indicated by the stiffness record in Figure 22 on page 72, the rate of damage growth accelerated rapidly near the end of life. Failure of all specimens under the low load level was by delamination of the exterior plies and crushing of the interior plies.

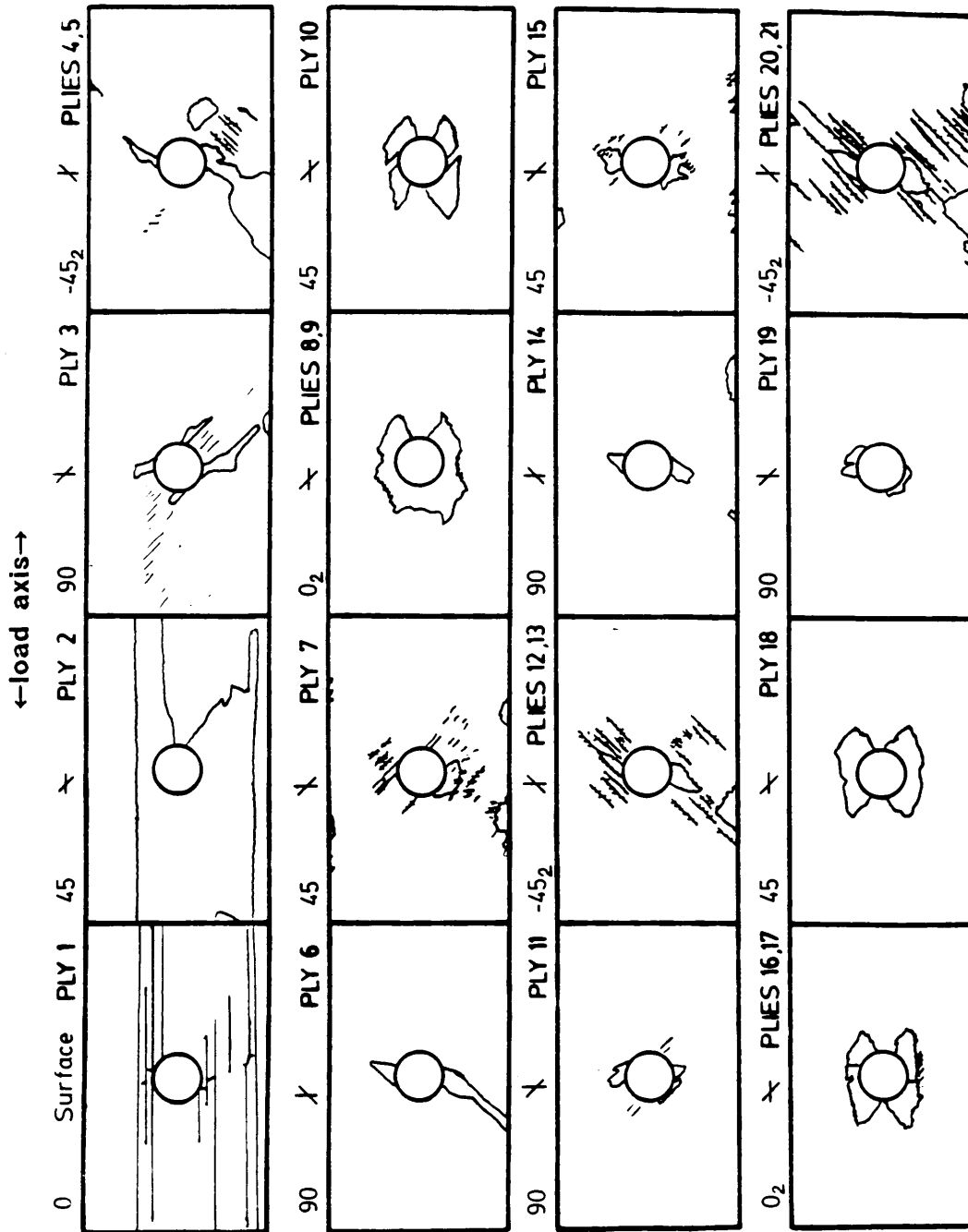


Figure 33. A depled, center-notched, AS4/1808, (0,45,90,-45)_{s4} specimen at a late stage of damage development under the low load level

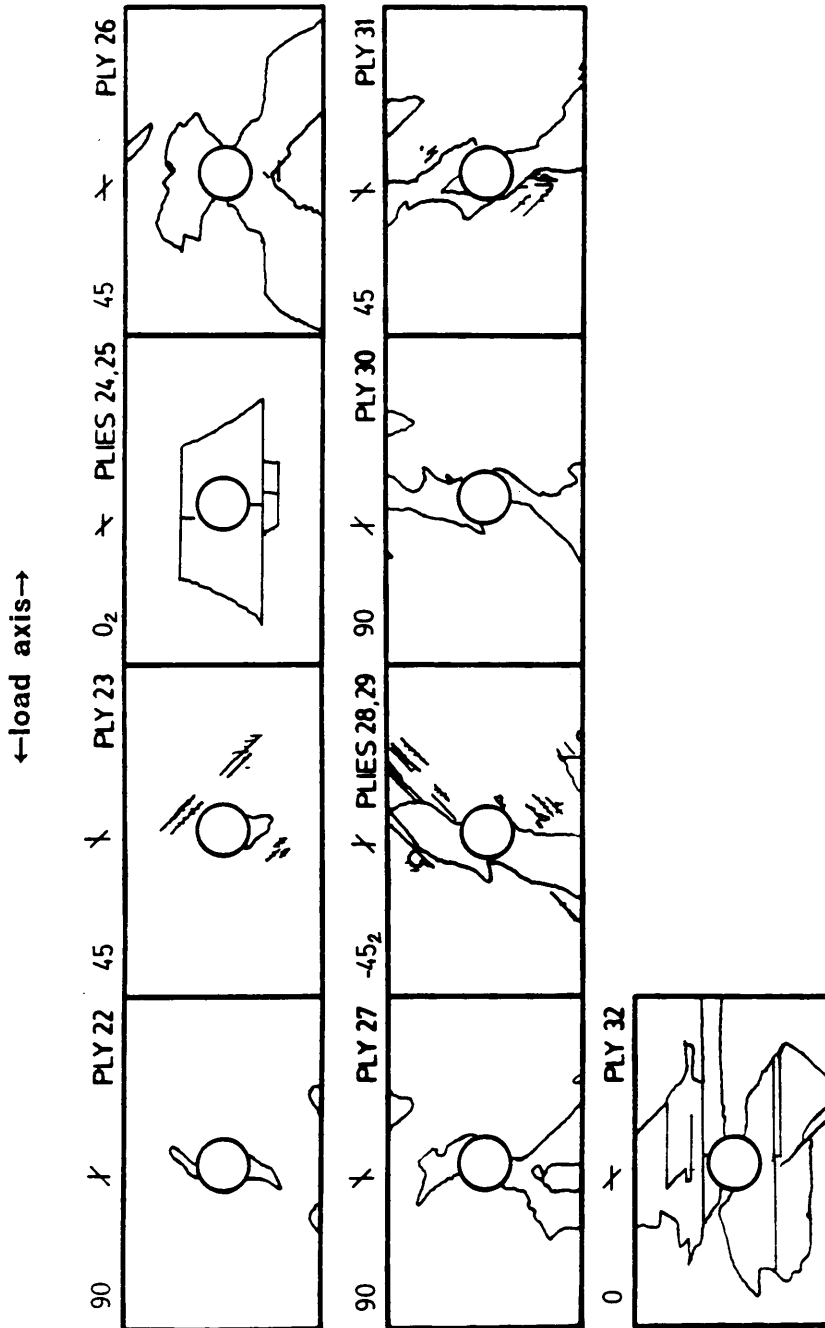


Figure 33 (Concluded)

4.2.2 Double-Edge-Notched Specimens

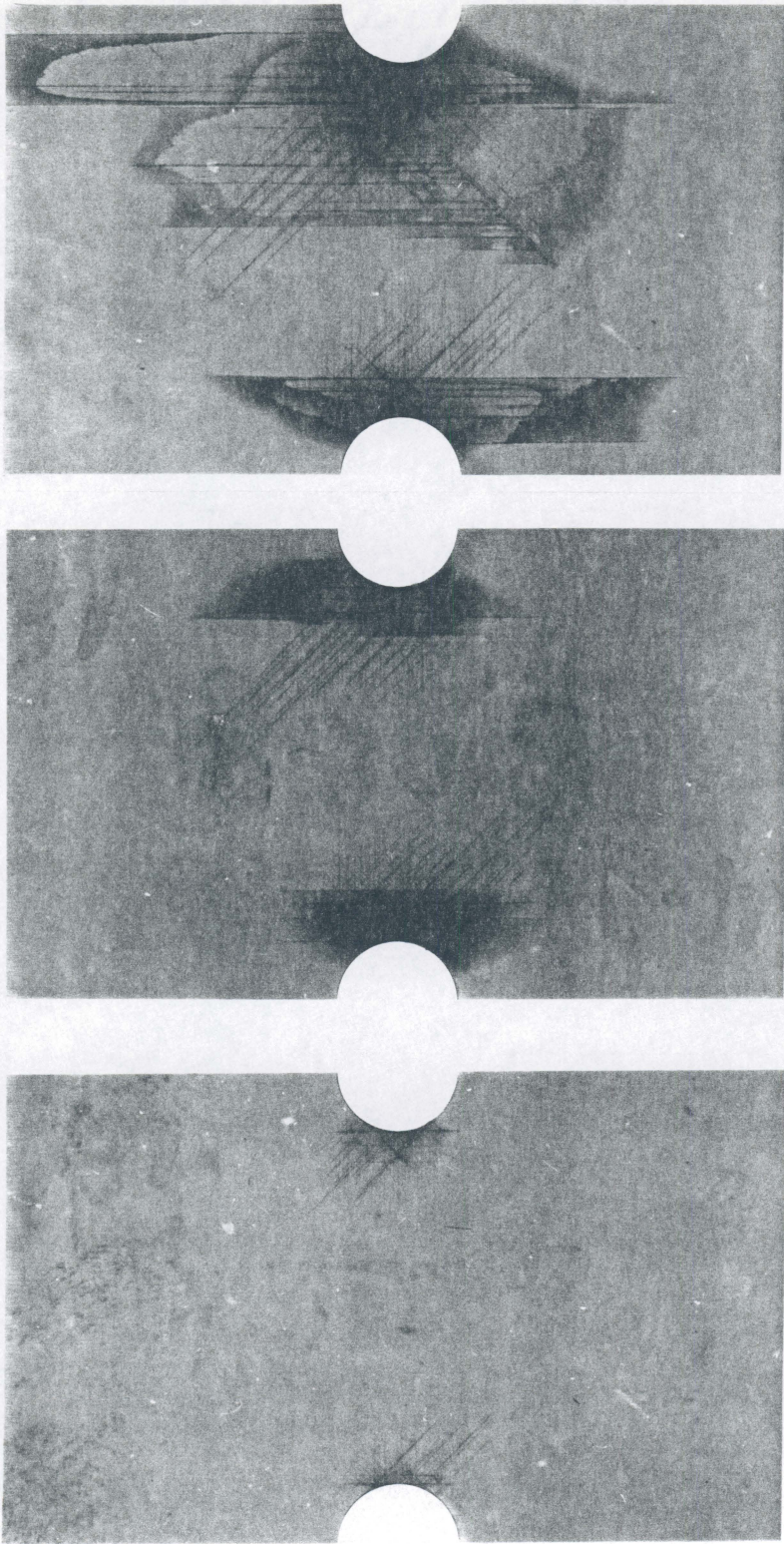
4.2.2.1 High Load Level

The high load level for double-edge-notched, AS4/1808, (0,45,90,-45)_{s4} specimens, 31.3 ksi, resulted in fatigue lifetimes between 6K and 80K cycles. The unusually wide disparity in fatigue lifetimes was caused by the same type of failure mode transition seen in the CN specimens. Overall, damage mechanisms in DEN specimens were similar to those in CN specimens. However, since these particular DEN specimens were analyzed for stress redistribution and residual strength data, radiographs of specimens at all three residual strength stopping points have been included in Figure 34 and Figure 35.

Early-life specimens contained incremental fractures of the surface 0-deg. plies along the +45-deg. directions, tangent to the notches. Longitudinal delaminations extending from the notches grew faster in the even quadrants than in the odd quadrants, as shown in the middle-life radiographs.

Radiographs of middle-life specimens showed signs of the failure mode transition seen previously in CN specimens. As was the case with CN specimens, the "high" load level chosen for DEN specimens was on the transition between ply fracture dominated behavior and delamination dominated behavior. Those specimens with the "high"-load mode of damage contained ply fractures near the notches in the outermost and second outermost 0-deg. plies by 50 percent of life. Those specimens with the "low"-load mode of damage had no internal 0-deg. ply fractures at this same percentage of life. The middle-life specimen shown in Figure 34b and Figure 35b is following the low-load type behavior.

Late-life specimens typically had 0-deg. ply fractures in one or more of the internal 0-deg. ply groups. Delaminations on the outermost 0/45 interfaces generally spanned most or all of the distance between the notches. Specimens dominated by 0-deg. ply fracture, such as the one shown in Figure 34c and Figure 35c, had less longitudinal growth of delaminations, more



a b c

Figure 34. Radiographs of double-edge-notched, AS4/1808, (0,45,90,-45)_{s4} specimens during high-load fatigue: (a) early; (b) middle; and (c) late life

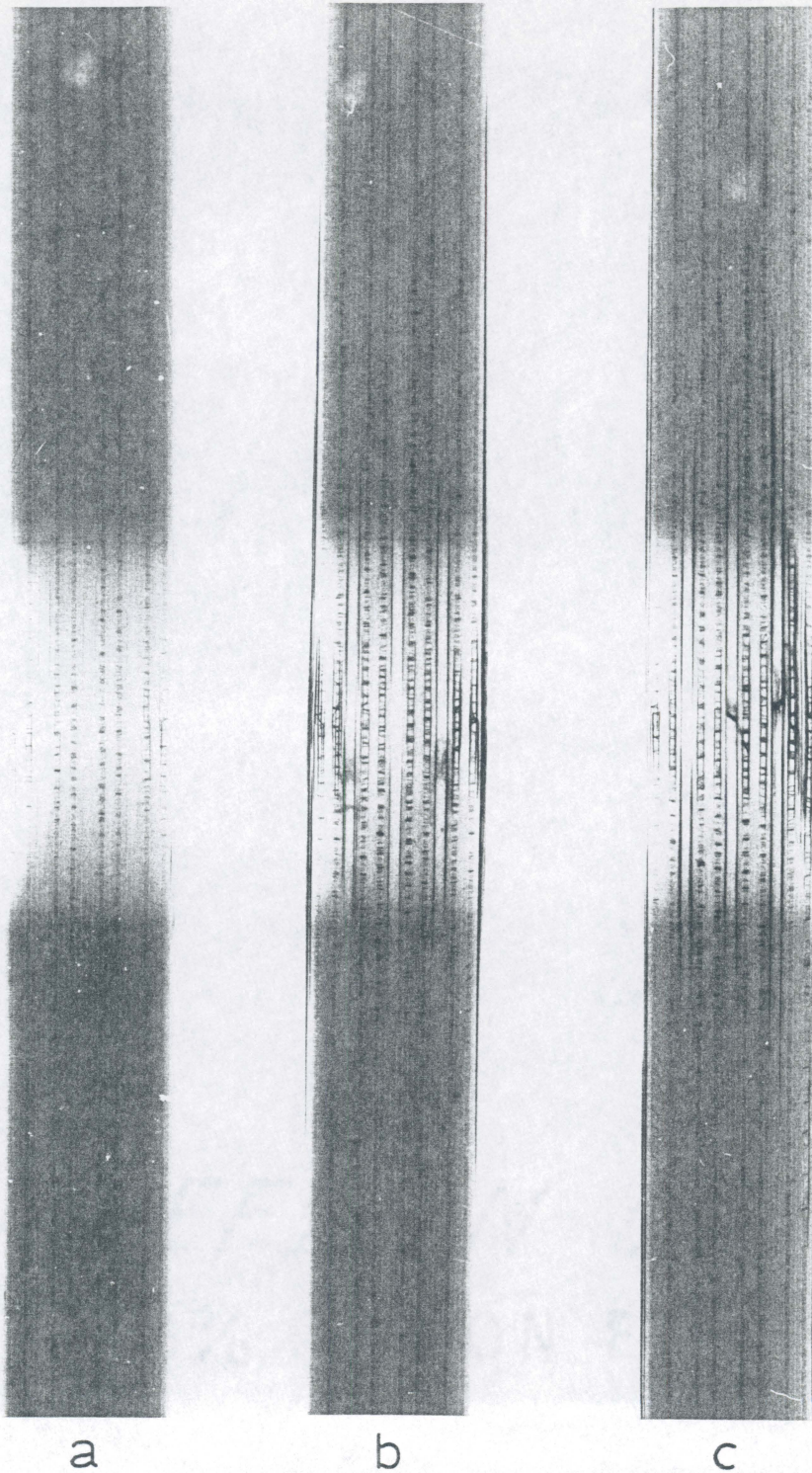


Figure 35. Edge radiographs of double-edge-notched, AS4/1808, (0,45,90,-45)_{s4} specimens during high-load fatigue: (a) early; (b) middle; and (c) late life

internal 0-deg. ply fractures, and significantly shorter fatigue lifetimes than those dominated by near-surface 0/45 interface delaminations. Failure in all high-load tests was compressive, however. Figure 36 shows the post-failure appearance of specimens with each of the two types of damage development. Note that the delamination-dominated specimen failed across a section of material that does not pass through the notches. In both cases, though, the failure mode was delamination of the outermost plies, and crushing of the internal, less delaminated plies.

4.3 AS4/1808, Orthotropic Laminate

4.3.1 Center-Notched Specimens

4.3.1.1 High Load Level

The high load level for center-notched, AS4/1808, $(0,45,0,-45)_{s4}$ specimens, 44.2 ksi, resulted in fatigue lifetimes of 3K to 16K cycles. After one load cycle, matrix cracks appeared in all plies around the notch. The 0-deg. matrix cracks initiated and grew tangentially to the hole, and were longest in the even quadrants. Secondary +45-deg. matrix cracks initiated along the 0-deg. tangent cracks, as did +45 deg. ply incremental fractures (Figure 23b). The 45-deg. ply fracture paths were approximately half as long as the 0-deg. matrix cracks they paralleled. Delaminations occurred within the next 10 cycles at the outermost 45/0 and 0/-45₂ interfaces in the second and fourth quadrants where the 0-deg. tangent cracks met the hole boundary. Within the next 100 cycles, delaminations existed on all interfaces between plies of different orientation. Delaminations adjacent to the outermost -45₂ ply groups were the largest of all delaminations in the longitudinal direction. The interaction of 0-deg. matrix cracks and adja-

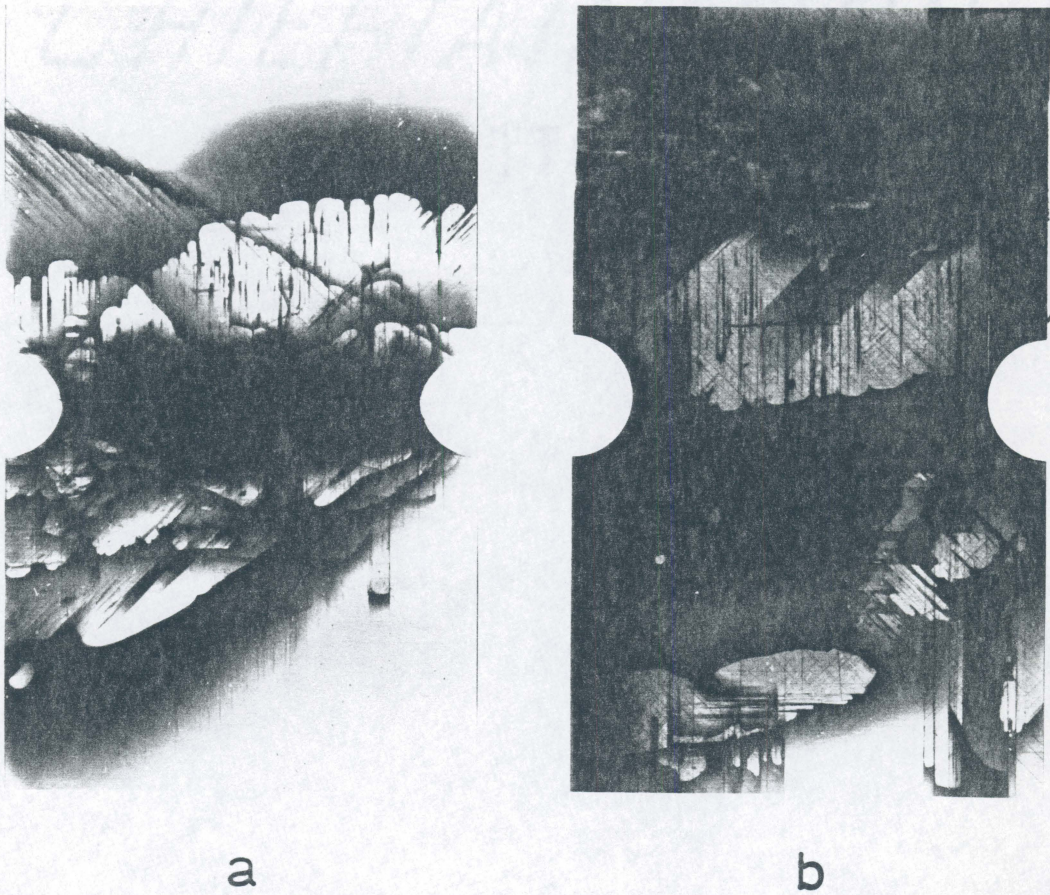
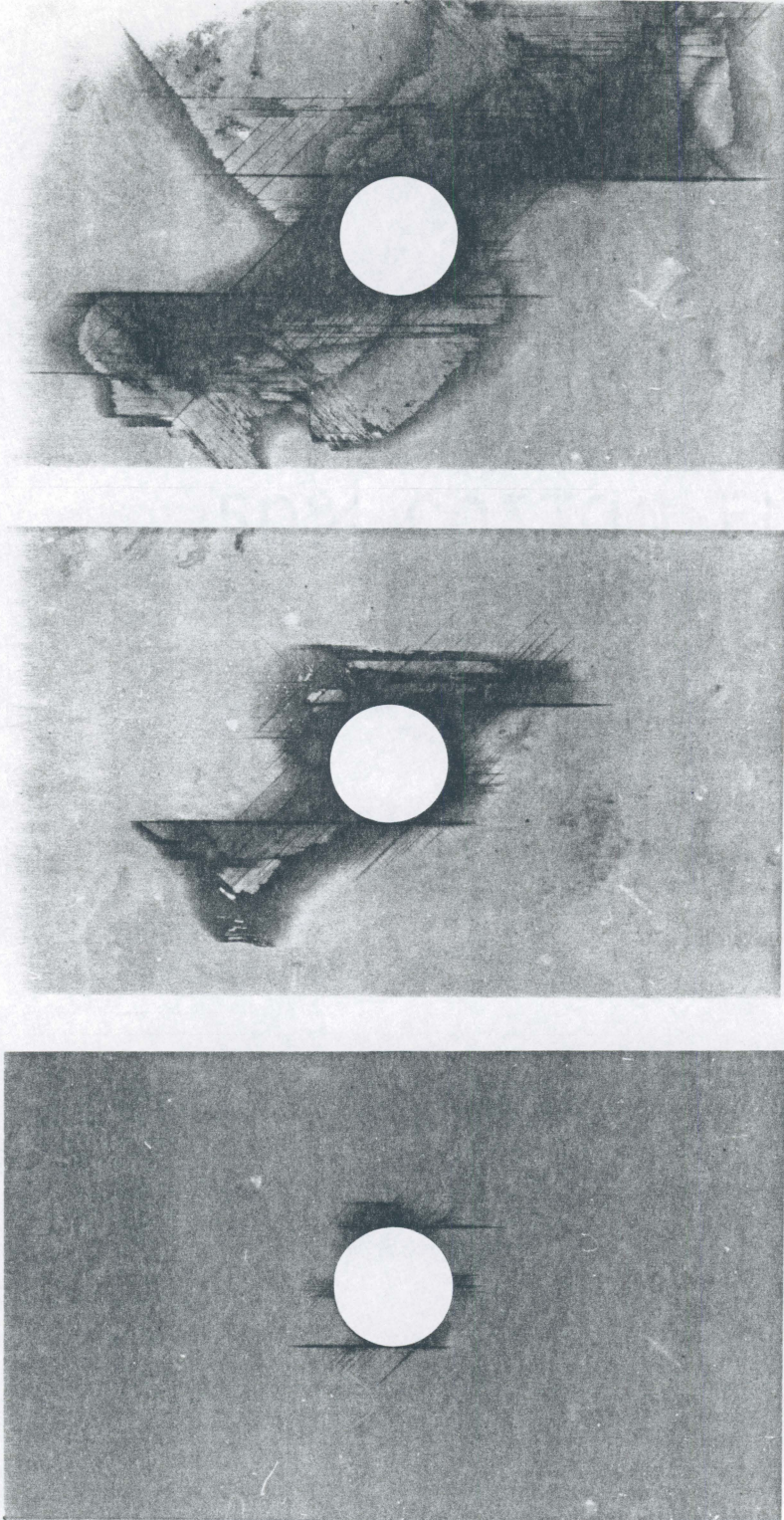


Figure 36. Radiographs of double-edge-notched, AS4/1808, $(0,45,90,-45)_{s4}$ specimens after fatigue failure: (a) ply fracture domination; (b) delamination domination

cent +45-deg. ply fracture paths that occurred in the even quadrants did not materialize in the odd quadrants because the +45-deg. plies bear significant load only in the even quadrants (i.e. those quadrants where the +45-deg. fibers do not intersect the hole boundary). The -45-deg. plies did not fracture near adjacent matrix cracks due to their double thickness in this lamination arrangement. In radiographs of an early-life residual strength specimen (Figure 37a and Figure 38a), a small 0-deg. ply fracture step appeared in the first quadrant, at the intersection of the 0- and -45-deg. matrix cracks tangent to the hole. In the edge-view radiograph, it can be seen that this fracture step extends through the first three plies. This fracture likely initiated in the third ply because of the stress disturbance caused by the adjacent -45-deg. matrix crack. Based on audible acoustic emissions and visual observations, it is known that the step-wise 0-deg. ply fractures occurred during compressive load excursions. Sketches of the damage seen in a depled early-life specimen (Figure 39) indicated that, in the absence of surface ply fracture, the patterns of matrix damage through the thickness of the specimen were nearly identical.

With additional load cycles, delaminations along the -45₂ ply groups grew along the large 0-deg. matrix cracks in the even quadrants. Delaminations on -45-deg. ply interfaces farther from the surface grew slower than those closer to the surface during the first half of fatigue life. Delaminations on the 0/45 interfaces grew little, if at all, unless a 0-deg. ply fracture was present, in which case substantial growth resulted. By the middle-life strength measurement point, delaminations near the tip of the 0-deg. tangent cracks in the even quadrants had typically initiated and grown a short distance from the notch (Figure 37b and Figure 38b). Near the points where -45-deg. matrix cracks tangent to the hole intersected the 0-deg. tangent cracks and their associated +45-deg. ply fracture paths in the even quadrants, the second 0-deg. ply from the surface often broke during a compressive load excursion and caused a dynamic crack to propagate to the surface of the specimen. In Figure 38b, however, the crack did not propagate to the surface, but, instead, caused delaminations on the two outermost interfaces. In general, the initiation of 0-deg. ply fractures occurred near large matrix cracks in the 45- and -45-deg. plies. Growth of 0-deg. ply fracture paths was along either the +45-



a
b
c

Figure 37. Radiographs of center-notched, AS4/1808, $(0,45,0,-45)_{s4}$ specimens during high-load fatigue: (a) early; (b) middle; and (c) late life

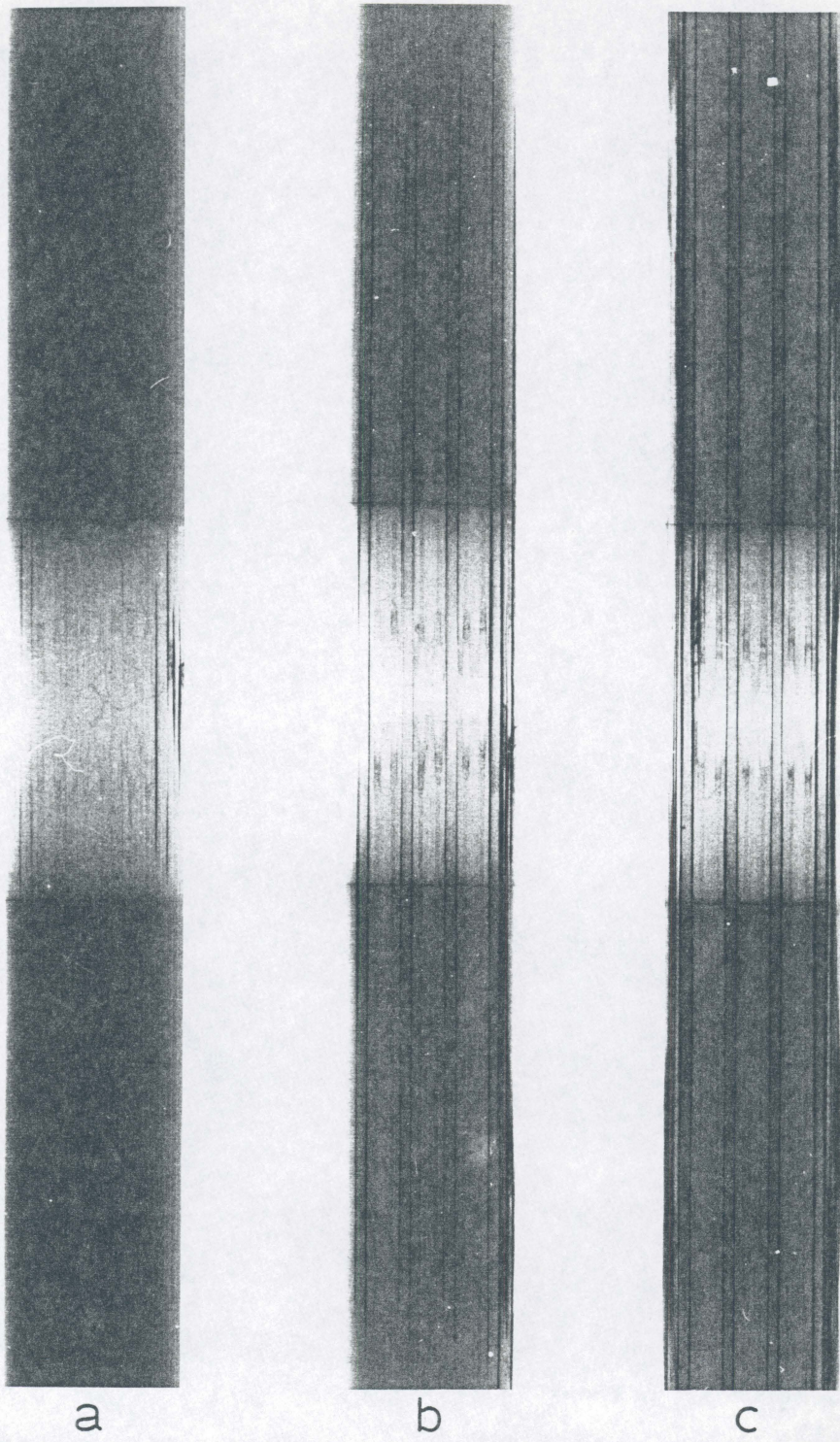


Figure 38. Edge radiographs of center-notched, AS4/1808, $(0,45,0,-45)_{s4}$ specimens during high-load fatigue: (a) early; (b) middle; and (c) late life

←load axis→

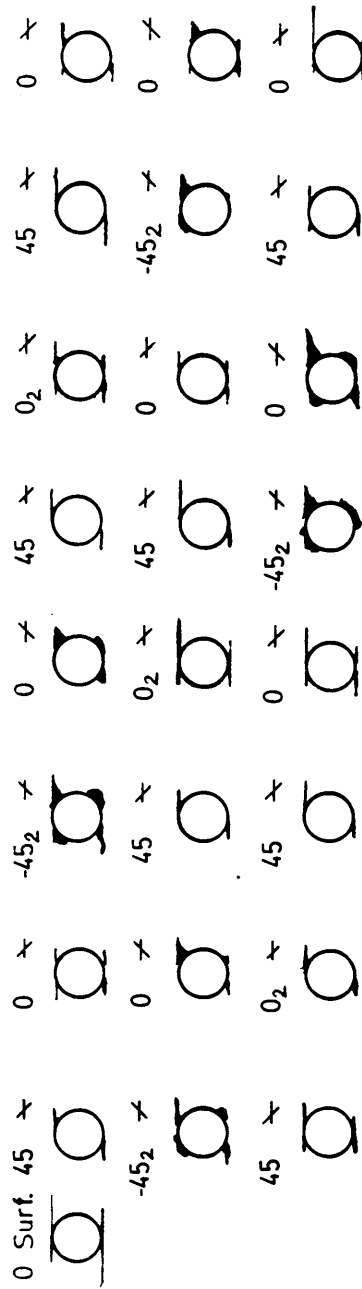


Figure 39. A depled, center-notched, AS4/1808, (0,45,0,-45)_{s4} specimen at an early stage of damage development under the high load level

or -45-deg. direction (or both, in alternate fashion), depending on the peculiar orientations of the plies adjacent to the 0-deg. ply and the local stress fields associated with damage in those plies.

Sketches of a deploded middle-life specimen (Figure 40) indicated that delaminations along the -45₂ ply groups were growing along 0-deg. matrix cracks tangent to the hole in the even quadrants. Ply fracture paths in the 45-deg. plies were nearly as long as the 0-deg. matrix cracks which they followed. There was little difference in the damage patterns through the thickness of the laminate.

During the second half of the fatigue life, up to approximately the last 10 percent of life, delaminations along the -45₂ plies grew at a somewhat constant rate. During this time, 0-deg. ply fractures on the surfaces, along with the associated matrix cracking and delamination of the surface 0-deg. plies, approached the straight edges of the specimen. During the last 10 percent of life, delamination growth rates accelerated greatly, and crushing of the interior plies caused fatigue failure of the specimen. Figure 37c and Figure 38c show a typical late-life damage state, just prior to fatigue failure. Most late-life damage growth occurred in the even quadrants, remote from the hole. The difference in the longitudinal extents of delamination as a function of distance from the surface decreased toward the end of life.

Sketches of the damage seen in a deploded, late-life specimen (Figure 41) revealed that delaminations initiated and grew near 0-deg. ply fracture sites in the two outermost 0-deg. plies. The 45-deg. ply fracture paths were still the same length as the 0-deg. matrix cracks tangent to the hole. Ply fracture paths in 0-deg. plies bounded by only +45-deg. plies always followed the +45-deg. direction, while those in 0-deg. plies bounded by +45- and -45-deg. plies followed either the +45- or -45-deg. directions.

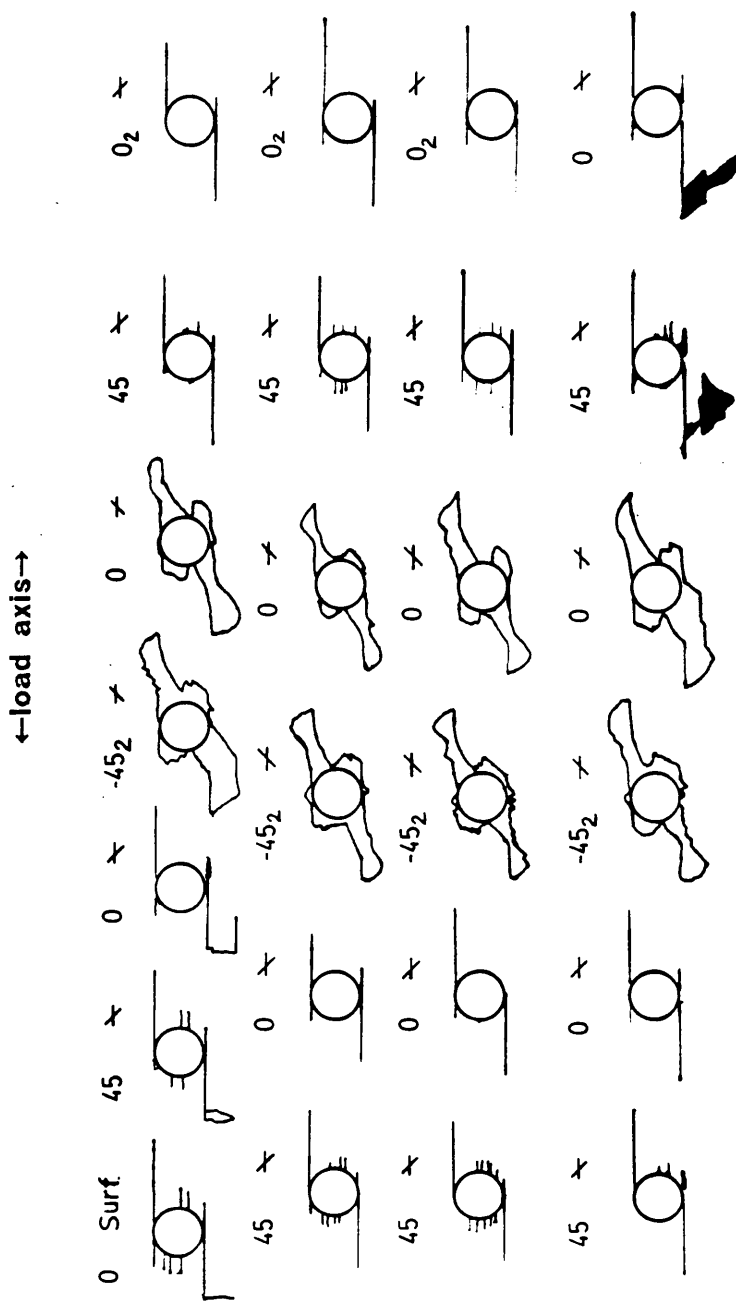


Figure 40. A depled, center-notched, AS4/1808, (0,45,0,-45)_{s4} specimen at a middle stage of damage development under the high load level

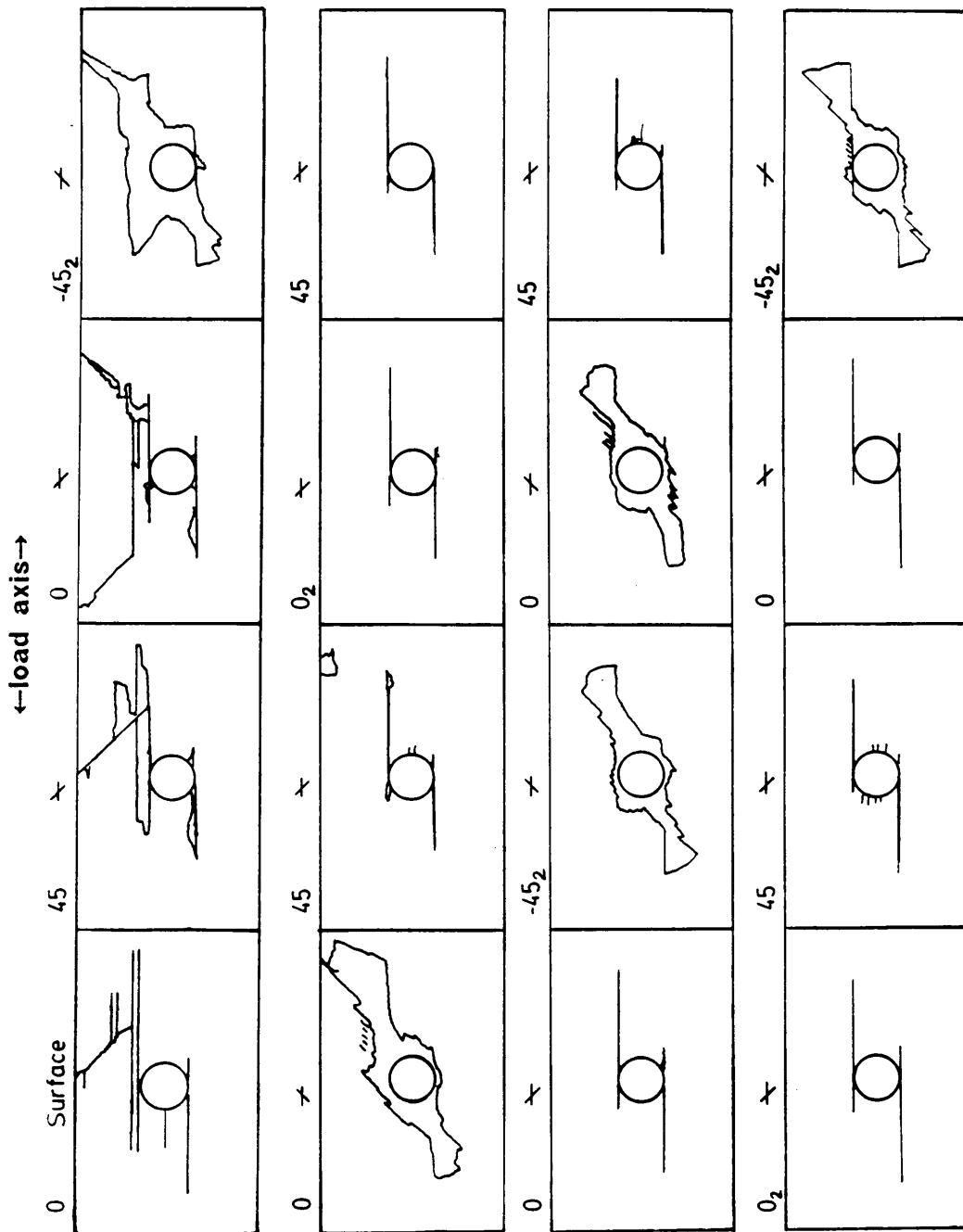


Figure 41. A depled, center-notched, AS4/1808, (0,45,0,-45)_{s4} specimen at a late stage of damage development under the high load level

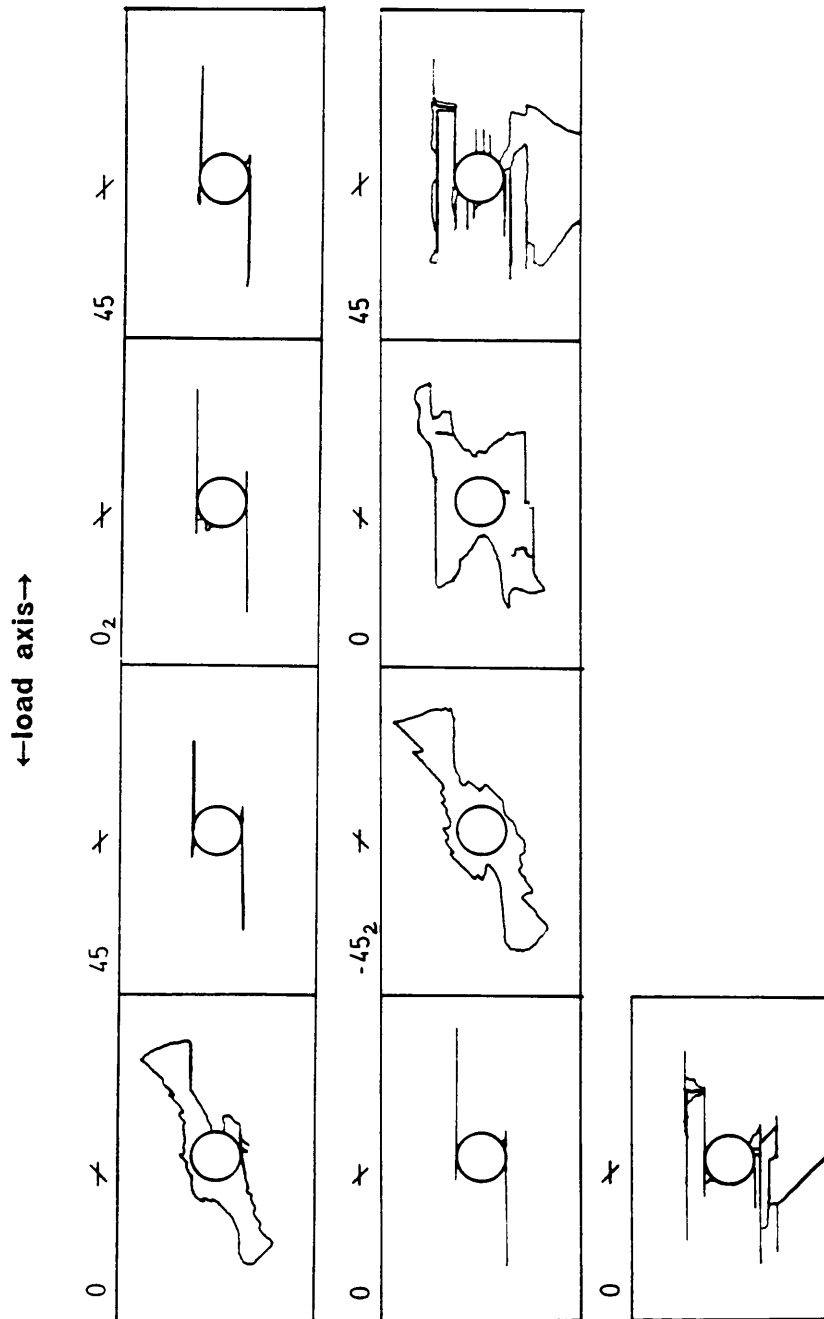
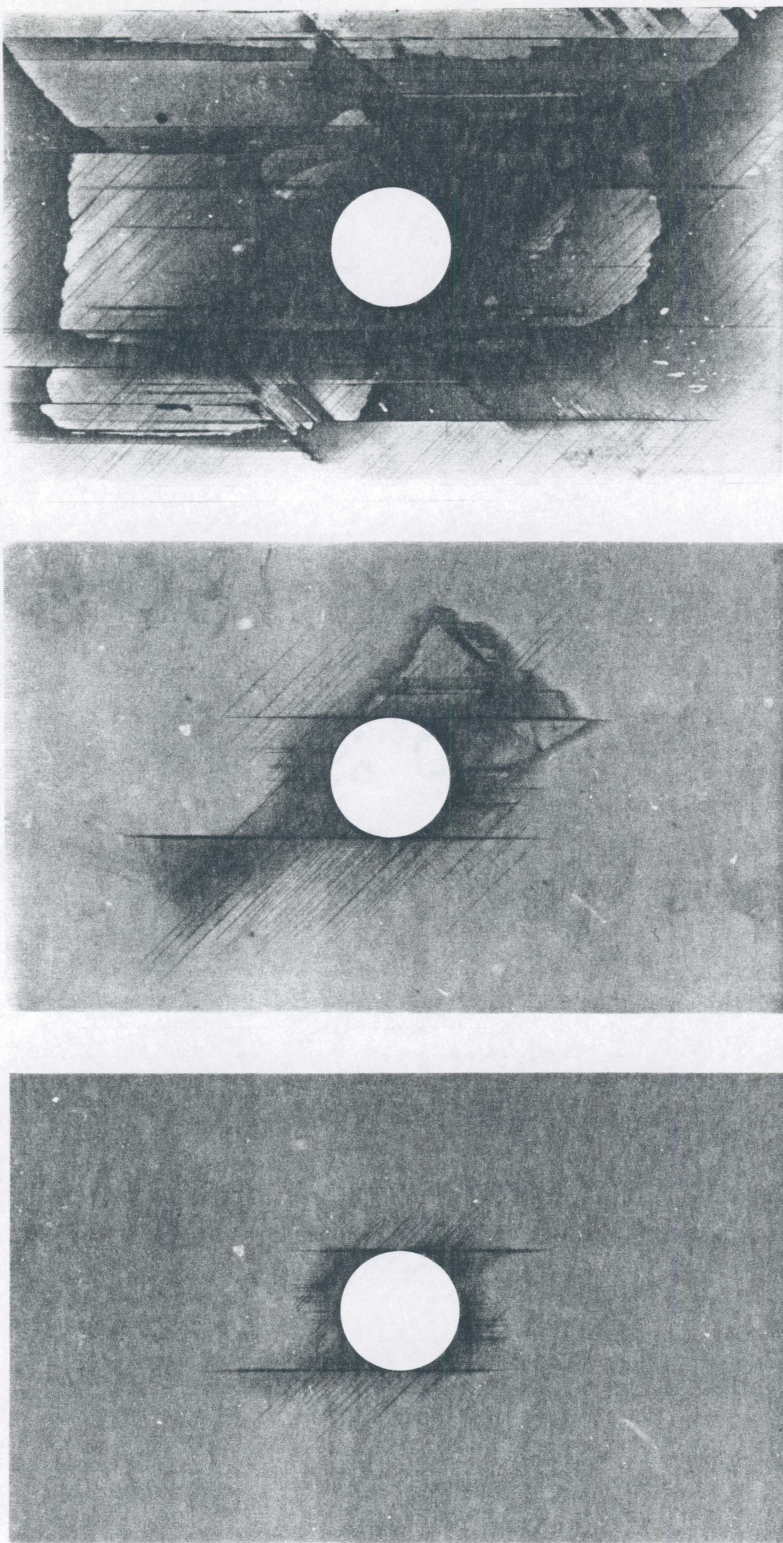


Figure 41 (Concluded)

4.3.1.2 Low Load Level

The low load level for center-notched, AS4/1808, (0,45,0,-45)_{s4} specimens, 33.1 ksi, resulted in fatigue lifetimes of 200K to 900K cycles. During the first load cycle, -45-deg. matrix cracks initiated and grew nearly perpendicularly to the hole, and 0-deg. matrix cracks initiated and grew tangentially to the hole. During the next 10 cycles, +45-deg. matrix cracks initiated nearly perpendicularly to the hole. After about one thousand cycles, delaminations initiated in all four corners formed by the intersection of the 0-deg. tangent cracks and the hole boundary, on the outermost 0/45 and 0/-45 interfaces. The length of the 0-deg. tangent cracks in all four quadrants up to this time were roughly equivalent. After about 5K cycles, these cracks became longer in the even quadrants as the +45-deg. plies began to fracture along the 0-deg. tangent cracks in those quadrants. Compared with the high-load specimens, the 45-deg. ply fracture paths followed behind the tips of the 0-deg. tangent cracks more in the low-load specimens. At the early-life residual strength measurement point, delaminations were located mostly between the 0-deg. tangent cracks, adjacent to the -45-deg. ply groups (Figure 42a and Figure 43a), although these delaminations did extend somewhat into the ligaments of material transverse to the hole. Also at this time, delaminations were longest on the outermost -45-deg. ply interfaces (Figure 44).

Before half of the fatigue lifetime was exceeded, 0/45 interface delaminations beneath the surface 0-deg. plies overtook the -45₂ ply-group delaminations in length because of the presence of delamination-inducing 0-deg. ply fractures on the surfaces. At the middle-life residual strength measurement point, delaminations adjacent to the -45-deg. plies were growing transversely to the hole, as evidenced by the continuous dark lines crossing the centerline of the notch in the edge radiograph (Figure 42b and Figure 43b). The deply data also indicated a disparity in the damage patterns as a function of distance from the surface that emerged by half of the lifetime (Figure 45). The tips of the 45-deg. ply fracture paths lagged behind the 0-deg. tangent cracks, particularly in the plies farthest from the surface (unlike the high-load



a b c

Figure 42. Radiographs of center-notched, AS4/1808, (0,45,0,-45)_{s4} specimens during low-load fatigue: (a) early; (b) middle; and (c) late life

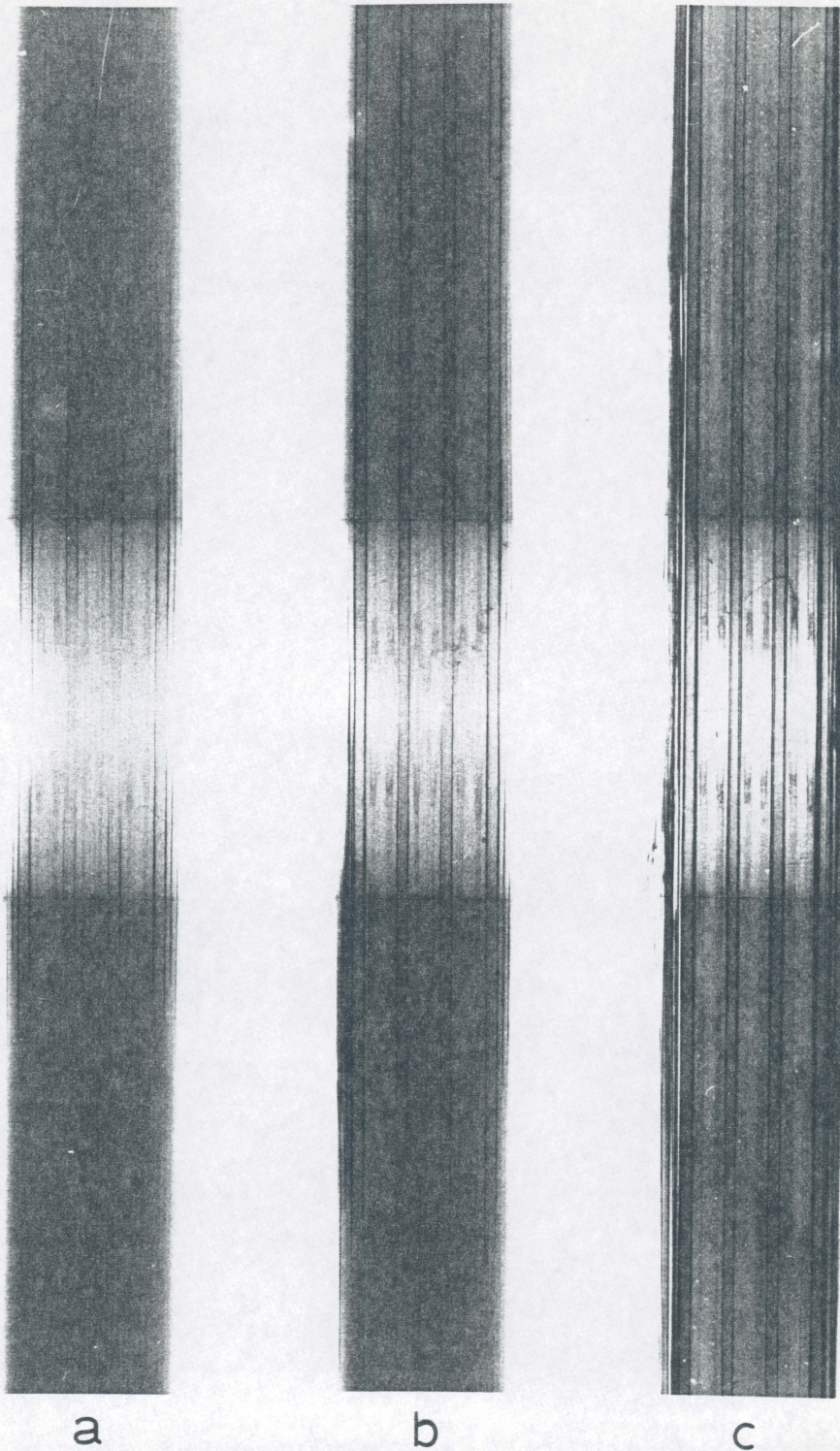


Figure 43. Edge radiographs of center-notched, AS4/1808, (0,45,0,-45)_{s4} specimens during low-load fatigue: (a) early; (b) middle; and (c) late life

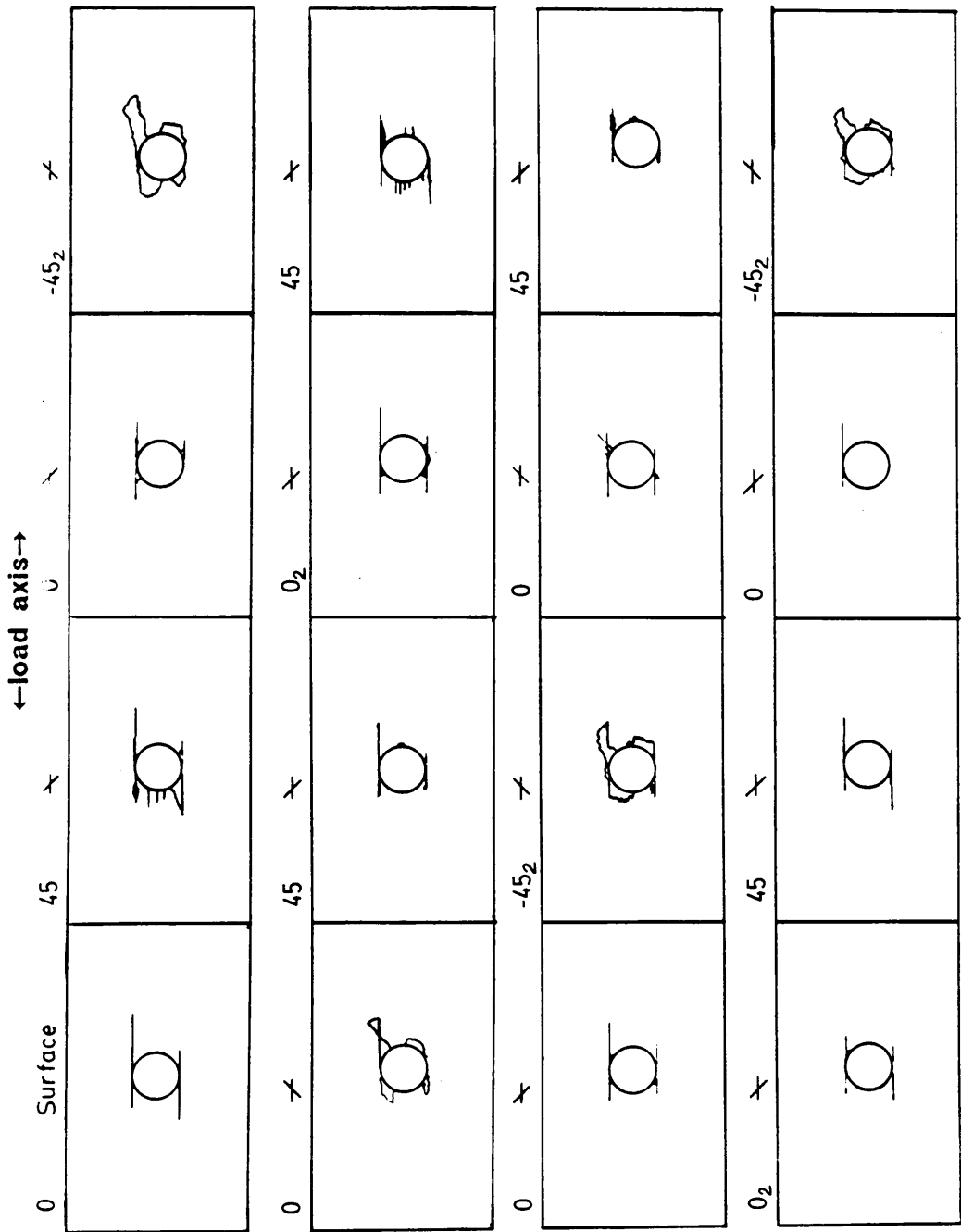


Figure 44. A depled, center-notched, AS4/1808, (0,45,0,-45)_{s4} specimen at an early stage of damage development under the low load level

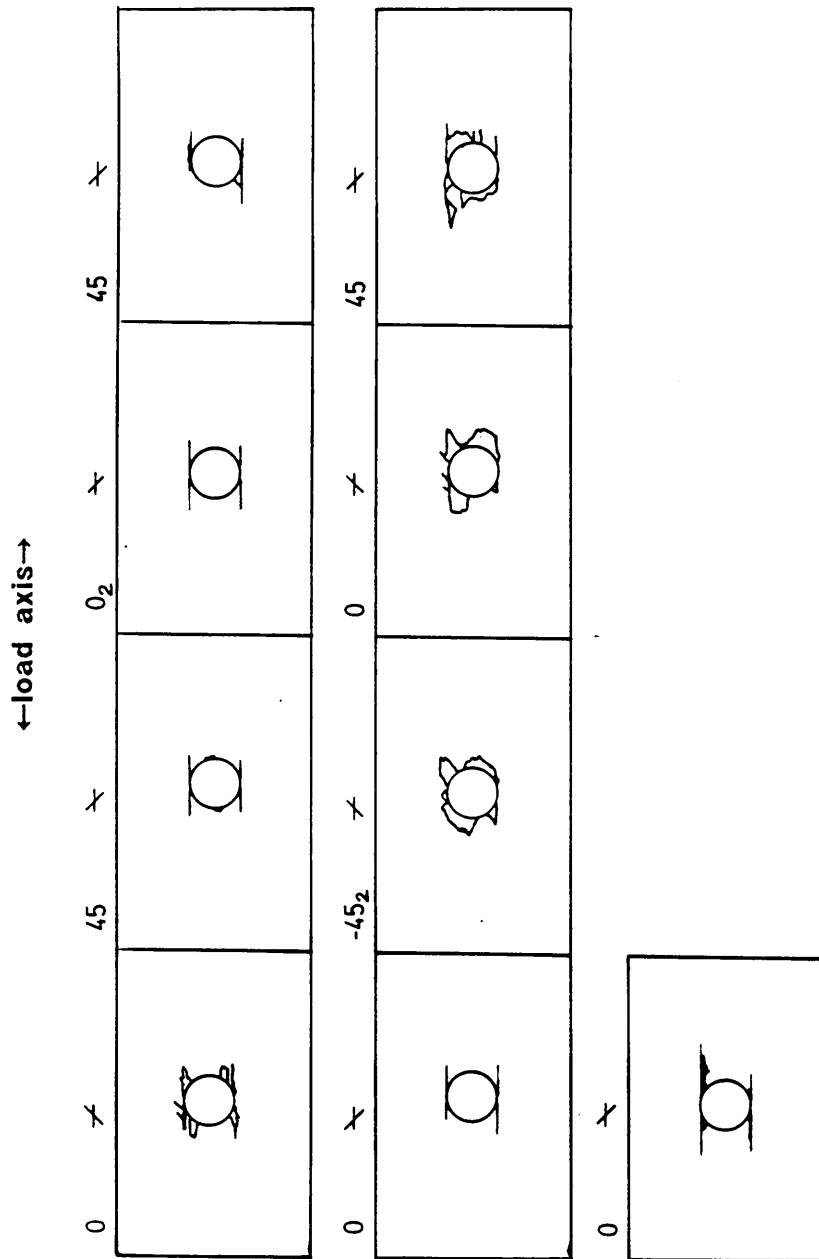


Figure 44 (Concluded)

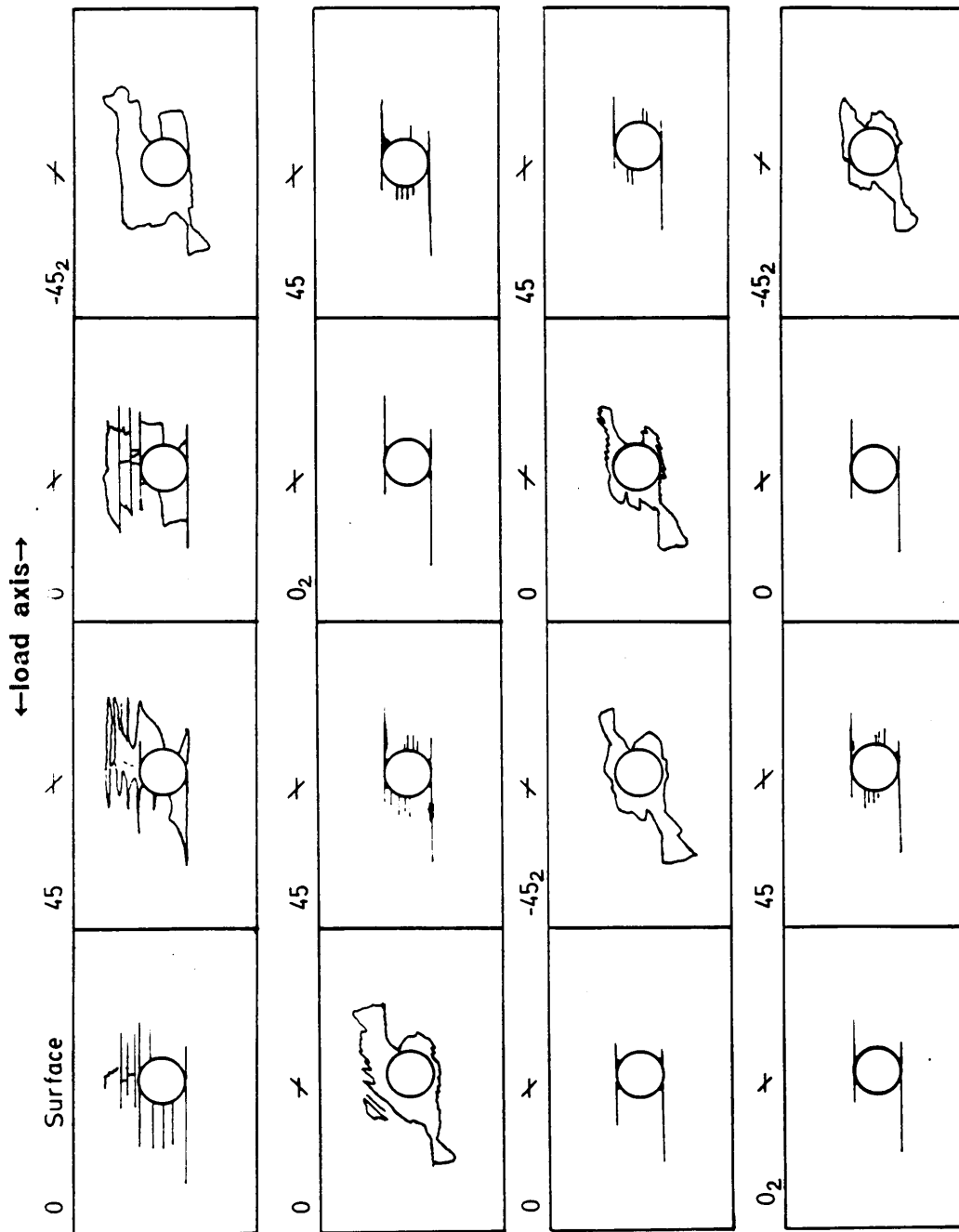


Figure 45. A depled, center-notched, AS4/1808, (0,45,0,-45)_{s4} specimen at a middle stage of damage development under the low load level

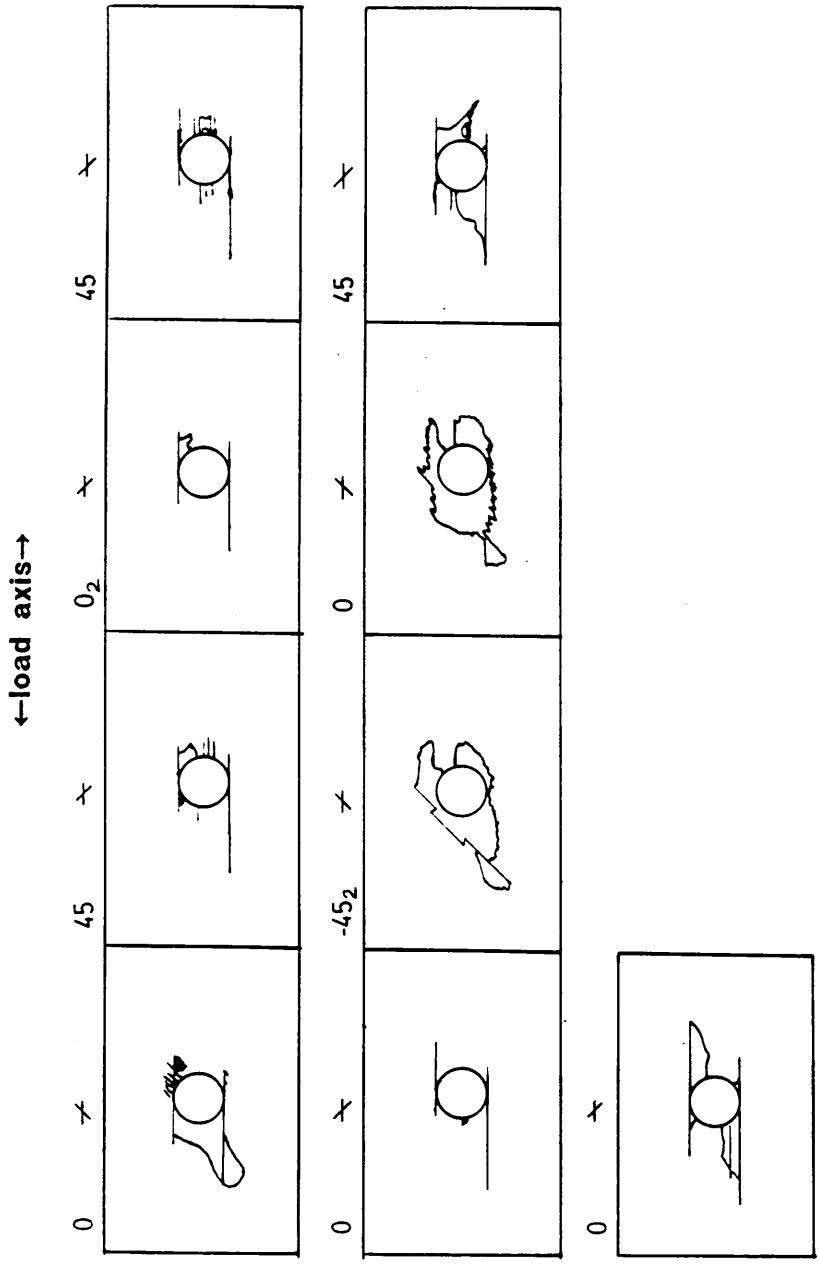


Figure 45 (Concluded)

specimens). Zero-deg. ply fracture paths initiated and grew closer to the hole centerline than in the high-load specimens.

During the second half of the fatigue life, 0/-45 interface delaminations near the tips of the 0-deg. matrix cracks constituted most of the new damage growth. Matrix cracks, surface 0-deg. ply incremental fracture paths along the 45-deg. direction, and delaminations adjacent to the surface 0-deg. plies grew into the load-bearing ligaments of material aside the notch. In a typical late-life residual strength specimen (Figure 42c and Figure 43c), surface ply delaminations extended almost entirely over the specimen's gage length. No interior 0-deg. ply fractures were seen in the low-load specimens. Therefore, the only fiber fracture mechanism observed in the interior of the laminate was +45-deg. ply fracture. Fatigue failure of the specimens was by unstable delamination growth and crushing of the interior, less-delaminated plies.

Deply data (Figure 46) supported the above observations, and indicated that the paths of fiber fracture along the 0-deg. tangent cracks in the 45-deg. plies were shorter in the low-load specimens than in the high-load specimens. In the low-load, late-life deply specimen, there was also a larger disparity in the damage patterns as a function of location through the thickness, compared to specimens at an earlier stage of life or specimens cycled at the high load level.

4.4 Summary of Damage Mechanisms

Damage mechanisms in the two materials investigated presently, AS4/1808 and AS4/3501-6, were fundamentally similar for a particular load level and lamination arrangement. Matrix cracks, delaminations, and ply fractures were evident in all cases studied, but the distribution, relative quantity, and interaction of these damage types depended, in order

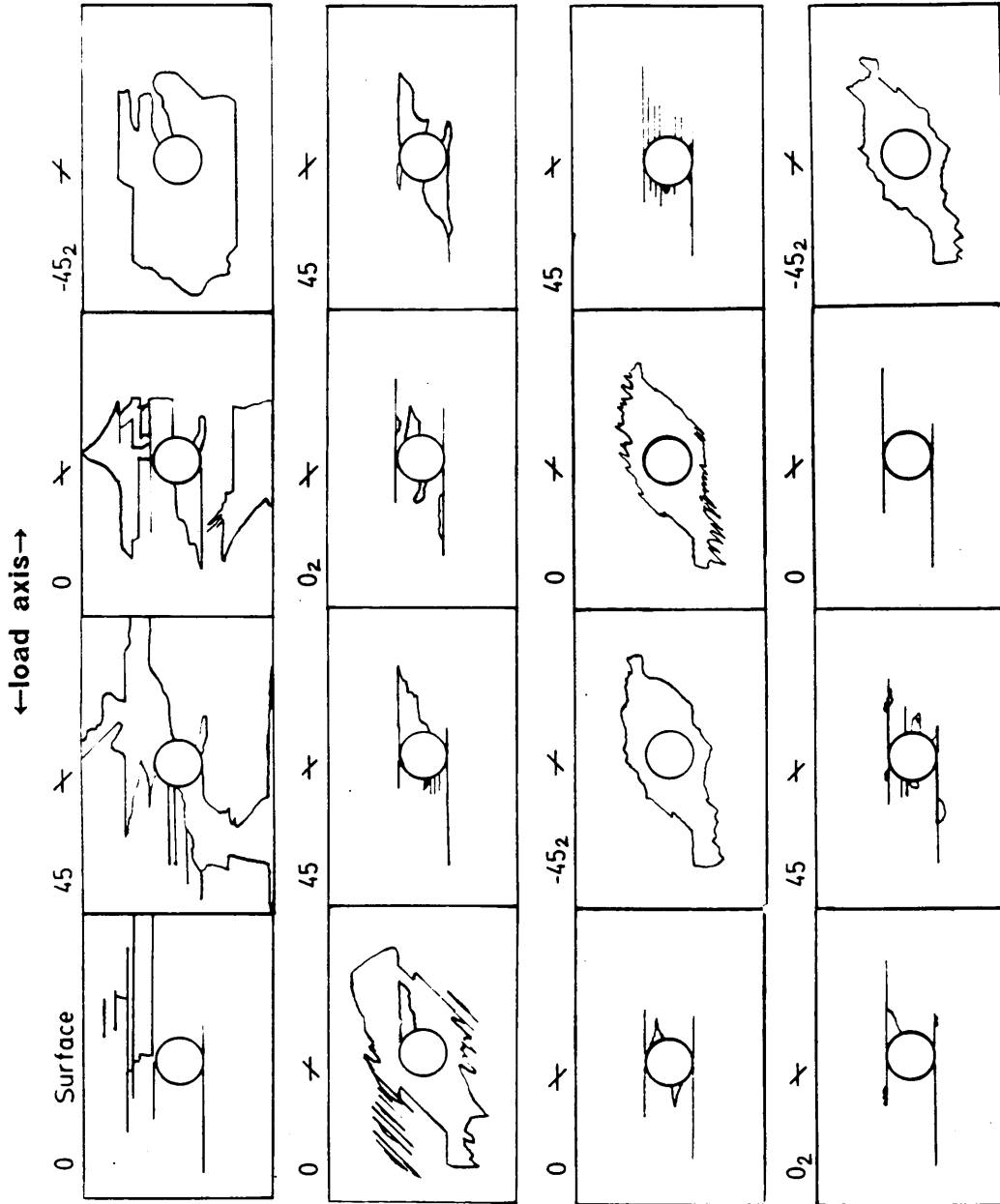


Figure 46. A depled, center-notched, AS4/1808, (0,45,0,-45)_{s1} specimen at a late stage of damage development under the low load level

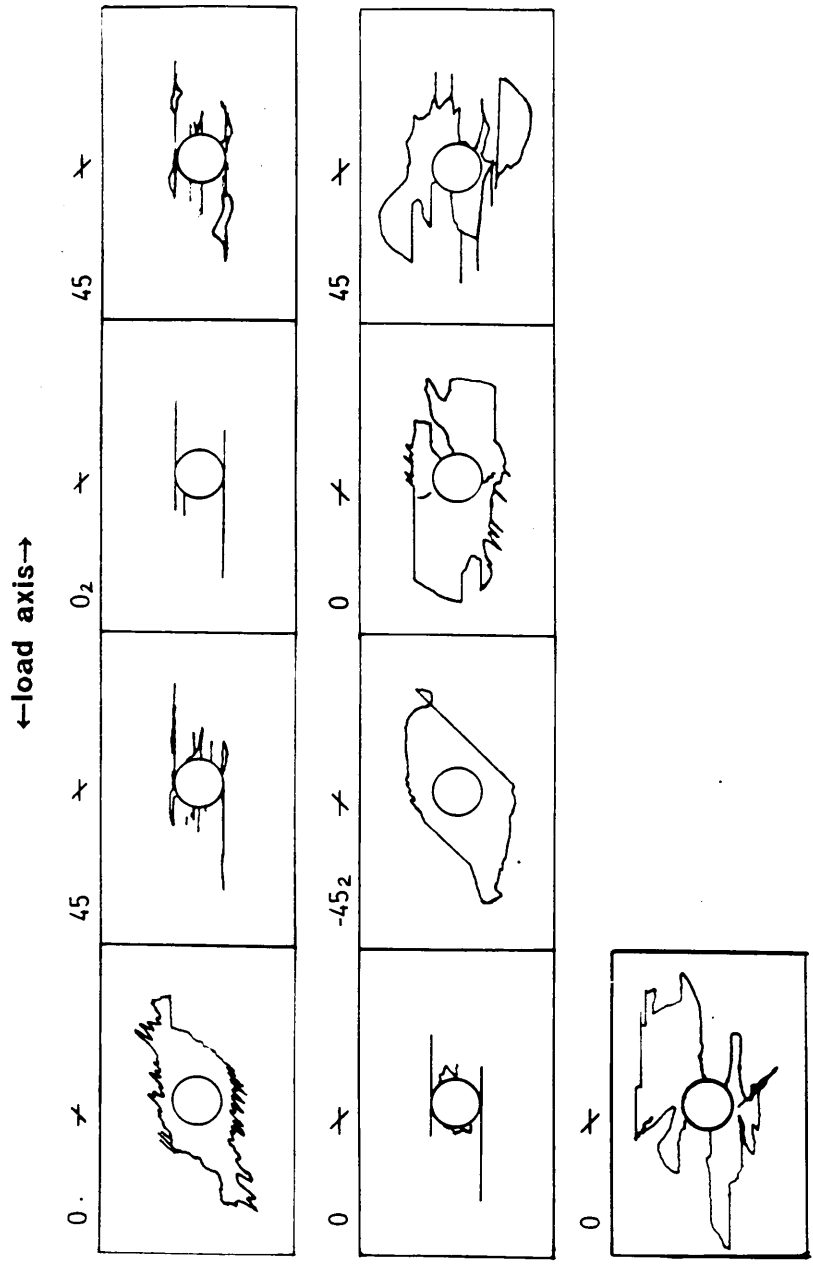


Figure 46 (Concluded)

of *decreasing* influence, on the lamination arrangement, load level, material system, and notch configuration.

4.4.1 Effect of Lamination Arrangement

Damage in the $(0,45,0,-45)_{s4}$ specimens was more directional than damage in the $(0,45,90,-45)_{s4}$ specimens due to the more highly anisotropic strength properties of the orthotropic laminate. Specifically, lines of intense damage tangent to the notch in the load direction were more prominent in the orthotropic laminate because of this laminate's lower in-plane shear strength along this path. The early presence of large matrix cracks tangent to the notch in all 0-deg. plies caused failure of the +45-deg. plies along this tangent path in the even quadrants around the notch, in cases where the +45-deg. fibers carried a significant load. Once the +45-deg. plies broke along the 0-deg. matrix cracks in the even quadrants and interacted with the matrix cracks, these 0-deg. tangent damage zones grew more rapidly than the odd quadrant damage zones. Delaminations in the orthotropic laminate were largest along the -45₂ ply groups in the even quadrants. Smaller delaminations were noted along the 0-deg. ply interfaces. The concentration of damage at the tips of the 0-deg. tangent damage zones in the even quadrants resulted in essentially undamaged ligaments of material adjacent to the notch. This situation existed until the last stage of fatigue lifetime, when delaminations grew over much of the gage length.

Incremental compressive fractures of the surface 0-deg. plies along the +45-deg. direction occurred in both laminates. Later in the fatigue lifetime, similar fracture paths occurred in interior 0₂ ply groups located between +45-deg. plies. Single-thickness 0-deg. plies in the interior of the orthotropic laminate were located adjacent to +45- and -45-deg. plies, and fractured in compression near the intersection of the 0- and -45-deg. matrix cracks that originated tangent to the notch. These internal ply fractures grew incrementally along either the

+45- or -45-deg. direction (or both, in alternate fashion), and served as precursors for the transverse growth of delamination in the orthotropic laminate near the end of life.

The damage pattern in the $(0,45,90,-45)_{s4}$ specimens reflected the influence of the off-axis plies (comprising 75 percent of the thickness of this laminate). Matrix crack growth in the 90-deg. plies led to a more transversely-oriented growth of delamination from the notch at an earlier fraction of life. The implications of these significant differences in delamination characteristics shall become evident in the discussions on residual strength later. The incidence of step-wise 0-deg. ply fracture was higher in the quasi-isotropic laminate, especially in the internal 0-deg. ply groups. Both laminates failed during a compressive load cycle after near-surface delaminations grew in an unstable manner and the internal plies crushed near the notch(es).

4.4.2 Effect of Load Level

The high load level resulted in a more concentrated, or localized, damage pattern than the low load level. Though the fundamental damage modes present in both loading regimes were identical, their relative abundance and degree of interaction depended highly on the maximum load level (or, perhaps, the loading rate, since all tests were run at the same frequency, not stress rate). For instance, in all specimens studied, damage under the high load was more directionally-oriented than under the low load. With low loads, incremental ply fractures and delaminations near the surface of the specimens were significantly more extensive than similar damage modes farther from the surface. This difference was less evident under high loads.

In $(0,45,90,-45)_{s4}$ specimens, damage grew preferentially along the transverse centerline through the notch during high-load fatigue. Damage in low-load fatigue specimens grew by essentially the same mechanisms, but over a larger area of the specimen, often resulting in nearly-completely delaminated surface plies. Delaminations on 0/45 interfaces closer to the

surface had greater longitudinal dimensions than similar interfaces located in the interior of the laminate. This difference was greater in low-load specimens than in high-load specimens. Only the low-load specimens developed longitudinal delaminations of the 0-deg. surface ply that extended from the notch to the grips (usually in the even quadrants, at first), causing a large middle-life stiffness reduction. Conceptually, the critical size for unstable delamination growth should be higher during lower compressive load excursions. Lower loads should, therefore, result in more delamination since fatigue failure in all cases was by the unstable delamination of near-surface 0-deg. plies and the resulting overload of interior plies. Matrix cracks always appeared over a larger area in the low-load specimens. The last important difference between high- and low-load damage mechanisms in $(0,45,90,-45)_{s4}$ laminates was the earlier occurrence of interior 0-deg. ply fracture under high loads. If such fractures occurred at all in the low-load specimens, they occurred during the last 10 percent of life.

In high-load $(0,45,0,-45)_{s4}$ specimens, 0-deg. ply fracture was seldom blunted by the occurrence of delaminations that isolated the subject 0-deg. ply from its cracked, off-axis neighbors. Instead, through-the-thickness fractures in principal load bearing plies (along with delamination in their wake) continued to grow, eventually causing compressive fatigue failure. In the low-load specimens, 0-deg. ply fractures near the tips of the 0-deg. tangent cracks were frequently preempted by delaminations along the -45_2 ply groups in this same locale. Without the influence of a bonded neighboring ply, 0-deg. ply fractures were never observed. The same can be said for the $+45$ -deg. ply fracture paths that followed the adjacent 0-deg. matrix cracks tangent to the notch in the even quadrants. No such fractures occurred after the growth of delaminations between the 0- and $+45$ -deg. plies.

Under low-level cyclic loads, there was less interaction of damage modes in adjacent plies in the $(0,45,0,-45)_{s4}$ laminate. For example, the 45-deg. ply fracture paths tangent to the notch were nearly the same length as the 0-deg. ply matrix cracks that they paralleled in high-load specimens. However, the 45-deg. ply fracture paths in low-load specimens were much shorter than the 0-deg. matrix cracks. In low-load fatigue, there was more matrix damage (transverse cracks and delaminations) than in high-load fatigue, and that damage was more evenly re-

presented in all four quadrants around the notch. Damage in the high-load specimens was relatively more concentrated in the even quadrants, especially in the first half of the fatigue lifetime.

4.4.3 Effect of Material System

Transverse matrix cracks appeared over a greater area and with a greater density in the 3501-6 material than in the 1808 material. Delaminations were approximately equivalent in location, size, and extent in both materials. More precisely, the 1808 high-load specimens had larger surface ply delaminations than the 3501-6 high-load specimens, but this effect could have been caused by the slightly longer fatigue lives in the 1808 material at the chosen high load levels (longer fatigue lives corresponded with larger delaminations). The 1808 specimens displayed 0- and 45-deg. ply fracture modes earlier and over a larger area than did the 3501-6 specimens. Therefore, the competing, strip-like delaminations of the surface 0-deg. plies were more likely to occur in the 3501-6 specimens than in the 1808 specimens.

In the $(0,45,0,-45)_{s4}$ specimens, material comparisons could be made only at the high load level. The skewed appearance of the damage patterns was more pronounced in the 1808 material than in the 3501-6 material in the second half of the fatigue lifetime. The 1808 material was also more likely than the 3501-6 material to exhibit ply fracture in the second-outermost 0-deg. ply and growth of such fractures along the -45-deg. direction. These results suggest that matrix damage in adjacent off-axis plies had a stronger influence on the fracture of the 0-deg. plies in the 1808 material.

4.4.4 Effect of Notch Configuration

There was more scatter in the fatigue lives of DEN specimens than of CN specimens due to the greater variability of damage in the DEN specimens. For example, the AS4/1808, (0,45,90,-45)_{s4} DEN specimens tested under the high load level exhibited greater failure mode transitions than did the CN specimens under the high load level. The non-symmetric development of damage was also more prevalent in DEN specimens, due to their similarity to unnotched specimens (i.e., less notch influence in the damaged specimen).

By the end of life, longitudinal surface ply delaminations in DEN specimens were longer in the even quadrants than in the odd quadrants. These differences were less dramatic in the CN specimens. In the DEN (0,45,90,-45)_{s4} specimens, fatigue failure was often preceded by the appearance of a narrow strip of delamination spanning the distance between the notches along the outermost 90-deg. ply. Life-limiting delaminations in the CN specimens grew over a shorter distance between the notch and the straight edge(s), but at a slower rate than the life-limiting delaminations in the DEN specimens. Hence, the last stage of fatigue life was longer in the CN specimens than in the DEN specimens (as seen in the stiffness records, Figure 21 and Figure 22).

Chapter V

Stress Redistribution Mechanisms

Matrix cracks, frequently the first damage mode to appear in practical carbon fiber reinforced plastic materials, set the internal stress state for subsequent damage development. Insight into this stress redistribution problem was obtained with a sequence of SPATE thermographs of a center-notched, 42-ply, carbon epoxy laminate with matrix cracks that initiated and grew in the 90-deg. surface ply during tensile cyclic loading (Figure 47). The SPATE sequence shown in Figure 47 includes the undamaged condition, 90-deg. crack initiation, and 90-deg. crack saturation. Also evident in the heavily-damaged specimen was a near-surface delamination corresponding to the black (no temperature change) area surrounding the notch. There are two special features of the SPATE thermographs that should be noted. The first is the reduction in load carried by the material immediately adjacent to and along the length of each 90-deg. matrix crack. The second is the eventual reduction of load carried by the 90-deg. surface ply over the entire gage-length of the specimen as the crack spacing became asymptotically smaller with increasing load cycles. In this manner, stress was increasingly transferred to undamaged plies until a saturated 90-deg. ply crack spacing was approached.

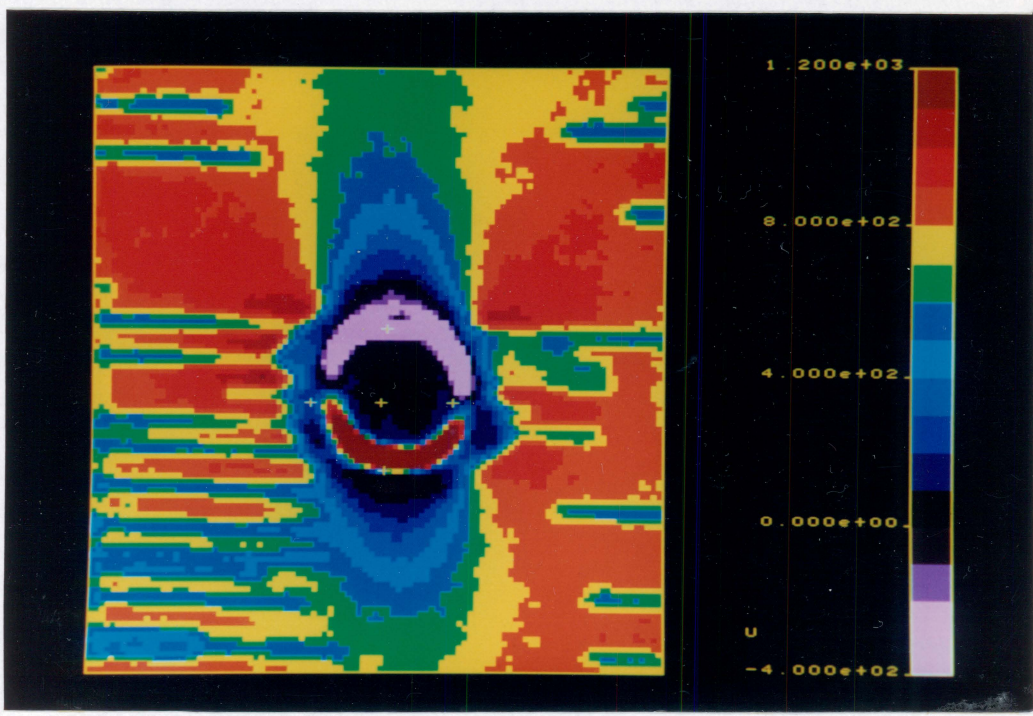
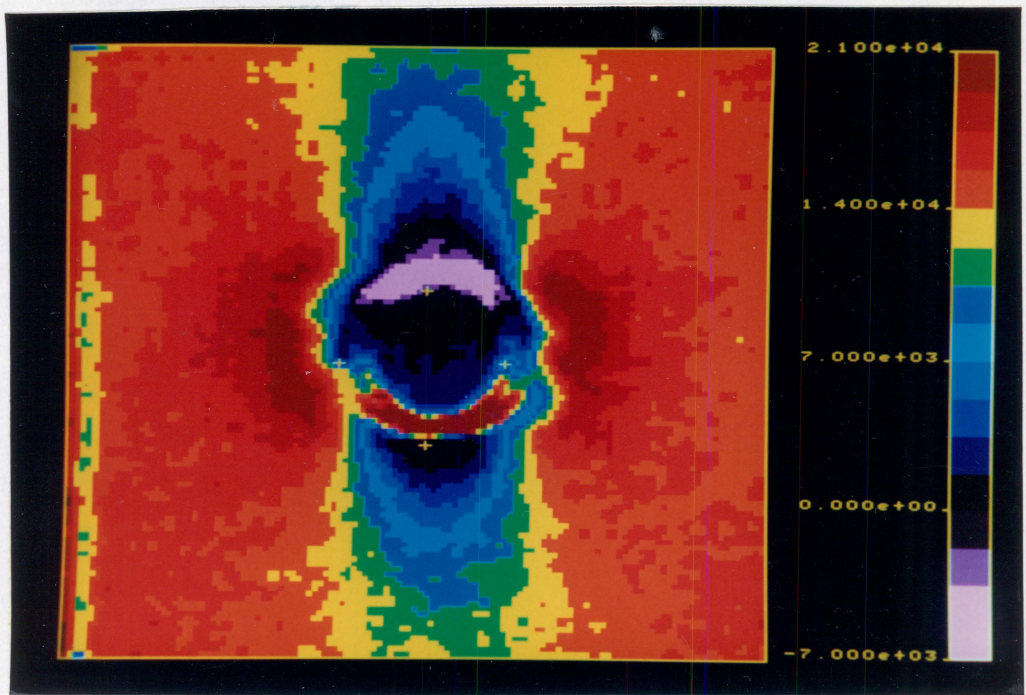
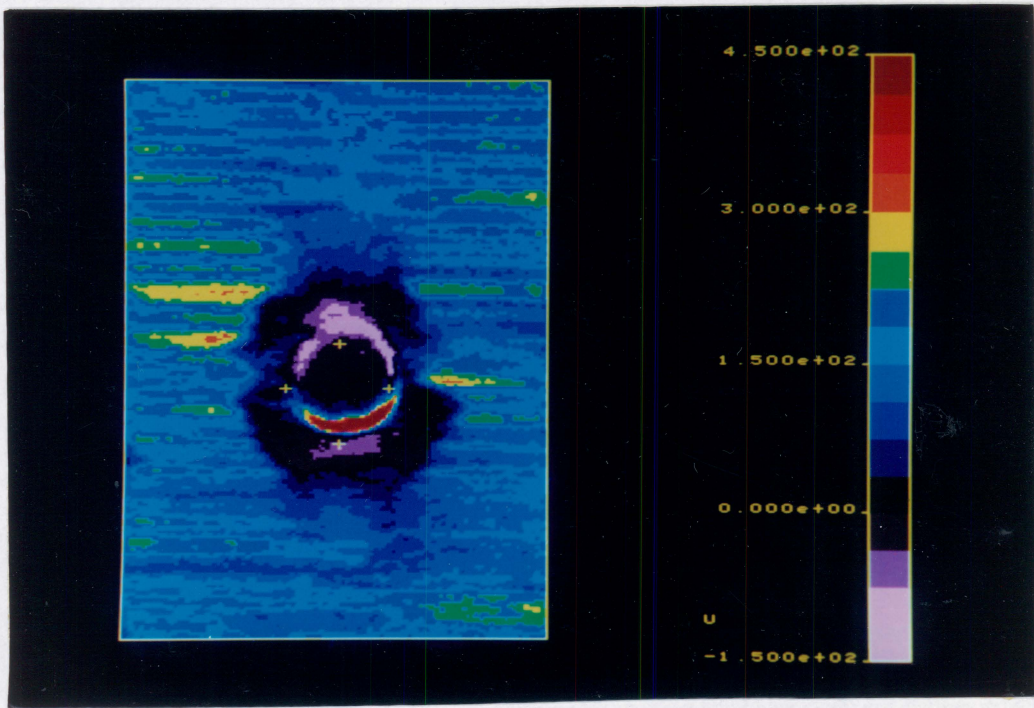


Figure 47. SPATE thermographs of matrix crack development: (a) undamaged; (b) after tensile fatigue ($R=0.1$); (c) after tensile-compressive fatigue ($R=-1$), near fatigue failure

GRAFFIATA BOND

50% COTTON FIBER



C

Figure 47. (Concluded)

Although the delamination around the notch in Figure 47c appeared in the SPATE thermograph as an area of negligible temperature change, it would be a misinterpretation to assume that this portion of the surface ply carried no load at all. Recalling the expression for adiabatic temperature change in a ply, $\Delta T = K_1\sigma_1 + K_2\sigma_2$, it is clear that certain nonzero combinations of stress components result in no net temperature change, as does the null stress state. In this particular case (Figure 47c), additional information obtained via penetrant-enhanced X-ray radiography suggested that the surface ply could still carry load in the fiber direction, but not transverse to the fibers.

Fiber reinforced composites in structural applications are usually designed such that most of the load is carried by the fibers. Therefore, one can expect significant disturbances in the stress field to arise from fiber fracture. For example, recall Figure 23 on page 77 illustrating the incremental, 0-deg. surface ply fracture pattern often seen on the surface of test specimens. Immediately ahead of the crack front, a zone of high stress concentration formed, leading to a repetition of the incremental damage growth process. A better appreciation for the severity of this migrating zone of stress concentration is offered by the SPATE thermograph of a AS4/1808, (0,45,90,-45)_{s4} specimen in Figure 48. The adiabatic temperature change near the crack tip was approximately 2.9 times greater than that in the far-field area of the laminate, slightly greater than the typical ratio of 2.8 measured adjacent to the hole in undamaged specimens. Additional experimental evidence obtained using the photoelastic coating technique also revealed the large strain concentration typically seen with this type of damage [58]. Therefore, not only was there a strain concentration in the intact 0-deg. fibers ahead of the crack tip, but at least a portion of the laminate underlying the surface damage zone near the notch was also subjected to a strong strain concentration due to the local reduction in compliance caused by the 0-deg. ply fiber fractures. Two directions of damage growth during cyclic loading, in-plane and through-the-thickness, were thus affected by damage-induced stress redistribution.

Numerous parameters influence the details of damage development and stress redistribution in fiber reinforced composite laminates during cyclic loading, although only a few have

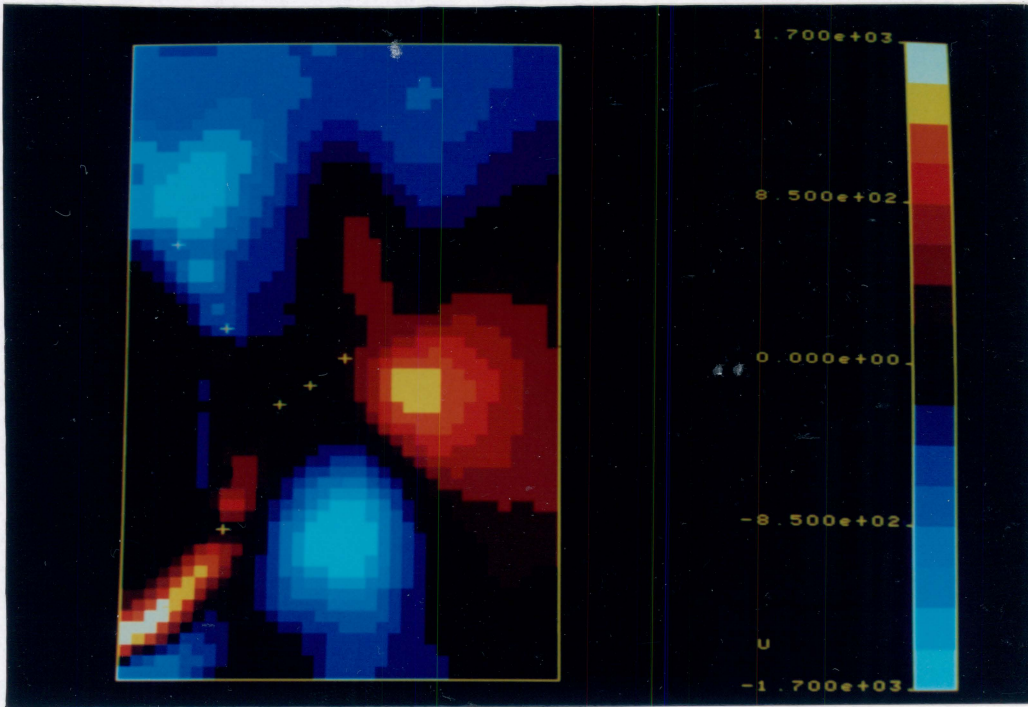


Figure 48. SPATE thermograph of a 0-deg. surface ply fracture

been experimentally investigated. Those that will be discussed next are: lamination arrangement, material system, loading regime, and, to a lesser extent, notch configuration. The discussion will focus on comparisons, not details.

Lamination arrangement influences the damage initiation and growth patterns in CFRP laminates because of the anisotropic strength characteristics of the individual plies. That is, the matrix-dominated shear and transverse strengths are significantly lower than the fiber-dominated longitudinal strength. SPATE thermographs of $(0,45,90,-45)_{s4}$ and $(0,45,0,-45)_{s4}$ AS4/1808 laminates obtained at regular intervals in their respective fatigue lifetimes indicated that their different modes of fatigue damage growth resulted in different distributions of stress around the notch.

The highest adiabatic temperature change (ATC) in the surface 0-deg. ply of the $(0,45,90,-45)_{s4}$ laminate during high-load fatigue occurred adjacent to the notch in the undamaged specimen, but it shifted in the transverse direction such that it remained immediately in front of the 0-deg. ply fiber fracture path or delamination zone (or both) growing from the notch. Concurrently, the ATC within the delaminated zone decreased to a value of nearly zero. Adiabatic thermoelastic emissions in four different specimens at sequential states of fatigue life are shown in Figure 49 and Figure 50. The lower ATC measured within the growing damage zone near the notch was caused by either: (a) an actual decrease in fiber-direction stress in those cases where the surface 0-deg. ply has fractured and delaminated in the incremental fashion of Figure 23 on page 77; or (b) the purely uniaxial load imposed on the delaminated strips of 0-deg. ply adjacent to the notch in the absence of fiber fracture. Photoelastic coating data in either case indicated that strains inside the damage zone increased relative to the undamaged condition, and that areas of high strain concentration also existed immediately ahead of the advancing damage zone [58]. Fatigue damage in the $(0,45,90,-45)_{s4}$ laminate followed the path of the migrating zones of high strain concentration. SPATE data revealed only a small change in the uniformity of the far-field patterns as damage developed, a feature that contrasted with the $(0,45,0,-45)_{s4}$ laminate.

CRACK GROWTH

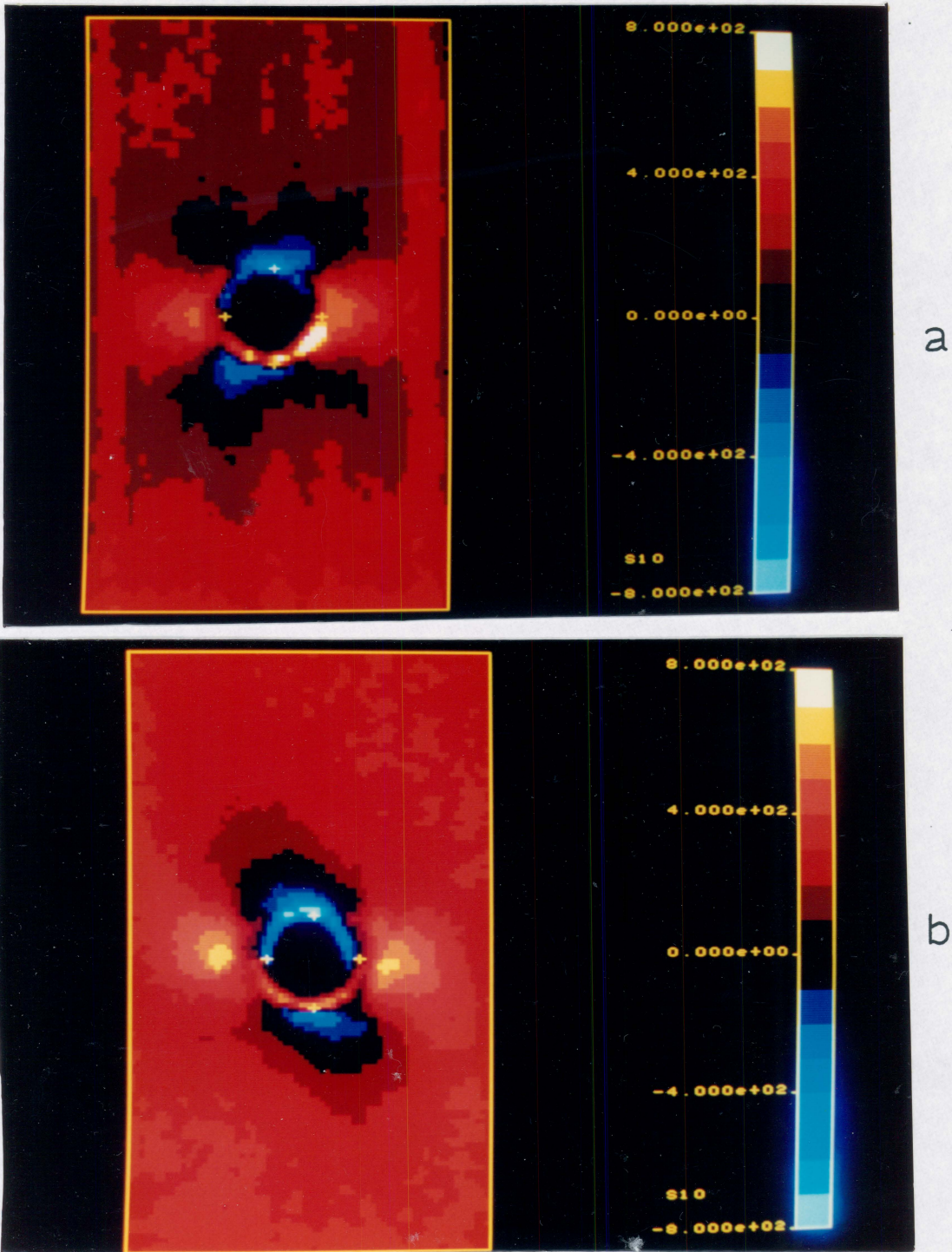
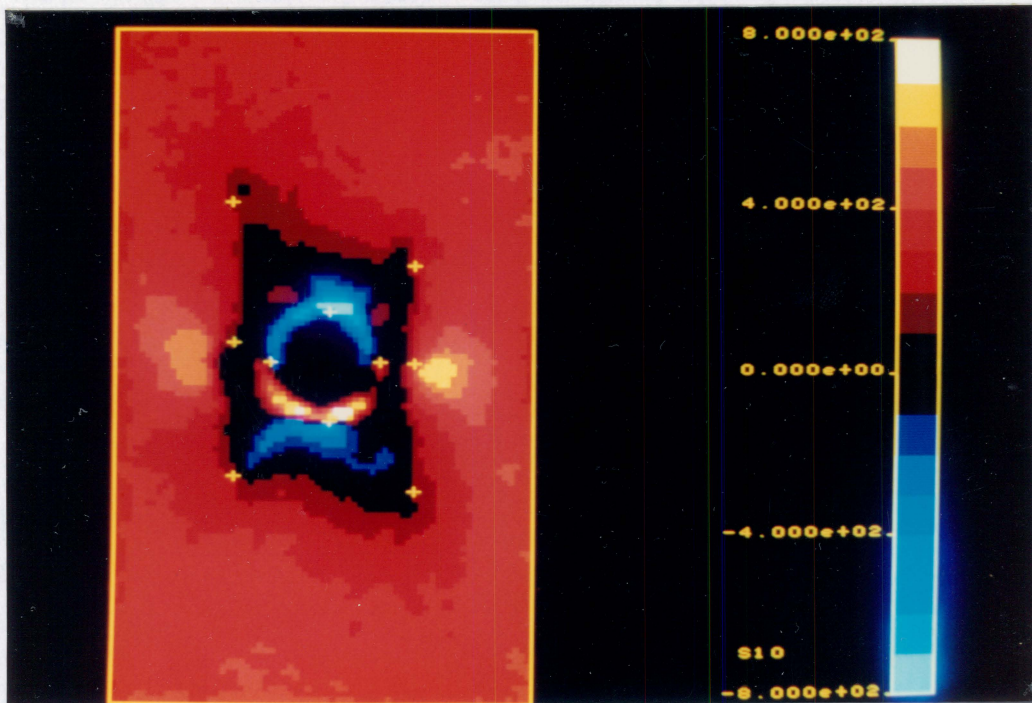
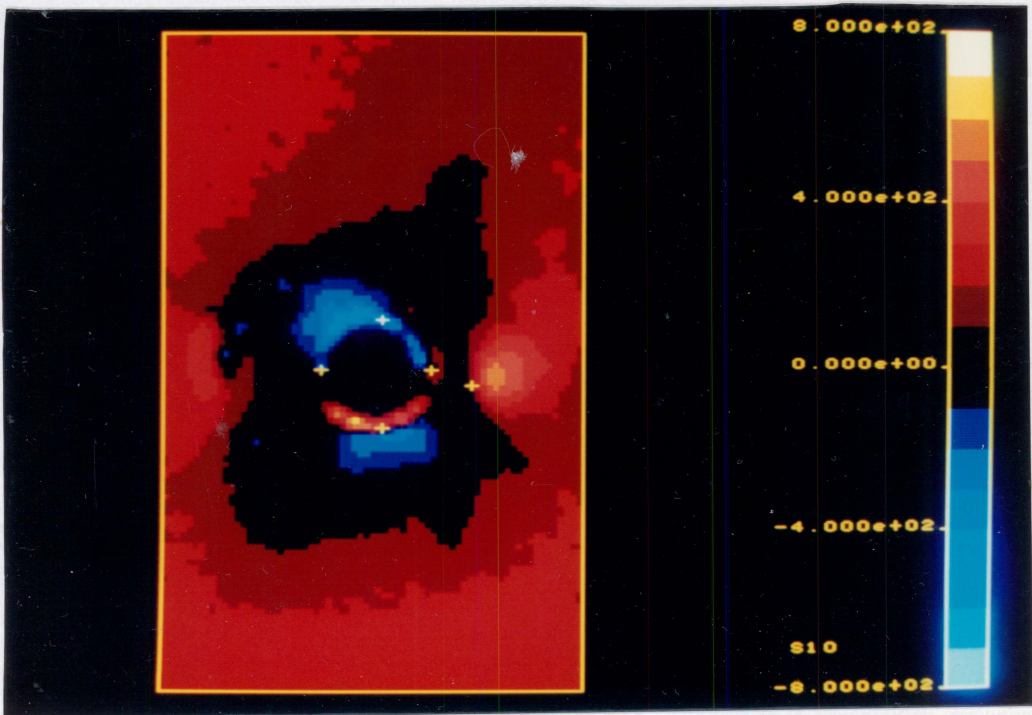


Figure 49. SPATE thermographs of four center-notched, AS4/1808, (0,45,90,-45)_{S4} specimens during high-load fatigue: (a) undamaged (back); (b) early life (front); (c) middle life (front); (d) late life (back)



c



d

Figure 49. (Concluded)

Correlations of the maximum ATC measurements on high-load, $(0,45,90,-45)_{s4}$ specimens with the tensile strength of those same specimens were quite good once inter-specimen variations in the ATC remote from the notch were eliminated by normalizing the maximum ATC near the notch by the remote ATC. In effect, "ATC concentration factors" were used as measures of worst-case stress concentrations in different specimens. Dividing the ATC concentration factor in the virgin specimen by the ATC concentration factors in the residual strength specimens resulted in the expected strengths listed in Table 6 for the $(0,45,90,-45)_{s4}$ specimens (the expected strengths for $(0,45,0,-45)_{s4}$ specimens were computed differently). The actual tensile strengths in Table 6 were normalized by the average strength of virgin specimens. Actual and expected strengths both increased up to half of the fatigue lifetime, and decreased near fatigue failure.

In AS4/1808, $(0,45,0,-45)_{s4}$ specimens, zones of high ATC moved longitudinally along the large 0-deg. cracks that formed tangent to the notch in the 0- and 45-deg. plies (Figure 51 and Figure 52). Near the tips of these cracks, there were small areas of stress concentration in the load-bearing ligaments of the 0-deg. plies. These zones shifted in the longitudinal direction as the 0-deg. cracks grew, and corresponded closely to the location of tensile fracture in residual strength tests (shown later in the chapter on residual strength). The maximum amplitude of ATC within these small zones was nearly the same as that found adjacent to the notch (over a larger area) in the undamaged specimen. Photoelastic coating data indicated that high shear strain concentrations formed at the 0-deg. tangent crack tips. Also, the photoelastic data showed that regions of material directly above and below the notch (between the 0-deg. tangent cracks) became somewhat decoupled from the remainder of the laminate and carried little load [58]. This information indicates that the stress distribution in the $(0,45,0,-45)_{s4}$ laminate became increasingly uniform as fatigue damage developed (provided no localized surface damage events occurred), resulting in a reduced notch effect as the two ligaments of material adjacent to the notch behaved more like straight-sided coupons. Near the end of life, the maximum ATC within the ligaments increased. This suggests that the

Table 6. Actual and expected normalized tensile strengths of center-notched, AS4/1808 specimens during high-load fatigue

Stack	Specimen Identification	Estimated % of Life	Actual S_f/S_f^\dagger	Expected S_f/S_f^\dagger
(0,45,90,-45) _{s4}	3-10	0	1.00	1.00
	3-12	5-10	1.11	1.27
	3-2	40-60	1.19	1.33
	2-3	≥90	.883	1.12
(0,45,0,-45) _{s4}	2-11	0	1.00	1.00
	3-3	5-10	1.16	0.71
	3-7	40-60	1.42	1.16
	2-18	≥90	1.10	1.05

† Strengths normalized by the average strength of virgin specimens.

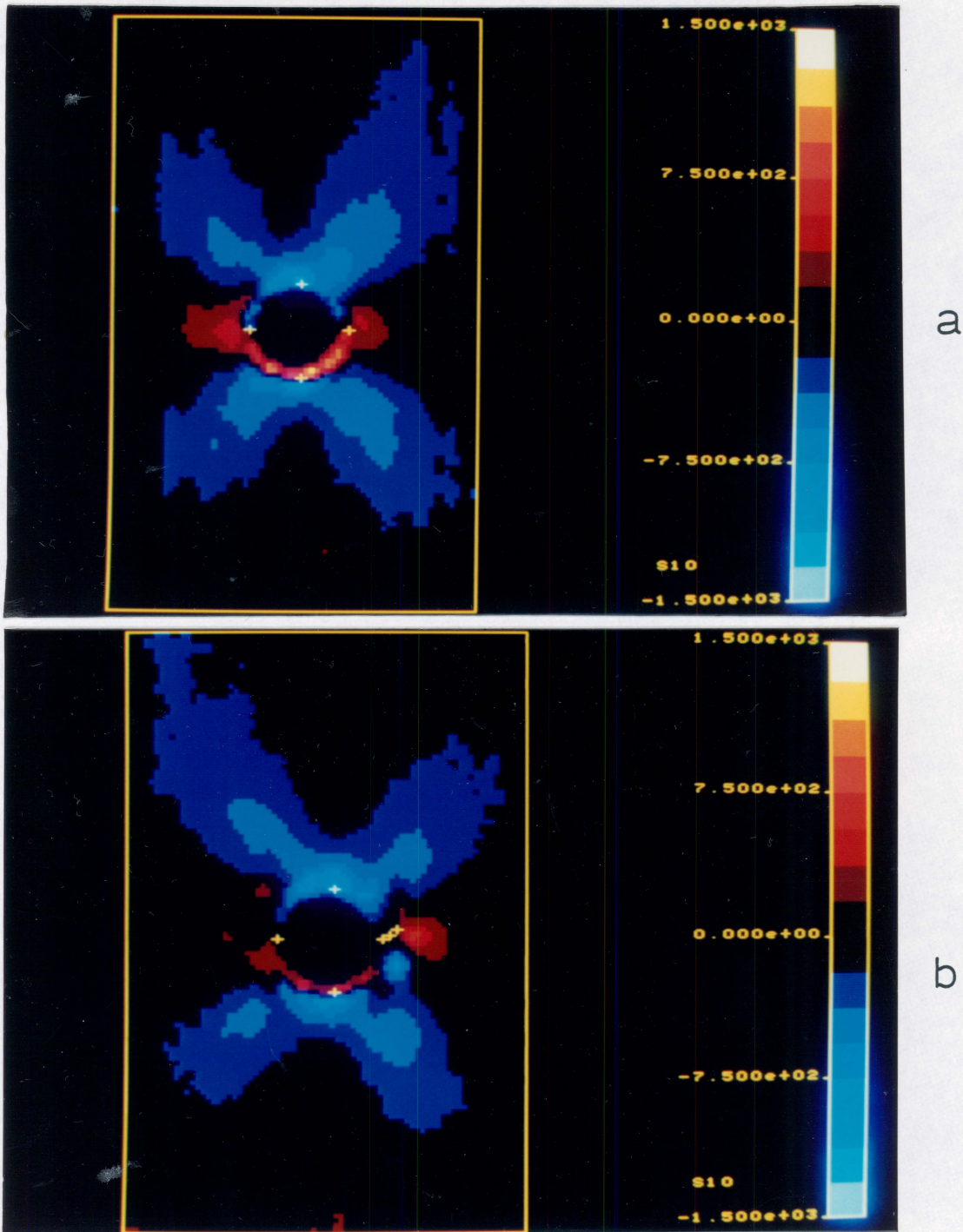


Figure 51. SPATE thermographs of four center-notched, AS4/1808, (0,45,0,-45)_{S4} specimens during high-load fatigue: (a) undamaged (back); (b) early life (front); (c) middle life (front); (d) late life (front)

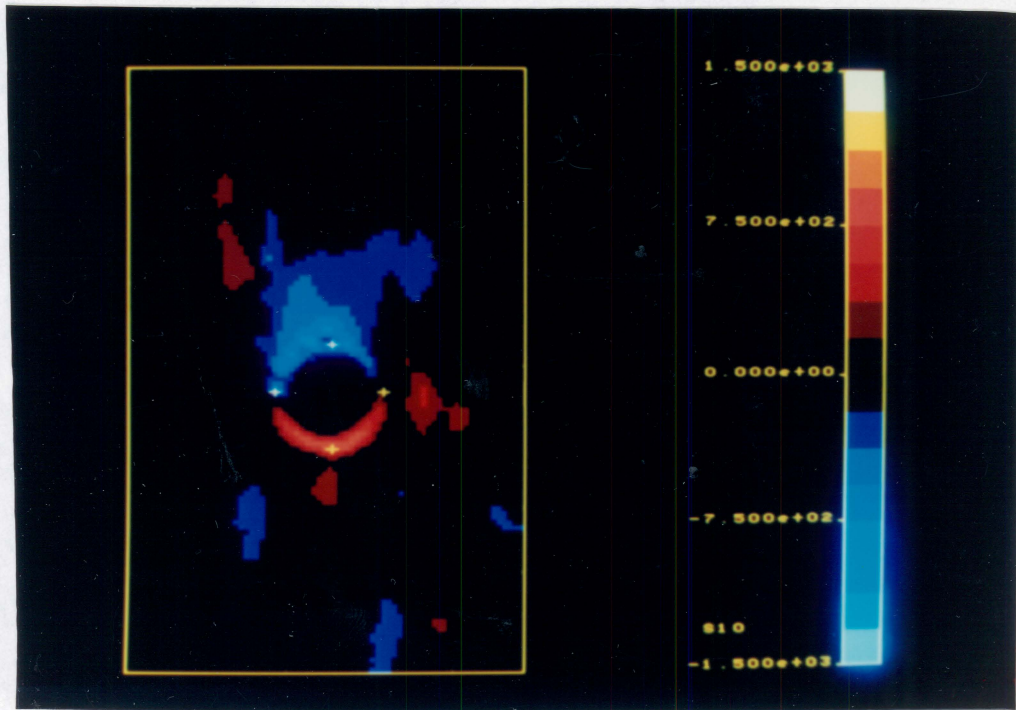
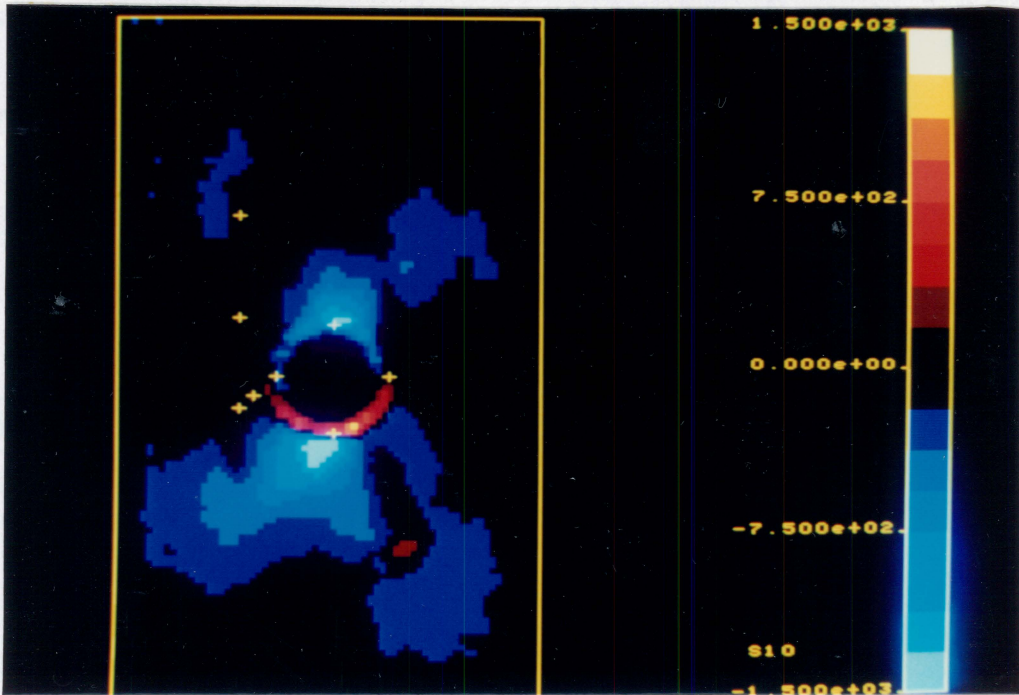


Figure 51. (Concluded)

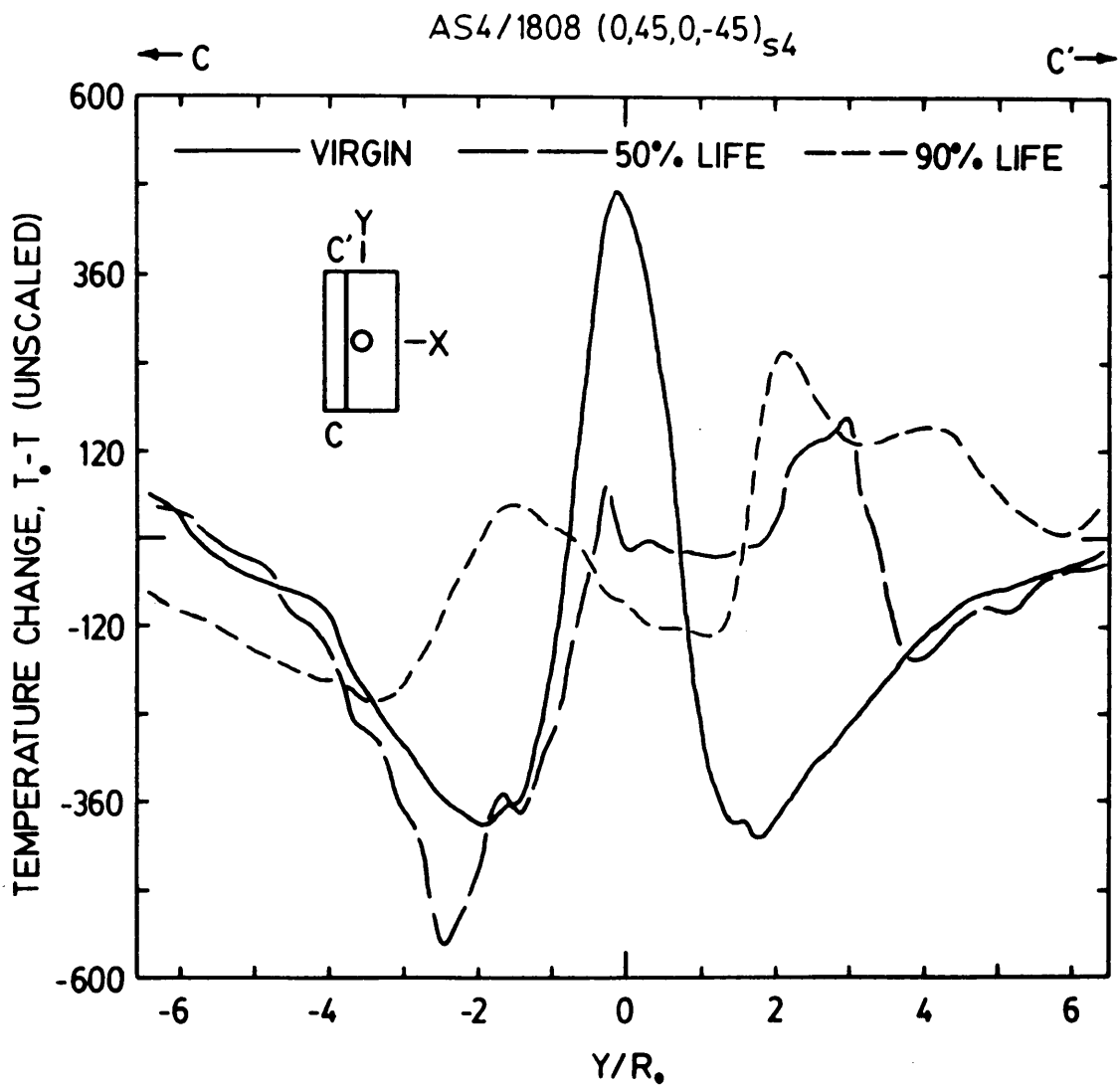


Figure 52. SPATE signal along Section C-C' in three center-notched, AS4/1808, (0,45,0,-45)_{s4} specimens during high-load fatigue: R_0 = hole radius.

surface 0-deg. plies carried an increasing proportion of the load as the stiffness of the ligaments decreased due to off-axis matrix cracking.

Expected strengths of center-notched, AS4/1808, (0,45,0,-45)_{s4}, residual strength specimens could not be computed as they were for (0,45,90,-45)_{s4} specimens because the far-field value of ATC was zero in the (0,45,0,-45)_{s4} specimens. (One cannot compute an ATC concentration factor by dividing the maximum ATC by zero). Consequently, the highest value of ATC measured in the virgin specimen was divided by the highest value of ATC in each residual strength specimen to arrive at the expected strengths listed in Table 6. The effect of inter-specimen variation in ATC was therefore not eliminated in the calculations for orthotropic specimens as it was for quasi-isotropic specimens. Despite this handicap, the expected strengths for all stages of fatigue life except "early" followed the trends in the actual tensile strengths of the test specimens (increasing up to middle life, and decreasing slightly near fatigue failure). The low expected strength of the early-life specimen resulted from the extremely high value of ATC measured at the tip of a short 0-deg. ply fracture adjacent to the hole. Apparently, the small volume of highly stressed material in front of the crack tip did not govern the failure of the specimen.

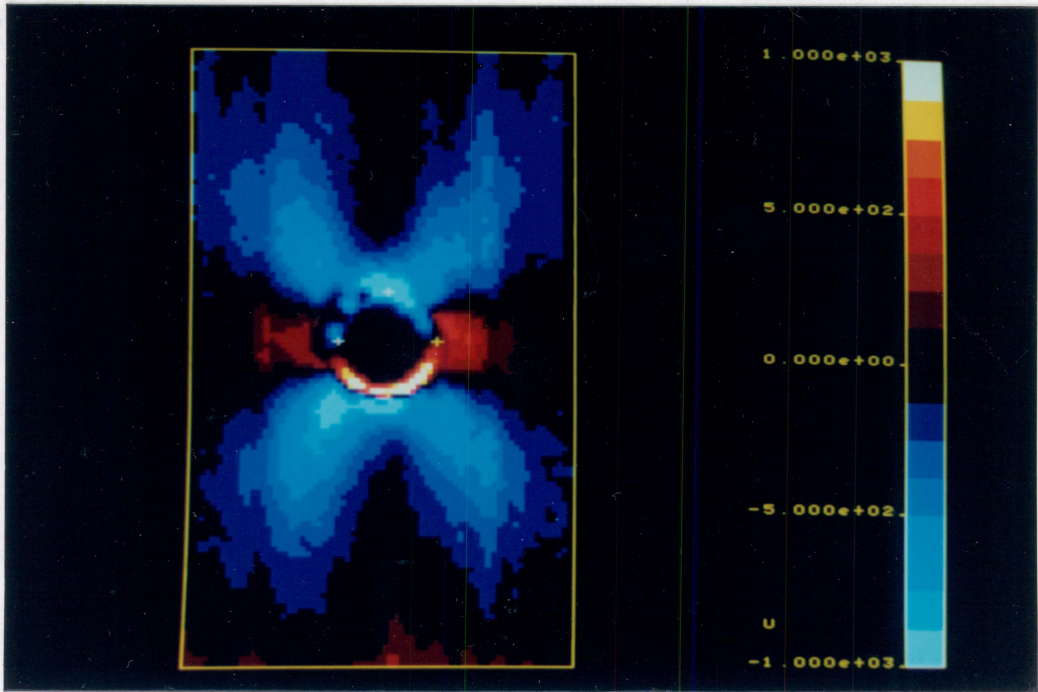
In summary, the statements one can make regarding stress redistribution in the two notched AS4/1808 laminates examined are as follows:

1. Areas of major stress concentration were intrinsically related to the existing damage state.
2. Areas of major stress concentration corresponded to areas of subsequent damage growth.
3. Values of ATC corresponded well with trends in tensile strength during the fatigue lifetime.
4. The nature of stress redistribution in the orthotropic laminate was such that for a large portion of the fatigue lifetime the two ligaments of material adjacent to the notch saw little stress concentration due to the original notch.

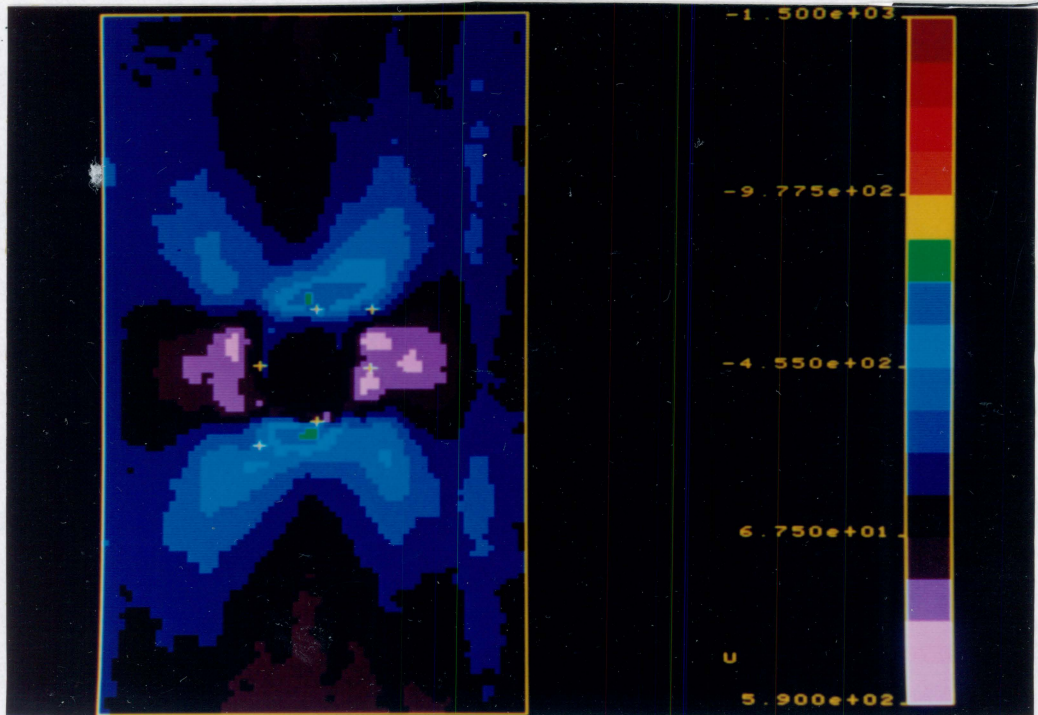
Using SPATE data to predict the tensile strength of specimens is, at best, unreliable. For example, the expected strength increases of the quasi-isotropic specimens in Table 6 were higher than the expected strength increases of the orthotropic specimens. In reality, the orthotropic specimens had higher strength increases than the quasi-isotropic specimens. A possible explanation for this discrepancy is that the interior plies of the laminate may govern strength, particularly when the surface plies are heavily damaged. Hence, stress patterns in the surface plies may lead to inaccurate strength predictions.

The second parameter affecting the damage development and stress redistribution in CFRP laminates is material system. The previous chapter on damage mechanisms described the differences in fatigue response of AS4/3501-6 and AS4/1808 specimens. Presently, stress redistribution mechanisms in center-notched, AS4/3501-6 and AS4/1808, $(0,45,0,-45)_{s4}$ specimens during high-load fatigue will be compared. Up to approximately one third of the fatigue lifetime, there was little difference in their respective SPATE thermographs (compare the AS4/3501-6 thermographs in Figure 53 with the AS4/1808 thermographs in Figure 51 on page 136). At approximately one half of each material's respective fatigue lifetime, though, differences emerged. The most prominent among these was the lack of high stress concentrations near the tips of the 0-deg. tangent cracks in the AS4/3501-6 laminate. (Recall that the 0-deg. tangent cracks were shorter and more similar in length in all four quadrants in the AS4/3501-6 specimens.) There was, overall, a more uniform thermoelastic emission in the two ligaments of material adjacent to the notch in the AS4/3501-6 laminate, leading one to expect higher residual tensile strengths than in the AS4/1808 laminate. It will be shown later that the residual tensile and compressive strengths of middle-life AS4/3501-6 specimens were only slightly higher than their AS4/1808 counterparts.

Next, the effect of cyclic load excursions on stress redistribution in the notched $(0,45,90,-45)_{s4}$ AS4/1808 laminate under the "high" and "low" load levels described earlier. In these cases, compressive failures were precipitated by large amounts of delamination throughout the unsupported gage length, but significant differences were seen in the damage and stress redistribution patterns prior to failure (see Damage Mechanisms).

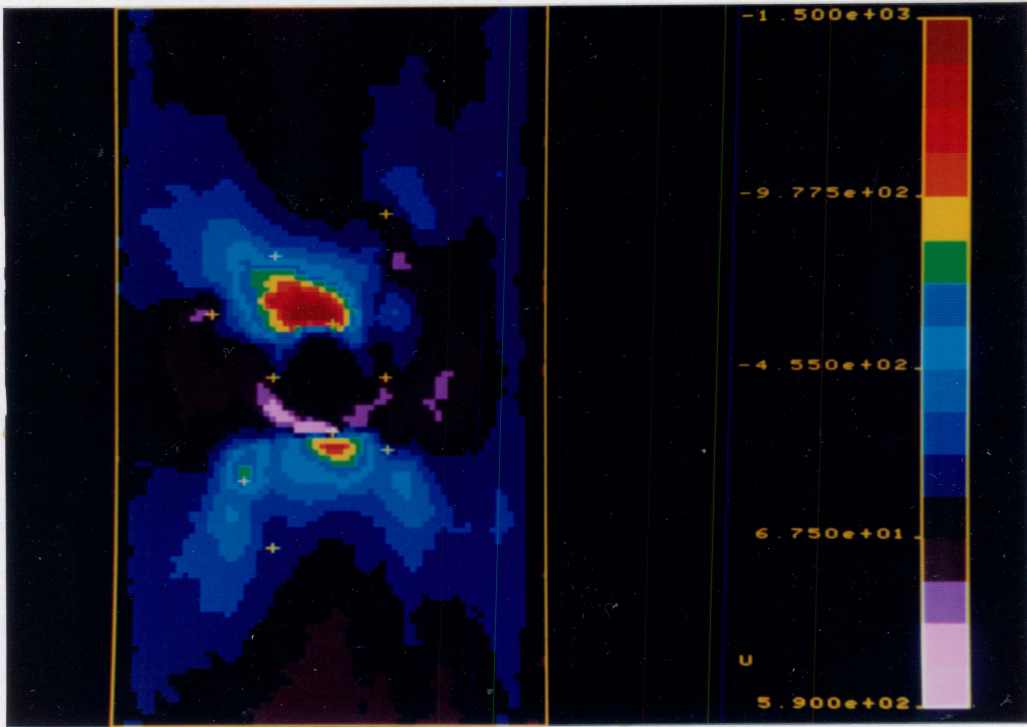


a

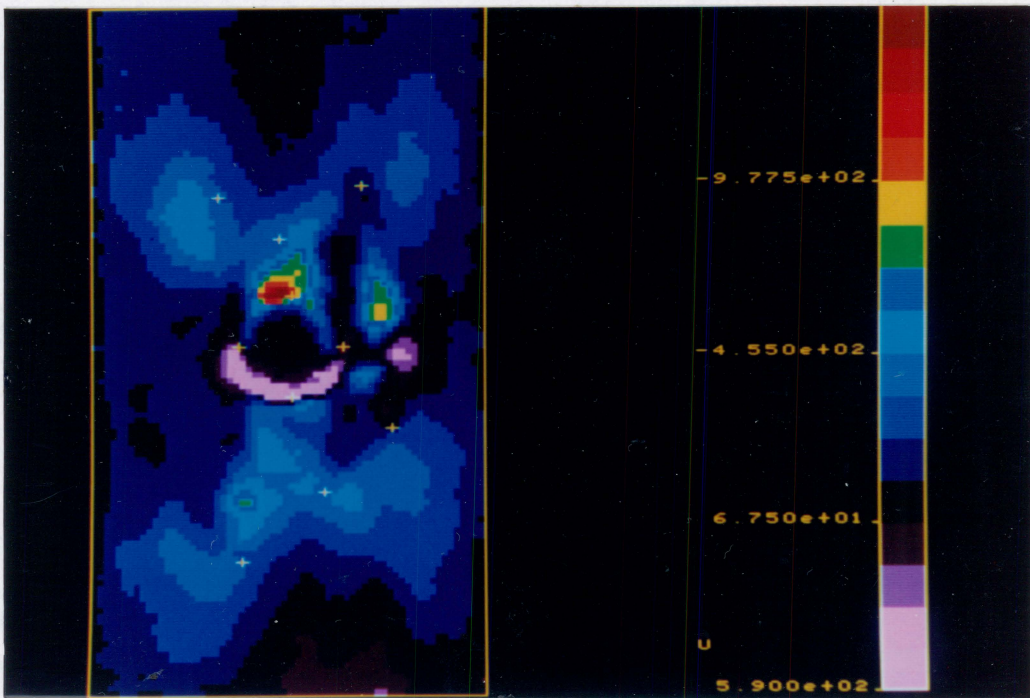


b

Figure 53. SPATE thermographs of four center-notched, AS4/3501-6, (0,45,0,-45)_{s4} specimens during high-load fatigue: (a) undamaged (back); (b) early life (back); (c) middle life (back); (d) late life (back)



c



d

Figure 53. (Concluded)

SPATE thermographs of the low-load specimens taken three times during the fatigue lifetime are shown in Figure 54 for comparison with the high-load specimens shown at comparable fractions of the fatigue lifetime in Figure 49 on page 131. In the early-life thermographs, the primary difference between the load levels was the larger area of reduced ATC adjacent to the notch with the low load level. In both cases, the low ATC area was caused by 0-deg. ply fractures or delaminations under the surface 0-deg. ply (or both). Zero-deg. ply fiber fractures and associated delaminations, which were more likely to form under the high load amplitude, maintained a high stress concentration and resulted in a predominantly transverse direction of damage growth. In the low-load situation, delaminations often occurred in the absence of 0-deg. fiber fractures, resulting in a tendency for longitudinal delamination growth and less stress concentration in the surface ply for most of the fatigue lifetime. This information is supported by the mid-life SPATE thermographs shown in Figure 49c and Figure 54b. In the high-load specimens, the zones of high ATC that shifted in the transverse direction as damage grew away from the notch underwent only a slight change in magnitude throughout the fatigue lifetime. In the low-load specimens, those zones disappeared entirely by mid-life, and reappeared in the last 10 percent of life. The initial decrease and subsequent increase in maximum ATC in the low-load specimens corresponded well with the initial increase and subsequent decrease in residual tensile strength throughout the fatigue lifetime. On the average, the residual tensile strengths of low-load specimens were slightly higher than those of high-load specimens at equal fractions of their respective fatigue lifetimes. Unfortunately, the SPATE data did not represent the entire stress redistribution process in the laminate; only that in the surface plies. For example, the high- and low-load specimen thermographs at mid-life (Figure 49c and Figure 54b) differed, but the residual tensile strengths of these *particular* specimens were nearly identical (both were 119 percent of the average virgin specimen strength).

Another stress redistribution mechanism existing in laminates subjected to compressive load excursions stems from the tendency of damage, particularly delaminations, to initiate and grow fastest near the free surfaces [2,6,108], as described in the chapter on damage mech-

50% COTTON FIBER

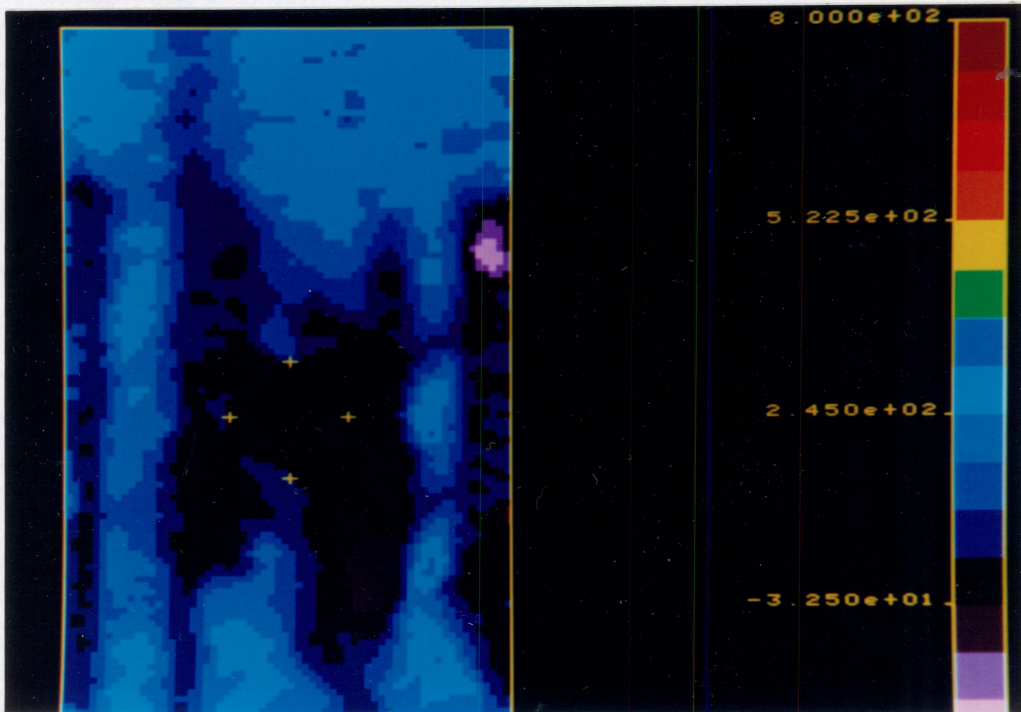
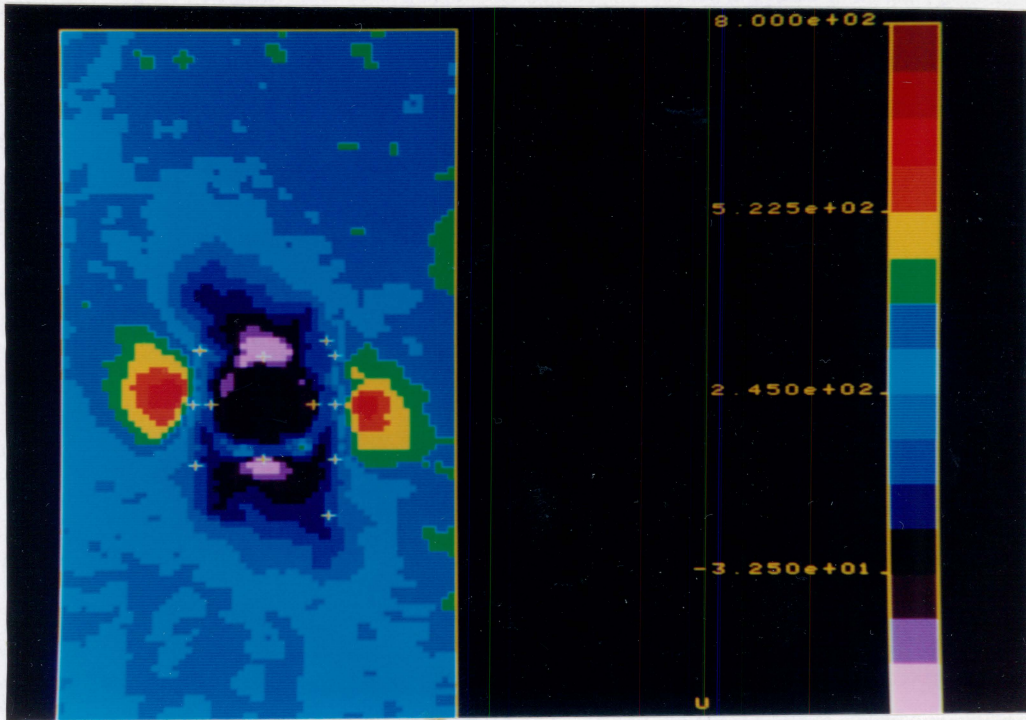
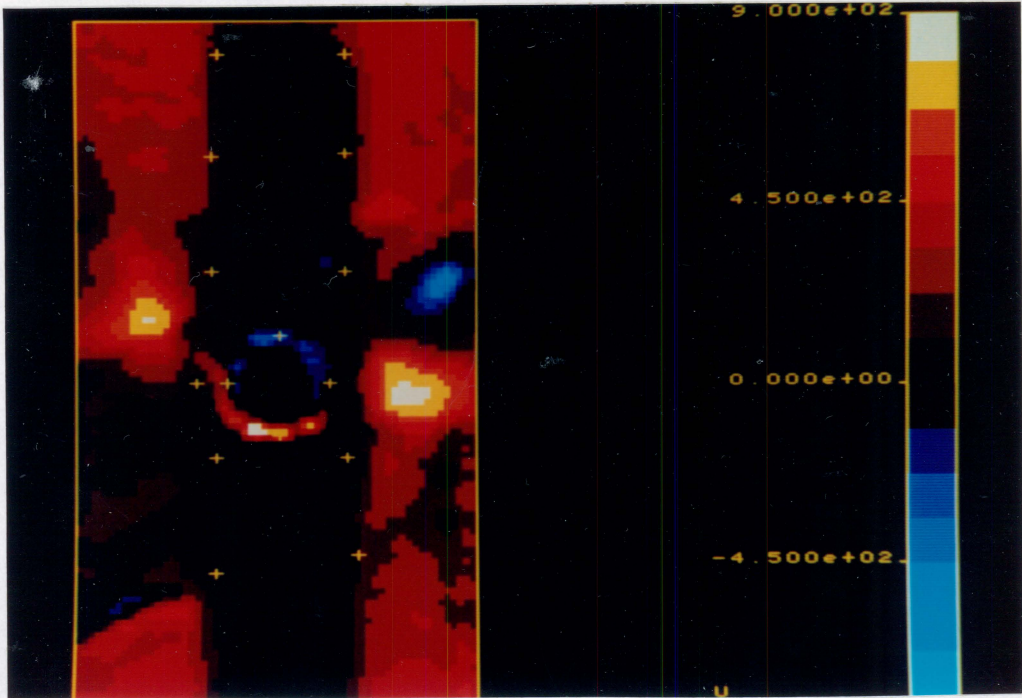


Figure 54. SPATE thermographs of three center-notched, AS4/1808, $(0,45,90,-45)_{s4}$ specimens during low-load fatigue: (a) early life (front); (b) middle life (front); (c) late life (front)

CHIEFTAIN BOND

50% COTTON FIBER



C

Figure 54. (Concluded)

anisms. When delaminated outer plies of a laminate buckle under compressive loading, a greater proportion of the load must be carried by the inner, less-delaminated plies since they possess greater lateral support and stiffness. No experimental, through-the-thickness measurements of stress redistributions were obtained in the present investigation, though such measurements would aid the explanation of many anomalous residual strength results (i.e., those where the stress concentration on the surface ply decreased, but the residual tensile strength did not increase).

Due to the compressive load excursions applied to the specimens in the present investigation, slight imperfections in the material and misalignment of the loading axis caused unsymmetric damage development and stress distributions through the thickness. The associated asymmetry of the specimen's stiffness caused out-of-plane bending (especially under compressive loads), and exaggerated the unequal rates of damage development on the opposing surfaces of the specimen. Compared to specimens with a centrally-located notch, damage-induced bending was more prevalent in specimens with double-edge notches. For example, compare the SPATE thermographs of the front and back surfaces of a DEN, AS4/3501-6, (0,45,0,-45)_{s4} laminate near the end of its high-load fatigue life with a thermograph of an undamaged specimen (Figure 55). Under a fully-reversed cyclic load history, fiber fractures and delaminations that initiated on the front surface 0-deg. ply led to larger local compressive strains and, consequently, a faster local damage growth rate. Near impending laminate failure — when the thermographs in Figure 55 were obtained — the front surface 0-deg. ply carried little load in the area between the notches, while the back surface 0-deg. ply remained relatively intact. Fatigue failure occurred when the interior plies, beginning with the side under the most compression, failed during a compressive load excursion.

Aside from the matter of global laminate bending, the fatigue response of laminates with DEN or CN notch configurations is rather invariant, especially in the late portion of life when additional damage growth is influenced more by the earlier damage pattern than the initial stress concentration caused by the notch itself. Indeed, Morton et al. [109] have shown that circular holes and sharp slits result in different early-life (and undamaged) strengths, but in-

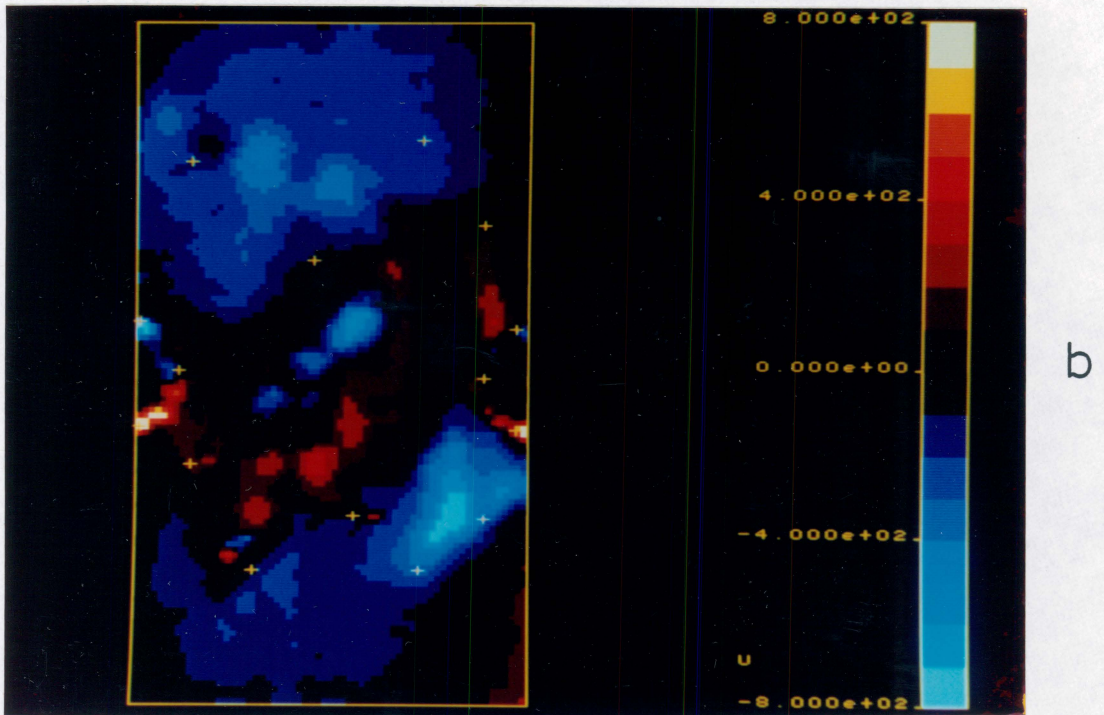
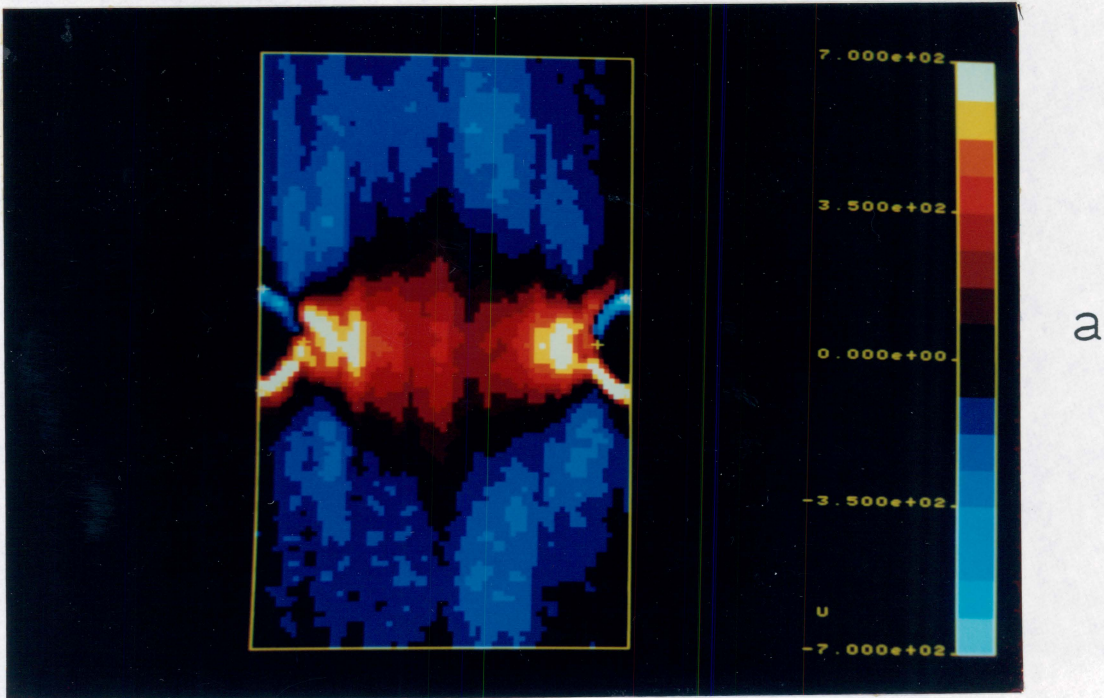
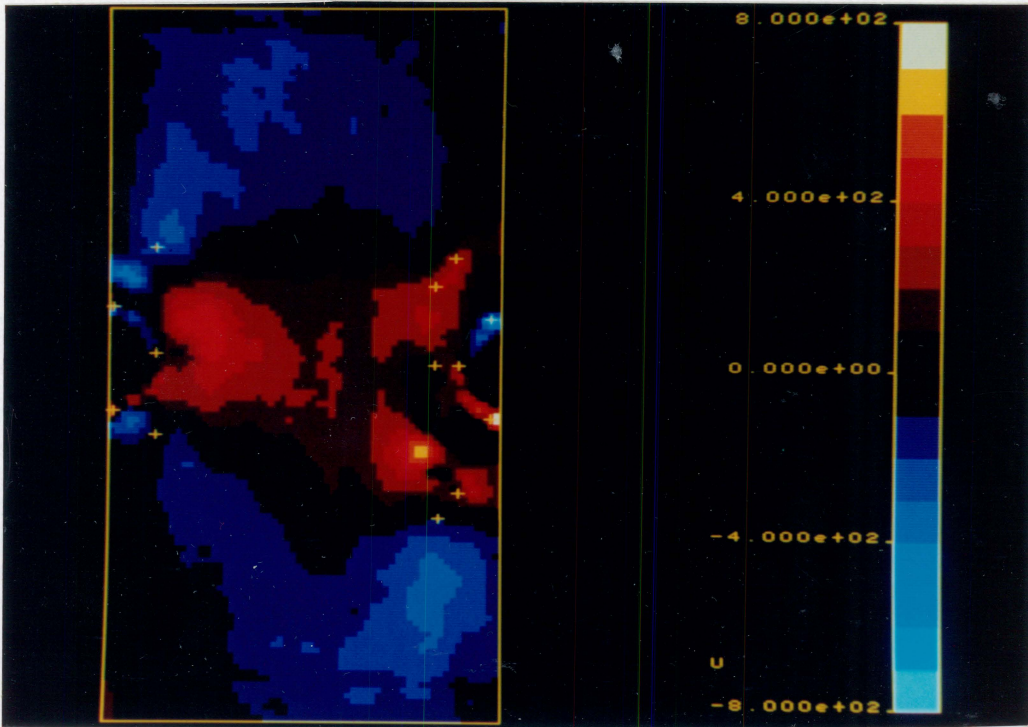


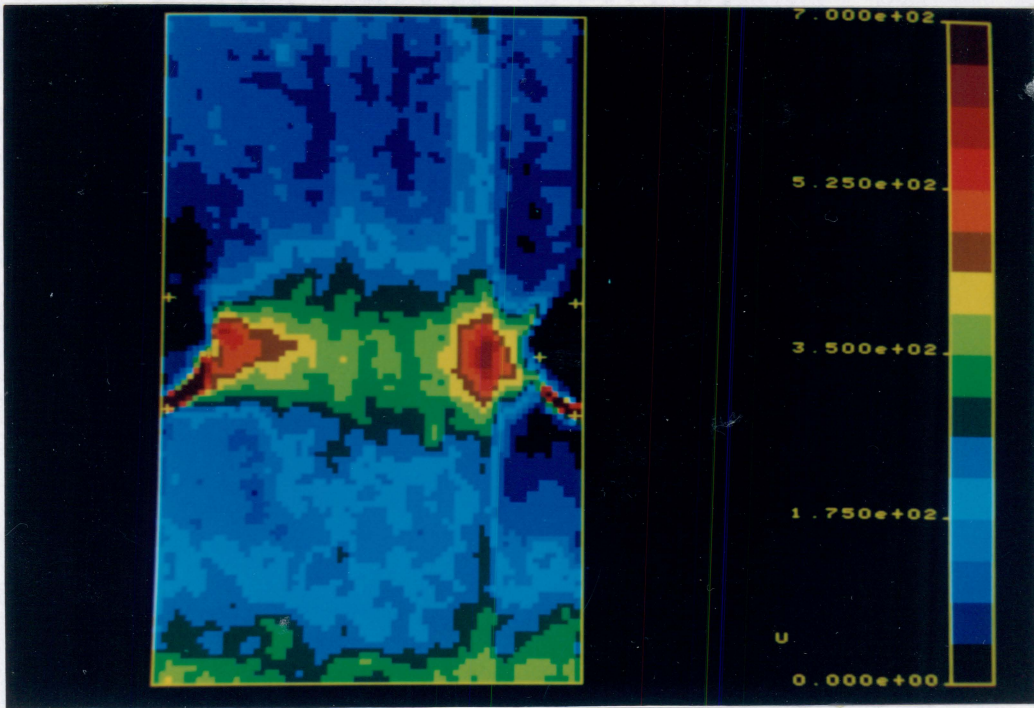
Figure 55. SPATE thermographs of AS4/3501-6, (0,45,0,-45)_{s4}, DEN specimens during high-load fatigue: (a) no. 3-13, back, undamaged; (b) no. 6-4, front, near failure; (c) no. 6-4, back, near failure



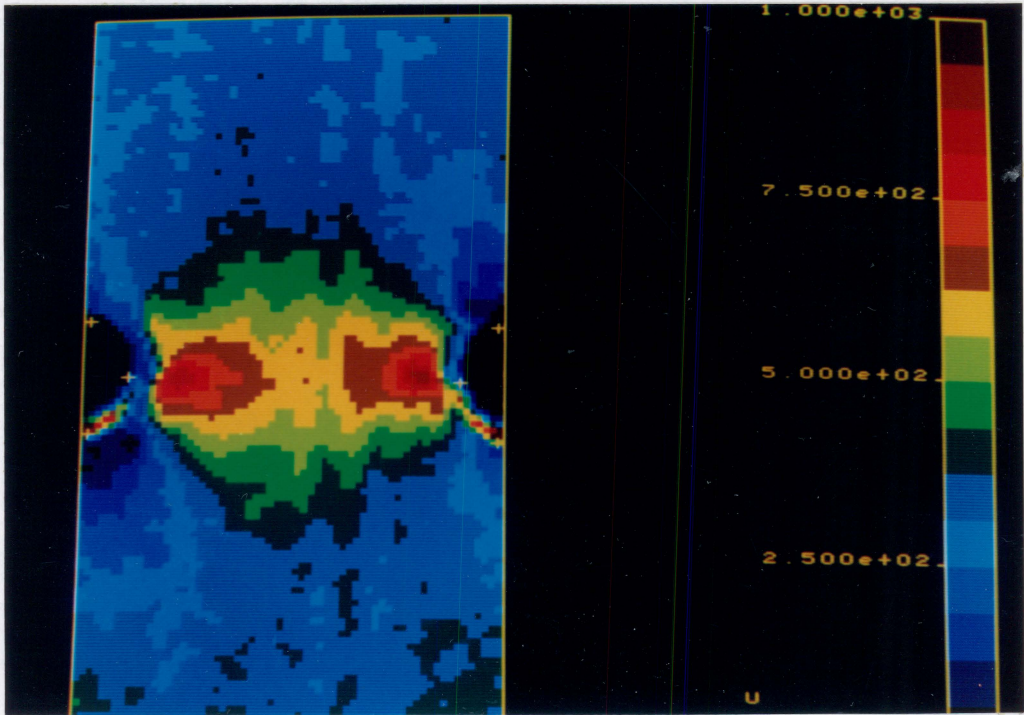
C

Figure 55. (Concluded)

creasingly similar strengths later in the fatigue lifetime. In the present study, high-load fatigue damage development and stress redistribution data for AS4/1808, (0,45,90,-45)_{s4} specimens with double semi-circular edge notches were compared to the data obtained from center-notched specimens. It was found that damage initiation and growth for the two notch configurations were nearly the same, as was the failure mode. With a few exceptions, DEN specimens had slightly more longitudinal delamination growth and slightly higher residual tensile and compressive strengths than their center-notched counterparts at comparable fractions of their respective fatigue lifetimes. A sequence of SPATE thermographs of DEN specimens during high-load fatigue development shows the effect of the increased longitudinal delamination on the surface stress pattern (Figure 56). As damage grew, the two regions of high stress initially located adjacent to the notches moved toward the centerline of the specimen and eventually coalesced near fatigue failure.



a



b

Figure 56. SPATE thermographs of four double-edge-notched, AS4/1808, (0,45,90,-45)_{S4} specimens during high-load fatigue: (a) undamaged (back); (b) early life (front); (c) middle life (front); (d) late life (front).

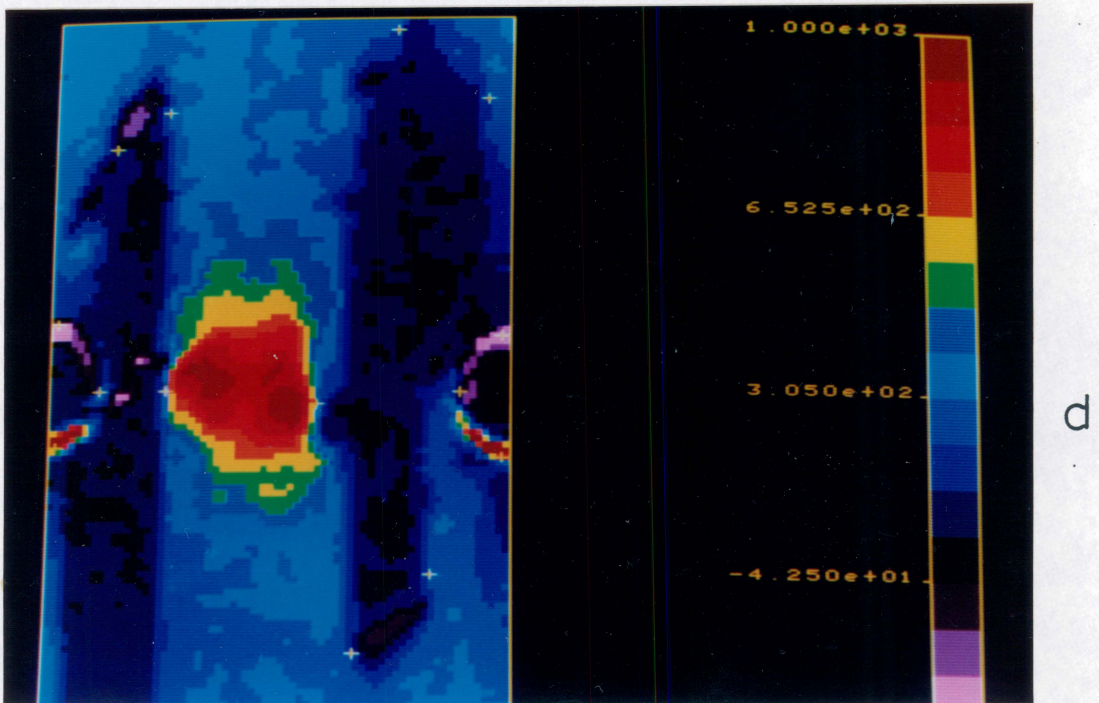
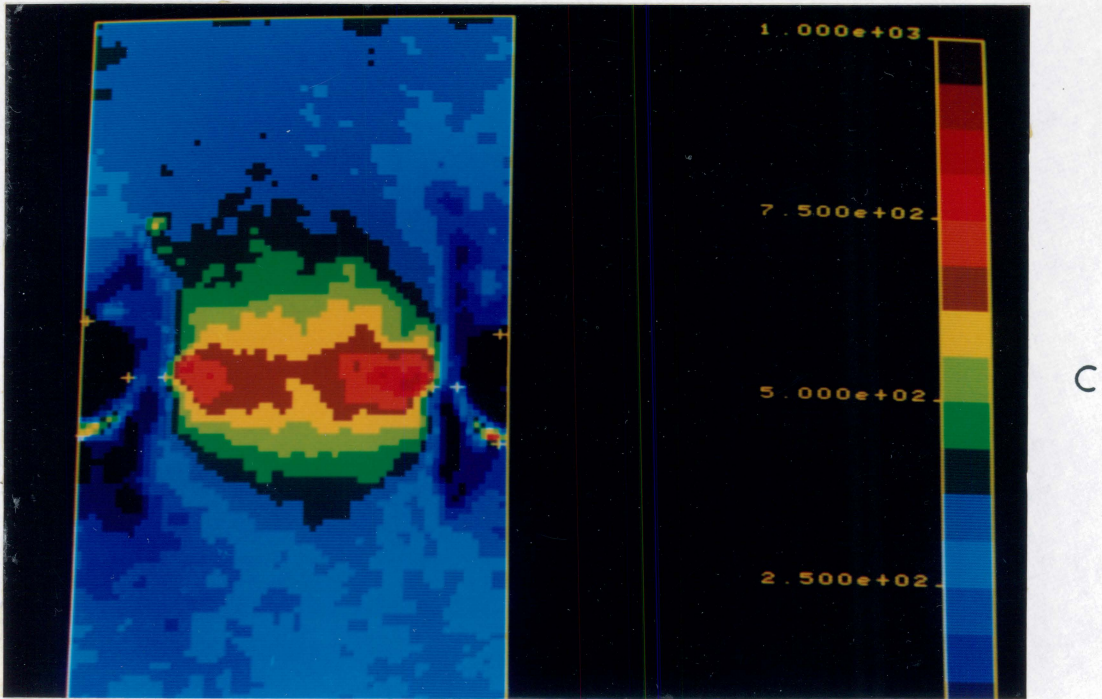


Figure 56. (Concluded)

Chapter VI

Residual Strength

Residual tensile and compressive strengths (S_t and S_c , respectively) and stiffnesses (E_t and E_c , respectively) measured at the early, middle, and late stages of fatigue life were normalized by their respective values in virgin specimens given in Table 3 and Table 5. Plots of normalized tensile and compressive strengths versus the estimated fraction of fatigue life are superposed so that trends in the two components of strength can be easily compared. Cyclic load amplitudes, normalized by the tensile and compressive strengths of virgin specimens (refer to Table 4), are indicated on the vertical axes of the strength graphs as points of reference. The discussion of residual strength focuses on the data for six test types studied in detail: 1808-A-CN (high and low load levels); 1808-A-DEN (high load level); 1808-B-CN (high and low load levels); and 3501-B-CN (high load level). Residual strength data for the center-notched AS4/1808 specimens are the most extensive. Therefore, strength data for the DEN and AS4/3501-6 specimens will be compared to this best-characterized data set.

6.1 AS4/1808, Quasi-Isotropic Laminate

Normalized residual stiffness and strength data for center-notched, AS4/1808, (0,45,90,-45)_{s4} specimens during high- and low-load fatigue are given in Table 7. The strength data are presented graphically in Figure 57 and Figure 58. Averaged, normalized strengths of early-, middle-, and late-life specimens are listed in Table 8 for comparison with other test types.

The tensile strength increased for the early- and middle-life measurement points, and decreased for the late-life measurement point. High-load specimens had lower residual tensile strengths than low-load specimens in the second half of the lifetime, perhaps due to the larger number of broken 0-deg. plies near the notch in high-load specimens during this part of life. The compressive strength decreased monotonically throughout the fatigue lifetime. Values of residual compressive strength between the two loading regimes were comparable until impending failure. At that time, delaminations had grown larger and residual compressive strengths had decreased more in low-load specimens than in high-load specimens.

The rate of compressive strength change during high-load fatigue was similar to the rate of stiffness change (Figure 22); rapid until the end of stage I, slower in stage II, and rapid once again in stage III. The sharp decline in stiffness near the middle of life in low-load tests did not seem to cause any anomalies in the middle-life residual strength measurements. This suggests that the damage that caused the stiffness change (surface 0-deg. ply delamination) was inconsequential to the strength. Judging by the proximity of the late-life compressive strengths to the maximum compressive load excursions ("C," on the graphs), one may conclude that these specimens clearly failed in compression. The failure mode transition that manifested itself after approximately half of the fatigue lifetime in high-load specimens caused two fiber fracture dominated specimens to have significantly lower residual tensile strengths than the remaining delamination dominated specimens during that time period (these were the two tensile data points below 1.0 in the high-load figure).

Table 7. Normalized residual stiffness and strength of center-notched, AS4/1808, (0,45,90,-45)_{s4} specimens

Spcmn. I.D.	Load Level	No. Cycles	Est. % Life	E_r/E_r^0	E_c/E_c^0	S_r/S_r^0	S_c/S_c^0
3-12	high	1305	5-10	.930	.955	1.11	—
7-4	high	1000	5-10	.953	.950	1.03	—
8-10	high	1000	5-10	.960	.961	1.06	—
2-1	high	904	5-10	.935	.924	—	.839
8-9	high	1000	5-10	.932	.953	—	.856
7-3	high	1000	5-10	.956	.964	—	.863
3-2	high	9240	40-60	.850	.918	1.19	—
8-3	high	3500	40-60	.878	.892	.963	—
7-2	high	3500	40-60	.908	.920	1.16	—
3-14	high	9400	40-60	.851	.892	—	.896
8-12	high	3500	40-60	.899	.902	—	.808
7-14	high	2500	40-60	.804	.808	—	.750
2-3	high	11024	≥90	.674	.732	.883	—
8-11	high	6300	≥90	.910	1.58	1.02	—
8-5	high	16514	≥90	.716	.810	1.01	—
2-2	high	8800	≥90	.821	1.14	—	.628
8-1	high	51627	≥90	.688	.729	—	.711
8-4	high	11811	≥90	.637	.583	—	.706
6-6	low	25000	5-10	.917	.910	1.10	—
7-1	low	25000	5-10	.893	.919	1.17	—
7-8	low	24000	5-10	.895	.893	1.10	—
6-4	low	61500	5-10	.876	.868	—	.852
7-7	low	25000	5-10	.901	.898	—	.810
7-6	low	50000	5-10	.919	.898	—	.981
6-10	low	1443000	40-60	.655	.612	1.19	—
7-9	low	1052000	40-60	.757	.786	1.24	—
8-8	low	595000	40-60	.747	.741	1.18	—
6-12	low	2792000	40-60	.724	.771	—	.769
7-11	low	2275240	40-60	.734	.725	—	.795
7-5	low	931200	40-60	.717	.689	—	.853
4-9	low	2115050	≥90	.399	.325	1.18	—
7-10	low	3465800	≥90	.507	.500	1.16	—
7-13	low	453910	≥90	.468	.447	1.03	—
2-15	low	2215030	≥90	.489	.408	—	.541
7-12	low	1253400	≥90	.614	.691	—	.615
8-2	low	1310000	≥90	.679	.744	—	.599

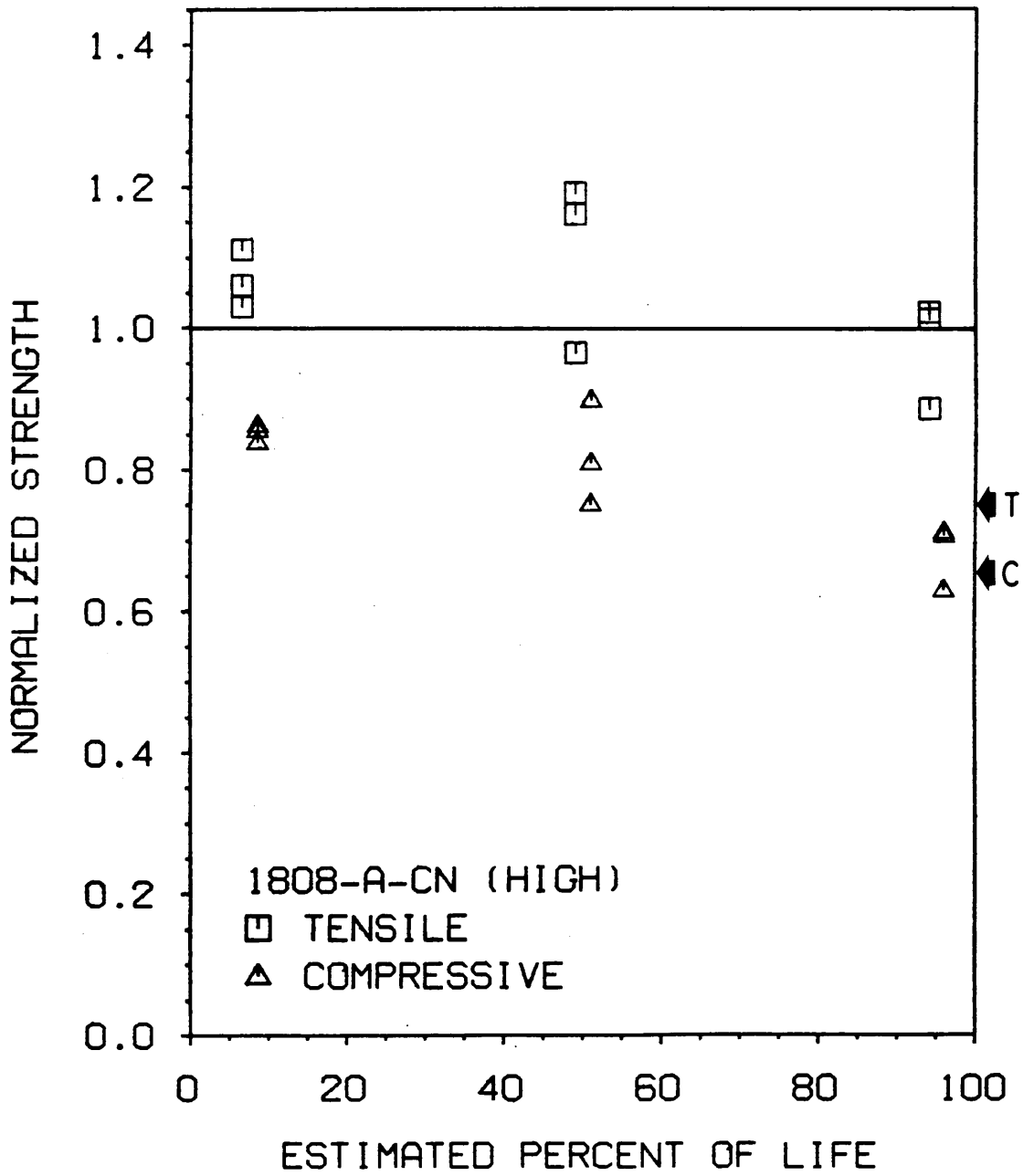


Figure 57. Normalized residual strength of center-notched, AS4/1808, (0,45,90,-45)_{s4} specimens during high-load fatigue

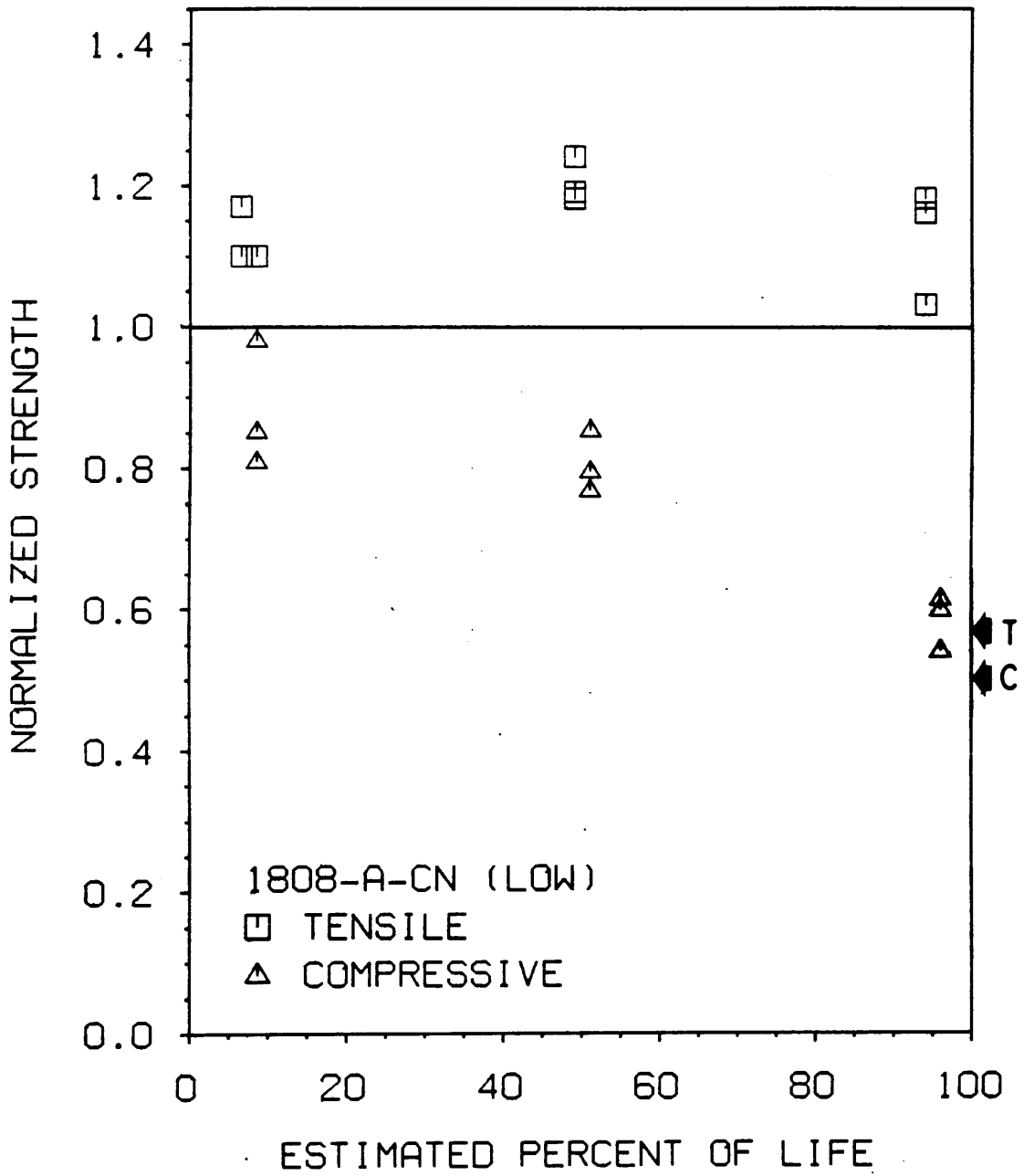


Figure 58. Normalized residual strength of center-notched, AS4/1808, (0,45,90,-45)_{s4} specimens during low-load fatigue

Table 8. Averaged, normalized, residual strength data

Specimen Type	Load Level	S_r/S_r^*			S_c/S_c^*		
		5-10% Life	40-60% Life	≥90% Life	5-10% Life	40-60% Life	≥90% Life
1808-A-CN	High	1.07 (3)	1.10 (3)	.971 (3)	.853 (3)	.818 (3)	.682 (3)
	Low	1.12 (3)	1.20 (3)	1.12 (3)	.881 (3)	.806 (3)	.585 (3)
1808-A-DEN	High	1.08 (3)	1.25 (3)	.998 (3)	.885 (3)	.822 (3)	.678 (2)
1808-B-CN	High	1.12 (3)	1.27 (3)	1.22 (3)	1.09 (3)	.934 (3)	.882 (2)
	Low	1.14 (3)	1.23 (3)	1.13 (3)	1.11 (3)	.998 (3)	.820 (2)
3501-B-CN	High	1.08 (3)	1.30 (3)	1.28 (2)	1.09 (3)	1.02 (2)	.879 (1)

* Numbers in parentheses indicate the number of tests performed.

The fracture appearance of these specimens after strength measurements at three stages of fatigue damage development and under both load levels were essentially similar. Typically, the final fracture paths in the 0-deg. plies passed through the center of the notch, predominantly perpendicular to the load axis. The final tensile fracture paths in specimens with 0-deg. ply fracture paths caused by fatigue grew in the transverse direction from the points where the earlier ply fractures stopped. Specimens with larger delaminations had relatively irregular fracture surfaces. The extent of pre-failure delamination was most evident in the post-fracture appearance of the compression specimens. Delaminated plies were free to buckle and, therefore, did not fracture as readily as the more constrained, undelaminated plies.

The double-edge notched specimens under the high load level behaved similarly to the center-notched specimens (Table 8, Table 9, and Figure 59). Except for the middle-life tensile strength — which was slightly higher in DEN specimens — all strength measurements were nearly equivalent in the CN and DEN notch configurations. Fracture appearances of DEN specimens were analogous to those in CN specimens. High-load DEN specimens on the “high-load” side of the damage mode transition had less delamination those on the “low-load” side of the transition, though no differences as clear as those seen in the post-fatigue-failure radiographs (Figure 36 on page 101) were seen among the residual strength specimens. As evidenced by the merging of residual compressive strengths and the maximum compressive fatigue load at the end of life, the DEN specimens failed in compression.

6.2 AS4/1808, Orthotropic Laminate

Normalized stiffness and strength data for center-notched, AS4/1808, (0,45,0,-45)_{s4} specimens are listed in Table 10. The averaged, normalized strengths are listed in Table 8. Figure 60 and Figure 61 illustrate the strength data graphically for the high and low load levels, respectively.

Table 9. Normalized residual stiffness and strength of double-edge-notched, AS4/1808, (0,45,90,-45)_{s4} specimens

Spcmn. I.D.	Load Level	No. Cycles	Est. % Life	E_r/E_r^0	E_c/E_c^0	S_r/S_r^0	S_c/S_c^0
3-7	high	800	5-10	.981	.970	1.02	—
4-4	high	904	5-10	.986*	.977*	1.14	—
4-13	high	904	5-10	.980*	.977*	1.08	—
3-1	high	960	5-10	.992	.969	—	.821
4-2	high	703	5-10	.986*	.984*	—	.891
4-1	high	904	5-10	.984*	.985*	—	.942
3-5	high	8600	40-60	.940	.940	1.29	—
4-8	high	9000	40-60	.950*	.943*	1.25	—
4-11	high	10000	40-60	.927*	.922*	1.20	—
3-3	high	8300	40-60	.951	.921	—	.820
4-7	high	4750	40-60	.942*	.946*	—	.846
4-14	high	3100	40-60	.928*	.932*	—	.799
2-12	high	5824	≥90	.643	.447	1.09	—
4-6	high	8070	≥90	.825*	.835*	.946	—
4-5	high	13960	≥90	.758*	.804*	.958	—
4-3	high	32630	≥90	.751	.584	—	.730
4-12	high	83860	≥90	.742*	.683*	—	.626

* Average stiffness, computed by averaging strains from front and back extensometers.

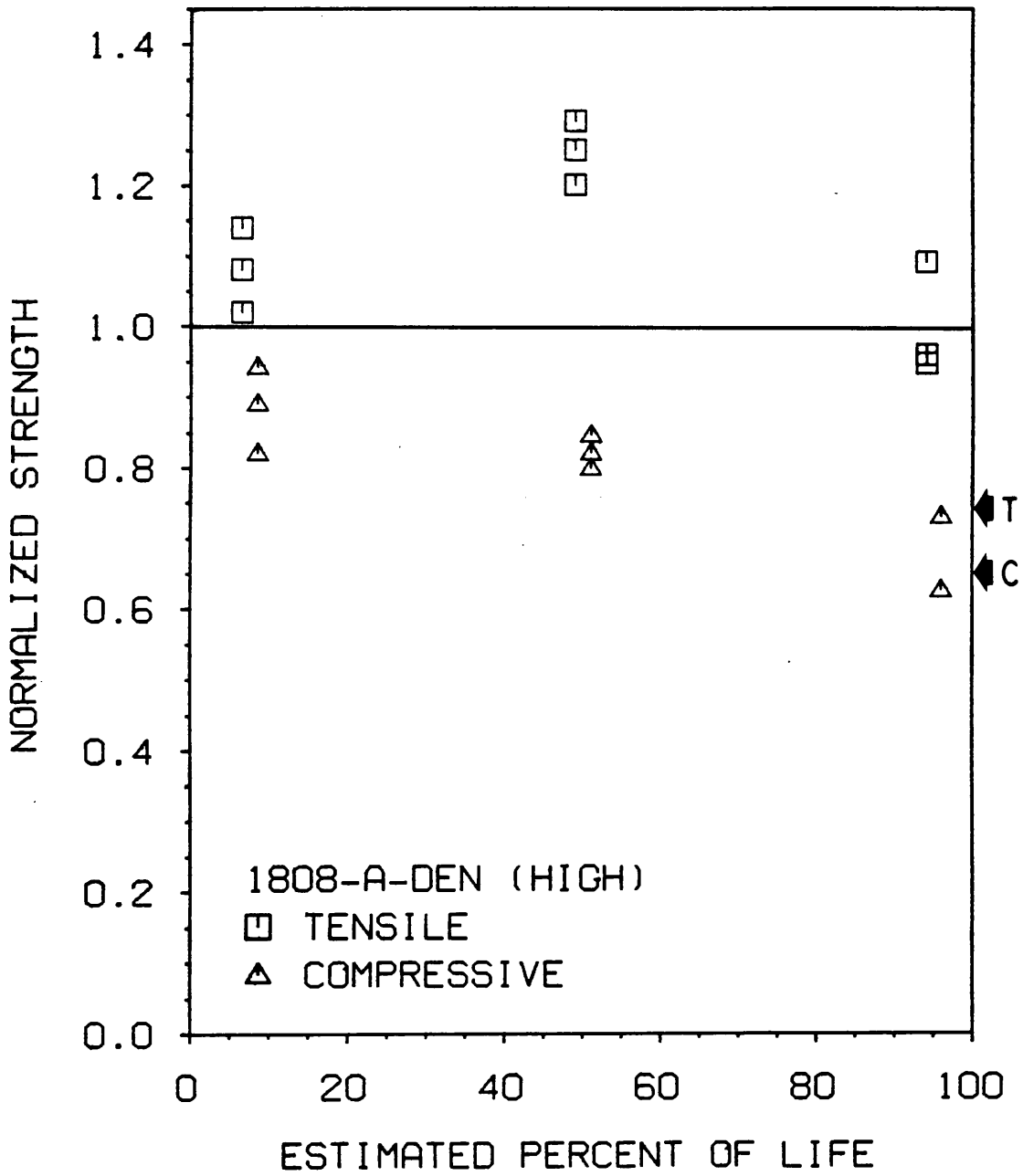


Figure 59. Normalized residual strength of double-edge-notched, AS4/1808, (0,45,90,-45)_{s4} specimens during high-load fatigue

Table 10. Normalized residual stiffness and strength of center-notched, AS4/1808, (0,45,0,-45)_{s4} specimens

Spcmn. I.D.	Load Level	No. Cycles	Est. % Life	E_t/E_t^o	E_c/E_c^o	S_t/S_t^o	S_c/S_c^o
3-3	high	250	5-10	.935	.923	1.16	—
6-8	high	616	5-10	.941	.946	1.14	—
6-14	high	200	5-10	.953	.993	1.07	—
3-5	high	350	5-10	.938	.941	—	1.04
6-2	high	690	5-10	.944	.959	—	1.11
6-10	high	200	5-10	.948	.966	—	1.12
3-7	high	3708	40-60	.793	.770	1.42	—
6-6	high	3360	40-60	.799	.857	1.13	—
4-8	high	4340	40-60	.748	.759	1.25	—
3-9	high	6570	40-60	.790	.871	—	1.02
6-12	high	3450	40-60	.845	.941	—	.879
4-2	high	3930	40-60	.805	.866	—	.904
2-18	high	10460	≥90	.673	.755	1.10	—
5-6	high	6880	≥90	.700	.610	1.27	—
4-14	high	8410	≥90	.657	.586	1.29	—
4-7	high	5760	≥90	.663	.730	—	.884
4-12	high	6900	≥90	.594	.570	—	.880
5-9	low	25860	5-10	.899	.894	1.16	—
4-11	low	10500	5-10	.898	.901	1.10	—
4-9	low	22000	5-10	.901	.906	1.17	—
5-13	low	60000	5-10	.890	.887	—	1.13
4-1	low	25000	5-10	.898	.901	—	1.06
4-3	low	31400	5-10	.902	.910	—	1.15
5-2	low	100000	40-60	.875	.893	1.26	—
5-1	low	230500	40-60	.801	.781	1.21	—
4-6	low	166000	40-60	.801	.809	1.22	—
5-4	low	188450	40-60	.798	.722	—	1.03
4-10	low	100010	40-60	.810	.838	—	1.03
5-10	low	100000	40-60	.706	.711	—	.933
3-1	low	291000	≥90	.524	.460	1.10	—
5-14	low	234900	≥90	.652	.624	1.06	—
4-5	low	524000	≥90	.530	.465	1.22	—
5-5	low	782910	≥90	.684	1.09	—	.960
6-4	low	255210	≥90	.582	.492	—	.679

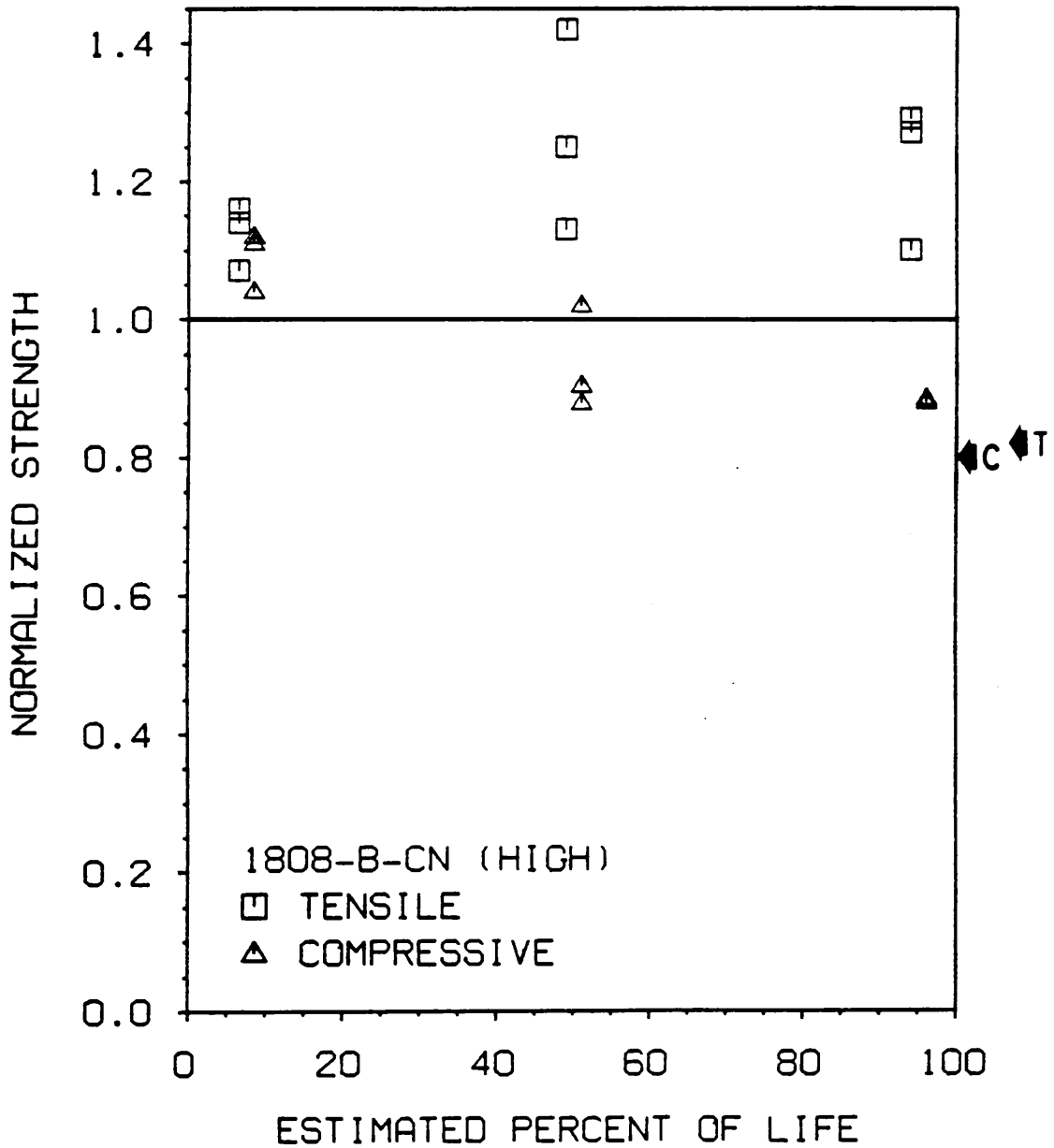


Figure 60. Normalized residual strength of center-notched, AS4/1808, (0,45,0,-45)_{s4} specimens during high-load fatigue

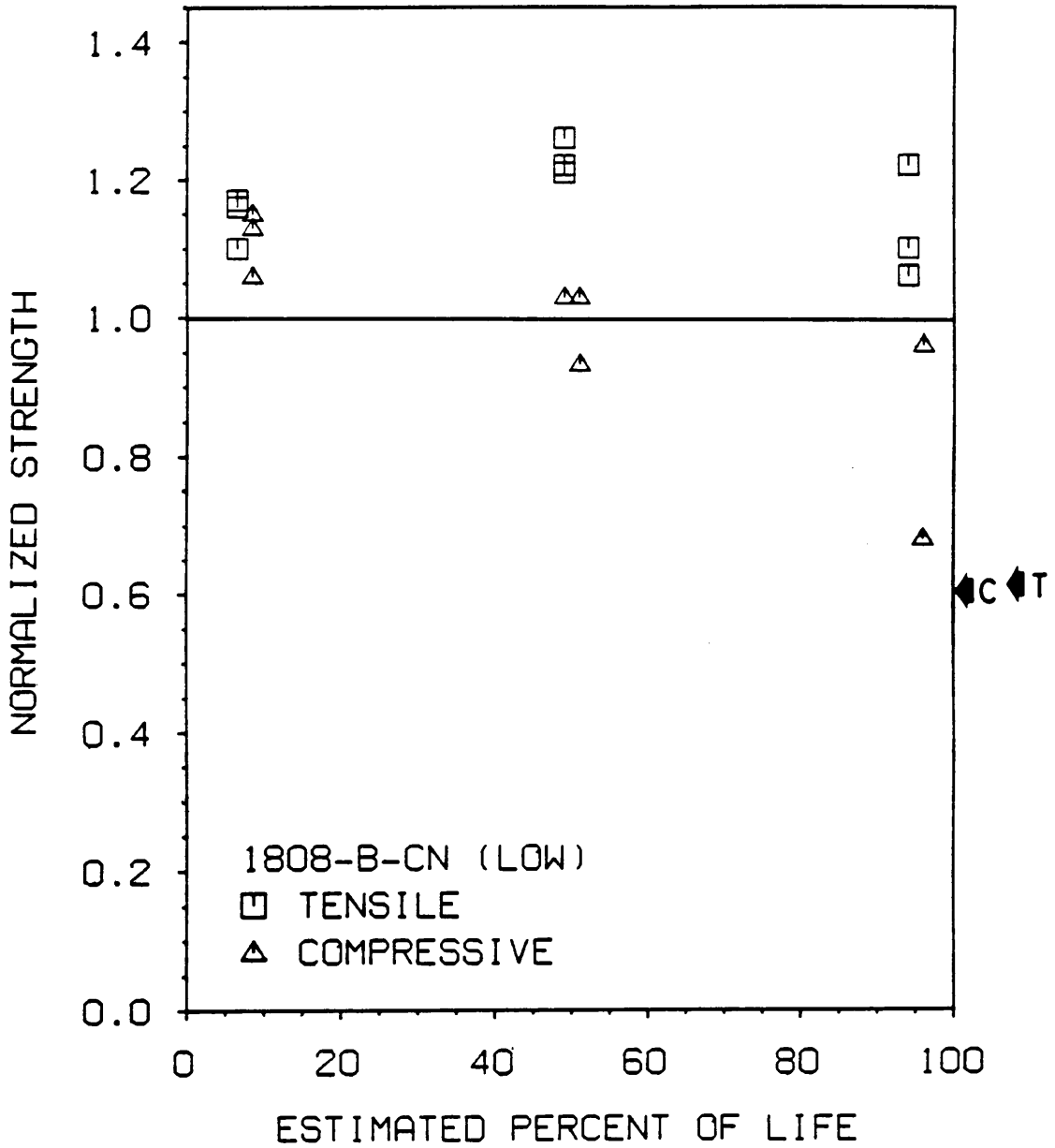


Figure 61. Normalized residual strength of center-notched, AS4/1808, (0,45,0,-45)_{s4} specimens during low-load fatigue

The tensile strengths of high- and low-load specimens increased approximately the same amount at the early- and middle-life measurement points. By the end of high- and low-load fatigue lifetimes, tensile strengths decreased, but remained above 1.0. The averaged tensile strengths of middle- and late-life specimens were higher during high-load fatigue than during low-load fatigue, though the data overlapped significantly. Due to the greater localization of damage in variable locations in high-load specimens, there was more scatter in the high-load residual strength data.

The compressive strengths of high- and low-load specimens both increased at the early-life measurement point, and decreased somewhat linearly with respect to cycles after that time. During the period when the normalized compressive strength was greater than 1.0, damage around the notch was comprised primarily of matrix cracks. Only after the appearance of delaminations did the compressive strength decrease. Compressive strengths were slightly higher in low-load specimens than in high-load specimens at the early- and middle-life measurement points, though the differences were not very significant. Reduced compressive strengths in the second half of life caused compressive fatigue failures under both loading regimes. The lower compressive strength of low-load specimens near fatigue failure could be related to the greater extent of delaminations in those specimens.

Much can be learned about the effect of fatigue damage on the failure mode in residual strength tests by examining the fracture surfaces after failure. The appearance of internal 0-deg. plies was particularly interesting since it is these plies that apparently controlled fracture (the exterior plies were usually replete with through-the-thickness fiber fractures and delaminations, and were difficult to characterize because of their highly variable appearance). Schematic illustrations of the location of fracture and delamination of the internal 0-deg. plies in center-notched, AS4/1808, (0,45,0,-45)_{s4} laminates after tensile and compressive strength measurements are shown (to scale) in Figure 62. As fatigue damage increased, the tensile fracture path of the internal 0-deg. plies shifted farther from the transverse centerline. Apparently, the tensile fracture process began near the tips of the 0-deg. cracks tangent to the hole in the even quadrants, near the highly-stressed areas seen in the SPATE patterns. In

$(0,45,0,-45)_{S4}$

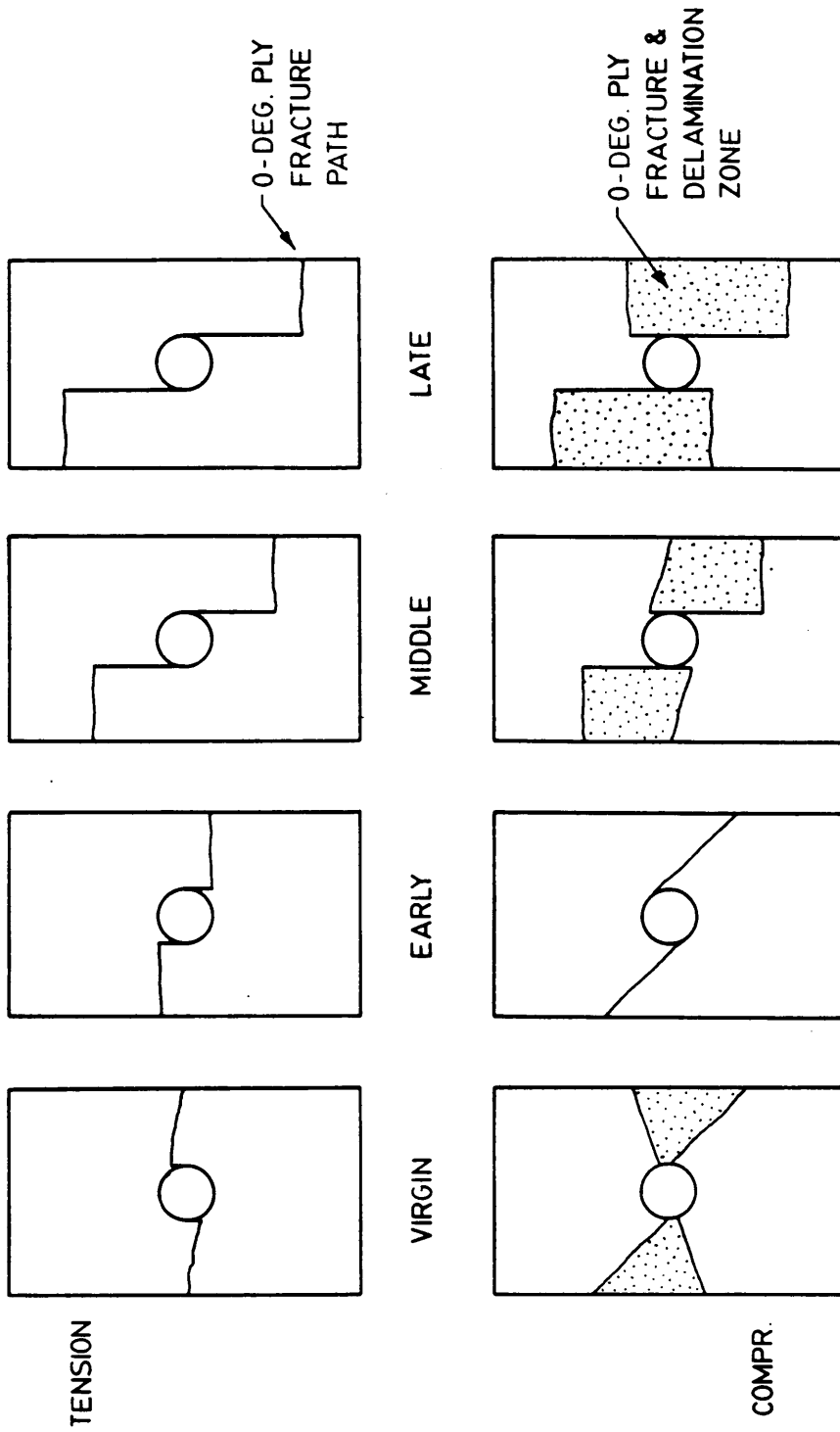


Figure 62. Schematic illustration of 0-deg. ply fracture and delamination in AS4/1808, $(0,45,0,-45)_{S4}$ specimens after residual strength tests

terms of the fracture mode, the damage pattern in these fatigue-damaged specimens could effectively be replaced by a slanted slit with the two ends of the slit located at the tips of the 0-deg. tangent cracks. Since the growth of the 0-deg. tangent cracks slowed in the second half of the lifetime, the location of fracture also remained nearly the same. Therefore, near the end of life, local stress redistribution mechanisms must have played a more active role in strength reduction than global stress redistribution mechanisms.

In residual compressive strength specimens, there were some radical failure mode changes that may explain the unusual residual compressive strength characteristics of this laminate. In virgin specimens, there was a mixed mode of failure in compression. One mode consisted of buckling and delamination of all 0-deg. plies along the transverse centerline. The other failure mode consisted of shear-kinking with little delamination along a -45-deg. path tangent to the notch. The early-life specimens, which were the strongest of all in compression, almost always failed in the shear mode. The middle- and late-life specimens underwent delaminations and 0-deg. ply fractures in the two longitudinal ligaments of material adjacent to the notch. The longitudinal shift of the fracture locus in compression tests was less extreme than in tension tests.

6.3 AS4/3501-6, Orthotropic Laminate

Normalized residual stiffness and strength data for center-notched, AS4/3501-6, (0,45,0,-45)_{s4} specimens under the high load level are listed in Table 8 and Table 11. The strength data are graphically represented in Figure 63. Overall, the residual strength behavior of AS4/3501-6, (0,45,0,-45)_{s4}, CN specimens was similar to analogous AS4/1808 specimens at the same load level. Rapid increases in tensile and compressive strengths at the early-life measurement point indicated that strength at this time in life was controlled by the relaxed stress concentration near the notch, and not by delaminations. Later in life, lower

Table 11. Normalized residual stiffness and strength of center-notched, AS4/3501-6, (0,45,0,-45)_{s4} specimens

Spcmn. I.D.	Load Level	No. Cycles	Est. % Life	E_r/E_0^p	E_c/E_0^c	S_r/S_0^p	S_c/S_0^c
4-18	high	114	5-10	.952	.949	1.04	—
9-9	high	2000	5-10	.945	.935	1.07	—
9-5	high	600	5-10	.890	.902	1.12	—
6-11	high	907	5-10	.954	.952	—	1.11
9-7	high	470	5-10	.931	.943	—	1.10
9-1	high	770	5-10	.945	.936	—	1.05
4-17	high	5000	40-60	.890	.902	1.18	—
9-8	high	5000	40-60	.804	.842	1.34	—
9-10	high	9640	40-60	.804	.743	1.38	—
6-3	high	2947	40-60	.889	.932	—	.956
9-14	high	3860	40-60	.844	.810	—	1.08
6-9	high	13820	≥90	.600	.497	1.23	—
9-6	high	13000	≥90	.628	.480	1.32	—
3-7	high	13190	≥90	.611	.541	—	.879

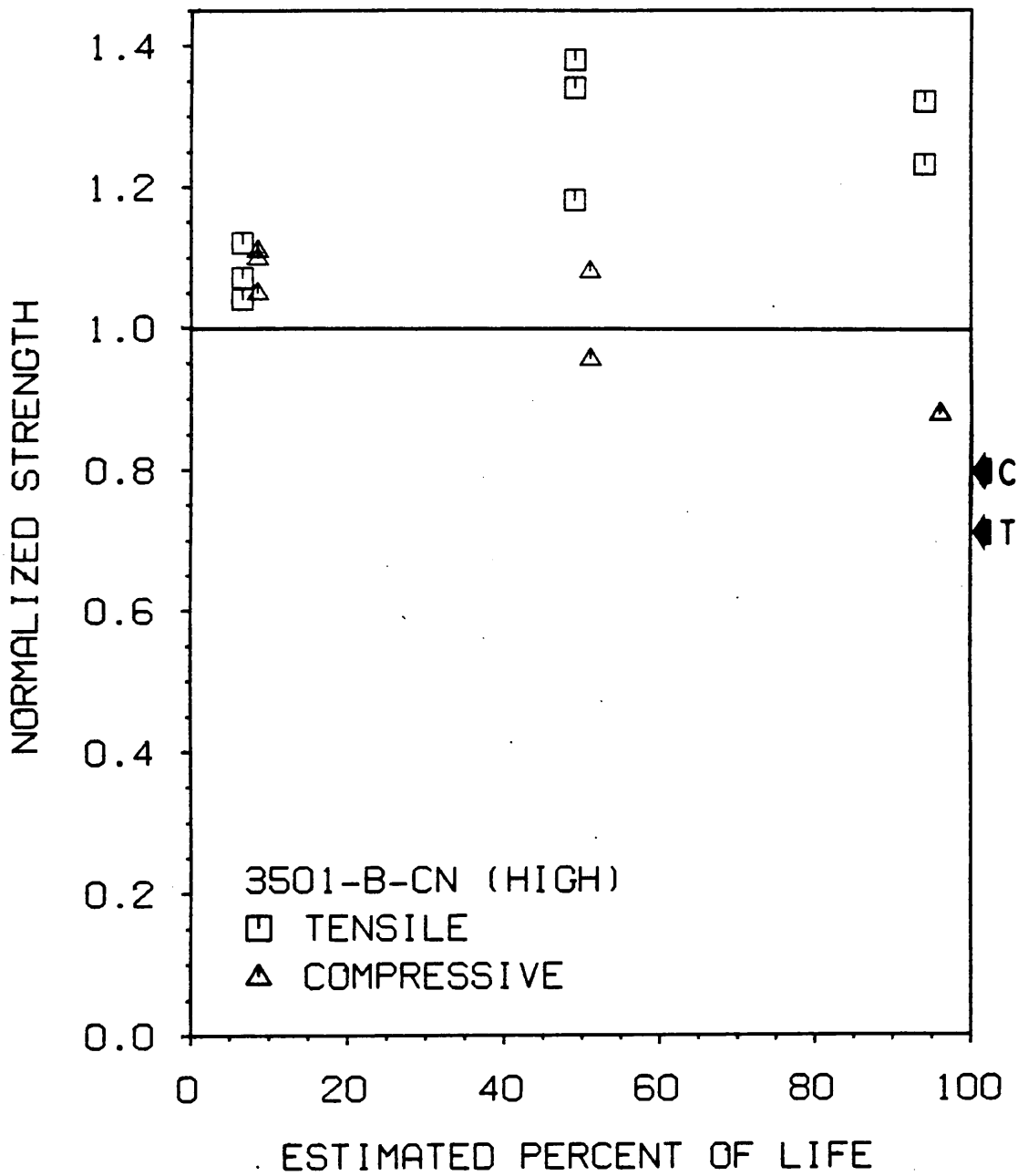


Figure 63. Normalized residual strength of center-notched, AS4/3501-6, (0,45,0,-45)_{s4} specimens during high-load fatigue

compressive strengths and, eventually, fatigue failure were caused by delaminations. The average tensile strength of these specimens were highest at the middle-life measurement point, and dropped slightly by the late-life measurement point. Failure modes of the AS4/3501-6 specimens were similar to those described in Figure 62 except for a relatively slower shifting of the tensile fracture path in the longitudinal direction. This observation was consistent with the shorter 0-deg. cracks tangent to the notch in the AS4/3501-6 specimens compared to the AS4/1808 specimens.

6.4 Summary of Residual Strength Data

In the present investigation, the most important factor affecting the residual strength characteristics of notched carbon epoxy laminates was the lamination arrangement. Fatigue damage accumulation had a stronger effect on failure modes and residual strengths in the $(0,45,0,-45)_{s4}$ laminates than in the $(0,45,90,-45)_{s4}$ laminates. This difference can be mostly attributed to the more complete notch blunting and the later onset of delamination in the $(0,45,0,-45)_{s4}$ laminate. Matrix cracks and delaminations in both laminates improved the tensile strength of the specimens because tensile strength depends highly on the stress concentration near the notch. Only in the $(0,45,0,-45)_{s4}$ laminate, however, was the stress concentration near the notch blunted without the presence of delaminations; thus causing the residual compressive strength to be improved for a short time.

The second most important influence on residual strength was the load level. The effect of load level was more evident in the quasi-isotropic laminate than in the orthotropic laminate because of the greater dependence of damage patterns on load level in the former laminate. High load levels resulted in a ply fracture dominated, transversely directed damage pattern that limited reductions in the notch effect during the lifetime. The delamination dominated, longitudinally directed pattern of damage in low-load specimens was associated with higher

tensile strengths throughout the lifetime, but lower compressive strengths at the middle- and late-life measurement points.

Material system in the present investigation was not a strong influence on the residual strength of $(0,45,0,-45)_{s4}$ laminates during high-load fatigue. The only differences ascertained in the present investigation were the slightly higher middle-life residual compressive strength and late-life tensile strength of the AS4/3501-6 material compared to the AS4/1808 material. This was despite the shorter 0-deg. cracks tangent to the notch in the AS4/3501-6 specimens. Perhaps a stronger material dependence would emerge in the more matrix-sensitive quasi-isotropic laminate. The effect of notch configuration on the residual strength of AS4/1808, $(0,45,90,-45)_{s4}$ specimens during high-load fatigue was not significant except for the higher middle-life tensile strength in the DEN specimens.

Chapter VII

Considerations for a Strength Model

7.1 Background

The development of a mechanistic model of strength is a challenging problem that requires a complete understanding of the intrinsic strength of a material and the stress state imposed on that material. Because composite materials are composed of more than one material, the strength of each constituent influences the strength of the overall structure. In the case of CFRP materials, such constituent strengths may be highly anisotropic. Two modeling difficulties associated with CFRP materials are the anisotropic strength properties of the constituents and the complex internal stress states commonly associated with multi-phase materials.

Under long term loading conditions, damage initiates and grows in composites in a non-homogeneous manner. That is, damage appears in several modes, in certain portions of the material. There is nonhomogeneous damage development through the thickness of a laminate and, if a stress concentrator is present, in the plane of the laminate. The results of the present investigation, and many others before it, have indicated that not all modes of damage

are deleterious to the strength of the laminate. Reasons for changes in residual strength have been proposed by carefully measuring damage accumulation and stress redistribution. It appears that during the fatigue lifetime of a notched composite laminate there are competing strength-altering mechanisms in action. Matrix damage causes load to be transferred to the undamaged portions of the composite — usually the fibers. Local stress concentrations caused by these subcritical damage events also threaten the survival of the remaining, undamaged portion of material. At the same time, subcritical damage events benefit the overall strength of notched laminates because of the localization of damage near the highly-stressed area. (The lack of a single, dominant flaw is one of the most attractive features of practical composites from the fatigue viewpoint, but certainly not from the modeling viewpoint). Since stress cannot be effectively transferred through the damaged material, it is redistributed around the damage, farther from the original stress concentrator (the notch). The present investigation has shown that the particular manner in which stresses are redistributed depends on the particular manner in which damage grows from a notch. In turn, the residual strength of the structure depends on the magnitude and distribution of the internal loads. Hence, a multitude of factors that affect the type and distribution of damage — lamination arrangement, load level, material system, and, to a lesser extent, notch type — influence the remaining strength of the material. Designing a general model of such a situation seems, at first, intractable. Indeed, the amount of data required to construct a model incorporating all these parameters is formidable. Hence, the problem must be attacked one step at a time. The knowledge gained in the present investigation constitutes such a first step.

A methodology for prediction of notched laminate strength and fatigue life proposed in Ref. [50] builds upon an earlier model of unnotched laminate residual strength and fatigue life [49]. A premise of the model is that damage patterns and failure modes for particular load histories can be characterized with several, simple, (and low cost) laboratory experiments. The discipline of mechanics is then called upon to describe the internal stress state of the material — particularly that element of material considered to be "critical" to survival. Strength degradation of the critical element is incorporated into the model through a series of experiments

with basic building blocks of the composite material, such as a unidirectional ply or the fibers themselves. For a given failure mode, the model predicts the strength of the critical element of material. If the failure mode changes, the model must adapt to such a change (it should, ideally, predict the change).

The results of the present investigation indicate the need for a model capable of handling changes in the damage patterns and the corresponding global stress distributions and ultimate fracture appearances. The tensile fracture appearances reflected the different damage patterns and global stresses in the material, but were actually all governed by the same phenomenon— fiber fracture. Compressive failures were more complicated due to delaminations, and cannot be modeled until a firm grasp of the simpler tensile problem is at hand.

The model proposed in Ref. [50] utilizes an effective notch geometry to approximate the global strain distribution resulting from fatigue damage accumulation near a circular hole. To calibrate the model, global strain distributions can be obtained in the laboratory, perhaps by the SPATE, moiré, or photoelastic techniques. The measured strain distributions are approximated with Lekhnitskii's elasticity solution for strains in an infinite, homogeneous, anisotropic plate with an elliptical opening under a homogeneous, in-plane load [30]. With the strain distribution and strength degradation in the critical element characterized throughout the load history, predictions of remaining strength are possible. Important data needed for generality of the model include:

- Identification of the critical element and its failure mode(s).
- Dependence of the strength of the critical element on the load history, environment, time, or other factors worthy of concern.
- Dependence of the local strains in the critical element on the global strain distribution and the local damage state.
- Dependence of the global strain distribution on the damage state.
- Dependence of the existing damage state on the previous load history.

With a sufficient amount of designed-in flexibility founded on a comprehensive experimental testing program involving simple specimens, the model can be used to *predict* the strength (and life) of complex engineering structures without extensive testing of those structures.

Though the validity of modeling the nonhomogeneous stress distribution around a circular hole in a CFRP laminate with an ellipse is subject to debate, there is one important advantage of the technique over more accurate, though complex, techniques; namely, simplicity. Rather than a finite element solution, Lekhnitskii's closed form solution is easily adaptable to the repetitive calculations often needed to compute the residual strength of laminates under variable long term loading conditions.

7.2 Elliptical Hole Model

Several considerations associated with the implementation of an elliptical hole model are now to be discussed. As a first-cut failure criterion, consider the global strain concentration factor (SCF) on the boundary of the ellipse as a function of the aspect ratio of the major and minor axes (a/b) when the load angle, ϕ , equals zero (Figure 64). In the $(0,45,90,-45)_{s4}$ laminate, the SCF decreases from 3.22 when $a/b = .9$ to 2.33 when $a/b = 1.5$ (Figure 65). Over the same range of a/b , the SCF in the $(0,45,0,-45)_{s4}$ laminate decreases from 3.77 to 2.66. Incidentally, the SCF's at $a/b = 1$ are 3.00 in the quasi-isotropic laminate, and 3.49 in the orthotropic laminate. The tensile strengths corresponding to this range of a/b are shown in Figure 66, where the strength of a plate with an elliptical hole is expressed as a percentage of the strength of the same plate with a circular hole.

Estimated values of a/b for the required SCF reduction are listed in Table 12 for the middle-life tensile specimens. If these a/b values may be interpreted as an effective damage zone, the model suggests that the ellipse would be longer in the orthotropic laminate than in the quasi-isotropic laminate. Values of a were computed for the middle-life tensile specimens

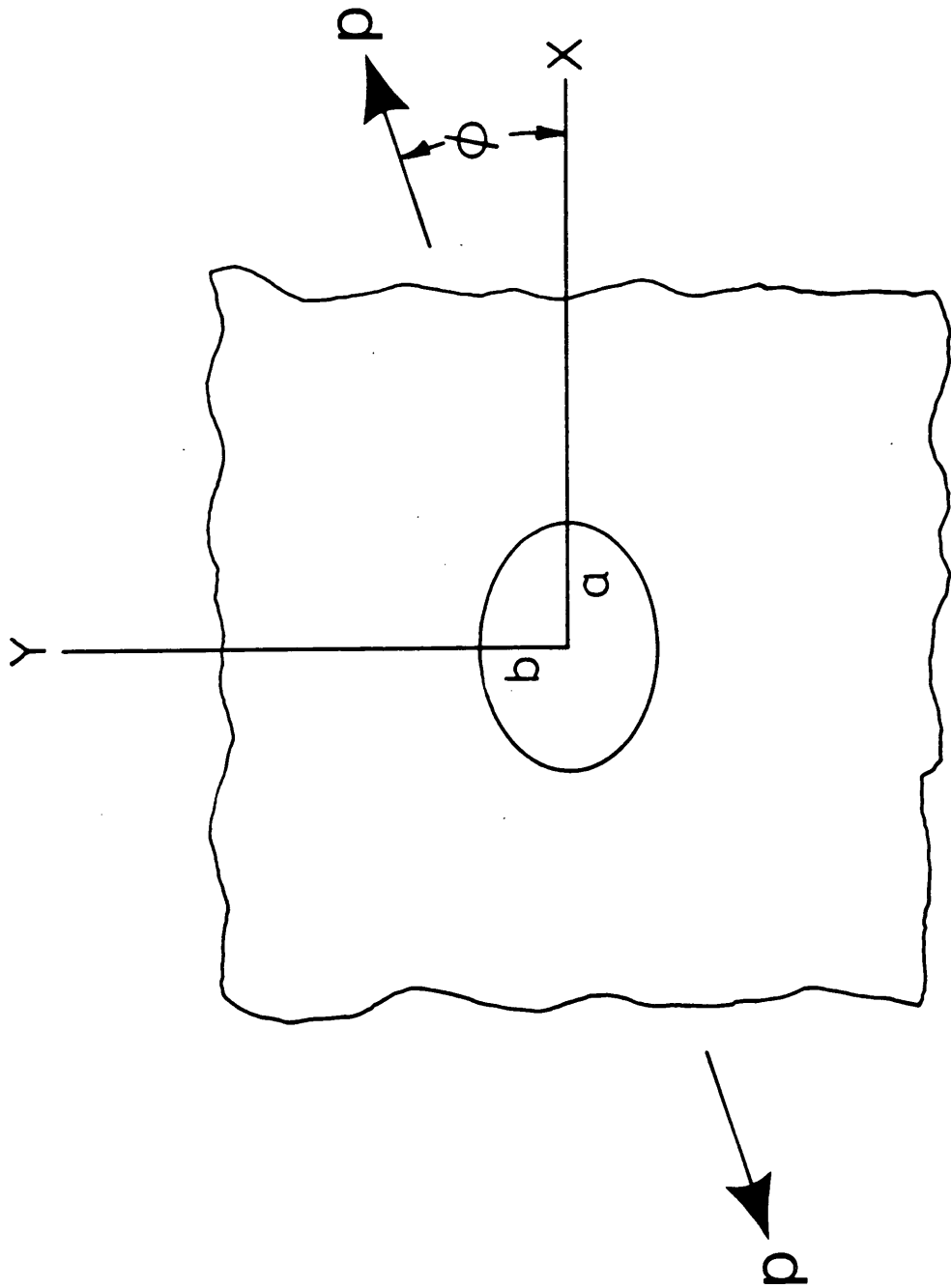


Figure 64. Infinite plate with an elliptical hole under uniform uniaxial stress

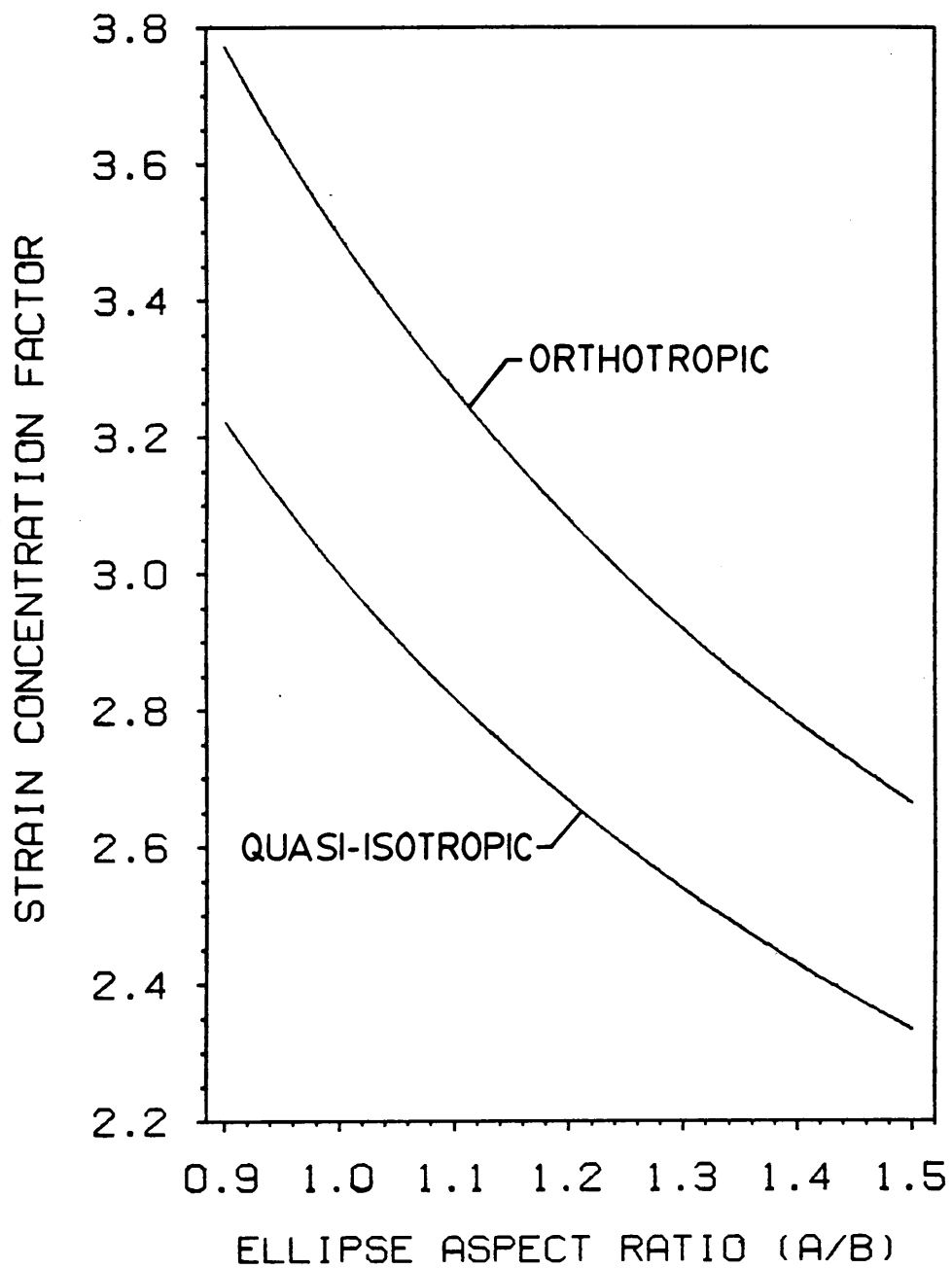


Figure 65. Strain concentration factors in the quasi-isotropic and orthotropic laminates with an elliptical hole

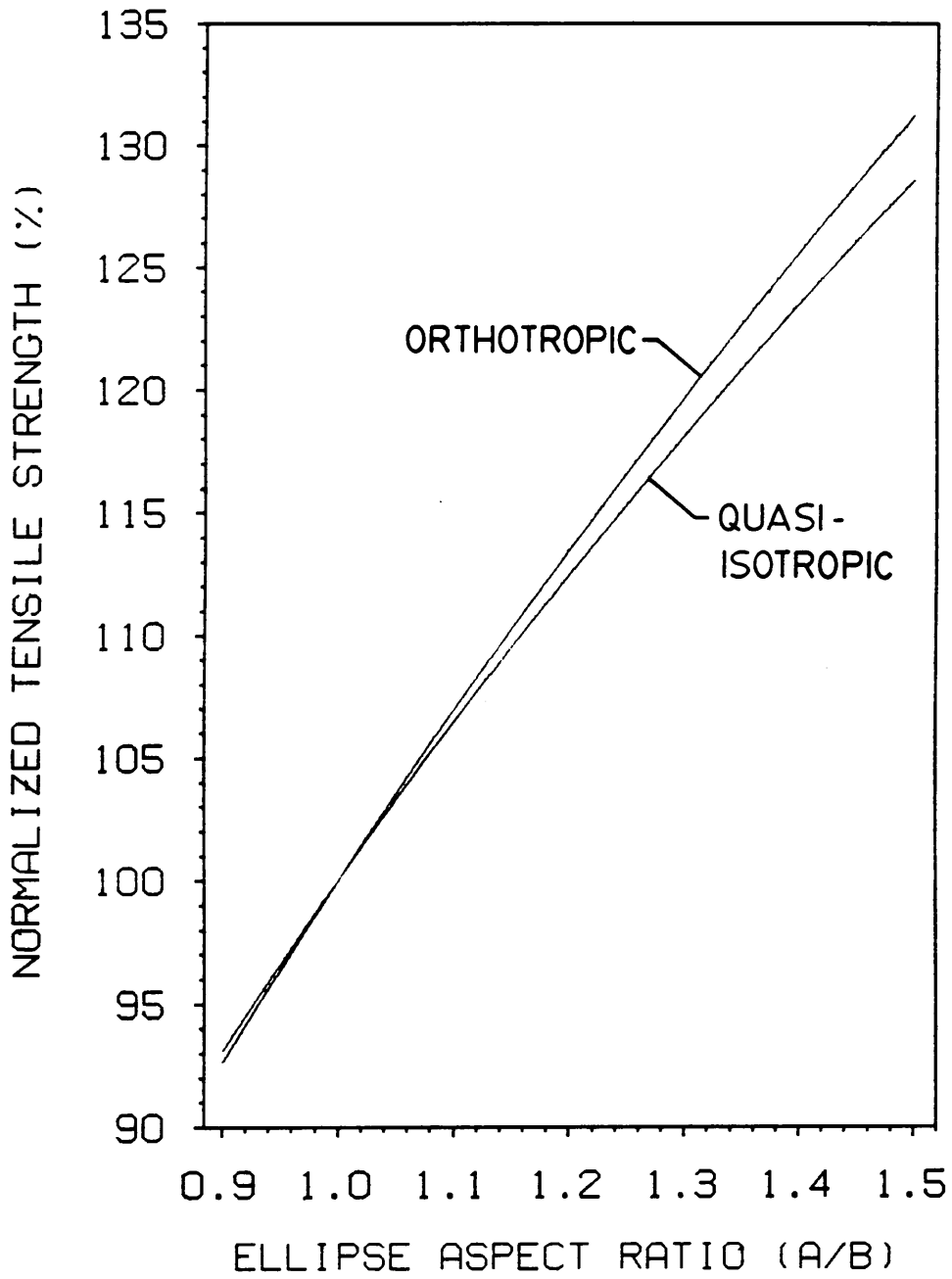


Figure 66. Normalized tensile strength of a plate with an elliptical hole

Table 12. Ellipse aspect ratios for middle-life tensile specimens

Specimen Type	Load Level	a/b from SCF Reduction	a/b from Radiography
1808-A-CN	High	1.16	1.01
	Low	1.33	2.89
1808-B-CN	High	1.42	2.46
	Low	1.35	2.13
3501-B-CN	High	1.48	1.59

by averaging the length of the 0-deg. ply matrix cracks tangent to the hole in the even quadrants. Values of b were computed by averaging the largest transverse dimension of damage in those same specimens (recognizing that this dimension was, in all cases, determined by surface ply damage). The resulting ratios of a/b , listed in Table 12, agree generally, but not quantitatively, with the values of a/b required for the SCF reduction in the model. Therefore, there is little guidance from damage evaluation on specifically how to alter the dimensions of the ellipse to predict tensile strength.

Stiffness is the next candidate for a possible indicator of the ellipse configuration. Using Lekhnitskii's elasticity solution for displacements around an elliptical opening [30], effective stiffnesses analogous to those values measured in the laboratory can be calculated over a 1-in. extensometer centered on a 0.375-in. hole. Allowing the ellipse to grow in the longitudinal direction until a/b equals 1.5 (the highest value required to obtain any of the experimental residual strength measurements) results in effective stiffnesses as low as approximately 94 percent of the stiffness calculated using a circular hole (Figure 67). Clearly, there is insufficient stiffness reduction in the model to establish a relationship between the extensometer stiffness and the residual tensile strength. That is, adjusting the longitudinal dimension of the ellipse to match the measured strengths results in insufficiently low values of stiffness degradation. The only alternative is to extend the transverse dimension of the ellipse based on the damage pattern. This, however, will require further extensions of the longitudinal dimension to achieve the SCF required by the tensile residual strength measurements. This exercise is left for future investigations.

Using SPATE data to derive the ellipse dimensions is not practical, given the highly irregular appearance of the measured patterns. The SPATE data could possibly be used to determine the location, size, and shape of the ellipse such that the distribution of stress in the zone of material believed to be critical to failure is modeled correctly (wherever that zone may be located in the laminate). Improvements in the accuracy of the model for adiabatic temperature change is required before this task can be addressed seriously.

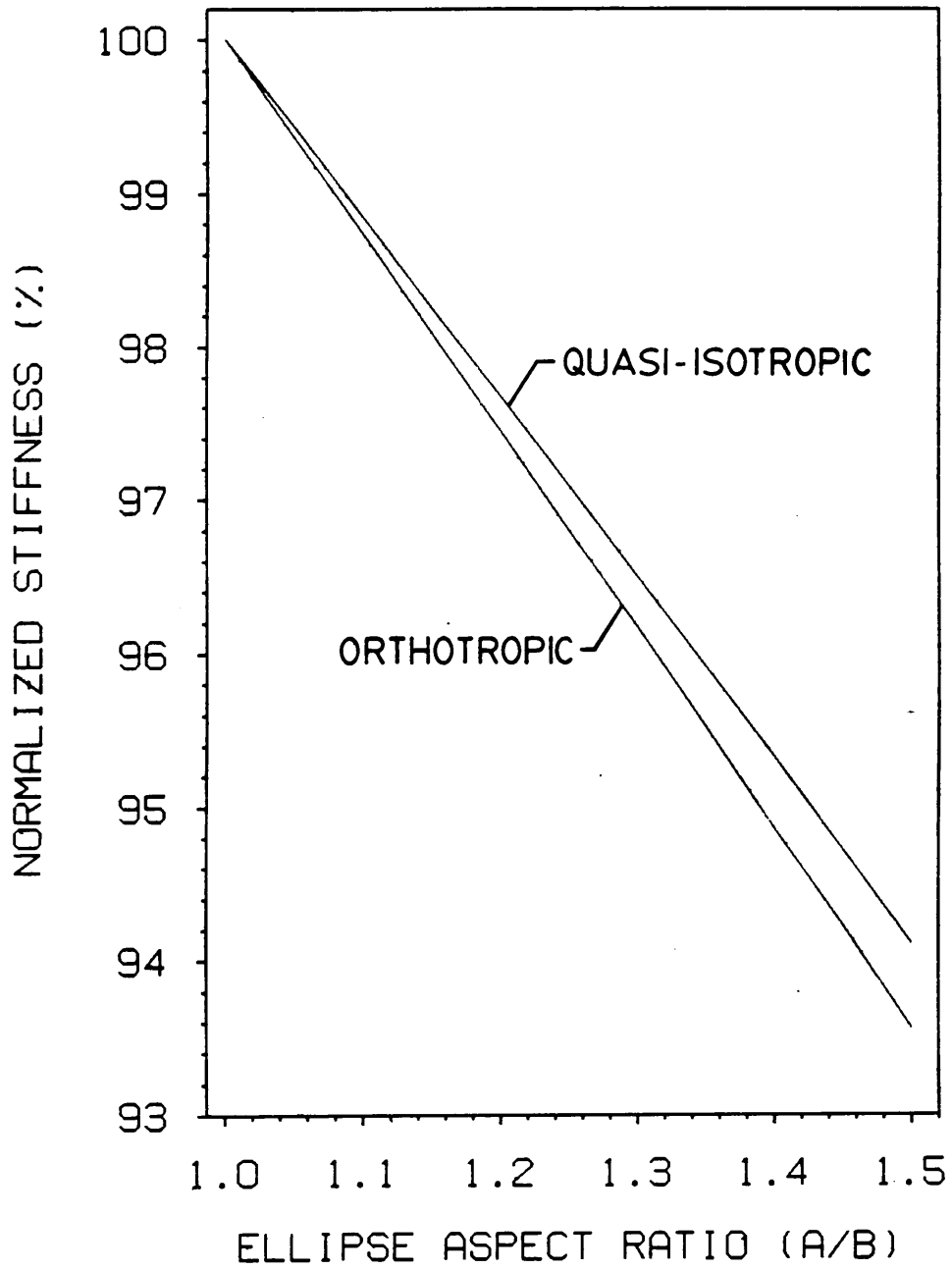


Figure 67. Normalized, effective stiffness in a plate with an elliptical hole

The author cannot state at this time whether or not a cogent scheme for deriving the shape and location of the ellipse can be found. If one concentrates mainly on the strength values and not on the damage patterns, stress patterns, stiffness measurements, or fracture patterns, the probability of success will be greatly improved, but the desired flexibility of the model will be lost.

Chapter VIII

Conclusions

8.1 *Investigative Methods*

The complementary data provided by stiffness monitoring and X-ray radiography were essential to estimate the fatigue "age" of specimens slated for destructive testing prior to fatigue failure. Counting cycles to estimate the "age" of specimens would not have been satisfactory, given the large amount of scatter in fatigue lifetimes.

The inability to accurately resolve stress or strain components from SPATE measurements was a severe handicap. The importance of knowing such components in materials with anisotropic strength properties cannot be understated. A means of directly measuring full-field strains in the 0-deg. fiber direction would have been more useful in understanding the effects of stress redistribution on residual strength. The interrogation of surface 0-deg. plies for stress redistribution data had limited utility since the interior plies apparently controlled residual tensile and compressive strength. Peak temperature change measurements in highly stressed areas of the laminate needed to be normalized by the temperature change in a re-

mote, undamaged portion of the specimen to facilitate comparisons among different specimens.

8.2 Fatigue Response

Relationships between the fully-reversed, cyclic loading history, damage development, stress redistribution, residual tensile and compressive strengths, and failure modes have been identified for the two material systems, two laminate configurations, two load levels, and two notch configurations included in the present test program. Conclusions concerning damage development, stress redistribution, and residual strength are presented next.

8.2.1 Damage Development

The direction and form of damage growth in notched laminates were determined principally by the lamination arrangement and load level. Damage growth favored the transverse direction in the laminate with a higher percentage of off-axis plies and in specimens under high-amplitude cyclic load histories. The transverse mode of damage growth consisted of relatively more 0-deg. ply fracture and less delamination than the longitudinal mode of damage growth. Low load specimens and quasi-isotropic specimens had more delaminations and matrix cracks than high-load and orthotropic specimens. Matrix cracks were more extensive in AS4/3501-6 specimens than in AS4/1808 specimens. Delaminations, however, were similar in form and extent in both material systems, despite the improved toughness of the 1808 matrix.

Incremental fractures of principal load-bearing plies were precipitated by matrix cracks in adjacent plies. The interaction of these damage modes was therefore highly dependent on the

stacking sequence. In the AS4/1808 material, incremental fractures of 0-deg. plies were always followed by delaminations of the broken 0-deg. plies. However, if a 0-deg. ply delaminated first, fiber fractures did not occur in the delaminated portion of the ply, perhaps because the delamination buffered the 0-deg. ply from the stress concentration caused by the matrix crack. Similarly, delaminations on the outermost 0/45 interfaces prevented fractures of the 45-deg. plies along the 0-deg. matrix cracks tangent to the notch in the orthotropic laminate. This behavior is in contrast to the large number of broken 0-deg. fibers scattered within delaminated areas in center-notched, T300/5208, (0,45,90,-45)_{s4} laminates in Ref. [76].

Damage, especially delamination, was usually more extensive closer to the surface of the specimens, causing a transfer of load into the interior plies. This surface effect was less obvious in specimens under high load levels.

8.2.2 Stress Redistribution

During fatigue, zones of high stress concentration observed with the SPATE apparatus were always located in areas of the specimen soon to be invaded by matrix and fiber damage. Depending on the peculiar mode of damage growth, highly stressed areas shifted either transversely from the notch (as in the quasi-isotropic specimens) or longitudinally from the notch (as in the orthotropic specimens). The highly stressed areas were located at or near the locus of tensile fracture in residual strength tests. Comparing specimens at various points in their fatigue lifetimes, the magnitude of the highly stressed area was lower in specimens having a higher residual tensile strength. In several instances, there was no correlation of the residual tensile strength and the stress concentration in the surface ply. In some of those cases, particularly those involving late-life specimens with extensive surface ply damage, failure was assumed to be initiated by the failure of highly stressed fibers in some location not visible to the SPATE apparatus (perhaps in the interior of the laminate). In other cases, inordinately high, but extremely localized, stress concentrations did not correspond to pro-

portionally lower tensile strengths, perhaps because of the occurrence of additional stress relaxation mechanisms during the course of the residual strength test.

The tendency for delaminations to grow unstably under compressive loads could not be ascertained with the SPATE technique. Hence, there was no correlation between stress patterns and residual compressive strengths except in the few situations where there were no appreciable delaminations. In the absence of extensive delaminations, the stress concentration near the notch controlled the compressive strength of the specimens.

8.2.3 Residual Strength

Matrix cracks and delaminations blunted the original stress concentration near the notch, but caused new stress concentrations to appear immediately ahead of the damage zone. Up to and including the last strength measurement point just prior to fatigue failure, residual tensile strengths remained greater than the tensile strengths of virgin specimens except when extensive 0-deg. ply fractures emanated from the notch in several plies through the thickness. Compressive strengths decreased in the presence of 0-deg. ply fractures or delaminations transverse to the notch. Therefore, residual compressive strengths decreased monotonically throughout the fatigue lifetime in all cases except those involving orthotropic specimens prior to the onset of 0-deg. ply fractures or delaminations immediately adjacent to the notch.

Since 0-deg. fibers controlled the tensile strength of the laminates used in the present investigation, specimens with a larger amount of 0-deg. ply fractures had higher stress concentrations throughout their fatigue lifetimes and failed at lower tensile loads than specimens with less 0-deg. ply fractures. Hence, tensile strengths were lower in quasi-isotropic specimens and in high-load fatigue tests. Residual compressive strengths were found to depend more on the extent and location of damage (particularly delamination) and less on the magnitude of stress concentrations than did residual tensile strengths.

Chapter IX

Recommendations

Several focused research areas that would complement the present work are given below. Initiatives in many of these areas were established during the course of the present work, but were incomplete at the time of this writing.

Damage Mechanisms and Residual Strength

- Compare the effect of different matrix materials on the residual strength of the quasi-isotropic laminate.
- Deploy residual strength specimens (perhaps immediately prior to fracture) to determine the critical failure locations of the internal 0-deg. plies more accurately.
- Determine the proper procedure for deploying the AS4/3501-6 material without causing additional fiber damage.
- Measure residual strengths at more points in the fatigue lifetime to construct strength "curves."

- Measure the maximum adiabatic temperature change and the tensile strength of several virgin specimens to assess the degree of correlation between SPATE measurements and ultimate loads.
- Quantitatively relate the locus of fracture initiation and the locus of high adiabatic temperature change in tensile residual strength specimens.

Stress Redistribution

- Remove outer plies (by sanding, perhaps) before using the SPATE technique on fatigue-damaged specimens to determine stress distributions in internal 0-deg. plies.
- Measure strains in the 0-deg. fiber direction at locations believed to be critical to failure of the specimen (perhaps at locations suggested by full-field SPATE, moiré, or photoelastic coating data).

The SPATE Technique

- Assess the importance of nonadiabatic effects in SPATE measurements involving fiber composites — particularly the effect of loading rate and frequency on the cyclic temperature change.
- Improvement of the micromechanical model for predicting SPATE measurements:
 - incorporation of nonadiabatic effects
 - evaluation of the accuracy of the microconstituent strains
- Investigation of the possibility of measuring subsurface temperature changes to evaluate stresses in interior 0-deg. plies.

Elliptical Hole Model for Strength

- Use the elliptical hole model in conjunction with a more accurate failure criterion, such as the two or three parameter models of Refs. [22,27].

- Allow the principal axes of the ellipse to tilt in order to accommodate the nonsymmetric damage and stress patterns and failure modes seen in $(0,45,0,-45)_{s4}$ specimens.
- Investigate the possibility of using damage dimensions from interior 0-deg. plies for deriving the aspect ratio of the ellipse in the elliptical hole model (using deply data).

References

1. Hahn, H. T., Ed., *Composite Materials: Fatigue and Fracture, STP 907*, ASTM, Philadelphia, 1986.
2. Bakis, C. E. and Stinchcomb, W. W., "Response of Thick, Notched Laminates Subjected to Tension-Compression Cyclic Loads," *Composite Materials: Fatigue and Fracture, STP 907*, H. T. Hahn, Ed., ASTM, Philadelphia, 1986, pp. 314-334.
3. Simonds, R. A., Bakis, C. E., and Stinchcomb, W. W., "Effects of Matrix Toughness on Fatigue Response of Graphite Fiber Composite Laminates," *Composite Materials: Fatigue and Fracture (2nd Symp.), STP 1012*, P. A. Lagace, Ed., ASTM, Philadelphia, 1988 (in press).
4. Kress, G. R. and Stinchcomb, W. W., "Fatigue Response of Notched Graphite/Epoxy Laminates," *Recent Advances in Composites in the United States and Japan, STP 864*, J. R. Vinson and M. Taya, Eds., ASTM, Philadelphia, 1985, pp. 173-196.
5. Wagnecz, L., "Material Properties and Damage Mechanisms of Woven Graphite Polyimide Composite Materials," Masters Thesis, College of Engineering, Virginia Polytechnic Institute and State University, Blacksburg, VA, June 1987.
6. Morton, J., Kellas, S., and Bishop, S. M., "Fatigue Damage Development in a Notched Carbon Fibre Composite," *Comp. Struct.*, **5** (1986), pp. 143-157.

7. Bishop, S. M. and Dorey, G., "The Effect of Damage on the Tensile and Compressive Performance of Carbon Fibre Laminates," *AGARD Conf. Proc. No. 355*, North Atlantic Treaty Organization, 12-14 April 1983, pp. 10.1-10.10.
8. Black, N. F. and Stinchcomb, W. W., "Compression Fatigue Damage in Thick, Notched Graphite/Epoxy Laminates," *Long-Term Behavior of Composites, STP 813*, T. K. O'Brien, Ed., ASTM, Philadelphia, 1983, pp. 95-115.
9. Ramani, S. V. and Williams, D. P., "Notched and Unnotched Fatigue Behavior of Angle-Ply Graphite/Epoxy Composites," *Fatigue of Filamentary Composite Materials, STP 636*, K. L. Reifsnider and K. N. Lauraitis, Eds., ASTM, Philadelphia, 1977, pp. 27-46.
10. Walter, R. W., Johnson, R. W., June, R. R., and McCarty, J. E., "Designing for Integrity in Long-Life Composite Aircraft Structures," *Fatigue of Filamentary Composite Materials, STP 636*, K. L. Reifsnider and K. N. Lauraitis, Eds., ASTM, Philadelphia, 1977, pp. 228-247.
11. Hedgepeth, J. M., "Stress Concentrations in Filamentary Structures," NASA TN-D882, Nat. Aeronautics and Space Admn., May 1961.
12. Hedgepeth, J. M. and Van Dyke, P., "Local Stress Concentrations in Imperfect Filamentary Composite Materials," *J. Comp. Mater.*, **1** (1967), pp. 294-309.
13. Van Dyke, P. and Hedgepeth, J. M., "Stress Concentration From Single Fiber Failures in Composite Materials," *Textile Res. J.*, **39** (1969), pp. 618-626.
14. Rosen, B. W., "Tensile Failure of Fibrous Composites," *AIAA J.*, **2** (1964), pp. 1985-1991.
15. Zweben, C., "Fracture Mechanics and Composite Materials: A Critical Analysis," *Analysis of the Test Methods for High Modulus Fibers and Composites, STP 521*, ASTM, Philadelphia, 1973, pp. 65-97.
16. Goree, J. G. and Gross, R. S., "Stresses in a Three-Dimensional Unidirectional Composite Containing Broken Fibers," *Eng. Fract. Mech.*, **13** (1980), pp. 395-405.
17. Goree, J. G. and Gross, R. S., "Analysis of a Unidirectional Composite Containing Broken Fibers and Matrix Damage," *Eng. Fract. Mech.*, **13** (1980), pp. 563-578.
18. Batdorf, S. B., "Tensile Strength of Unidirectionally Reinforced Composites — I" *J. Reinf. Plast. and Comp.*, **1** (1982), pp. 153-164.

19. Batdorf, S. B. and Ghaffarian, Reza, "Tensile Strength of Unidirectionally Reinforced Composites — II" *J. Reinf. Plast. and Comp.*, **1** (1982), pp. 165-176.
20. Batdorf, S. B. and Ghaffarian, Reza, "Size Effect and Strength Variability of Unidirectional Composites," *Int. J. Fract.*, **26** (1984), pp. 113-123.
21. Waddoups, M. E., Eisenmann, J. R., and Kaminski, B. E., "Macroscopic Fracture Mechanics of Advanced Composite Materials," *J. Comp. Mater.*, **5** (1971), pp. 446-454.
22. Whitney, J. M. and Nuismer, R. J., "Stress Fracture Criteria for Laminated Composites Containing Stress Concentrations," *J. Comp. Mater.*, **8** (1974), pp. 253-265.
23. Karlak, R. G., "Hole Effects in a Related Series of Symmetrical Laminates," *Proc. Failure Modes in Composites, IV*, Metallurgical Soc. AIME, Chicago, 1977, pp. 105-117.
24. Caprino, G., "On the Prediction of Residual Strength for Notched Laminates," *J. Mater. Sci.*, **18** (1983), pp. 2269-2273.
25. Daniel, I. M., Rowlands, R. E., and Whiteside, J. B., "Effects of Material and Stacking Sequence on Behavior of Composite Plates with Holes," *Exp. Mech.*, **14** (1974), pp. 1-9.
26. Whitney, J. M. and Kim, R. Y., "Effect of Stacking Sequence on the Notched Strength of Laminated Composites," *Composite Materials: Testing and Design (4th Conf.)*, STP 617, ASTM, Philadelphia, 1977, pp. 229-242.
27. Pipes, R. B., Wetherhold, R. C., and Gillespie, J. W., Jr., "Notched Strength of Composite Materials," *J. Comp. Mater.*, **12** (1979), pp. 148-160.
28. Garbo, S. P. and Ogonowski, J. M., "Strength Predictions of Composite Laminates with Unloaded Fastener Holes," *AIAA J.*, **18** (1980), pp. 585-589.
29. Tan, S. C., "Notched Strength Prediction and Design of Laminated Composites Under In-Plane Loadings," *J. Comp. Mater.*, **21** (1987), pp. 751-780.
30. Lekhnitskii, S. G., *Anisotropic Plates*, transl. from the 2nd Russian ed. by S. W. Tsai and T. Cheron, Gordon and Breach, New York, 1968.
31. Poe, C. C., Jr. and Sova, K. A., "Fracture Toughness of Boron/Aluminum Laminates With Various Proportions of 0° and ±45° Plies," NASA TP-1707, Nat. Aeronautics and Space Admn., 1980.

32. Morley, J. G., "On the Development of a General Theory for the Mechanics of Tensile Fracture of Fibre Reinforced Materials," *J. Mater. Sci.*, **20** (1985), pp. 1794-1806.
33. Chou, S. C., Orringer, O., and Rainey, J. H., "Post-Failure Behavior of Laminates: II — Stress Concentration," *J. Comp. Mater.*, **11** (1977), pp. 71-78.
34. Witt, W. P. and Palazotto, A. N., "Numerical and Experimental Comparison of the Notch Tip Stresses in a Laminated Plate," *AIAA J.*, **17** (1979), pp. 500-506.
35. Sandhu, R. S., Gallo, R. L., and Sendeckyj, G. P., "Initiation and Accumulation of Damage in Composite Laminates," *Composite Materials: Testing and Design (6th Conf.)*, STP 787, I. M. Daniel, Ed., ASTM, Philadelphia, 1982, pp. 163-182.
36. Lee, J. D., "Three Dimensional Finite Element Analysis of Damage Accumulation in Composite Laminate," *Computers & Structures*, **15** (1982), pp. 335-350.
37. Irvine, T. B. and Ginty, C. A., "Progressive Fracture of Fiber Composites," *J. Comp. Mater.*, **20** (1986), pp. 166-184.
38. Chang, F.-K. and Chang, K.-Y., "A Progressive Damage Model for Laminated Composites Containing Stress Concentrations," *J. Comp. Mater.*, **21**, pp. 834-855.
39. Rhodes, M. D., Mikulas, M. M. Jr., and McGowan, P. E., "Effects of Orthotropy and Width on the Compression Strength of Graphite-Epoxy Panels with Holes," *AIAA J.*, **22** (1984), pp. 1283-1292.
40. Nuismer, R. J. and Labor, J. D., "Application of the Average Stress Failure Criterion: Part II — Compression," *J. Comp. Mater.*, **13** (1979), pp. 49-60.
41. Rosen, B. W., "Mechanics of Composite Strengthening," *Fiber Composite Materials*, ASM, 1965, pp. 37-75.
42. Greszczuk, L. B., "Microbuckling of Lamina-Reinforced Composites," *Composite Materials: Testing and Design (3rd Symp.)*, STP 546, ASTM, Philadelphia, 1974, pp. 5-29.
43. Hahn, H. T. and Williams, J. G., "Compression Failure Mechanisms in Unidirectional Composite," NASA TM 85834, Langley Research Center, Nat. Aeronautics and Space Admn., Hampton, VA, Aug. 1984.

44. Gurdal, Z. and Haftka, R. T., "Compressive Failure Model for Anisotropic Plates with a Cutout" *AIAA J.*, **25** (1987), pp. 1476-1481.
45. Nemeth, M. P., "Buckling Behavior of Orthotropic Composite Plates with Centrally Located Cutouts," Ph.D. Dissertation, College of Engineering, Virginia Polytechnic Institute and State University, Blacksburg, VA, May 1983.
46. Shivakumar, K. N. and Whitcomb, J. D., "Buckling of a Sublaminar in a Quasi-Isotropic Composite Laminate," *J. Comp. Mater.*, **19** (1985), pp. 2-18.
47. Halpin, J. C., Johnson, T. A., and Waddoups, M. R., *Int. J. Fract. Mech.*, **8** (1972), pp. 465-472.
48. Broutman, L. J. and Sahu, S., "A New Theory to Predict Cumulative Fatigue Damage in Fiberglass Reinforced Plastics," *Composite Materials: Testing and Design (2nd Conf.)*, STP 497, ASTM, Philadelphia, 1972, pp. 170-188.
49. Reifsnider, K. L. and Stinchcomb, W. W., "A Critical-Element Model of the Residual Strength and Life of Fatigue-Loaded Composite Coupons," *Composite Materials: Fatigue and Fracture*, STP 907, H. T. Hahn, Ed., ASTM, Philadelphia, 1986, pp. 298-313.
50. Reifsnider, K. L. and Bakis, C. E., "Modeling Damage Growth in Notched Composite Laminates," *Proc. Japan-US Symp. on Composite Materials*, Tokyo, 22-24 June 1986.
51. Highsmith, A. L. and Reifsnider, K. L., "Internal Load Distribution Effects During Fatigue Loading of Composite Laminates," *Composite Materials: Fatigue and Fracture*, STP 907, H. T. Hahn, Ed., ASTM, Philadelphia, 1986, pp. 233-251.
52. Jamison, R. D., "Fiber Fracture in Composite Laminates," *Proc. 6th ICCM and 2nd ECCM*, Vol. 3, F. L. Mathews, N. C. R. Buskell, J. M. Hodgkinson, and J. Morton, Eds., Elsevier, Amsterdam, 1987, pp. 3.185-3.199.
53. Jamison, R. D., "On the Interrelationship Between Fiber Fracture and Ply Cracking in Graphite/Epoxy Laminates," *Composite Materials: Fatigue and Fracture*, STP 907, H. T. Hahn, Ed., ASTM, Philadelphia, 1986, pp. 252-273.

54. Reifsnider, K. L., Stinchcomb, W. W., and Henneke, E. G., II, "Defect-Property Relationships in Composite Laminates," AFML Technical Report 76-81, Part IV, Wright-Patterson AFB, Dayton, OH, April 1979.
55. O'Brien, T. K., "Characterization of Delamination Onset and Growth in a Composite Laminate," *Damage in Composite Materials, STP 775*, K. L. Reifsnider, Ed., ASTM, Philadelphia, 1982, pp. 140-167.
56. Highsmith, A. L. and Reifsnider, K. L., "On Delamination and the Damage Localization Process," *Fracture of Fibrous Composites — AMD Vol. 74*, C. T. Herakovich, Ed., ASME, New York, 1985, pp. 71-87.
57. Sundaresan, M. J. and Henneke, E. G., II, "SEM Observations of Failure Process in Unidirectional Composite Materials," *Composite Materials: Testing and Design (9th Symp.)*, STP xxx, S. P. Garbo, Ed., ASTM, Philadelphia, in press.
58. Bakis, C. E., Yih, H. R., Reifsnider, K. L., and Stinchcomb, W. W., "Damage Initiation and Growth in Notched Laminates Under Reversed Cyclic Loading," *Composite Materials: Fatigue and Fracture (2nd Symp.)*, STP 1012, P. A. Lagace, Ed., ASTM, Philadelphia, 1988 (in press).
59. Simonds, R. A. and Stinchcomb, W. W., "Response of Notched AS4/PEEK Laminates to Tension/Compression Loading," *Advances in Thermoplastic Matrix Composite Materials*, STP xxx, Golam Newaz, Ed., ASTM, Philadelphia, in press.
60. Curtis, P. T., "An Investigation of the Tensile Fatigue Behavior of Improved Carbon Fibre Composite Materials," *Proc. 6th ICCM and 2nd ECCM Conf.*, Vol. 4, F. L. Mathews, N. C. R. Buskell, J. M. Hodgkinson, and J. Morton, Eds., Elsevier, Amsterdam, 1987, pp. 4.54-4.64.
61. Baron, Ch. and Schulte, K. "Fatigue Damage Response of CFRP with Toughened Matrices and Improved Fibers," *Proc. 6th ICCM and 2nd ECCM Conf.*, Vol. 4, F. L. Mathews, N. C. R. Buskell, J. M. Hodgkinson, and J. Morton, Eds., Elsevier, Amsterdam, 1987, pp. 4.65-4.75.

62. Baron, Ch., Schulte, K., and Harig, H., "Influence of Fibre and Matrix Failure Strain on Static and Fatigue Properties of Carbon Fibre-Reinforced Plastics," *Composites Science and Technology*, **29** (1987), pp. 257-272.
63. Daniel, I. M., "Mixed Mode Failure of Composite Laminates," *Exp. Mech.*, **25** (1985), pp. 413-420.
64. Wood, J. D., "Detection of Delamination Onset in a Composite Laminate Using Moiré Interferometry," *J. Comp. Tech. & Res.*, **7** (1985), pp. 121-128.
65. Reifsnider, K. L., Stinchcomb, W. W., and O'Brien, T. K., "Frequency Effects on a Stiffness-Based Fatigue Failure Criterion in Flawed Composite Specimens," *Fatigue of Filamentary Composite Materials*, STP 636, K. L. Reifsnider and K. N. Lauraitis, Eds., ASTM, Philadelphia, 1977, pp. 171-184.
66. Phillips, E. P., "Effects of Truncation of a Predominantly Compression Load Spectrum on the Life of a Notched Graphite/Epoxy Laminate," *Fatigue of Fibrous Composite Materials*, STP 723, ASTM, Philadelphia, 1981, pp. 197-212.
67. Bakis, C. E., Simonds, R. A., and Stinchcomb, W. W., "A Test Method to Measure the Response of Composite Materials Under Reversed Cyclic Loads," *Test Methods and Design Allowables for Fiber Composites (2nd Conf.)*, STP 1003, C. C. Chamis and K. L. Reifsnider, Eds., ASTM, Philadelphia, 1988.
68. Evans, R. E. and Masters, J. E., "A New Generation of Epoxy Composites for Primary Structural Applications: Materials and Mechanics," *Toughened Composites*, STP 937,, N. J. Johnston, Ed., ASTM, Philadelphia, 1987, pp. 413-436.
69. Masters, J. E., "Characterization of Impact Damage Development in Graphite/Epoxy Laminates," *Fractography of Modern Engineering Materials: Composites and Metals*, STP 948, J. E. Masters and J. J. Au, Eds., ASTM, Philadelphia, 1987, pp. 238-258.
70. Ratwani, M. M., and Kan, H. P., "Effect of Stacking Sequence on Damage Propagation and Failure Modes in Composite Laminates," *Damage in Composite Materials*, STP 775, K. L. Reifsnider, Ed., ASTM, Philadelphia, 1982, pp. 211-228.

71. Reifsnider, K. L., Stinchcomb, W. W., Bakis, C. E. and Yih, H. R., "Investigation and Modeling of Damage Growth in Composite Laminates," AFOSR Contract No. 85.0087, Bolling AFB, Washington, DC, July 1986.
72. O'Brien, T. K., "Stiffness Change as a Nondestructive Damage Measurement," *Mechanics of Nondestructive Testing*, W. W. Stinchcomb, Ed., Plenum Press, New York, 1980, pp. 101-121.
73. Reifsnider, K. L. and Highsmith, A. L., "The Relationship of Stiffness Changes in Composite Laminates to Fracture-Related Damage Mechanisms," *Proc. 2nd USA-USSR Symp. on Fracture of Composite Materials*, Lehigh Univ., Bethlehem, PA, March 1981, pp. 9-12.
74. Reifsnider, K. L. and Stinchcomb, W. W., "Stiffness Change as a Fatigue Damage Parameter for Composite Laminates," *Advances in Aerospace Structures, Materials and Dynamics — AD-06*, U. Yuceoglu, R. L. Sierakowski and D. A. Glasgow, Eds., ASME, New York, 1983.
75. Owens, G. R., "An Experimental Investigation of the Material Response of Graphite/Polyphenylene Sulfide," Masters Thesis, College of Engineering, Virginia Polytechnic Institute and State University, Blacksburg, VA, Aug., 1986.
76. Bakis, C. E., "Fatigue Response of Notched Laminates Subjected to Tension-Compression Loading," Masters Thesis, College of Engineering, Virginia Polytechnic Institute and State University, Blacksburg, VA, Dec., 1984.
77. Rummel, W. D., Tedrow, T., and Brinkerhoff, H. D., "Enhanced X-Ray Stereoscopic NDE of Composite Materials," AFWAL-TR-80-3053, Final Report, AFWAL, FDL, AFSC, Wright-Patterson AFB, Ohio, June 1980.
78. Sendekyj, G. P., Maddux, G. E., and Porter, E., "Damage Documentation in Composites by Stereo Radiography," *Damage in Composite Materials, STP 775*, K. L. Reifsnider, Ed., ASTM, Philadelphia, 1982, pp. 16-26.
79. Freeman, S. M., "Characterization of Lamina and Interlaminar Damage in Graphite/Epoxy Composites by the Deply Technique," *Composite Materials: Testing and Design (6th Conf.)*, STP 787, I. M. Daniel, Ed., ASTM, Philadelphia, 1982, pp. 50-62.

80. D. E. Oliver, "Stress Pattern Analysis by Thermal Emission," *Handbook on Experimental Mechanics*, A. S. Kobayashi, Ed., SEM, Prentice-Hall (1987), pp. 610-620.
81. R. T. Potter, "Stress Analysis in Laminated Fiber Composites by Thermoelastic Emission," *Proc. 2nd Intl. Conf. on Stress Anal. by Thermoelastic Tech.*, Paper No. 20, 17-18 Feb. 1987, London.
82. P. Stanley and W. K. Chan, "SPATE Stress Studies of Plates and Rings Under In-Plane Loading," *Exp. Mech.*, **26** (1986), pp. 360-370.
83. M. H. Belgen, "Structural Stress Measurements with an Infrared Radiometer," *ISA Trans.*, **6** (1967), pp. 49-53.
84. Bakis, C. E. and Reifsnider, K. L., "Nondestructive Evaluation of Fiber Composite Laminates by Thermoelastic Emission," *Review of Progress in Quantitative NDE*, **7B**, D. O. Thompson and D. E. Chimenti, Eds., Plenum, 1988, pp. 1109-1116.
85. B. N. Cox and D. E. Pettit, "Nondestructive Evaluation of Composite Materials Using the Stress Pattern Analysis by Thermal Emissions Technique," *Proc. SEM Spring Conf. on Exp. Mech.*, 14-19 June 1987, Houston, TX.
86. Lohr, D. T. and Sandor, B. I., "Impact Damage Analysis by Differential Infrared Thermography," *Proc. SEM Fall Conf.*, Savannah, GA, 1987.
87. Lohr, D. T., Enke, N. F., and Sandor, B. I., "Analysis of Fatigue Damage Evolution by Differential Infrared Thermography," *Proc. SEM Fall Conf.*, Savannah, GA, 1987.
88. Neubert, H., Schulte, K., and Harig, H., "Evaluation of the Damage Development in CFRP by Monitoring Load Induced Temperature Changes," *Composite Materials: Testing and Design (9th Symp.)*, STP xxx, S. P. Garbo, Ed., ASTM, Philadelphia, in press.
89. W. Thomson, "On the Dynamical Theory of Heat," *Trans. Roy. Soc. Edinburgh*, **20** (1853), pp. 261-288.
90. W. Thomson, "On the Thermo-Elastic and Thermo-Magnetic Properties of Matter," *Qtlly. J. Math.*, **1** (1857), pp. 57-77.
91. Joule, J. P., "On Some Thermo-dynamic Properties of Solids," *Philos. Trans. Roy. Soc.*, **149** (1859), pp. 91-131.

92. Compton, K. T. and Webster, D. B., "Temperature Changes Accompanying the Adiabatic Compression of Steel," *Phys. Rev., Series 2*, **5** (1915), pp. 159-166.
93. Dillon, O. W. and Tauchert, T. R., "The Experimental Technique for Observing the Temperatures Due to the Coupled Thermoelastic Effect," *Int. J. Solids Str.*, **2** (1966), pp. 385-390.
94. Stanley, P. and Chan, W. K. "Quantitative Stress Analysis by Means of the Thermoelastic Effect," *J. Strain Anal.*, **20** (1985), pp. 129-137.
95. Gilmour, I. W., Trainor, A., and Haward, R. N., "The Thermoelastic Effect in Glassy Polymers," *J. Polym. Sci.: Polym. Phys. Ed.*, **16** (1978), pp. 1277-1290.
96. Haward, R. N. and Trainor, A., "The Thermoelastic Effect in PMMA," *J. Mater. Sci.*, **9** (1974), pp. 1243-1254.
97. Jordan, E. H. and Sandor, B. I., "Stress Analysis from Temperature Data," *J. Testing and Eval., JTEVA*, **6** (1978), pp. 325-331.
98. Enke, N. F. and Sandor, B. I., "Cyclic Plasticity Analysis by Differential Infrared Thermography," *Proc. VI Intl. Congr. Exper. Mech.*, Vol. II, Portland OR, 6-10 June 1988, SEM, Bethel CT, pp. 837-842.
99. Higuchi, M. and Imai, Y., "Rheological Interpretation of Heat Generation Associated with Fatigue of Polycarbonate," *J. Appl. Polym. Sci.*, **14** (1970), pp. 2377-2383.
100. M. A. Biot, "Thermoelasticity and Irreversible Thermodynamics," *J. Appl. Phys.*, **27** (1956), pp. 240-253.
101. W. Nowacki, *Dynamic Problems of Thermoelasticity*, Noordhoff (1975).
102. Huang, Y. M., Hamdi AbdelMohsen, M. H., Lohr, D., Feng, Z., Rowlands, R. E., and Stanley, P., "Determination of Individual Stress Components from SPATE Isopachics Only," *Proc. VI Intl. Congr. Exper. Mech.*, Vol. I, Portland OR, 6-10 June 1988, SEM, Bethel CT, pp. 578-584.
103. Hudson, R. D., Jr., *Infrared System Engineering*, Wiley, New York, 1969.
104. Lesniak, J. R., "Internal Stress Measurements," *Proc. VI Intl. Congr. Exper. Mech.*, Vol. II, Portland OR, 6-10 June 1988, SEM, Bethel CT, pp. 825-829.

105. Jones, R. M., *Mechanics of Composite Materials*, Scripta, 1975, Washington, D.C.
106. C. C. Chamis, "Simplified Composite Micromechanics Equations for Hygral, Thermal, and Mechanical Properties," *SAMPE Q'tly.*, **15** (1984), pp. 14-23.
107. Kriz, R. D. and Stinchcomb, W. W., "Effects of Moisture, Residual Thermal Curing Stresses, and Mechanical Load on the Damage Development in Quasi-Isotropic Laminates," *Damage in Composite Materials, STP 775*, K. L. Reifsnider, Ed., ASTM, Philadelphia, 1982, pp. 63-80.
108. Harris, C. E. and Morris, D. H., "An Evaluation of the Effects of Stacking Sequence and Thickness on the Fatigue Life of Quasi-Isotropic Graphite/Epoxy Laminates," NASA CR-172169, Langley Research Center, Hampton, VA, April 1983.
109. J. Morton, S. Kellas, and S. M. Bishop, "The Effect of Environment on the Fatigue Damage Development in Notched Carbon Fibre Composites," *Proc. 6th ICCM and 2nd ECCM*, Vol. 4, F. L. Mathews, N. C. R. Buskell, J. M. Hodgkinson, and J. Morton (Eds.), Elsevier, Amsterdam, 1987.

**The vita has been removed from
the scanned document**